Solution methods for failure analysis of massive structural elements

Andjelka Stanic

Par **Andjelka STANIC**

Solution methods for failure analysis of massive structural elements

Thèse présentée en cotutelle
pour l'obtention du grade
de Docteur de l'UTC

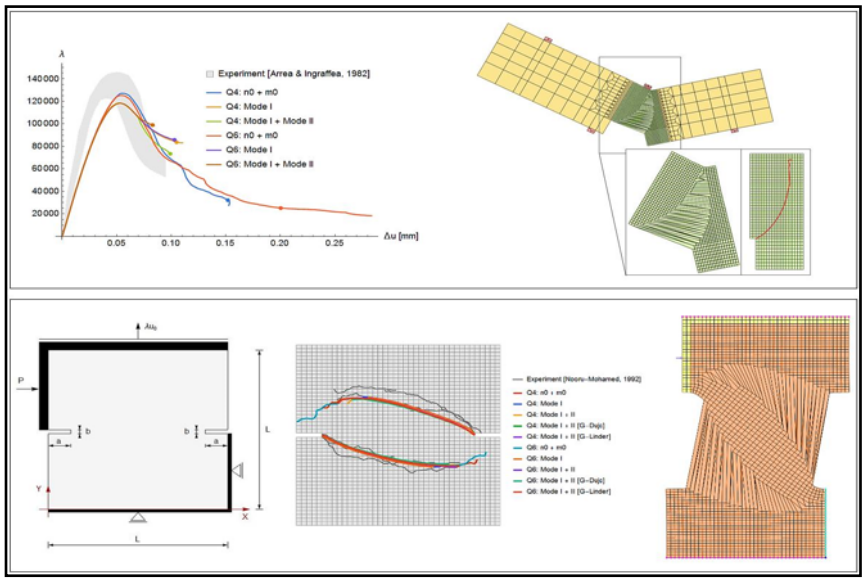

Soutenue le 7 décembre 2017
Spécialité : Mécanique Avancée **:** Unité de recherche en Mécanique - Laboratoire Roberval (UMR-7337)

D2383

THÈSE DE DOCTORAT

DE L'UNIVERSITÉ DE TECHNOLOGIE DE COMPIÈGNE

Présentée par

Andjelka STANIC

pour obtenir le grade de

DOCTEUR DE L'UNIVERSITÉ DE TECHNOLOGIE DE COMPIÈGNE

Spécialité : Mécanique Avancée

Sujet de la thèse

SOLUTION METHODS FOR FAILURE ANALYSIS OF MASSIVE STRUCTURAL ELEMENTS

Soutenue à Ljubljana le 7 décembre 2017 devant le jury composé de :

Président :	M. Matjaz MIKOS, Professeur, Université de Ljubljana, Slovénie
Rapporteurs :	M. Gordan JELENIC, Professeur, Université de Rijeka, Croatie
	M. Marko KEGL, Professeur, Université de Maribor, Slovénie
Examinatrice :	Mme Delphine BRANCHERIE, Maîtresse de conférences, Université de technologie de Compiègne, France
Directeurs :	M. Adnan IBRAHIMBEGOVIC, Professeur des universités, Université de technologie de Compiègne, France
	M. Bostjan BRANK, Professeur, Université de Ljubljana, Slovénie

Univerza
v Ljubljani
Fakulteta
za gradbeništvo
in geodezijo

UNIVERSITÉ DE TECHNOLOGIE
DE COMPIÈGNE

École doctorale Sciences pour l'Ingénieur
Laboratoire Roberval - UMR CNRS 7337

DOKTORSKI ŠTUDIJSKI
PROGRAM III. STOPNJE
GRAJENO OKOLJE

ANDJELKA STANIC

SOLUTION METHODS FOR FAILURE ANALYSIS OF MASSIVE STRUCTURAL ELEMENTS

Doctoral thesis

This doctoral thesis was prepared in accordance with the French-Slovenian Doctorate co-supervision agreement between the University of Technology of Compiègne and the University of Ljubljana.

Supervisors:

Bostjan BRANK, University of Ljubljana, Slovenia

Adnan IBRAHIMBEGOVIC, Université de Technologie de Compiègne, France

Ljubljana, December 7, 2017

BIBLIOGRAPHIC-DOCUMENTALISTIC INFORMATION AND ABSTRACT

UDC:	**519.876.5:624.012:624.07(043)**
Author:	**Andjelka Stanic**
Supervisor:	**Prof. Bostjan Brank, Ph.D.**
Co-supervisor:	**Prof. Adnan Ibrahimbegovic, Ph.D.**
Title:	**Solution methods for failure analysis of massive structural elements**
Document type:	**Doctoral Dissertation**
Notes:	**178 p., 33 tab., 113 fig., 252 eq., 89 ref.**
Keywords:	**finite element method, failure analysis, path-following method, localized failure, embedded discontinuity**

Abstract

The thesis studies: (i) the methods for failure analysis of solids and structures, and (ii) the embedded strong discontinuity finite elements for modelling material failures in quasi brittle 2d solids.

As for the failure analysis, the consistently linearized path-following method with quadratic constraint equation is first presented and studied in detail. The derived path-following method can be applied in the nonlinear finite element analysis of solids and structures in order to compute a highly nonlinear solution path. However, when analysing the nonlinear problems with the localized material failures (i.e. material softening), standard path-following methods can fail. For this reason we derived new versions of the path-following method, with other constraint functions, more suited for problems that take into account localized material failures. One version is based on adaptive one-degree-of-freedom constraint equation, which proved to be relatively successful in analysing problems with the material softening that are modelled by the embedded-discontinuity finite elements. The other versions are based on controlling incremental plastic dissipation or plastic work in an inelastic structure. The dissipation due to crack opening and propagation, computed by e.g. embedded discontinuity finite elements, is taken into account. The advantages and disadvantages of the presented path-following methods with different constraint equations are discussed and illustrated on a set of numerical examples.

As for the modelling material failures in quasi brittle 2d solids (e.g. concrete), several embedded strong discontinuity finite element formulations are derived and studied. The considered formulations are based either on: (a) classical displacement-based isoparametric quadrilateral finite element or (b) on quadrilateral finite element enhanced with incompatible displacements. In order to describe a crack formation and opening, the element kinematics is enhanced by four basic separation modes and related kinematic parameters. The interpolation functions that describe enhanced kinematics have a jump in displacements along the crack. Two possibilities were studied for deriving the operators in the local equilibrium equations that are responsible for relating the bulk stresses with the tractions in the crack. For the crack embedment, the major-principle-stress criterion was used, which is suitable for the quasi brittle materials. The normal and tangential cohesion tractions in the crack are described by two uncoupled, non-associative damage-softening constitutive relations. A new crack tracing algorithm is proposed for computation of crack propagation through the mesh. It allows for crack formation in several elements in a single solution increment. Results of a set of numerical examples are provided in order to assess the performance of derived embedded strong discontinuity quadrilateral finite element formulations, the crack tracing algorithm, and the solution methods.

INFORMATION BIBLIOGRAPHIQUE-DOCUMENTAIRE ET RESUME

CDU :	**519.876.5:624.012:624.07(043)**
Auteur :	**Andjelka Stanic**
Directeur de thèse :	**prof. Bostjan Brank, Ph.D.**
Co-directeur de thèse :	**prof. Adnan Ibrahimbegovic, Ph.D.**
Titre :	**Méthodes de résolution des problèmes à rupture des éléments structures massives**
Type de document :	**Mémoire de thèse de doctorat**
Notes :	**178 p., 33 tab., 113 fig., 252 éq., 89 ref.**
Mots-clés :	**méthode des éléments finis, analyse à rupture, méthode de continuation, rupture localisée, discontinuité forte**

Résumé

Objectifs de la thèse : (i) l'analyse à rupture de structure de type solides et membranes et (ii) la modélisation de la rupture quasi-fragile par la méthode des éléments finis à forte discontinuité en cas de solide 2D.

Dans ce travail, La méthode de continuation avec une équation de contrainte quadratique est présentée sous sa forme linéarisée. Cette méthode est généralement utilisée pour l'analyse des systèmes fortement non linéaires. Cependant, en présence de ruptures locales, la méthode de continuation standard peut échouer. Afin d'améliorer la performance de cette méthode, nous proposons de nouvelles versions plus sophistiquées qui prennent en compte les ruptures locales des matériaux. D'une part, une version est basée sur une équation supplémentaire adaptative imposant une limitation. Cette version est considérée relativement satisfaisante pour les matériaux adoucissants qui sont modélisés par la méthode des éléments finis à forte discontinuité. D'autres versions sont basées sur le contrôle de la dissipation incrémentale pour les matériaux inélastiques. La dissipation due à la formation de fissure et sa propagation, calculée par la méthode des éléments finis à forte discontinuité, est prise en compte. Les avantages et les inconvénients de différentes versions de la méthode de continuation sont discutés en s'appuyant sur une série d'exemples numériques.

Plusieurs formulations d'éléments finis à forte discontinuité sont présentées en détails pour l'analyse de rupture quasi-fragile. Les approximations discrètes du champ de déplacement sont basées sur (a) des éléments quadrilatérales isoparamétriques ou (b) des éléments quadrilatérales enrichis par la méthode des modes incompatibles. Afin de décrire la formation d'une fissure ainsi que son ouverture, la cinématique de l'élément est enrichie par quatre modes de séparation et des paramètres cinématiques. Les fonctions d'interpolation décrivant la cinématique enrichie possèdent un saut dans le déplacement le long de la fissure. Deux possibilités sont étudiées pour le calcul des opérateurs qui relient les contraintes de compressibilité aux tractions dans la fissure. Pour l'encastrement de la fissure, le critère de la contrainte principale est le plus adéquat pour les matériaux quasi-fragiles. Les contraintes de cohésion normale et tangentielle sont décrites selon une loi de comportement d'endommagement avec adoucissement. Cette dernière est découplée et non associative. On a également proposé un nouvel algorithme de repérage de fissure pour l'évaluation de la propagation de la fissure à travers le maillage. Cet algorithme est capable de détecter la formation de la fissure dans plusieurs éléments en un seul incrément. Plusieurs exemples numériques sont réalisés afin de montrer la performance de l'élément quadrilatéral à forte discontinuité ainsi que l'algorithme de repérage de fissure proposé.

BIBLIOGRAFSKO-DOKUMENTACIJSKA STRAN IN IZVLEČEK

UDK:	**519.876.5:624.012:624.07(043)**
Avtor:	**Andjelka Stanić**
Mentor:	**prof. dr. Boštjan Brank**
Somentor:	**prof. dr. Adnan Ibrahimbegović**
Naslov:	**Metode za porušno analizo masivnih konstrukcijskih elementov**
Tip dokumenta:	**Doktorska disertacija**
Obseg in oprema:	**178 str., 33 pregl., 113 sl., 252 en., 89 ref.**
Ključne besede:	**metoda končnih elementov, porušna analiza, metoda sledenja ravnotežne poti, lokalizirana porušitev, vgrajena nezveznost**

Izvleček

Doktorska disertacija obravnava: (i) metode za porušno analizo trdnih teles in konstrukcij, ter (ii) končne elemente z vgrajeno močno nezveznostjo za modeliranje materialne porušitve v kvazi krhkih 2d trdnih telesih.

Za porušno analizo smo najprej preučili konsistentno linearizirano metodo sledenja ravnotežne poti s kvadratno vezno enačbo (metoda krožnega loka). Metoda omogoča izračun analize nelinearnih modelov, ki imajo izrazito nelinearno ravnotežno pot. Kljub temu standardne metode sledenja poti lahko odpovedo, kadar analiziramo nelinearne probleme z lokalizirano materialno porušitvijo (mehčanje materiala). Zato smo izpeljali nove različice metode sledenja poti z drugimi veznimi enačbami, ki so bolj primerne za probleme z lokalizirano porušitvijo materiala. Ena različica temelji na adaptivni vezni enačbi, pri kateri vodimo izbrano prostostno stopnjo. Izkazalo se je, da je metoda relativno uspešna pri analizi problemov z materialnim mehčanjem, ki so modelirani s končnimi elementi z vgrajeno nezveznostjo. Druge različice temeljijo na kontroli plastične disipacije ali plastičnega dela v neelastičnem trdnem telesu ali konstrukciji. Upoštevana je tudi disipacija zaradi širjenja razpok v elementih z vgrajeno nezveznostjo. Prednosti in slabosti predstavljenih metod sledenja ravnotežnih poti z različnimi veznimi enačbami so predstavljeni na številnih numeričnih primerih.

Za modeliranje porušitve materiala v kvazi krhkih 2d trdnih telesih (npr. betonskih) smo izpeljali različne formulacije končnih elementov z vgrajeno močno nezveznostjo v pomikih. Obravnavane formulacije temeljijo bodisi (a) na klasičnem izoparametričnem štirikotnem končnem elementu bodisi (b) na štirikotnem končnem elementu, ki je izboljšan z nekompatibilnimi oblikami za pomike. Nastanek in širjenje razpoke opišemo tako, da kinematiko v elementu dopolnimo s štirimi osnovnimi oblikami širjenja razpoke in pripadajočimi kinematičnimi parametri. Interpolacijske funkcije, ki opisujejo izboljšano kinematiko, zajemajo skoke v pomikih vzdolž razpoke. Obravnavali smo dva načina izpeljave operatorjev, ki nastopajo v lokalni ravnotežni enačbi in povezujejo napetosti v končnem elementu z napetostmi na vgrajeni nezveznosti. Kriterij za vstavitev nezveznosti (razpoke) temelji na kriteriju največje glavne napetosti in je primeren za krhke materiale. Normalne in tangentne kohezijske napetosti v razpoki opišemo z dvema nepovezanima, poškodbenima konstitutivnima zakonoma za mehčanje. Predlagamo novi algoritem za sledenje razpoki za izračun širjenja razpoke v mreži končnih elementov. Algoritem omogoča formacijo razpok v več končnih elementih v enem obtežnem koraku. Izračunali smo številne numerične primere, da bi ocenili delovanje izpeljanih formulacij štirikotnih končnih elementov z vgrajeno nezveznostjo in algoritma za sledenje razpoki kot tudi delovanje metod sledenja ravnotežnih poti.

ZAHVALA

V času doktorskega študija sem sodelovala z ljudmi, ki so z veseljem delili svoje znanje z menoj in me usmerjali pri mojem raziskovalnem delu. Ob zaključku študija se zahvaljujem vsem profesorjem, sodelavcem in prijateljem, ki so mi pomagali med študijem. Posebno zahvalo namenjam svojemu mentorju, prof. dr. Boštjanu Branku. Najprej za priložnost, da sem lahko študirala in raziskovala pod njegovim vodstvom, potem za podporo pri delu, tudi takrat, ko se je zdelo, da je bil ves trud zaman. Hvala. En del študija sem opravila v Franciji, na Université de Technologie de Compiègne, v laboratoriju Roberval. Tam sem sodelovala s somentorjem, prof. dr. Adnanom Ibrahimbegovicem, ki se mu zahvaljujem za nasvete in ideje pri reševanju zapletenih problemov. Posebna hvala dr. Delphine Brancherie, ki mi je pomagala pri izpeljavi osnovnih končnih elementov z vgrajeno nezveznostjo. Zahvaljujem se Abir Boujelben, ki je prevedla povzetek v francoščino. Na tem mestu se želim zahvaliti tudi kolegom v Franciji za vsa skupna druženja: Ismar, Mijo, Eduard, Nam Do, Abir, Teja, Emina, Pablo, Emir, Ivan, Sara in Milan.

Iskrena hvala prof. dr. Jožetu Korelcu, ki me je vpeljal v svet programiranja in mi tudi pomagal pri implementaciji zahtevnih algoritmov. Zahvaljujem se dr. Blažu Hudobivniku, ki mi je pomagal odpraviti marsikaterega hrošča v moji računalniški kodi.

Zahvaljujem se mojim sošolkam, Teji Čeru in Petri Triller, za prijateljstvo in za skupne seminarske naloge. Tisočkrat hvala Brigiti, Snežni, moji sestri Valentini in staršem, Mariji in Ivanu, ki so mi stali ob strani in me spodbujali. Predvsem sem hvaležna mojim staršem za zgled, da je v življenju vredno vztrajati.

TABLE OF CONTENTS

LIST OF FIGURES

KAZALO SLIK

LIST OF TABLES

KAZALO PREGLEDNIC

1 INTRODUCTION

1.1 Motivation

One of the steps in the development of the structural elements in engineering is performing the experimental analysis in the laboratory, e.g. failure test on a reinforced concrete beam or concrete plate. Well-appointed laboratory enables to measure a lot of physical parameters during the observation: material parameters, dimensions of specimens, boundary and loading conditions, velocity, temperature, etc. The measurements provide a deep insight into behaviour of the specimen. Sometimes the experiment is not possible to perform due to the enormous dimensions or economic reasons. On the other side, the failure tests are limited on small number of specimens; preparation can be long and demanding. Therefore, besides the experimental analysis a computer simulation might be done to improve the development process.

The Computational Mechanics is used to develop a method that will enable to perform a reliable computer simulation regarding the experimental results from the laboratory. The numerical simulation procedure consists of modelling and performing analysis. Generally, we use the finite element method. A numerical model is a simplified approximation of the specimen, i.e. a mesh of finite elements with boundary conditions (supports and loads). The numerical model is analysed by appropriate path-following method and the result is a diagram, an equilibrium path. Namely, when the analysis is computed, we solve a set of equilibrium equations in the background. The equilibrium equations are based on the principles of mechanics and describe the system behaviour. In case of geometrically and/or materially nonlinear system, the equilibrium equations are highly nonlinear and they can be solved only by a proper path-following method.

The subject of the research work is development of enhanced models and computer simulations of structures under extreme loading conditions. We consider complex problems in nonlinear solid mechanics that take into account material failure phenomena. One example concerns determination of the onset and propagation of cracks in a concrete structural element. When we analyse such problems, the standard approach and computational methods can fail. For this reason we are trying to develop new method that will enable to compute the response of the nonlinear structure. Results of computer simulation will provide better understanding of structural problems related to durability of construction material under extreme loading conditions. Many examples of practical interest for model concern the structure and infrastructure increased durability, which could lead to great economic benefits.

1.2 Path-following methods

When solving a geometrically and/or materially nonlinear quasi-static time-independent solid or structural problem by the finite element method, a path-following strategy is often necessary in order to successfully compute a sequence of deformed configurations of the finite element mesh. The pioneering work on this topic was done by (Riks, 1979), (Crisfield, 1981), and (Ramm, 1981). From a mathematical viewpoint, those works relate to the solution of a parameterized set of non-linear equations, see e.g. (Rheinboldt, 1986). The Crisfield's method, called the arc-length method, seems to become the most popular (Crisfield, 1981, 1991, 1997). During the years, several modifications of different aspects of the Crisfield's arc-length method have been proposed, see e.g. (Alfano and Crisfield, 2001, 2003), (Geers, 1999, 1999b) and (Ritto-Correa and Camotim, 2008). Those modifications have been mainly concerned with the determination of the path travel in the predictor phase of the solution search, e.g. (Feng et al., 1995, 1996), (de Souza Neto and Feng, 1999), and with the choice of the form of the constraint equation, e.g. (de Borst, 1987), (Geers, 1999, 1999b), (Alfano and Crisfield, 2003). One of the basic features of the Crisfield's approach – keeping the constraint equation of its original form, when solving a system of nonlinear equations by the Newton-Raphson method – has remained unchanged in the vast majority of those proposals. Discussions on the path-following method with linearized constraint equation, which is sometimes called the consistently linearized path-following method, have been reported by e.g. (Schweizerhof and Wriggers, 1986), (Eriksson, 1989), (Carrera, 1994) and (Ritto-Correa and Camotim, 2008). We note that the term »consistently linearized« is here used in a sense that all governing equations, i.e. the equilibrium equations and the constraint equation, are linearized when searching for the solution of those equations in the framework of path-following method.

In this work, the consistently linearized path-following method is revisited. We apply it for geometrically nonlinear and elasto-plastic problems, as well as for the problems modelling the material failure (often referred to as the material softening problems) that are solved by the embedded-discontinuity finite element method (ED-FEM). Two types of constraint equations are considered: a quadratic one (that includes as special cases popular spherical and cylindrical forms, e.g. (Crisfield, 1991)), and another one that constrains only one degree-of-freedom (DOF), i.e. the critical DOF. The considered quadratic constraint equation (that combines increments of displacements, prescribed displacements and applied forces) is efficient for many geometrically and materially nonlinear problems that may include sharp turning points and/or bifurcation points. The corresponding consistently linearized path-following method can be effectively used with different nonlinear finite element formulations (e.g. displacement-based, stress-hybrid, incompatible-modes, and enhanced-assumed-strain elements) as well as with the elements having finite rotations DOFs and non-symmetric stiffness matrix.

However, the quadratic constraint equation cannot handle well the problems with the material softening. This has been well known, thus, the alternatives have been searched for such type of problems, see e.g. (de Borst, 1987), (Geers, 1999, 1999b), (Alfano and Crisfield, 2001, 2003), (Verhoosel et al., 2009) and (Pohl et al., 2014). As shown in the above mentioned works, the use of a new type of constraint equation, instead of the quadratic one, can lead to a path-following method that can solve the problems with the material

softening. In (Geers, 1999, 1999b), (Alfano and Crisfield, 2003) and (Pohl et al., 2014) the following idea was presented in different variations: a suitable subset of the degrees-of-freedom of the considered problem was chosen to be used in a constrained equation, and the subset was allowed to change from one increment to another. In this work, a similar idea, a one-DOF (i.e. the critical DOF) constraint equation that may change from increment to increment, is successfully applied for problems with material failure (i.e. material softening) that are computed by the embedded-discontinuity (ED) finite elements, e.g. (Armero and Ehrlich, 2006), (Dujc et al., 2010), (Dujc et al., 2010b), (Jukić et al., 2013), (Jukić et al., 2014).

Besides the above mentioned consistently linearized path-following methods, we also briefly discuss direct computation of critical points; see e.g. (Wriggers and Simo, 1990), (Eriksson, 1998), (Kouhia and Mikkola, 1999), (Parente Junior et al., 2006) and (Korelc, 2010) for further discussions on this topic. We perform direct computation of critical points by using a suitable constraint function in the framework of the linearized path-following method. In particular, the eigenvector-free constraint function (Korelc, 2010) is applied together with the automatic differentiation tool (Korelc, 2015) in order to get the exact derivatives of the constraint function. The exact derivatives provide a basis for a robust algorithm for an eigenvalue-free direct computation of critical points for problems with relatively small number of DOFs.

A specific path-following method is usually designed for a specific class of problems. The characteristic part of any path-following method is the constraint equation. Recently, (Verhoosel et al., 2009) presented constraint equations that are controlling energy dissipation in an inelastic material. In (Verhoosel et al., 2009), several constraint equations were presented, in particular for geometrically linear and geometrically nonlinear elasto-damage, and geometrically linear elasto-plasticity (without hardening).

In this work we extent the ideas of (Verhoosel et al., 2009) to geometrically nonlinear elasto-plasticity. In particular, we derive explicit and implicit constraint equations that control plastic dissipation for small strain elasto-plasticity with hardening (see e.g. (Simo and Hughes, 2000), (Ibrahimbegovic, 2009) for details on computational elasto-plasticity). The implementation of an explicit constraint equation in the framework of the consistently linearized path-following method, see e.g. (Schweizerhof and Wriggers, 1986), (Eriksson, 1989), (Wriggers, 2008), is rather straightforward. Namely, all the ingredients of the explicit constraint equation are already computed in the course of geometrically nonlinear elasto-plastic analysis, e.g. (Dujc and Brank, 2008) and (Wagner and Gruttmann, 2005). On the other hand, an implicit constraint equation is much more complex and its implementation is quite demanding.

An application of here presented formulations to embedded discontinuity finite elements, e.g. (Dujc et al., 2010, 2010b), (Jukić et al., 2013, 2014), that are used to model material failures, are presented in (Brank et al., 2016).

1.3 Enhanced finite element models for failure analysis (ED-FEM)

The occurrence of one or more macroscopic cracks in a structural element is a serious structural damage. The cracks may propagate and create a mechanism that may provoke the structural element failure. The numerical modeling of the formation and propagation of cracks in various materials is of great practical importance in engineering. For this reason, the numerical formulations for simulations of such problems have been under research, development and improvement for many years. The bases for such formulations are the theoretical works, which can be roughly divided into the two groups. One group of the theories belongs to the fracture mechanics and the other group of the theories falls into the mechanics of solids and structures. The latter group turned to be more suitable basis for numerical formulations that fall into the class of (extended) nonlinear finite element methods.

When deriving a finite element formulation that includes modeling of formation and propagation of cracks due to material failure, one must face problem of high mesh-sensitivity of the results, which is well-documented and well-researched. The problem occurs at its worst shape when strain-softening is added to standard inelastic constitutive relations (e.g. elasto-plasticity or elasto-damage) in order to model (smeared) cracks. The term strain-softening applies to that part of the constitutive relations, where by increasing strain the stress decreases. Many procedures have been proposed to mitigate the problem of unreliability of numerical results. Some of the most used are reviewed in e.g. (Ibrahimbegovic, 2009).

Recently two methods were proposed that almost completely eliminate the problem of mesh-sensitivity of the results. There is a considerable chance that these two methods will gradually make numerical simulations of the formation and propagation of cracks more robust, effective and simple to use. The first method is called the XFEM (Extended Finite Element Method). One of its versions has been already implemented in widely used commercial code for finite element analyses (Abaqus, 2015). The second method is called the Embedded Discontinuity Finite Element Method or the Embedded Strong Discontinuity Finite Element Method, abbreviated as ED-FEM or a similar acronym, e.g. (Linder and Armero, 2007), (Dujc et al., 2010), (Dujc and Brank, 2012), (Jukić et al., 2013), (Pirmanšek et al., 2017). The crack is modeled in both XFEM and ED-FEM as a surface for 3d problems, as a line for 2d problems and as a point for 1d problems. Across the crack, the displacements are discontinuous, and the strains in the crack are unbounded. One has a strong discontinuity (i.e. a jump) in displacements across the crack, which is incorporated (embedded) in both XFEM and ED-FEM finite elements. At XFEM, the kinematics of the finite element with built-in strong discontinuity is described by additional global degrees of freedom at the global (i.e. structural) level. At ED-FEM, additional degrees of freedom are local and statically condensed at the element level. For this reason, the implementation of the ED-FEM finite element in the finite element computer code for structural analysis is quite straightforward.

We note that there is also a version of XFEM and ED-FEM with a weak discontinuity, where the displacements are continuous through a narrow band representing a smeared-crack zone (or fracture-process zone) and strains are discontinuous (and bounded) there, see e.g. (Manzoli and Shing, 2006). However, such formulations will not be discussed further in this work.

1.4 The goals of the thesis

The aim of the present doctoral dissertation is developing solution methods for failure analysis of highly nonlinear problems. Within the research work, we set the following goals:

- To study the concept of the path-following method with quadratic constraint equation.
- To derive advanced constraint function that enables solving the set of nonlinear equations. We review the following ideas for a constraint equation:
    - Standard arc-length method (quadratic constraint equation);
    - Constraint equation for direct computation of critical equilibrium points;
    - One-DOF-constraint equation;
    - Constraint equation to control plastic dissipation;
- Coding and verification of newly derived path-following methods.
- To study the finite element method with embedded discontinuity in case of quadrilateral finite elements
- To study the propagation of cracks through the mesh.
- Coding and verification of newly derived quadrilateral finite elements with embedded discontinuity.

The derived solution methods and finite elements were implemented into the computer code AceFEM, see (Korelc, 2015), that is a finite element environment for numerical simulations in *Wolfram Mathematica* (Wolfram, 2016). The same software is used for all numerical simulations in the dissertation.

1.5 The outline of the thesis

Chapter 1 introduces readers to the subject of the dissertation. The motivation and theoretical background for the research work are exposed.

Chapter 2 is dedicated to the revision of standard path following method with constraint equation. A detailed study of the standard path-following method with quadratic equation (arc-length method) was performed. The concept of the arc-length method is the basis for the following research activity. The structural problems that take into account geometrical and/or material nonlinearity (e.g. truss dome, cylindrical panel) are analysed by the consistently linearized arc-length method. The equilibrium path of the geometrically nonlinear structural problem consists of the critical equilibrium points (limit point, bifurcation point), which could be determined only by stability analysis. Therefore the path-following method with constraint for direct computations of critical points is examined. Additionally, the branch-switching constraint equation is derived to determine new equilibrium point after the bifurcation point. The implemented methods perform very well for many nonlinear cases. But still cannot handle well the structural problems with material nonlinearity. The path-following method with one-degree-of-freedom

constraint equation is developed. The method is used to analyse numerical examples with localized material failure such as planar steel frame, 3-point bending test and 4-point bending test of the concrete beam.

The path-following method that control plastic dissipation is considered in the chapter 3. The idea is to control energy dissipated by the structure in each incremental step of the solution procedure (Verhoosel et al., 2009). In this work we develop dissipation constraint for geometrically nonlinear elasto-plasticity. The method is applied to analyse the cylindrical panels, half-of-sphere model and pinched cylinder. We also derive the dissipation constraint for embedded discontinuity finite elements, which is used to compute planar steel frame.

Chapter 4 is devoted to the structural problems with material softening that are computed by the embedded-discontinuity finite elements. We present several formulations related to the plane stress and plane strain quadrilateral finite element with embedded strong discontinuity in displacement (ED-FE). We study in detail the essential items of ED-FE formulations to have deep insight into their influences on finite element's behaviour. The research covers the incompatible mode method and two versions of G-operators (from (Dujc et al., 2010) and (Linder and Armero, 2007)) that play role in the virtual strains at the embedded discontinuity. The ED-FEs with different combinations of properties were examined through the simple tests for one or two-finite element mesh configuration, see chapter 5. Also, the propagation of cracks during the analysis is investigated – a crack tracing algorithm is used to enforce the crack continuity through the mesh. Chapter 6 presents the results of a set of numerical examples that are performed to assess the derived formulations.

The final chapter provides the concluding remarks of the thesis.

2 PATH-FOLLOWING METHODS FOR STRUCTURAL FAILURE PROBLEMS

We revisit a consistently linearized path-following method that can be applied in the nonlinear finite element analysis of solids and structures in order to compute a solution path. Within this framework, two constraint equations are considered: a quadratic one (that includes as special cases popular spherical and cylindrical forms of constraint equation), and another one that constrains only one degree-of-freedom (DOF), the critical DOF. In both cases, the constrained DOFs may vary from one solution increment to another. The former constraint equation is successful in analysing geometrically nonlinear and/or standard inelastic problems with snap-throughs, snap-backs and bifurcation points. However, it cannot handle problems with the material softening that are computed e.g. by the embedded-discontinuity finite elements. This kind of problems can be solved by using the latter constraint equation. The plusses and minuses of the both presented constraint equations are discussed and illustrated on a set of numerical examples. Some of the examples also include direct computation of critical points and branch switching. The direct computation of the critical points is performed in the framework of the path-following method by using yet another constraint function, which is eigenvector-free and suited to detect critical points.

The rest of the chapter is organized as follows. In Section 2.1, the theory and the implementation of the consistently linearized path-following method with the quadratic constraint equation is presented. This is followed by a description of the consistently linearized path-following method with one-DOF constraint equation that can change from increment to increment and is suitable for computation of failure problems due to material softening by the ED finite elements; see Section 0. In Section 2.3, some stability analysis procedures are briefly discussed. A set of numerical examples showing structural failures due to geometrical nonlinearity, plasticity and material failure is presented in Section 2.4 in order to illustrate performance of the derived path-following methods. The conclusions are drawn in Section 2.5.

2.1 Path-following method with constraint equation of quadratic form

2.1.1 System of nonlinear equations

In the framework of nonlinear finite element analysis of solids and structures, we consider a system of nonlinear equations consisting of: (i) nodal equilibrium equations, resulting from the discretization of the weak form of the boundary value problem, and (ii) a constraint equation:

$$\boldsymbol{G}\big(\boldsymbol{p}(t),\lambda(t)\big)=\begin{Bmatrix}\boldsymbol{R}\big(\boldsymbol{p}(t),\lambda(t)\big)\\ g\big(\boldsymbol{p}(t)-\boldsymbol{p}(t-\Delta t),\lambda(t)-\lambda(t-\Delta t)\big)\end{Bmatrix}=\boldsymbol{0} \tag{2.1}$$

In (2.1), $t\geq 0$ defines a monotonically increasing parameter called the arc-length (or the pseudo-time), Δ is small change, $\boldsymbol{p}$ is a vector of unknown nodal displacements of the finite element mesh (in what follows, the

term "displacements" will apply for both displacements and rotations if present), λ is the load factor, g is a constrain function, and $\boldsymbol{R}$ is:

$$\begin{aligned} &\boldsymbol{R}\big(\boldsymbol{p}(t),\lambda(t)\big) = \boldsymbol{R}^{int}\big(\boldsymbol{p}(t)\big) - \boldsymbol{R}^{ext}\big(\boldsymbol{p}(t),\lambda(t)\big), \\ &\boldsymbol{R}^{ext}(\boldsymbol{p}(t),\lambda(t)) = \boldsymbol{q}_{ref}^{fix} + \overline{\boldsymbol{q}}\big(\boldsymbol{p}(t),\lambda(t)\big) \end{aligned} \tag{2.2}$$

Here, $\boldsymbol{R}^{int}$ and $\boldsymbol{R}^{ext}$ are vectors of internal and external nodal forces of the finite element mesh, respectively, which dimensions equal dimension of $\boldsymbol{p}$ (we will use the term "forces" to describe both forces and moments if present). Vector $\boldsymbol{R}^{ext}$ collects the equivalent nodal forces due to: (i) external loadings given in terms of volume, area, line and concentrated forces that may depend on $\boldsymbol{p}$, (ii) non-zero prescribed displacements $\widehat{\boldsymbol{p}} = \lambda\, \widehat{\boldsymbol{p}}_{ref}$, where $\widehat{\boldsymbol{p}}_{ref}$ is a fixed vector, and (iii) thermal loading that depends on λ. The dead load is applied by $\boldsymbol{q}_{ref}^{fix}$. A pattern of live loads is applied by $\overline{\boldsymbol{q}}$.

We search for the solution of (2.1) at the discrete pseudo-time points: $0 = t_0, t_1, \cdots, t_n, t_{n+1}, \cdots, t_{final}$. Let us assume as known a finite element mesh configuration at t_n defined by the pair $\{\boldsymbol{p}(t_n), \lambda(t_n)\} \equiv \{\boldsymbol{p}_n, \lambda_n\}$. When searching for configuration at $t_{n+1} = t_n + \Delta t_n$, we decompose $\boldsymbol{p}_{n+1}$ and λ_{n+1} into two parts:

$$\boldsymbol{p}_{n+1} = \boldsymbol{p}_n + \Delta\boldsymbol{p}_n, \qquad \lambda_{n+1} = \lambda_n + \Delta\lambda_n \tag{2.3}$$

where $\Delta\boldsymbol{p}_n$ and $\Delta\lambda_n$ are called the incremental displacement vector and the incremental load factor, respectively. Assuming that $\overline{\boldsymbol{q}}$ is a linear function of λ, i.e. $\overline{\boldsymbol{q}} = \lambda\boldsymbol{q}$, one can define:

$$\overline{\boldsymbol{q}}_{n+1} = \lambda_{n+1}\boldsymbol{q}_{n+1} = \lambda_n\boldsymbol{q}_n + \Delta(\lambda_n\boldsymbol{q}_n) \approx \lambda_n\boldsymbol{q}_n + \Delta\lambda_n\boldsymbol{q}_n \tag{2.4}$$

If $\boldsymbol{q}$ is configuration independent, then $\boldsymbol{q}_n$ in (2.4) is $\boldsymbol{q}_n = \boldsymbol{q}_{ref}$, where $\boldsymbol{q}_{ref}$ is a fixed vector (and $\approx$ in (2.4) changes to $=$). With (2.3), the equations (2.1) can be rewritten for the pseudo-time point t_{n+1} as:

$$\boldsymbol{G}_{n+1}(\boldsymbol{p}_n, \lambda_n; \Delta\boldsymbol{p}_n, \Delta\lambda_n) = \begin{Bmatrix} \boldsymbol{R}_{n+1}(\boldsymbol{p}_n, \lambda_n; \Delta\boldsymbol{p}_n, \Delta\lambda_n) \\ g_{n+1}(\Delta\boldsymbol{p}_n, \Delta\lambda_n) \end{Bmatrix} = \boldsymbol{0} \tag{2.5}$$

where $\boldsymbol{p}_n$ and λ_n are known and $\Delta\boldsymbol{p}_n$ and $\Delta\lambda_n$ are the unknowns.

The following quadratic constraint equation will be addressed in the rest of Section 2.1:

$$g_{n+1}(\Delta\boldsymbol{p}_n, \Delta\lambda_n) = \Delta\boldsymbol{p}_n^T\boldsymbol{W}_n\Delta\boldsymbol{p}_n + \psi_1^2\Delta\lambda_n^2\boldsymbol{q}_n^T\boldsymbol{H}_n\boldsymbol{q}_n + \psi_2^2\Delta\lambda_n^2\widehat{\boldsymbol{p}}_{ref}^T\widehat{\boldsymbol{W}}_n\widehat{\boldsymbol{p}}_{ref} - \Delta l_n^2 = 0 \tag{2.6}$$

where $\psi_1 \geq 0$ and $\psi_2 \geq 0$ are scaling factors, Δl_n is given data for the increment $[t_n, t_{n+1}]$, and $\boldsymbol{W}_n$, $\boldsymbol{H}_n$ and $\widehat{\boldsymbol{W}}_n$ are diagonal scaling matrices (the index *n* suggests that they may change from increment to increment). When setting $\psi_2 = 0$ and $\boldsymbol{W}_n = \boldsymbol{H}_n = \boldsymbol{I}$ (where $\boldsymbol{I}$ is the identity matrix) in (2.6), the spherical arc-length constraint equation is obtained (Crisfield, 1991). For widely used cylindrical arc-length constraint equation (Crisfield, 1991), one should set $\psi_1 = \psi_2 = 0$ and $\boldsymbol{W}_n = \boldsymbol{I}$.

2.1.2 Linearization

The equations (2.5) are nonlinear with respect to $\Delta\boldsymbol{p}_n$ and $\Delta\lambda_n$, thus, the solution is searched iteratively by the Newton-Raphson method. At an iteration *i*, the following linear system of equations has to be solved:

$$\begin{bmatrix} \boldsymbol{K}^i_{n+1}\left(\boldsymbol{p}^i_{n+1},\lambda^i_{n+1}\right) & \boldsymbol{R}^i_{n+1,\lambda}\left(\boldsymbol{p}^i_{n+1},\lambda^i_{n+1}\right) \\ \left[g^i_{n+1,\boldsymbol{p}}(\Delta\boldsymbol{p}^i_n)\right]^T & g^i_{n+1,\lambda}(\Delta\lambda^i_n) \end{bmatrix} \begin{Bmatrix} \Delta\widetilde{\boldsymbol{p}}^i_n \\ \Delta\tilde{\lambda}^i_n \end{Bmatrix} = -\begin{Bmatrix} \boldsymbol{R}^i_{n+1}\left(\boldsymbol{p}^i_{n+1},\lambda^i_{n+1}\right) \\ g^i_{n+1}(\Delta\boldsymbol{p}^i_n,\Delta\lambda^i_n) \end{Bmatrix} \tag{2.7}$$

for the pair $\left\{\Delta\widetilde{\boldsymbol{p}}^i_n,\Delta\tilde{\lambda}^i_n\right\}$. Here, $\boldsymbol{p}^i_{n+1}=\boldsymbol{p}_n+\Delta\boldsymbol{p}^i_n$ and $\lambda^i_{n+1}=\lambda_n+\Delta\lambda^i_n$, see (2.3), and $\boldsymbol{p}_n$ and λ_n are converged values at t_n. The iterative update of the displacement vector and the load factor, respectively, will provide the next iterative guess of the incremental displacement vector, the incremental load factor, and the corresponding total values:

$$\begin{aligned} \Delta\boldsymbol{p}^{i+1}_n &= \Delta\boldsymbol{p}^i_n+\Delta\widetilde{\boldsymbol{p}}^i_n, \qquad \Delta\lambda^{i+1}_n=\Delta\lambda^i_n+\Delta\tilde{\lambda}^i_n \\ \boldsymbol{p}^{i+1}_{n+1} &= \boldsymbol{p}_n+\Delta\boldsymbol{p}^{i+1}_n, \qquad \lambda^{i+1}_{n+1}=\lambda_n+\Delta\lambda^{i+1}_n \end{aligned} \tag{2.8}$$

By considering chosen constraint equation (2.6), one can conclude on the following terms in (2.7):

$$g^i_{n+1,\boldsymbol{p}}=\frac{\partial g^i_{n+1}}{\partial\Delta\boldsymbol{p}^i_n}=2\boldsymbol{W}_n\Delta\boldsymbol{p}^i_n \tag{2.9}$$

$$g^i_{n+1,\lambda}=\frac{\partial g^i_{n+1}}{\partial\Delta\lambda^i_n}=2\Delta\lambda^i_n\psi_1^2\boldsymbol{q}^T_n\boldsymbol{H}_n\boldsymbol{q}_n+2\Delta\lambda^i_n\psi_2^2\widehat{\boldsymbol{p}}^T_{ref}\widehat{\boldsymbol{W}}_n\widehat{\boldsymbol{p}}_{ref} \tag{2.10}$$

In (2.7), $\boldsymbol{K}^i_{n+1}$ is the tangent stiffness matrix. To get $\boldsymbol{R}^i_{n+1,\lambda}$ in (2.7), the following derivation is performed:

$$\boldsymbol{R}^i_{n+1,\lambda}=\frac{\partial\boldsymbol{R}^i_{n+1}}{\partial\Delta\lambda^i_n}=-\frac{\partial\boldsymbol{R}^{ext,i}_{n+1}}{\partial\Delta\lambda^i_{n+1}} \tag{2.11}$$

For the thermal loading contribution to $\boldsymbol{R}^i_{n+1,\lambda}$ we refer to (Parente Junior et al, 2006).

2.1.3 Bordering algorithm

System of linear equations (2.7) can be solved effectively by the bordering algorithm, see e.g. (Wriggers, 2008). In order to apply the algorithm, the iterative update of the iterative displacements $\Delta\widetilde{\boldsymbol{p}}^i_n$ is additively decomposed into two parts:

$$\Delta\widetilde{\boldsymbol{p}}^i_n=\Delta\widetilde{\boldsymbol{p}}^i_{n\boldsymbol{p}}+\Delta\tilde{\lambda}^i_n\Delta\widetilde{\boldsymbol{p}}^i_{n\lambda} \tag{2.12}$$

By using decomposition (2.12) in the first equation in (2.7), one gets:

$$\boldsymbol{K}^i_{n+1}\Delta\widetilde{\boldsymbol{p}}^i_{n\boldsymbol{p}}+\Delta\tilde{\lambda}^i_n\left(\boldsymbol{K}^i_{n+1}\Delta\widetilde{\boldsymbol{p}}^i_{n\lambda}+\boldsymbol{R}^i_{n+1,\lambda}\right)=-\boldsymbol{R}^i_{n+1} \tag{2.13}$$

Equation (2.13) can be rewritten as:

$$\underbrace{\boldsymbol{K}^i_{n+1}\Delta\widetilde{\boldsymbol{p}}^i_{n\boldsymbol{p}} + \boldsymbol{R}^i_{n+1}}_{=\mathbf{0}} + \Delta\tilde{\lambda}^i_n \underbrace{\left(\boldsymbol{K}^i_{n+1}\Delta\widetilde{\boldsymbol{p}}^i_{n\lambda} + \boldsymbol{R}^i_{n+1,\lambda}\right)}_{=\mathbf{0}} = \mathbf{0} \tag{2.14}$$

which implies that it can be fulfilled by solving two systems of linear equations:

$$\boldsymbol{K}^i_{n+1}\Delta\widetilde{\boldsymbol{p}}^i_{n\boldsymbol{p}} = -\boldsymbol{R}^i_{n+1}, \quad \boldsymbol{K}^i_{n+1}\Delta\widetilde{\boldsymbol{p}}^i_{n\lambda} = -\boldsymbol{R}^i_{n+1,\lambda} \tag{2.15}$$

Equations (2.15) have the same matrix on the left hand side and different vectors at the right hand side. By using decomposition (2.12) in the second equation in (2.7), one gets:

$$g^{i,T}_{n+1,\boldsymbol{p}}\left(\Delta\widetilde{\boldsymbol{p}}^i_{n\boldsymbol{p}} + \Delta\tilde{\lambda}^i_n\Delta\widetilde{\boldsymbol{p}}^i_{n\lambda}\right) + g^i_{n+1,\lambda}\Delta\tilde{\lambda}^i_n = -g^i_{n+1} \tag{2.16}$$

which can be rewritten as

$$\Delta\tilde{\lambda}^i_n = \frac{-g^i_{n+1} - g^{i,T}_{n+1,\boldsymbol{p}}\,\Delta\widetilde{\boldsymbol{p}}^i_{n\boldsymbol{p}}}{g^{i,T}_{n+1,\boldsymbol{p}}\,\Delta\widetilde{\boldsymbol{p}}^i_{n\lambda} + g^i_{n+1,\lambda}} \tag{2.17}$$

An iterative solution of (2.7) is thus obtained by: (i) solving the linear systems (2.15), (ii) computing (2.17), and (iii) evaluating (2.12) and (2.8).

2.1.4 Implementation of the bordering algorithm

In order to start with the iterations, $i = 1,2,3,\cdots$, the initial guess for the incremental displacement vector and the incremental load factor, $\Delta\boldsymbol{p}^*_n$ and $\Delta\lambda^*_n$, respectively, is needed. Computation of the initial guess is called the predictor phase.

2.1.4.1 The predictor phase

Consider the converged configuration at t_n; we will mark the related values with the superscript "0". One has:

$$\Delta\boldsymbol{p}^0_n = \mathbf{0}, \quad \Delta\lambda^0_n = 0, \quad \boldsymbol{R}^0_{n+1} = \mathbf{0} \tag{2.18}$$

Equations (2.15) can be used to compute:

$$\Delta\widetilde{\boldsymbol{p}}^0_{n\lambda} = -(\boldsymbol{K}^0_{n+1})^{-1}\boldsymbol{R}^0_{n+1,\lambda}, \quad \Delta\widetilde{\boldsymbol{p}}^0_{n\boldsymbol{p}} = \mathbf{0} \tag{2.19}$$

In (2.19), $\boldsymbol{K}^0_{n+1}$ and $\boldsymbol{R}^0_{n+1,\lambda}$ are evaluated with the displacement vector $\boldsymbol{p}^0_{n+1} = \boldsymbol{p}_n$ and the load factor $\lambda^0_{n+1} = \lambda_n$. According to (2.12), the initial guess (the predictor) for the incremental displacement is:

$$\Delta\boldsymbol{p}^*_n = \Delta\lambda^*_n\Delta\widetilde{\boldsymbol{p}}^0_{n\lambda} \tag{2.20}$$

It seems reasonable to demand that the initial guess parameters satisfy the constraint equation $g_{n+1}^{*}=0$, see (2.6). Such a demand provides the initial guess (the predictor) for the incremental load factor $\Delta\lambda_n^{*}$:

$$\Delta\lambda_n^{*}=s_{n+1}\frac{\Delta l_n}{\sqrt{\Delta\widetilde{\boldsymbol{p}}_{n\lambda}^{0,T}\,\boldsymbol{W}_n\Delta\widetilde{\boldsymbol{p}}_{n\lambda}^{0}+\psi_1^2\boldsymbol{q}_n^T\boldsymbol{H}_n\boldsymbol{q}_n+\psi_2^2\widehat{\boldsymbol{p}}_{ref}^T\widehat{\boldsymbol{W}}_n\widehat{\boldsymbol{p}}_{ref}}},\qquad s_{n+1}=\pm 1 \tag{2.21}$$

Equation (2.21) indicates that the sign of the predictor of the incremental load factor has to be chosen. Several criteria have been proposed for the sign determination of the incremental load factor in the spherical/cylindrical arc-length method; see (Ritto-Correa and Camotim, 2008) for a recent review on this topic. Those criteria can be equally well applied for the present consistently linearized arc-length method with the quadratic constraint equation (2.6). In this work we will use:

$$s_{n+1}=sign((\boldsymbol{p}_n-\boldsymbol{p}_{n-1})^T\Delta\widetilde{\boldsymbol{p}}_{n\lambda}^{0}) \tag{2.22}$$

where $\boldsymbol{p}_n$ and $\boldsymbol{p}_{n-1}$ are converged values of the displacements at t_n and t_{n-1}, respectively. The criterion (2.22) was used and/or studied in (Jun and Hong, 1988), (Feng et al. 1995, 1996), (de Souza Neto and Feng, 1999), (Brank and Carrera, 2000) and (Ritto-Correa and Camotim, 2008). In conclusion of this section we can summarize: equations (2.19)-(2.22) provide the initial guess for the incremental displacement vector $\Delta\boldsymbol{p}_n^{*}$ as well as the initial guess for the incremental load factor $\Delta\lambda_n^{*}$.

2.1.4.2 The corrector phase

Once the predictors $\Delta\boldsymbol{p}_n^{*}$, $\Delta\lambda_n^{*}$ are known, the corrector phase can start by running the iteration loop $i=1,2,3,\cdots$. The predictors are used in the first iteration as:

$$\Delta\boldsymbol{p}_n^{1}=\Delta\boldsymbol{p}_n^{*},\quad \Delta\lambda_n^{1}=\Delta\lambda_n^{*},\quad \boldsymbol{p}_{n+1}^{1}=\boldsymbol{p}_n+\Delta\boldsymbol{p}_n^{1},\quad \lambda_{n+1}^{1}=\lambda_n+\Delta\lambda_n^{1} \tag{2.23}$$

For an i^{th} iteration the sequence of computations is as follows: (i) compute $\boldsymbol{K}_{n+1}^{i}\left(\boldsymbol{p}_{n+1}^{i},\lambda_{n+1}^{i}\right)$, $\boldsymbol{R}_{n+1}^{i}\left(\boldsymbol{p}_{n+1}^{i},\lambda_{n+1}^{i}\right)$, and $\boldsymbol{R}_{n+1,\lambda}^{i}\left(\boldsymbol{p}_{n+1}^{i},\lambda_{n+1}^{i}\right)$, (ii) solve equations (2.15), (iii) compute (2.17), (iv) evaluate (2.12) and (2.8). The following criterion can be chosen for exiting the iteration loop:

$$err=\sqrt{\frac{\Delta\widetilde{\boldsymbol{p}}_n^{i,T}\,\Delta\widetilde{\boldsymbol{p}}_n^{i}}{dim(\Delta\widetilde{\boldsymbol{p}}_n^{i})}+\left(\Delta\tilde{\lambda}_n^{i}\right)^2}\quad\leq\quad tol \tag{2.24}$$

where $dim(\Delta\widetilde{\boldsymbol{p}}_n^{i})$ is the dimension of vector $\Delta\widetilde{\boldsymbol{p}}_n^{i}$. If (2.24) holds, the equilibrium (converged) configuration at t_{n+1} is defined with $\Delta\boldsymbol{p}_n=\Delta\boldsymbol{p}_n^{i}+\Delta\widetilde{\boldsymbol{p}}_n^{i}$ and $\Delta\lambda_n=\Delta\lambda_n^{i}+\Delta\tilde{\lambda}_n^{i}$, see (2.8) and (2.3). The search for the solution at the next pseudo-time point $t_{n+2}=t_{n+1}+\Delta t_{n+1}$ can start (the above described algorithm is repeated by setting $t_{n+1}\rightarrow t_n, t_{n+2}\rightarrow t_{n+1}$). On the other hand, if criterion (2.24) is not fulfilled, a new iteration swap is performed for the same pseudo-time point t_{n+1} (the above described algorithm is repeated by setting $i+1\rightarrow i$).

2.1.5 Remarks on the considered path-following method and its implementation

To deal with the prescribed displacements it is not necessary to include them explicitly in (2.6). We did so in order to collect several types of external loadings in (2.6). This might improve the search for the solution.

For the structural finite elements with the finite rotations, the additive decomposition (2.3) and the additive update (2.8) are valid if the finite rotations parameters (that enter the vector $\boldsymbol{p}$) are additively updated. This kind of shell and beam finite elements are presented e.g. in (Brank et al., 1997), (Betsch et al., 1998), (Brank et al., 2002), (Ibrahimbegovic and Taylor, 2002), (Brank, 2005), (Kegl et al., 2008), (Dujc and Brank, 2012) (for mutual relationships between different parameterizations of finite rotations see e.g. (Brank and Ibrahimbegovic, 2001)). Thus, the above presented formulation is applicable for structural elements with additive update of nodal rotational parameters.

The presented path-following procedure can be applied also for the structural finite elements that use a finite rotation parameterization that demand the multiplicative update (e.g. (Simo and Vu-Quoc, 1986), (Simo et al., 1990), (Jelenić and Saje, 1995), (Betsch et al., 1998), (Jelenić and Crisfield, 1999)). In that case, however, the rotational degrees-of-freedom should be excluded from the constraint equation (2.6) by setting to 0 the corresponding diagonal terms in $\boldsymbol{W}_n$ and $\widehat{\boldsymbol{W}}_n$. Of course, the additive update (2.3) should be replaced by a corresponding multiplicative update that suits chosen rotational degrees-of-freedom.

The above path-following procedure has been presented for the displacement-based finite element formulations. For the hybrid-stress based, e.g. (Pian and Simihara, 1985), the incompatible-modes based, e.g. (Ibrahimbegovic and Wilson, 1991), and the enhanced-assumed-strain based (e.g. (Simo and Armero, 1992), (Brank, 2008), (Caseiro et al., 2013)) nonlinear structural and solid finite element formulations, the presented arc-length procedure is fully applicable. The above presented finite element and the assembled stiffness matrices, as well as the finite element and the assembled residual vectors, should be simply replaced by the corresponding ones obtained by a chosen hybrid-stress, incompatible-modes or enhanced-assumed-strain formulations.

The scaling matrices $\boldsymbol{W}_n$, $\boldsymbol{H}_n$ and $\widehat{\boldsymbol{W}}_n$ enable designing a constraint equation as a function of only a certain number of the degrees-of-freedom of the finite element mesh. Not all degrees-of-freedom are involved. The chosen degrees-of-freedom may vary from one increment to another. Such an approach is equivalent to the local sub-plane method of (Geers, 1999, 1999b).

As for the previous remark, the constraint equation can be defined with all the degrees-of-freedom of the finite element mesh, with their relative importance weighted through the scaling matrices $\boldsymbol{W}_n$, $\boldsymbol{H}_n$ and $\widehat{\boldsymbol{W}}_n$ according to some predefined criterion. Such an approach was studied in e.g. (de Borst, 1987) and (Geers, 1999, 1999b).

In relation to the two previous remarks, it would have been useful to derive an automated procedure for choosing: (i) either the most appropriate set of degrees-of-freedom in each increment or (ii) the most appropriate weights in the scaling matrices. However, such a procedure is not studied. For discussions on this subject see e.g. (Geers, 1999, 1999b) and (Alfano and Crisfield, 2001). A discussion on scaling factor ψ_1 and scaling matrix $\boldsymbol{W}_n$ can be found in (Crisfield, 1991) and references therein.

The value of Δl_n can be changed incrementally as $\Delta l_n = B(I_o, I_{n-1})\,\Delta l_{n-1}$, $\Delta l_n \in [\Delta l_{min}, \Delta l_{max}]$ The adjustable factor B is a function of two parameters: I_0, which is a desired number of incremental iterations, and I_{n-1}, which represents a number of iterations in the last converged increment. In the examples below, we determine B as (Korelc, 2014):

$$B = \begin{cases} 2 - \left(\dfrac{I_{n-1} - 1}{I_o - 1}\right)^2, & I_{n-1} < I_o \\ 1 - \dfrac{1}{2}\left(\dfrac{I_{n-1} - I_o}{N - I_o}\right)^2, & I_{n-1} \geq I_o \end{cases} \tag{2.25}$$

where N is the maximum allowed number of iterations. More usual choice is, see (Crisfield, 1991), $B = \left(\frac{I_0}{I_{n-1}}\right)^{\gamma}$, where the default value for γ is ½.

2.1.6 Optimal performance of the considered path-following method

The scaling matrices and scaling factors in the constraint equation (2.6) offer options to regulate the path-following procedure. Different problem-dependent scaling schemes have been advocated for $\boldsymbol{W}_n, \boldsymbol{H}_n$ and ψ_1 in e.g. (de Borst, 1987), (Crisfield, 1991), (Geers, 1999, 1999b), (Alfano and Crisfield, 2001). Unfortunately, a general theory for selecting optimal scaling values in (2.6) for a specific problem does not exist.

In this work, we will elaborate on scaling for a case $\boldsymbol{W}_n = \boldsymbol{H}_n = \widehat{\boldsymbol{W}}_n = \boldsymbol{I}$ and $\psi_2 = 0$. The aim is to find such a scaling that the first and the second term on the right side of (2.6) are of the same order. Obviously, the values of those two terms depend on the units, used for displacements and forces, and on ψ_1. Rather than fixing units of input data and searching for a suitable value of ψ_1, we set $\psi_1 = 1$ and look for appropriate units. We propose a simple test, summarized in Table 2.1, before running the analysis with the path-following method. If chosen input data units pass this test, we run the path-following procedure with $\psi_1 = 1$. Otherwise, the second part of the constraint equation (2.6) is predominant and dictates the procedure; in such a case we rather use $\psi_1 = 0$.

Table 2.1: A scaling test for input data.
Preglednica 2.1: Test merskih enot za vhodne podatke.

(i)	Choose units for displacements and forces. Set $\psi_1 = 0$.
(ii)	Compute one iteration (only the predictor phase, i.e. $n = 1$, $i = 0$). Compute $\left\|\Delta\tilde{\boldsymbol{p}}_{1\lambda}^0\right\|$ and $T = \dfrac{\left\|\Delta\tilde{\boldsymbol{p}}_{1\lambda}^0\right\|}{\|\boldsymbol{q}_1\|}$.
(iii)	For $0.1 \leq T \leq 10$ input units are OK.

2.2 Path-following method with control displacement constraint

In this section, we will replace the quadratic constraint equation (2.6) with a new one and describe the corresponding changes of the arc-length method presented in Section 2.1.

2.2.1 Control displacement constraint

Let us replace the quadratic constraint equation (2.6) with the following one:

$$g_{n+1}(\Delta \boldsymbol{p}_n) = \boldsymbol{w}_{n+1}^T \Delta \boldsymbol{p}_n - s_{n+1} \Delta \widehat{D}_n = 0, \qquad s_{n+1} = \text{sign}(\boldsymbol{w}_{n+1}^T \Delta \boldsymbol{p}_n) \tag{2.26}$$

Here, $\boldsymbol{w}_{n+1}$ is a vector of zero entries, except for a single non-zero entry that is set to 1 and defines the controlled (i.e. the constrained) incremental displacement. The value of the desired absolute change of the controlled incremental displacement is $\Delta \widehat{D}_n > 0$. The replacement of (2.6) with (2.26) implies the new forms of the vector $g_{n+1,\boldsymbol{p}}^i$ and the scalars needed in the algorithm described in Sections 2.1.2 and 2.1.3:

$$g_{n+1,\boldsymbol{p}}^i = \boldsymbol{w}_{n+1}^T, \qquad g_{n+1,\lambda}^i = 0 \tag{2.27}$$

$$\Delta \tilde{\lambda}_n^i = \frac{-\boldsymbol{w}_{n+1}^T \left(\Delta \boldsymbol{p}_n^i - \Delta \widetilde{\boldsymbol{p}}_{n\boldsymbol{p}}^i \right) + s_{n+1} \Delta \widehat{D}_n}{\boldsymbol{w}_{n+1}^T \Delta \widetilde{\boldsymbol{p}}_{n\lambda}^i} = \frac{d^i - a^i}{b^i + c^i} \tag{2.28}$$

$$a^i = \boldsymbol{w}_{n+1}^T \Delta \widetilde{\boldsymbol{p}}_{n\boldsymbol{p}}^i, \qquad b^i = \boldsymbol{w}_{n+1}^T \Delta \widetilde{\boldsymbol{p}}_{n\lambda}^i = \boldsymbol{w}_{n+1}^T \Delta \boldsymbol{p}_n^i - s_{n+1} \Delta \widehat{D}_n, \qquad c^i = 0, \qquad -d^i = g_{n+1}^i \tag{2.29}$$

With (2.26)-(2.29) in hand, the algorithm from Sections 2.1.2 and 2.1.3 can be applied. However, we have to choose either 1 or -1 for s_{n+1} in (2.26). In this work we assume that the change of the constrained displacement in the current increment $[t_n, t_{n+1}]$ has the sign of its change in the previous increment $[t_{n-1}, t_n]$, i.e.

$$s_{n+1} = \text{sign}(\boldsymbol{w}_{n+1}^T \Delta \boldsymbol{p}_n) = \text{sign}(\boldsymbol{w}_{n+1}^T \Delta \boldsymbol{p}_{n-1}) \tag{2.30}$$

where $\Delta \boldsymbol{p}_{n-1} = \boldsymbol{p}_n - \boldsymbol{p}_{n-1}$, and $\boldsymbol{p}_n$ and $\boldsymbol{p}_{n-1}$ are the converged values of the displacements at t_n and t_{n-1}, respectively.

2.2.2 Control displacement choice

The path-following procedure, described in section 2.2.1, is switched on when (or soon after) the material softening is triggered in at least one element of the mesh. It is assumed in this work that the material softening is described by the embedded-discontinuity (ED) finite elements with condensed ED parameters, see e.g. (Armero and Ehrlich, 2006), (Dujc et al. 2010, 2010b, 2013).

The search for a suitable degree-of-freedom candidate that will enter the constraint equation (2.26) in the current increment $[t_n, t_{n+1}]$ goes as follows:

- A set of finite elements that comply with the following demands is created: (i) the element has one or more active (i.e. non-zero) ED parameters at the pseudo-time t_n (the element ED parameters will be denoted as $\boldsymbol{\alpha}_n^{(e)}$), (ii) the value of each entry of $\boldsymbol{\alpha}_n^{(e)}$ is less than some prescribed maximal value, i.e. $\left|\left(\boldsymbol{\alpha}_n^{(e)}\right)_k\right| \leq \alpha_{n,MAX}$. This set will be called $Sels$.
- Among all the elements in $Sels$ we choose the one with the largest norm $\left\|\boldsymbol{\alpha}_n^{(e)}\right\|$ and call it the control element Cel.
- The values of all degrees-of-freedom of the control element Cel are checked in order to find the one that changed the most in the previous increment $[t_{n-1}, t_n]$. This will be the control (i.e. the constrained) displacement for the current increment $[t_n, t_{n+1}]$. It will be used in (2.26).
- When the control displacement is chosen, we can create vector $\boldsymbol{w}_{n+1}$ that is needed in (2.26)-(2.30).

The initial guess (the predictor) for the incremental displacement $\Delta\boldsymbol{p}_n^*$ equals:

$$\Delta\widetilde{\boldsymbol{p}}_{n\lambda}^0 = -(\boldsymbol{K}_{n+1}^0)^{-1}\boldsymbol{R}_{n+1,\lambda}^0, \quad \Delta\widetilde{\boldsymbol{p}}_{n\boldsymbol{p}}^0 = \boldsymbol{0} \quad \Rightarrow \quad \Delta\boldsymbol{p}_n^* = \Delta\lambda_n^*\Delta\widetilde{\boldsymbol{p}}_{n\lambda}^0 \tag{2.31}$$

We can now continue with the predictor phase of the bordering algorithm. From the requirement that the initial guess parameters need to satisfy the constraint equation $g_{n+1}^* = 0$, see (2.26), the initial guess (the predictor) for the incremental load factor $\Delta\lambda_n^*$ is computed as:

$$\Delta\lambda_n^* = \frac{s_{n+1}\Delta\widehat{D}_n}{\boldsymbol{w}_{n+1}^T\Delta\widetilde{\boldsymbol{p}}_{n\lambda}^0} \tag{2.32}$$

Once the predictors $\Delta\boldsymbol{p}_n^*$, $\Delta\lambda_n^*$ are known, the corrector phase can be started by running the iteration loop $i = 1,2,3,\cdots$. The predictors are used in the first iteration as $\Delta\boldsymbol{p}_n^1 = \Delta\boldsymbol{p}_n^*$ and $\Delta\lambda_n^1 = \Delta\lambda_n^*$, $\boldsymbol{p}_{n+1}^1 = \boldsymbol{p}_n + \Delta\boldsymbol{p}_n^1$ and $\lambda_{n+1}^1 = \lambda_n + \Delta\lambda_n^1$. For the i^{th} iteration the sequence of computations is as follows: (i) compute $\boldsymbol{K}_{n+1}^i(\boldsymbol{p}_{n+1}^i, \lambda_{n+1}^i)$, $\boldsymbol{R}_{n+1}^i(\boldsymbol{p}_{n+1}^i, \lambda_{n+1}^i)$, and $\boldsymbol{R}_{n+1,\lambda}^i(\boldsymbol{p}_{n+1}^i, \lambda_{n+1}^i)$, (ii) solve equations (2.15), (iii) evaluate (2.28), (iv) compute (2.12) and (2.8). The check (2.24) is chosen for an exit of the iteration loop (it is also used in the predictor step).

2.2.3 Implementation remarks

The above described path-following method is based on controlling incrementally a chosen DOF, i.e. the control displacement. It is very important to choose a suitable control displacement in each increment; if it is not the right one, the analysis will fail. The analysis works only if the control displacement is monotonically increasing or monotonically decreasing within the increment under consideration. The control displacement may change from one increment to another.

The prescribed incremental value of the current control displacement is $\Delta\widehat{D}_n$. We use an automatic incremental adjustment of $\Delta\widehat{D}_n$ with respect to the change of the current control displacement in the

previous increment, i.e. $\Delta\widehat{D}_n = \Delta\widehat{D}_n^{\#}$, where $\Delta\widehat{D}_n^{\#} = B(I_o, I_{n-1})\,\Delta\widehat{D}_{n-1}$ and $B(I_o, I_{n-1})$ is defined in (2.25). This works fine when the control displacements are of the same type in all increments; either displacements or rotations. The procedure does not work so nice if this is not the case. This problem may be solved by prescribing the incremental value of the current control displacement as $\Delta\widehat{D}_n = \Delta\widehat{D}_{n,mod}$, where

$$\Delta\widehat{D}_{n,mod} = \Delta\widehat{D}_n^{\#}\frac{\|\boldsymbol{w}_{n+1}^T\Delta\boldsymbol{p}_{n-1}\|}{\|\boldsymbol{w}_n^T\Delta\boldsymbol{p}_{n-1}\|}, \qquad \Delta\widehat{D}_{min} \le \Delta\widehat{D}_{n,mod} \le \Delta\widehat{D}_{max} \tag{2.33}$$

Here, vector $\boldsymbol{w}_n$ has all entries 0, except a single one (at the position related to the control displacement of the previous increment), which is 1. Similarly, vector $\boldsymbol{w}_{n+1}$ has all entries 0, except a single one (at the position related to the control displacement of the current increment), which is 1.

Once the control element Cel is chosen (according to the procedure described in the previous section), we determine absolute and relative displacement change of its displacements in the previous increment. The absolute change is:

$$(\Delta\boldsymbol{p}_{n-1})_{Cel} = (\boldsymbol{p}_n)_{Cel} - (\boldsymbol{p}_{n-1})_{Cel} \tag{2.34}$$

where $(\boldsymbol{p}_n)_{Cel}$ and $(\boldsymbol{p}_{n-1})_{Cel}$ are vectors of non-prescribed displacements of the control element Cel at t_n and t_{n-1}, respectively. The relative change of k-th component of vector $(\Delta\boldsymbol{p}_{n-1})_{Cel}$ is:

$$\left(\Delta p_{n-1,rel}\right)_{Cel,k} = \frac{(p_n)_{Cel,k} - (p_{n-1})_{Cel,k}}{(p_{n-1})_{Cel,k}} \tag{2.35}$$

If $(p_{n-1})_{Cel,k} = 0$, the relative change (2.35) is not computed. The control parameter is defined as $\max\left[\left|(\Delta p_{n-1})_{Cel,k}\right|, \left|\left(\Delta p_{n-1,rel}\right)_{Cel,k}\right|\right]$.

One could also use quadratic constraint equation (2.6) from Section 2.1 to formulate a one-DOF quadratic constraint. In that case, predictor and corrector would be computed in slightly different way that presented in Section 0. However, we preferred to use linear constraint equation (2.26).

2.3 Stability analysis

A more detailed stability analysis may be performed along with the path-following methods described above. Let us assume that each pseudo-time increment in the analysis does not include more than one critical point. In that case, the stability analysis may consist of the following steps:

(i) Begin with the path-following method, e.g. one of those described in Sections 2.1 and 0.

(ii) At each increment compute the number of negative pivots for the converged configuration. If that number did not change from the previous increment, go to (iv). If the number did changed, the critical point had been passed.

(iii) Do the following. (iiia) Step back one increment. (iiib) Perform direct computation of the critical point (e.g. as described below in Section 2.3.1). (iiic) Classify the critical point. If it is the

limit point, go to (iv). If it is the bifurcation point, apply a branch-switching procedure (e.g. the one described below in Section 2.3.2).

(iv) Continue the analysis with the chosen path-following method and check for the next critical point in accordance with (ii).

As pointed out by (Eriksson, 1998) the stability analysis of a perfect elastic structure (without any imperfections) may be seen as a simplification of the real structural behavior; however such an analysis can be very useful to get a deeper insight into the understanding of the behavior of many real structures.

2.3.1 Direct computation of critical point

Direct computation of a critical point at an increment $[t_n, t_{n+1}]$ can be done by using (2.5) with a special form of the constraint function g_{n+1}. In this work, we will use an eigenvector-free constraint function $g_{n+1}\left(\boldsymbol{K}_{n+1}(\boldsymbol{p}_{n+1})\right)$; see e.g. (Noguchi and Fujii, 2003), (Korelc, 2010) and references therein for eigenvector-free computations of critical point. In particular, we will use

$$g_{n+1} = det\boldsymbol{K}_{n+1} = \prod_{i=1}^{N} U_{ii,n+1} \tag{2.36}$$

where N is the dimension of $\boldsymbol{p}_{n+1}$ and $U_{ii,n+1}$ are the diagonal terms of the upper triangular matrix in $\boldsymbol{K}_{n+1} = \boldsymbol{L}_{n+1}\boldsymbol{U}_{n+1}$ decomposition. Obviously, the condition $det\boldsymbol{K}_{n+1} = 0$ holds for the searched configuration $\{\boldsymbol{p}_{n+1}, \lambda_{n+1}\}$, i.e. the searched configuration is the critical point. The procedure applied for solving (2.5) with constraint function (2.36) follows exactly the steps presented in Section 2.1 considering that (2.36) replaces (2.6).

The determinant of the stiffness matrix is not a practical stability indicator due to the fact that it can be an extremely large number that cannot be computed explicitly. However, the constraint function (2.36) can be used providing the following. (i) The linearized system (2.7) has to be normalized, see e.g. (Korelc, 2010) for details. (ii) The problem under consideration has to have small number of DOFs (i.e. small N). Namely, the convergence radius of the Newton-Raphson iterative procedure decreases rapidly for approximately $N > 10^4$; also, large N considerably increases possibility for spurious solutions, see e.g. (Korelc, 2010). In this work, the constraint function (2.36) was successfully used to compute numerical examples in Section 2.4, where N was up to 2100.

For a definition and implementation of alternative eigenvector-free and eigenvector based constraint functions, we refer to e.g. (Wriggers and Simo, 1990), (Eriksson, 1998), (Eriksson et al., 1999), (Kouhia and Mikkola, 1999), (Lopez, 2002), (Noguchi and Fujii, 2003) and (Korelc, 2010).

The procedure for critical point computation that is based on the constraint function (2.36) needs, see (2.7), the following expression

$$g^i_{n+1,\boldsymbol{p}} = tr\left(\frac{\partial g^i_{n+1}}{\partial \boldsymbol{K}^i_{n+1}} \boldsymbol{K}^i_{n+1,\boldsymbol{p}}\right) \tag{2.37}$$

where $\boldsymbol{K}^i_{n+1,\boldsymbol{p}}$ is directional derivative of stiffness matrix. Derivation of (2.37) can be a difficult task for many finite element formulations. Moreover, the computation of (2.37) can be very inefficient as mentioned in (Wriggers and Simo, 1990). However, it has been shown in (Korelc, 2010) that it is possible that (2.37) is evaluated efficiently on the basis of element-by-element assembly. It has been also shown in (Korelc, 2010) that the exact linearization of eigenvector-free constraint equation leads to a quite robust algorithm for direct computation of critical points for problems with relatively small *N*. For the bar and shell finite elements, used in Section 2.4, the derivative (2.37) was obtained by automatic differentiation tool AceGen (Korelc, 2015). Thus, the derivatives that we use for stability analysis in Section 2.4 are exact.

2.3.2 Classification of critical point and branch switching

Once (2.5) is solved with (2.36) as the constraint function, one gets a set $\{\boldsymbol{p}_{n+1}, \lambda_{n+1}\}$ that defines the configuration that is in a very close neighbourhood to the critical point. In what follows, we will not distinguish between that configuration and the critical point. For the critical point, the following condition holds besides $det\boldsymbol{K}_{n+1} = 0$

$$\boldsymbol{K}_{n+1}(\boldsymbol{p}_{n+1})\boldsymbol{\phi}_k = \boldsymbol{0}, \qquad k = 1,..,M \tag{2.38}$$

where $\boldsymbol{\phi}_k$ is the eigenvector of $\boldsymbol{K}_{n+1}$ that corresponds to the *k*-th zero eigenvalue. In (2.38), *M*=1 and $M > 1$ denote simple and multiple critical points, respectively. It is relatively easy to differentiate the limit from bifurcation point by using the standard criteria, see e.g. (Wriggers and Simo, 1990)

$$B = \left|\frac{\boldsymbol{\phi}_i^T \boldsymbol{R}_{n+1,\lambda}}{\left\|\boldsymbol{\phi}_i^T \boldsymbol{R}_{n+1,\lambda}\right\|}\right| \begin{cases} \leq tol_1 \implies \text{bifurcation point} \\ > tol_1 \implies \text{limit point} \end{cases} \tag{2.39}$$

where tol_1 is a small number (we used $tol_1 = 10^{-6}$ in Section 2.4). Further classification of the critical point can be made by information about the directional derivative $\boldsymbol{K}_{n+1,\boldsymbol{p}}$ at the critical point, see e.g. (Wriggers and Simo, 1990), (Kouhia and Mikkola, 1999), (Ohsaki and Ikeda, 2007). As shown above, knowledge of this derivative is required in (2.37). Thus, a by-pass product of the algorithm described in Section 2.3.1 is that the precise type of the critical point can be determined with a little additional computational effort.

A common case in engineering stability problems, particularly in structural mechanics, is the simple pitchfork bifurcation point, e.g. (Wriggers and Simo 1990), (Ohsaki and Ikeda 2007). For a pitchfork bifurcation, the transition to the secondary part is accomplished simply by adding the buckling mode to the displacements at the bifurcation point (Wriggers and Simo, 1990)

$$\boldsymbol{p}_2 = \boldsymbol{p}_{n+1} + \xi\boldsymbol{\phi}_1 \tag{2.40}$$

where ξ is a scalar weight. This is a justification for an ad-hoc procedure based on (2.40), which is used in engineering stability analysis and often called branch-switching, e.g. (Wagner and Wriggers, 1988), (Crisfield, 1997), (Parente Junior et al., 2006), (Zhou et al., 2015). The branch-switching procedure (2.40) is also applied in this work. The following predictor is used in the first increment of the branch-switching procedure for the simple bifurcation point

$$\Delta \boldsymbol{p}_n^* = \xi \boldsymbol{\phi}\,, \quad \Delta\lambda_n^* = 0\,, \quad \xi = \pm\Delta l_n^{(b)}, \quad \boldsymbol{\phi} = \frac{\boldsymbol{\phi}_1}{\|\boldsymbol{\phi}_1\|} \tag{2.41}$$

where $\Delta l_n^{(b)}$ is the length of that increment. For a multiple bifurcation point one can follow (Wagner and Wriggers, 1988)

$$\Delta \boldsymbol{p}_n^* = \xi \boldsymbol{\phi}\,, \quad \Delta\lambda_n^* = 0\,, \quad \xi = \pm\Delta l_n^{(b)}, \quad \boldsymbol{\phi} = \sum_i^M \tau_i \frac{\boldsymbol{\phi}_i}{\|\boldsymbol{\phi}_i\|} \tag{2.42}$$

where τ_i is scalar weight.

In (Parente Junior et al., 2006), they suggested to derive the corrector in the first increment of the branch-switching procedure (but only in that increment) based on the following constraint equation

$$g_{n+1}(\Delta \boldsymbol{p}_n, \Delta\lambda_n) = (\Delta \boldsymbol{p}_n^T \boldsymbol{\phi})^2 - \Delta l_n^{(\mathrm{b})^2} = 0 \tag{2.43}$$

In numerical examples presented in Section 2.4, we tested two correctors for the first increment of the branch-switching procedure: (i) the one based on (2.43), and (ii) the one based on (2.6). The former one had quadratic convergence. The latter one was more robust (it found solutions in the cases where the former one traced back for both plus and minus signs in the predictor (2.41) but its convergence was linear.

2.4 Numerical examples

The above presented consistently linearized path-following methods and the procedure for stability analysis were implemented in the computer code AceFEM (Korelc, 2015). In order to illustrate their performance, several examples are presented below. The examples 2.4.1 to 2.4.6 are solved by using the path-following method from Section 2.1. If not specified otherwise, the following scaling factors are used: $\psi_1 = \psi_2 = 1$, $\boldsymbol{W}_n = \boldsymbol{H}_n = \widehat{\boldsymbol{W}}_n = \boldsymbol{I}$. Stability analysis, as described in Section 2.3, is also performed for those examples. The "distance" to the critical point when the analysis switches to the direct computation of the critical point is somewhere between $(0, \Delta l_{max}]$. The examples 2.4.7 to 2.4.10 are solved by switching from the path-following method with the quadratic constraint equation (described in Section 2.1) to the path-following method with the one-DOF constraint equation (described in Section 0) once the former fails to converge.

The shell and bar finite elements are used in examples 2.4.1 to 2.4.6. The shell element is a 4-node large rotation element with 5 DOFs per node and with the assumed natural strain (ANS) formulation of (Bathe and Dvorkin, 1985) for the transverse shear strains. Large rotation update is based on the additive update of the rotation vector (Brank and Ibrahimbegovic, 2001), (Ibrahimbegovic et al., 2001). The used elasto-plastic formulation is presented in (Dujc and Brank, 2012). The bar element is the standard 2-node element. The beam and plane stress embedded discontinuity (ED) finite elements are used in examples 2.4.7 to 2.4.10. The beam ED finite element is presented in (Dujc et al., 2010) and (Piculin and Brank, 2015). The plane stress ED finite element is presented in (Dujc et al., 2010b) and (Dujc et al., 2013).

2.4.1 Two bar truss

A snap-through of a two-bar truss is considered (Figure *2.1*) in order to illustrate how the consistently linearized arc-length method works. The truss is loaded by a vertical force λF_{ref} at the apex. Due to the symmetry, one half of the truss is discretized by one geometrically nonlinear bar finite element of length $\sqrt{2}$, providing a one-degree-of-freedom system. Cylindrical arc-length method is used ($\psi_1 = 0, \boldsymbol{W}_n = \boldsymbol{H}_n = \boldsymbol{I}$), The data for the arc-length analysis is: $l_0 = 0.00005,\ \Delta l_{max} = 0.3, I_0 = 5$ and $tol = 10^{-10}$. Figure 2.2 shows the computed relation between the load-factor λ and the apex vertical displacement w, which is in perfect agreement with the analytical solution (Ibrahimbegovic, 2009). It also shows a zig-zag line, connecting the points of the iterative solutions, and the circles with radii Δl_n with their center points located at the corresponding incremental equilibrium points. Figure 2.3 illustrates how the circles with radii Δl_n are related to iterative solutions at the corresponding increment; the iterative solutions are on a vertical line tangent to a circle. This is also evident from Table 2.2: the iterative displacement does not change with iterations, only the iterative load factor does, see also Figure 2.4.

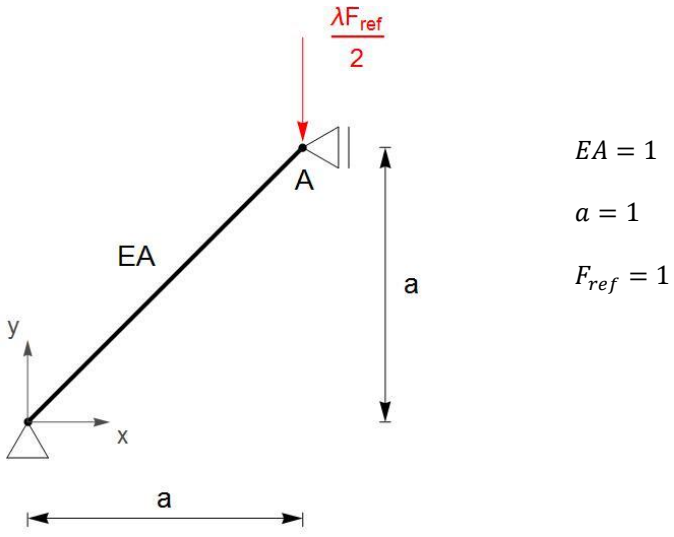

Figure 2.1: Two-bar truss: the problem data.

Slika 2.1: Tričlenski lok: vhodni podatki.

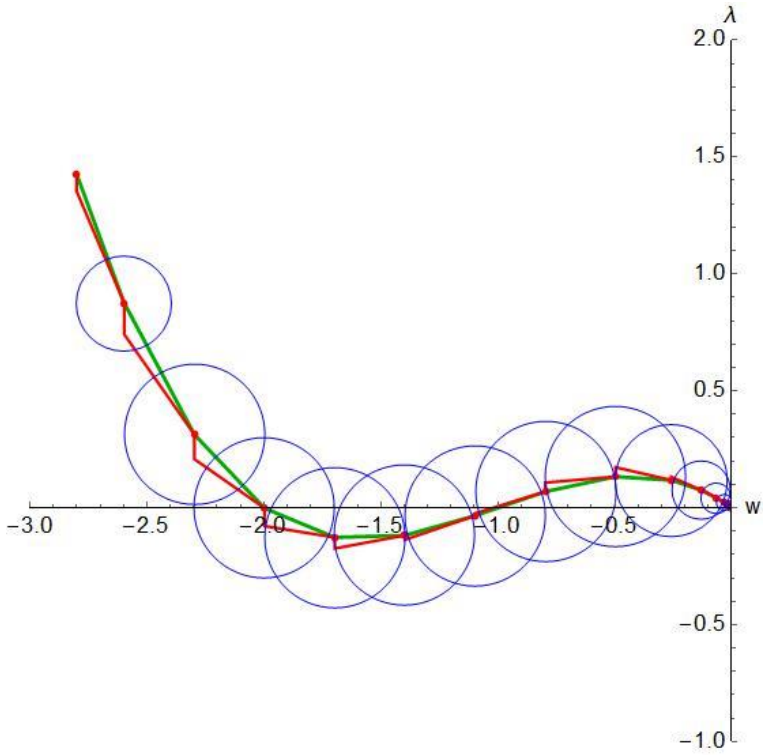

Figure 2.2: Two-bar truss: equilibrium path (the smooth line); line connecting iterative solutions (the zig-zag line); circles with radii Δl_n, center point of a circle is at the equilibrium point.

Slika 2.2: Tričlenski lok: ravnotežna pot (gladka krivulja); iterativne rešitve (cik-cak linija); krožnice z radiji Δl_n, središče posamezne krožnice leži v ravnotežni točki.

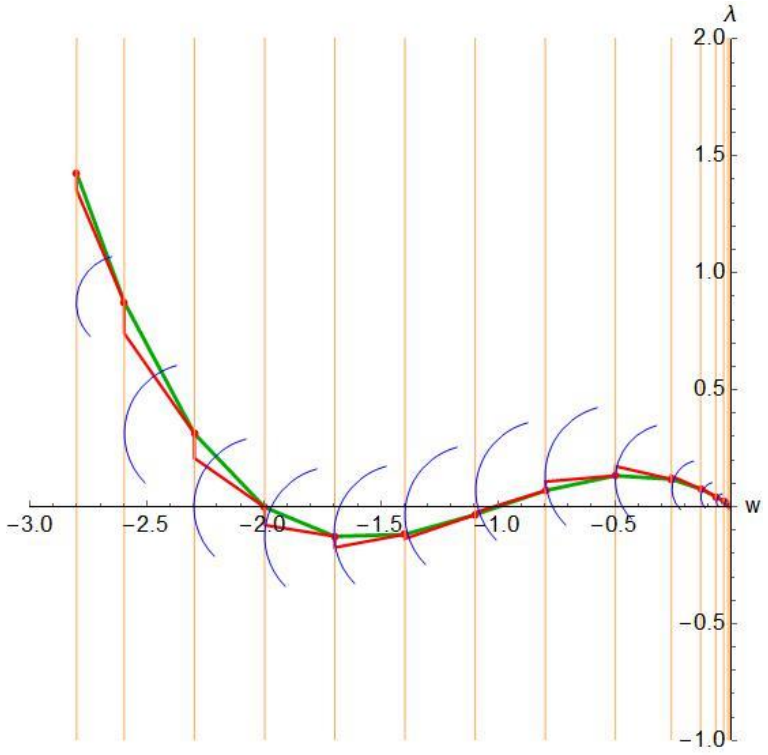

Figure 2.3: Two-bar truss: relation between the circles with the radii Δl_n and the iterative solutions.

Slika 2.3: Tričlenski lok: zveza med krožnicami z radiji Δl_n in iterativnimi rešitvami.

Table 2.2: Two-bar truss: iterative solutions in the first increment [$t_n = 0$, $t_{n+1} = t_1$]; the starting point is {w, λ} = {p_n, λ_n} = {0, 0}.

Preglednica 2.2: Tričlenski lok: iterativne rešitve v prvem koraku [$t_n = 0$, $t_{n+1} = t_1$]; začetna točka je {w, λ} = {p_n, λ_n} = {0, 0}.

Iteration i	Iterative solution	Convergence criterion
1	$p_{n+1}^1 = \Delta l_n$ $\lambda_{n+1}^1 = \frac{K_{n+1}^0}{0.5\,F_{ref}}\Delta l_n$	$\sqrt{\frac{[\Delta l_n]^2}{1} + \left[\frac{K_{n+1}^0}{0.5\,F_{ref}}\Delta l_n\right]^2} \leq tol$
2	$p_{n+1}^2 = \Delta l_n$ $\lambda_{n+1}^2 = \frac{K_{n+1}^0}{0.5\,F_{ref}}\Delta l_n + \frac{R_{n+1}^1}{0.5\,F_{ref}}$	$\sqrt{\frac{0}{1} + \left[\frac{R_{n+1}^1}{0.5\,F_{ref}}\right]^2} \leq tol$
3	$p_{n+1}^3 = \Delta l_n$ $\lambda_{n+1}^3 = \frac{K_{n+1}^0}{0.5\,F_{ref}}\Delta l_n + \frac{R_{n+1}^1}{0.5\,F_{ref}} + \frac{R_{n+1}^2}{0.5\,F_{ref}}$	$\sqrt{\frac{0}{1} + \left[\frac{R_{n+1}^2}{0.5\,F_{ref}}\right]^2} \leq tol$
4	$p_{n+1}^4 = \Delta l_n$ $\lambda_{n+1}^4 = \frac{K_{n+1}^0}{0.5\,F_{ref}}\Delta l_n + \frac{R_{n+1}^1}{0.5\,F_{ref}} + \frac{R_{n+1}^2}{0.5\,F_{ref}} + \frac{R_{n+1}^3}{0.5\,F_{ref}}$	$\sqrt{\frac{0}{1} + \left[\frac{R_{n+1}^3}{0.5\,F_{ref}}\right]^2} \leq tol$

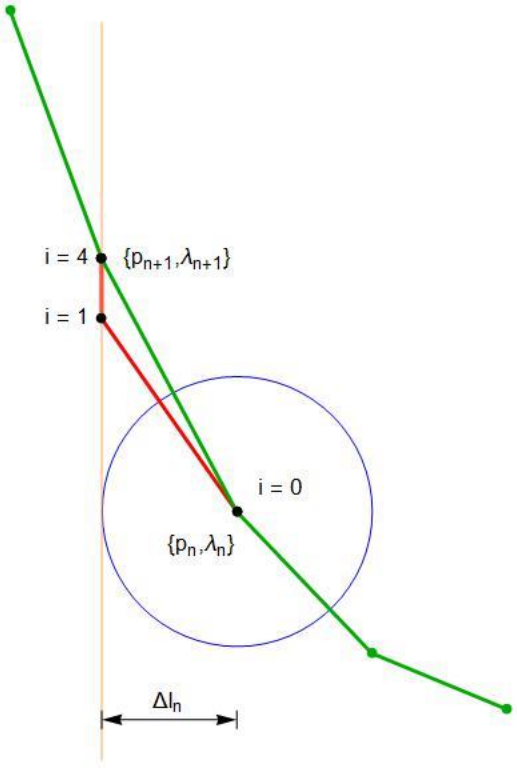

Figure 2.4: The increment with the initial point {p_n, λ_n} = {-2.3, 0.31}.

Slika 2.4: Inkrement z začetno točko {p_n, λ_n} = {-2.3, 0.31}.

2.4.2 Truss dome

This problem was studied e.g. in (Crisfield, 1997), (Thai and Kim, 2009) and (Wriggers, 2008). Truss dome, composed of 24 bars, is subjected to a point load $F = \lambda F_{ref}$ at its top, see Figure 2.5. Each bar has a cross-section area of 0.1 cm^2. The elastic modulus of the material is $E = 2.034\ 10^7$ N/cm^2. Each bar is modelled by one bar finite element.

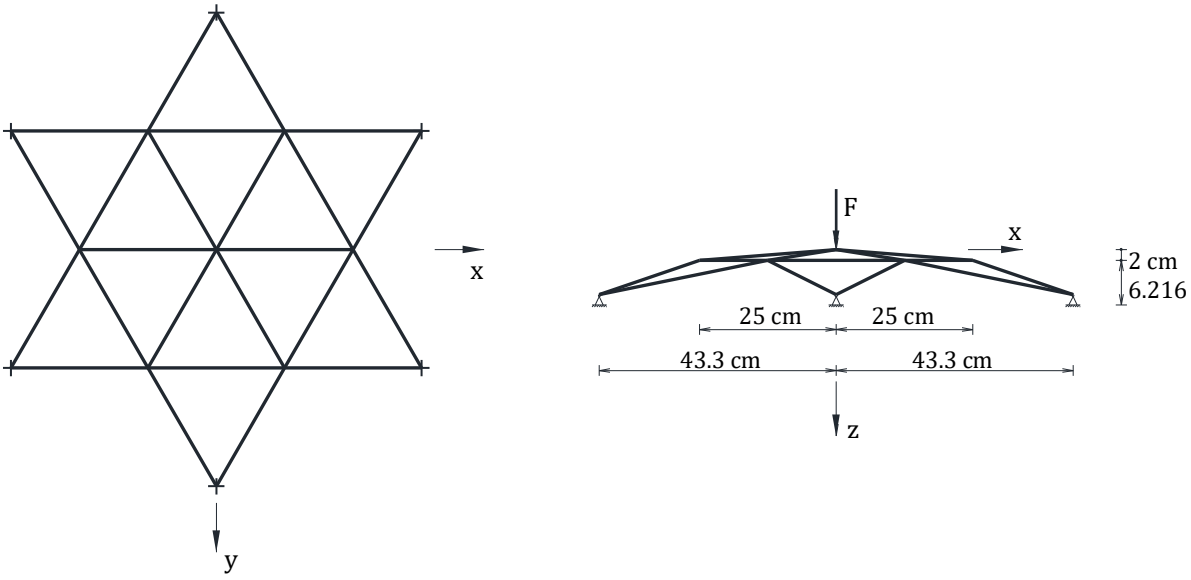

Figure 2.5: Truss dome problem.

Slika 2.5: Palična kupola.

Table 2.3: Truss dome: units of input data and value of T from Table 2.1.

Preglednica 2.3: Palična kupola: merske enote vhodnih podatkov in vrednosti T (Preglednica 2.1).

Units	F_{ref}	T
N, cm	1	0.0005
N, cm	100	0.0005
N, mm	1	0.0055
N, mm	1000	0.0055
kN, m	1	0.0055
kN, cm	0,001	0.5490
kN, cm	1	0.5490

Figure 2.6 illustrates a fundamental problem of the use of constraint equation with several terms: the scaling of the second part of the right side of eq. (2.6) can severely affect the results (note that the third part of (2.6) is zero for the considered problem). The scaling can be done either by ψ_1 and $\boldsymbol{W}_n$ or by units of input data. Here we set $\psi_1 = 1, \boldsymbol{W}_n = \boldsymbol{I}$ and perform the scaling with the units of input data. The results in Figure 2.6 suggest that the scaling is extremely important and that the value of Δl_{max} also affects results for

a non-optimal scaling. It can be seen from Figure 2.6 that the computed equilibrium points are not connected in the right order or/and a part of the response curve is missing due to large jumps between two subsequent computed points. This happens when the second part of (2.6) is dominant as illustrated in Figure 2.7 for the case B in Figure 2.6. In order to get the right results, the first and the second parts of the right side of (2.6) should be of the same order of magnitude.

The test from Section 2.1.6 can help to choose scaling that balances both parts of constraint equation (2.6).

Table 2.3 shows that choosing kN and cm as data units leads to an appropriate scaling according to the mentioned test (note that the value of F_{ref} has no effect on T). When this scaling is used, the right results are computed as shown in Figure 2.8. Figure 2.8 also shows that at proper scaling the influence of Δl_{max} on results is minimal. Figure 2.9 shows a balanced distribution of the first (i.e. displacement) and the second (i.e. applied loading) parts of the constraint equation (2.6) for an analysis with proper scaling. Note that close to the limit points the loading part tends towards zero.

More detailed stability analysis was computed as well. Figure 2.10 shows critical points located on the primary equilibrium path. Numerical values of critical points are presented in Table 2.7 showing that one has limit points (LP), simple bifurcation points (BP) and double bifurcation points (DBP). Figure 2.11 shows the secondary path from the first bifurcation point. The corrector in the first increment of the branch-switching procedure was based on (2.6).

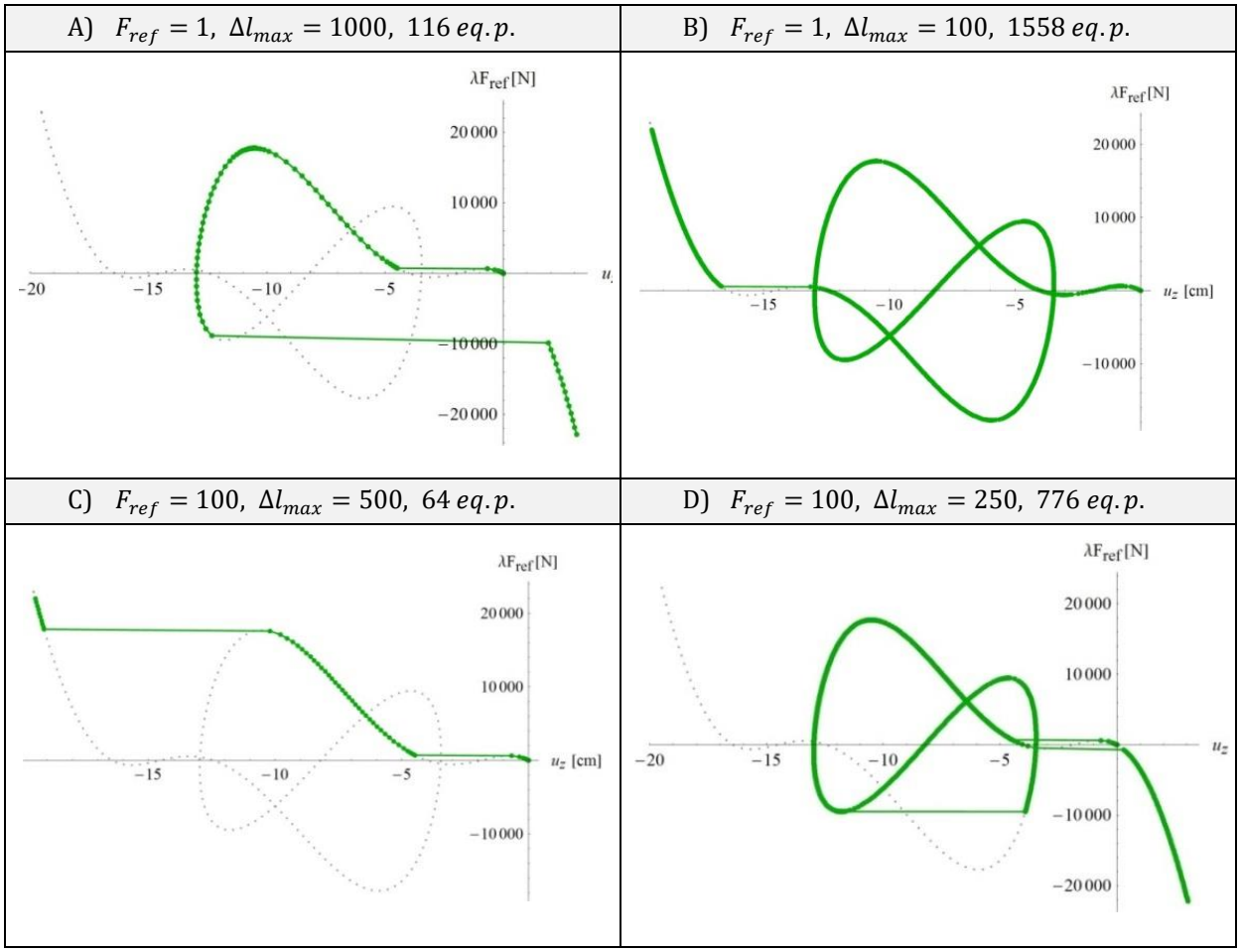

Figure 2.6: Computed solutions for different values of F_{ref} *and* Δl_{max} *(units are* N *and* cm, Δl_0 *=0.1,* $\Delta l_{min}=10^{-5}$, tol=10^{-8}, I_0=5*);* u_z *is vertical displacement under the force.*

Slika 2.6: Izračunane ravnotežne poti za različne vrednosti F_{ref} *in* Δl_{max} *(merski enoti sta* N *in* cm, Δl_0 *=0.1,* $\Delta l_{min}=10^{-5}$, tol=10^{-8}, I_0=5*);* u_z *je vertikalni pomik prijemališča sile.*

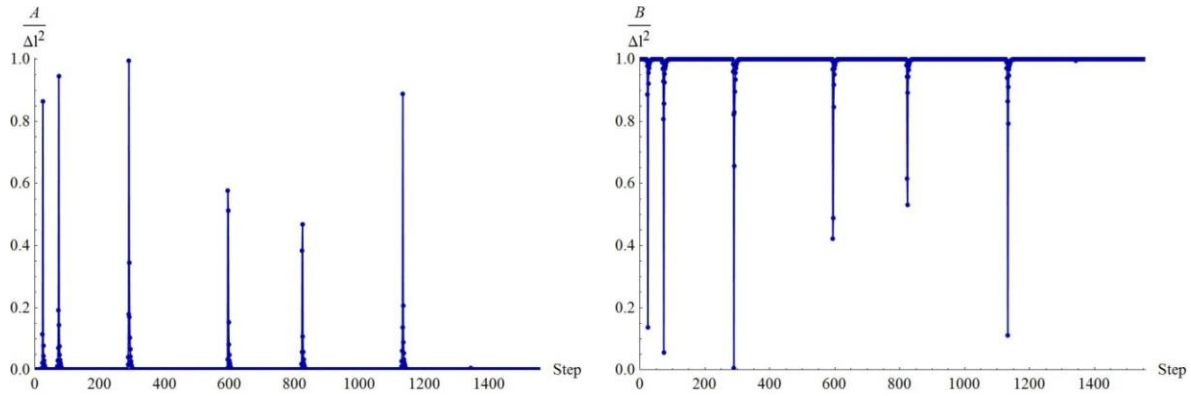

Figure 2.7: Displacement and loading parts of (2.6) at each increment, $A=(\Delta p_n)^T\Delta p^n$, $B=(\Delta\lambda_n)^2(q_{ref})^T q_{ref}$.

Slika 2.7: Vpliv delov vezne enačbe (2.6) zaradi pomika in obtežbe v vsakem inkrementu, $A=(\Delta p_n)^T\Delta p^n$, $B=(\Delta\lambda_n)^2(q_{ref})^T q_{ref}$.

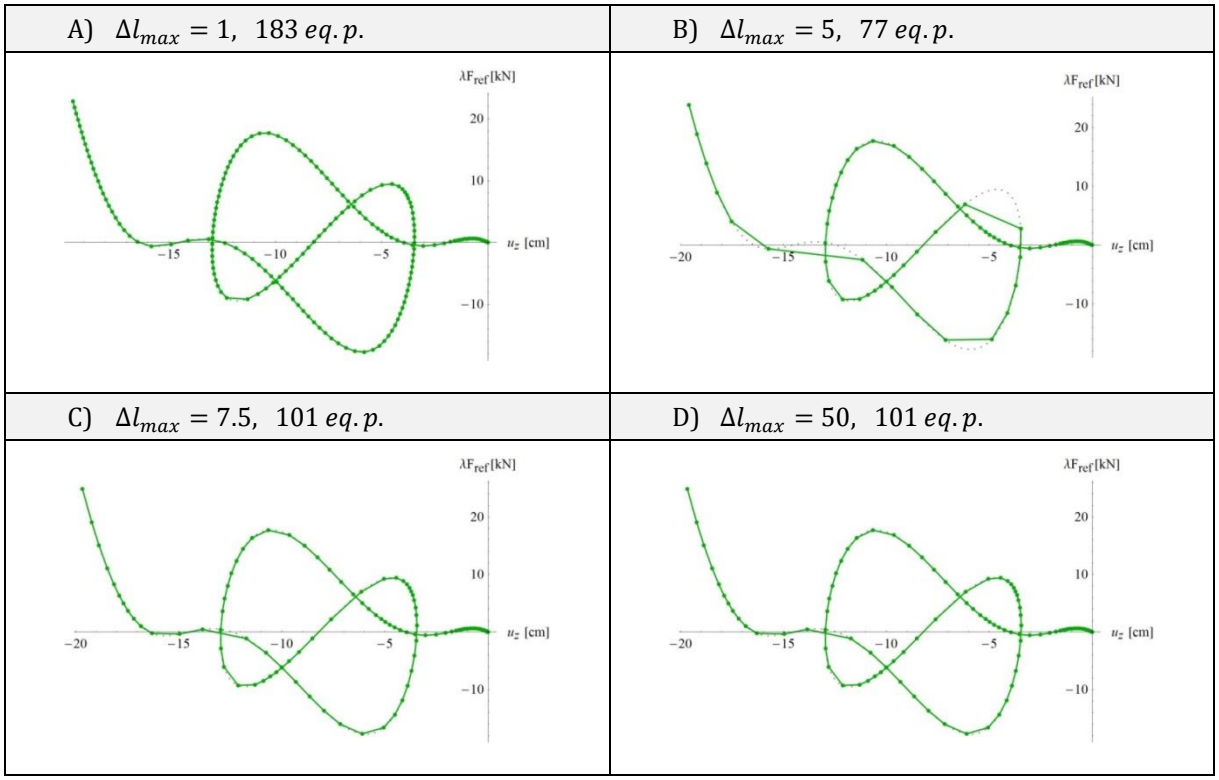

Figure 2.8: Computed solutions for different values of Δl_{max} (F_{ref} = 1 kN*, units are* kN *and* cm*, Δl_0 = 0.01, Δl_{min} = 10^{-5}, tol=10^{-8}, I_0 = 5).*

Slika 2.8: Izračunane ravnotežne točke za različne vrednosti Δl_{max} (F_{ref} = 1 kN*, merski enoti sta* kN *in* cm*, Δl_0 = 0.01, Δl_{min} = 10^{-5}, tol=10^{-8}, I_0 = 5).*

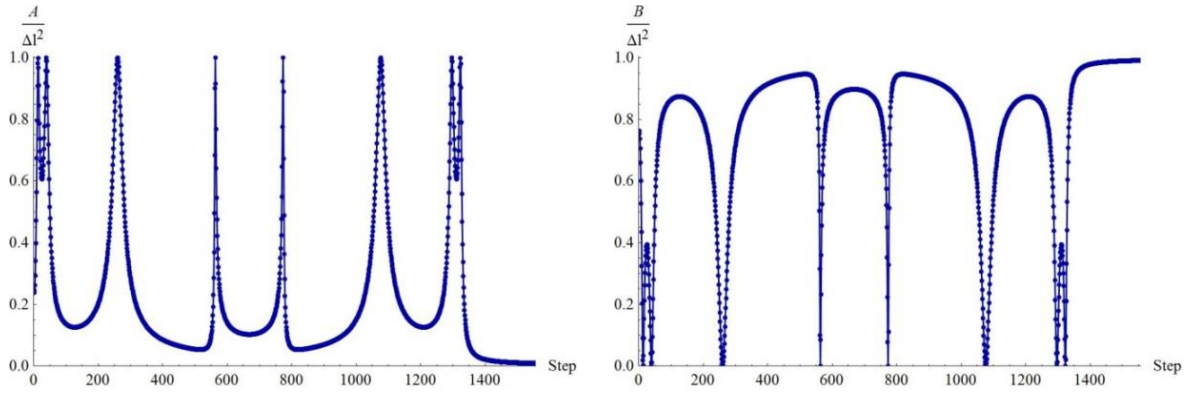

Figure 2.9: Displacement and loading parts of (2.6) at each increment, $A=(\Delta p_n)^T\Delta p_n$, $B=(\Delta\lambda_n)^2(q_{ref})^T q_{ref}$, for units kN *and* cm*, F_{ref} = 1* kN*, Δl_0 = 0.01, Δl_{min} = 10^{-5}, Δl_{max} = 0.1.*

Slika 2.9: Vpliv delov vezne enačbe (2.6) zaradi pomika in obtežbe v vsakem inkrementu, $A=(\Delta p_n)^T\Delta p_n$, $B=(\Delta\lambda_n)^2(q_{ref})^T q_{ref}$, za merski enoti kN *in* cm*, F_{ref} = 1* kN*, Δl_0 = 0.01, Δl_{min} = 10^{-5}, Δl_{max} = 0.1.*

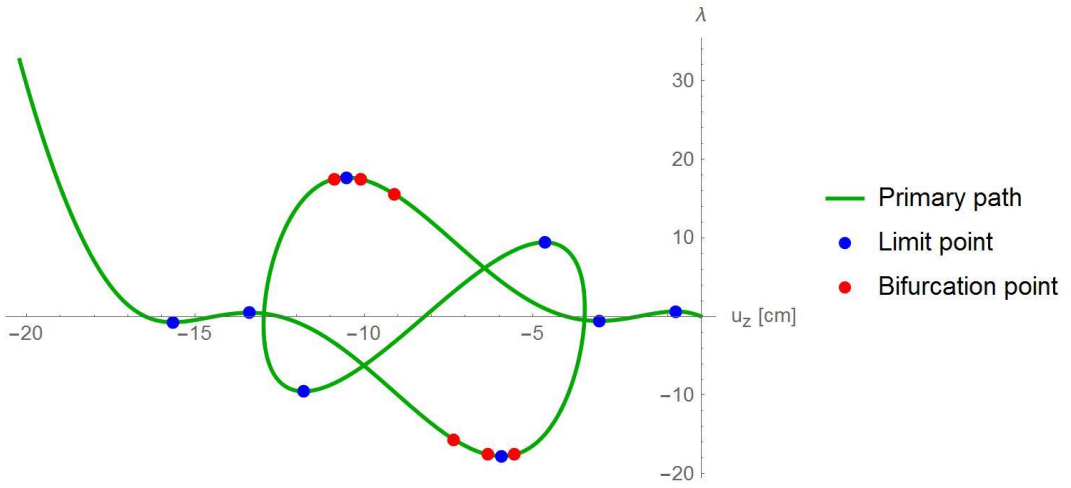

Figure 2.10: Truss dome equilibrium path critical points.

Slika 2.10: Palična kupola: graf ravnotežne poti s kritičnimi točkami.

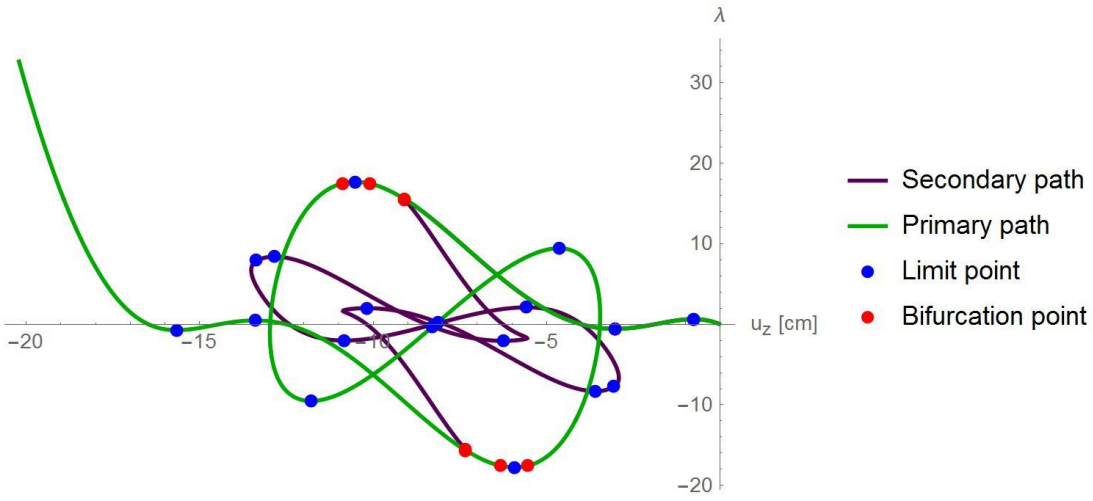

Figure 2.11: Primary and secondary path from the first bifurcation point.

Slika 2.11: Primarna ravnotežna pot in sekundarna veja iz prve bifurkacijske točke.

2.4.3 Cylindrical panel

We consider an isotropic cylindrical panel, originally presented in (Sabir and Lock, 1972) and later used in many papers on path-following methods, e.g. (Crisfield, 1981), (Eriksson, 1989), (Sze et al., 2004), (Zhou et al., 2015), see Figure 2.12. The shell of thickness t is subjected to a central point force λF_{ref}, where $F_{ref} =$ 3 kN. We consider three different discretizations of one quarter, one half (both with boundary conditions that take into account the symmetry) and complete structure, with meshes of 12 × 12, 12 × 24 and 24 × 24 elements, respectively. The data for the arc-length analysis of ¼ shell model and ½ shell models is: $\Delta l_0 = \Delta l_{max} = 0.05$, $I_0 = 5$ and $tol = 10^{-8}$. The data for the arc-length analysis of whole shell model is: $\Delta l_0 = \Delta l_{max} = 0.01$, $I_0 = 10$ and $tol = 10^{-8}$. The chosen units are kN and dm, since the values of T (see Section

2.1.6) for these units are 2.40, 1.62 and 1.09 for the three discretizations mentioned. The computation of critical points and the branch switching was done as described in Sections 2.3.1 and 2.3.2, respectively.

The results are shown in Figure 2.13 – Figure 2.15 and Table 2.8 – Table 2.13. Figure 2.13 shows the vertical displacement of the point of the force application u_z with respect to the load factor λ for discretization of one quarter of the shell. Our results are compared with the results of (Sze et al., 2004). In Figure 2.13, the critical points are also marked; the data for those points is shown in Table 2.8. The results for discretization of one half and complete shell are shown in Figure 2.14 and Table 2.9 – Table 2.11, and Figure 2.15 and Table 2.12 – Table 2.13, respectively. The number and characteristics of critical points depend on the assumptions on the problem symmetry. The corrector in the first increment of the branch-switching procedure was based on (2.6). The data for the arc-length analysis in branch switching increment is: $\Delta l_n^{(b)} = 0.001$, see equation (2.41), and $tol = 10^{-7}$. Other results on elastic stability analysis of cylindrical panels can be found in (Zhou et al., 2015).

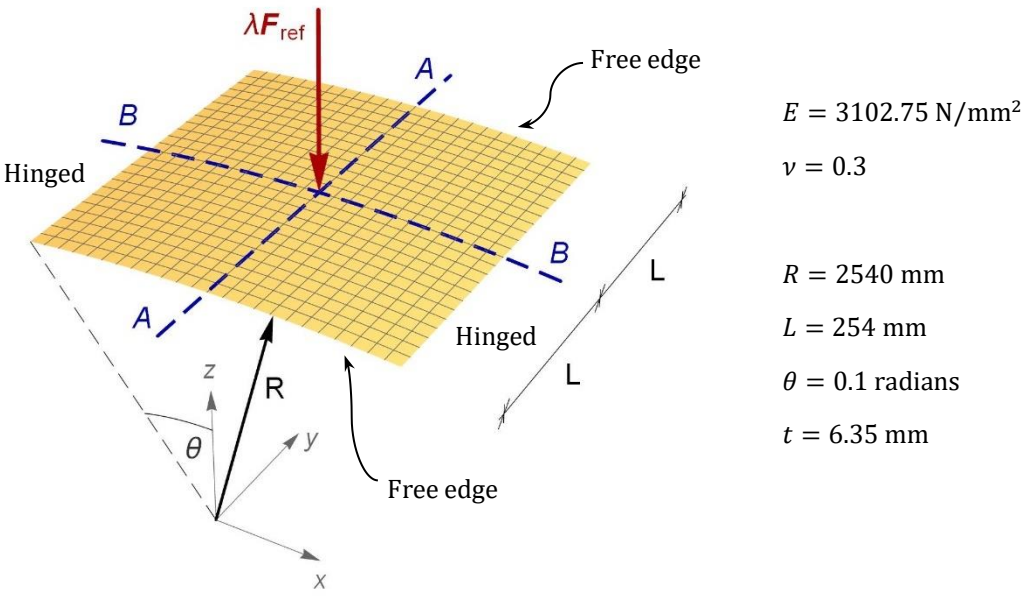

Figure 2.12: Cylindrical panel: the data.

Slika 2.12: Cilindrični panel: vhodni podatki.

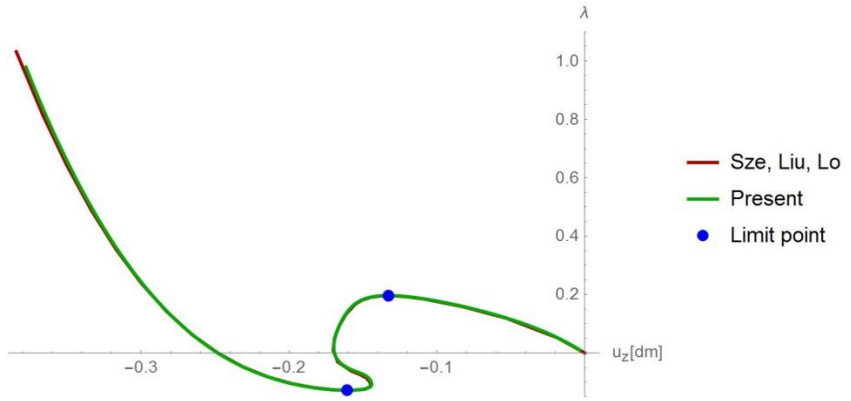

Figure 2.13: Cylindrical panel, ¼ of the shell discretization: load factor versus displacement under the force, and location of critical points.

Slika 2.13: Cilindrični panel, model ¼ lupine: diagram obtežni faktor v odvisnosti od pomika prijemališče sile z lokacijami kritičnih točk.

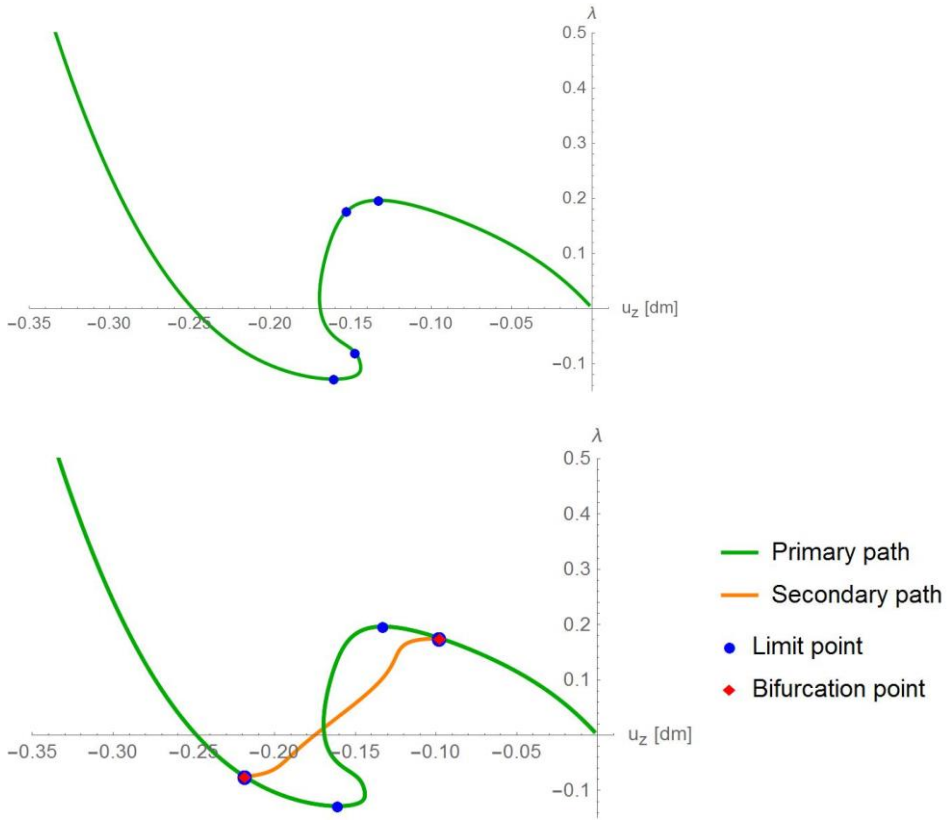

Figure 2.14: Cylindrical panel, ½ of the shell discretization. Top: load factor versus displacement under the force if symmetry along section A is assumed. Bottom: load factor versus displacement under the force (for primary and secondary paths) if symmetry along section B is assumed.

Slika 2.14: Cilindrični panel, model ½ lupine. Zgoraj: Diagram obtežni faktor v odvisnosti od pomika prijemališča sile, če privzamemo simetrijo vzdolž prereza A. Spodaj: Diagram obtežni faktor v odvisnosti od pomika prijemališča obtežbe (za primarno in sekundarno pot), če privzamemo simetrijo vzdolž prereza B.

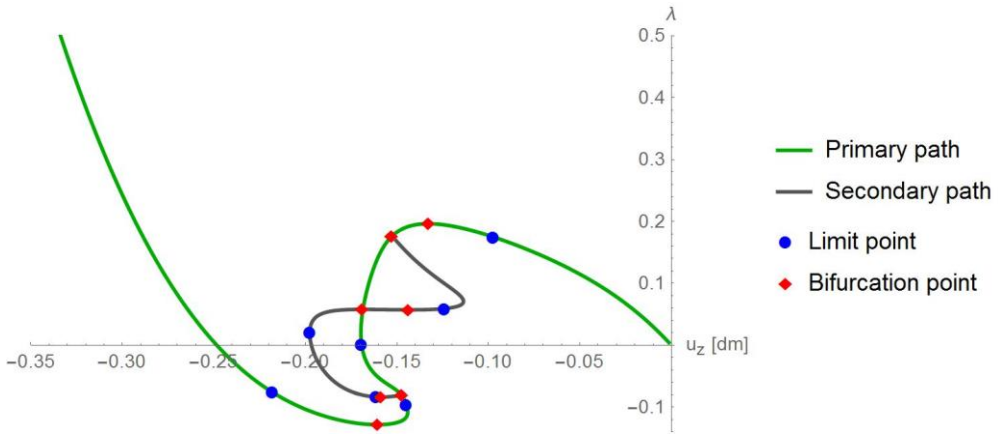

Figure 2.15: Cylindrical panel, complete shell discretization: load factor versus displacement under the force for primary and secondary paths, and location of critical points.

Slika 2.15: Cilindrični panel, diskretizacija cele lupine: Diagram obtežni faktor v odvisnosti od pomika prijemališča sile za primarno in sekundarno pot, ter lokacije kritičnih točk.

Typical convergence for the determination of the critical point is presented in the Table 2.4. The convergence is reached if either $\left|\Delta\tilde{\lambda}_{\mathrm{n}}^{\mathrm{i}}\right| \leq 10^{-5}$ or $err \leq 10^{-6}$. The convergence is good at the close vicinity to the critical point (sometimes one iteration is enough).

Table 2.5 shows typical convergence for the branch switching increment (5 to 20 iterations are usually needed to obtain the converged solution for $err \leq 10^{-7}$).

Table 2.4: Cylindrical panel: convergence when computing the first critical point for the ¼ the shell model (see Figure 2.13).

Preglednica 2.4: Cilindrični panel: konvergenca pri izračunu prve kritične točke za ¼ modela lupine (glej Slika 2.13).

Iteration i	$\Delta\tilde{\lambda}_n^i$, see eq. (2.17)	err, see eq. (2.24)
1	8.24-04	8.24E-04
2	-3.65-04	3.65E-04
3	-5.47E-06	5.47E-06

Table 2.5: Cylindrical panel: convergence for the branch switching increment from the second bifurcation point of the complete shell model (see Figure 2.15).

Preglednica 2.5: Cilindrični panel: konvergenca v prvem inkrementu sekundarne poti iz druge bifurkacijske točke za celoten model lupine (glej Slika 2.15).

Iteration i	err, see eq. (2.24)
1	4.96E-05
2	3.08E-06
3	1.31E-06
4	5.50E-07
5	2.29E-07
6	9.55E-08

2.4.4 Very thin cylindrical panel

A very thin cylindrical panel from Figure 2.16 is considered. It is subjected to a central point force $F = \lambda F_{ref}$, where $F_{ref} = 1$ N. Finite element mesh consists of 20×20 elements. The data for the path-following analysis is: $\Delta l_0 = \Delta l_{max} = 2$, $I_0 = 5$ and convergence tolerance is 10^{-8}.

Due to the very small thickness to radius ratio, the load factor λ versus the displacement under the force u_z curve has many snap-throughs, snap-backs and bifurcation points, see Figure 2.17. Figure 2.17 shows that after the first snap through (at small load factor $\lambda = 165.4$, see point "1" on Figure 2.17) a "cyclic" response of the shell is observed, with an increasing absolute value of λ at each subsequent "turning point" (observe points "3", "5", "7" and "9" on Figure 2.17). It can be seen from the deformed finite element configurations, marked with "0"-"11" in Figure 2.18, that the stiffness of the shell increases due to the increasing number of waves in the shell deformed configuration.

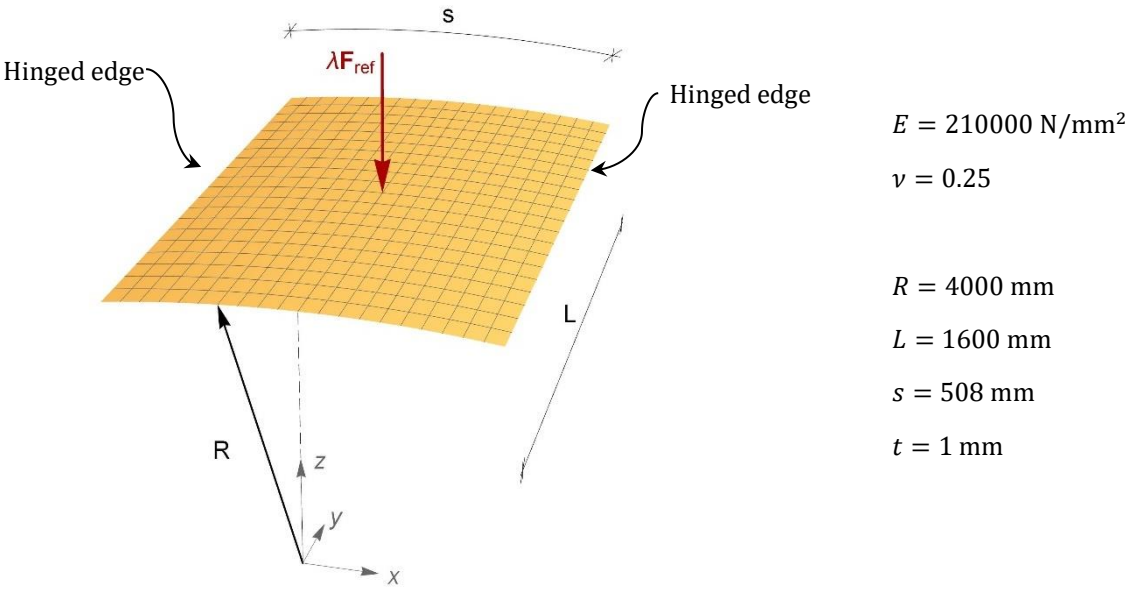

Figure 2.16: Thin cylindrical panel: the data

Slika 2.16: Tanek cilindrični panel: vhodni podatki.

Note, that some snap-throughs and snap-backs in Figure 2.17 are artificial due to the finite element discretization, and that a finer mesh produces a smoother curve. Such a phenomenon was also observed for geometrically nonlinear elastic shells in (Crisfield and Peng, 1996) and (Brank, 2008). Artificial buckling for not very fine meshes may be related to the fact that the smoothness of the $\lambda(u_z)$ curve in the present analysis with 20×20 elements depends on the chosen maximal arc length increment Δl_{max}. In the analysis, Δl_{max} influences criterion (2.22), which defines the sign of $\Delta\lambda_n^*$ in the predictor phase, see (2.21). Namely, the criterion (2.22) uses the results of the last converged point on the equilibrium path. If the increment is not small enough, the arc-length analysis might overlook an important change on the equilibrium path, and

the criterion returns a wrong sign for the current increment. Therefore, we used for this problem a small value for Δl_{max}. The critical points were not computed for this example.

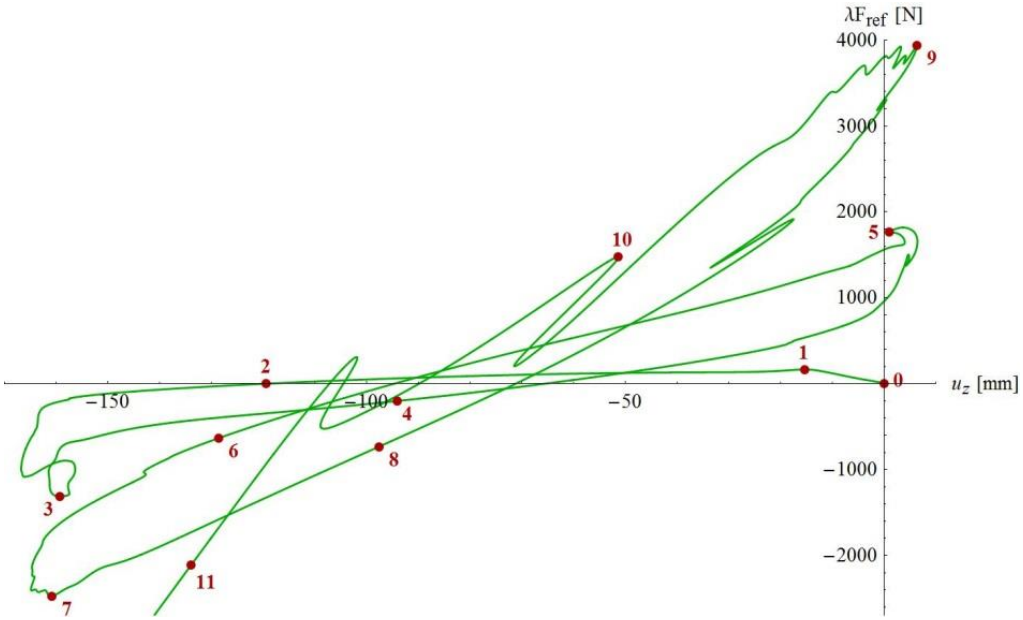

Figure 2.17: Thin cylindrical panel: λ versus the displacement under the force u_z *curve.*

Slika 2.17: Tanek cilindrični panel: Graf krivulje obtežni faktor λ *v odvisnosti od pomika prijemališča sile* u_z.

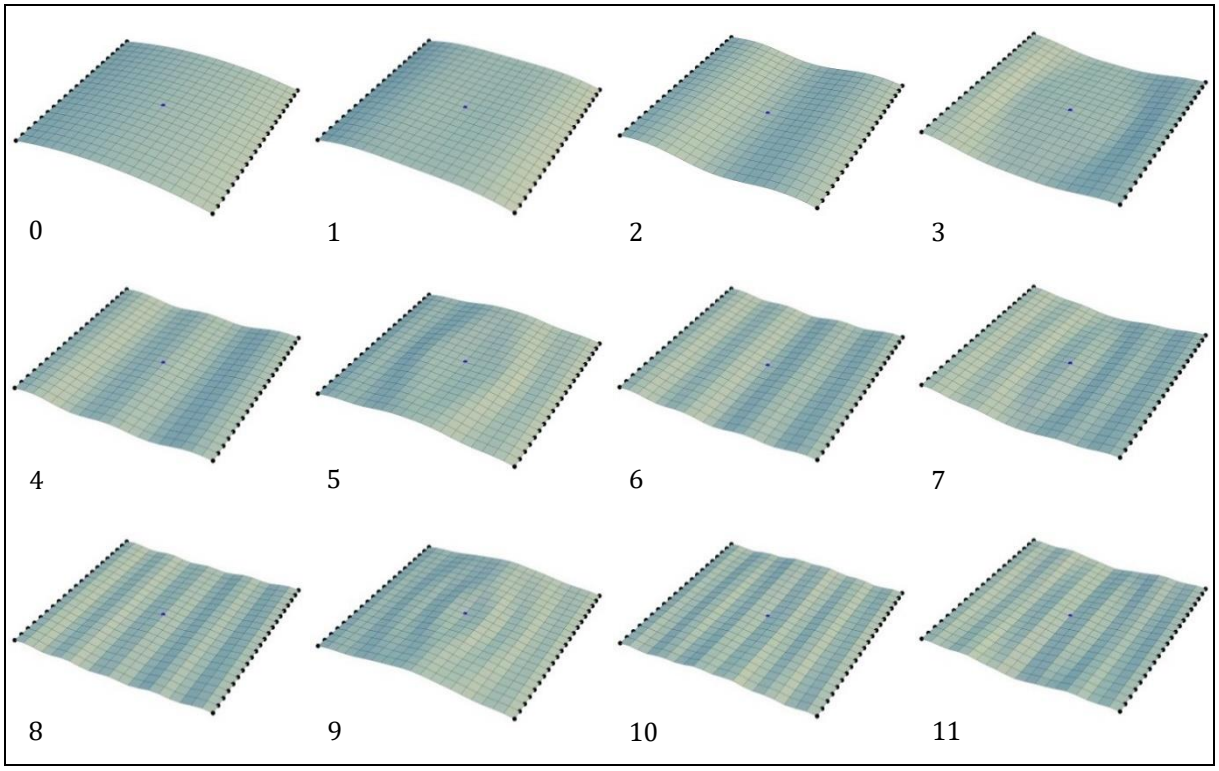

Figure 2.18: Thin cylindrical panel: deformed configurations at equilibrium points marked on Figure 2.17.

Slika 2.18: Tanek cilindrični panel: deformacijske konfiguracije v ravnotežnih točkah označenih na Slika 2.17.

2.4.5 L-shaped plate

This example was investigated by (Simo et al., 1990) and (Ritto-Correa and Camotim, 2008). An L-shaped plate is clamped at one end and subjected to an in-plane force $F = \lambda F_{ref}$, where $F_{ref} = 1$, at the free end (at point A in Figure 2.19). In this work, a mesh of 6 elements along the plate width b and 51 elements along the plate length $a + b$ is considered. Material properties are: Young's modulus $E = 71240$ and Poisson's ratio $\nu = 0.31$. The shell thickness is 0.6. In order to change the bifurcation point on the equilibrium path into the limit point, an out-of-plane perturbation force $= \frac{1}{1000} F_{ref}$ is applied at the point A (Figure 2.19). Nonlinear analysis is performed in two steps. In the first step, the plate is loaded by the perturbation force P. In the second step, computed by the arc-length method, the force F is applied by keeping the force P fixed. Input data for the arc-length analysis in the second step is $l_0 = 0.001$, $\Delta l_{max} = 50, I_0 = 12$ and $tol = 10^{-10}$. In this example, the same results are obtained for different values of the scale factor ψ_1 and for different values of the maximal arc length increment Δl_{max}. The results are shown in Figure 2.20 and Figure 2.21, where u_x is the displacement of the point A in the direction of the x axis. In Table 2.6, we present computed bifurcation force for the "tensile" load F and zero perturbation force P; the bifurcation force was obtained by using very small maximal arc-length increment Δl_{max} and by checking for the appearance of the first negative pivot in the structural stiffness matrix.

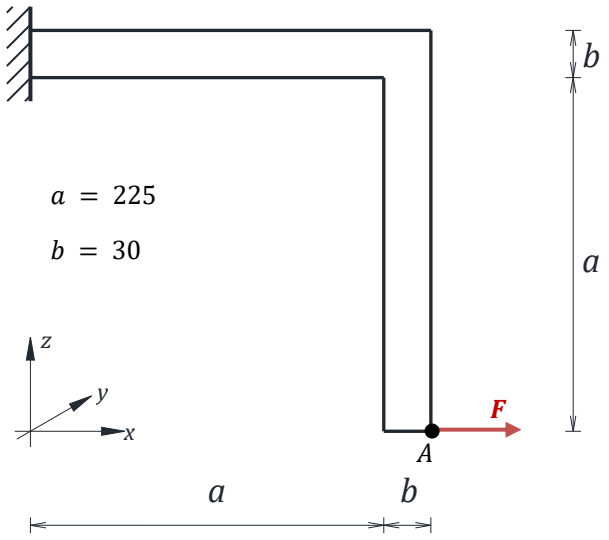

*Figure 2.19: L-shaped plate subjected to the tensile force **F**.*

*Slika 2.19: L-plošča obremenjena z natezno silo **F**.*

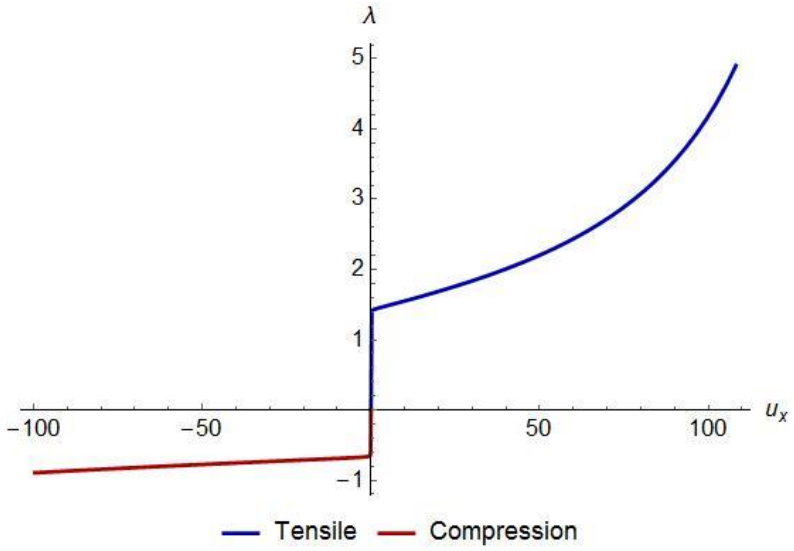

Figure 2.20: L-shaped plate: load factor versus displacement of the point A *in the x-axis direction.*

Slika 2.20: L-plošča: Diagram obtežni faktor v odvisnosti od pomika točke A v x-smeri.

Table 2.6: L-shaped plate: bifurcation forces (tensile load case)

Preglednica 2.6: L-plošča: sila v bifurkacijski točki (natezni obtežni primer).

Reference	Element type	Number of elements	Bifurcation force
(Simo & Vu-Quoc, 1986)	Beam	20	1.090
(Simo, Fox & Rifai, 1990)	Shell	100	1.128
Present	Shell	576	1.126

Figure 2.21: L-shaped plate: deformed finite element configurations; a) "tensile" force and b) "compressive" force.

Slika 2.21: L-plošča: deformirane konfiguracije mreže končnih elementov; a) "natezna" sila in b) "tlačna" sila.

2.4.6 Axially loaded cylindrical panel

A cylindrical panel problem, see Figure 2.22, with the geometry taken from (Jun and Hong, 1988), is subjected to the prescribed axial displacement $\lambda\hat{p}_{ref}$, where $\hat{p}_{ref} = 1$ mm. The material data is: Young's modulus $E = 2.1 \cdot 10^5$ N/mm^2, Poisson's coefficient $\nu = 0.25$, yield stress $\sigma_y = 235$ N/mm^2, and no plastic hardening. The used finite element mesh consists of 20 elements per edge. Elastic and elasto-plastic analyses were performed with the path-following data $\Delta l_0 = 0.1$, $\Delta l_{max} = 1, I_0 = 8$ and convergence tolerance 10^{-8}. The scaling test, related to initial units (N, mm), see Section 2.1.6, yields $T = 0.55$. In (2.6), $\psi_2 = 1$ was used.

The results of the elastic analysis are shown in Figure 2.23 and Figure 2.25, and the results of the elasto-plastic analysis are shown in Figure 2.24 and Figure 2.26. On Figure 2.23 and Figure 2.25, the axial displacement $u_x = \lambda\hat{p}_{ref}$ is presented with respect to the sum of the nodal axial reaction forces at the clamped edge R_x. The first buckling load is at $\lambda\hat{p}_{ref} = 2.9011$ mm ($R_x = 0.9411 \cdot 10^6$ N) and $\lambda\hat{p}_{ref} = 0.6603$ mm ($R_x = 0.1974 \cdot 10^6$ N) for the elastic and elasto-plastic analysis, respectively. Very sharp turning points can be observed on Figure 2.23. It seems that part of the curve between the points "2" and "3" backtracks; however, this is not the case, although "1"-"2" and "2"-"3" curves are in some parts nearly overlapping. The elasto-plastic curve on Figure 2.24 is much smoother and lower than the one from the elastic analysis. In point "4" on Figure 2.24, the applied arc-length procedure chooses the path of elastic unloading of the complete structure in favour of the continuation of the plastic loading. This is an illustration of a non-desired continuation of equilibrium path, related to complete elastic unloading of a structure, which is discussed e.g. in (Pohl et al., 2014). The remedy for this kind of unloading can be switching to path-following method based on controlling plastic dissipation. This kind of path-following method will be presented in the Chapter 3. The results of stability analysis for elastic structure are presented in Figure 2.27 (where load factor versus vertical displacement of the middle point of the panel is shown) and Table 2.14, where critical points data is listed. The analysis was performed with $\Delta l_0 = \Delta l_{max} = 0.05$, $I_0 = 8$ and $tol = 10^{-8}$. Displacement and loading parts of (2.6) at each increment are illustrated in Figure 2.28.

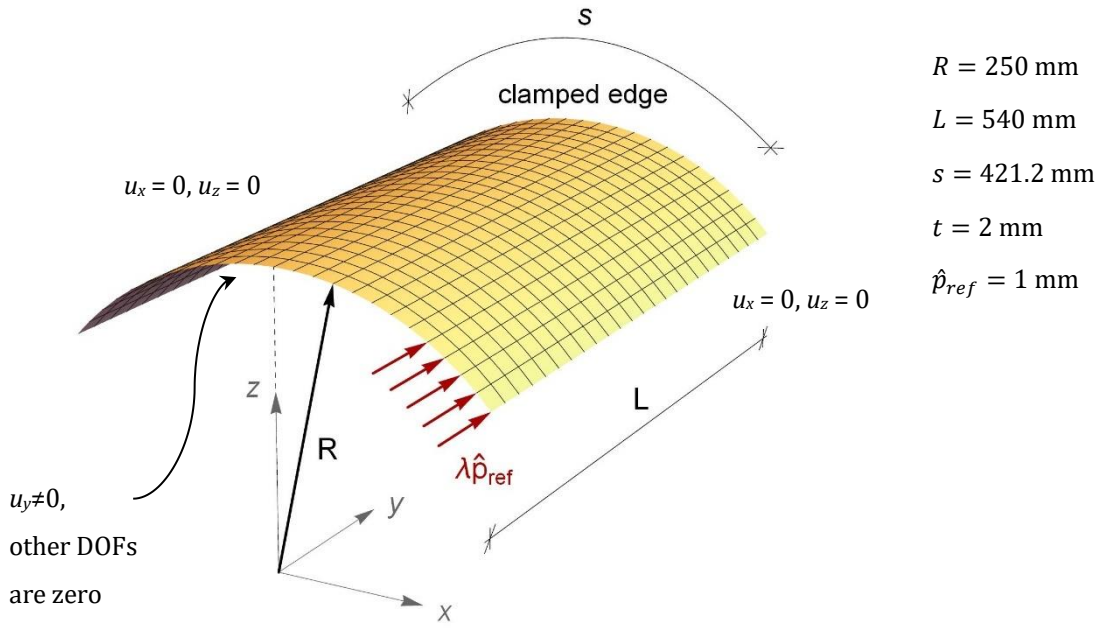

Figure 2.22: Axially loaded panel: geometry and boundary conditions.

Slika 2.22: Osno obremenjen panel: geometrija in robni pogoji.

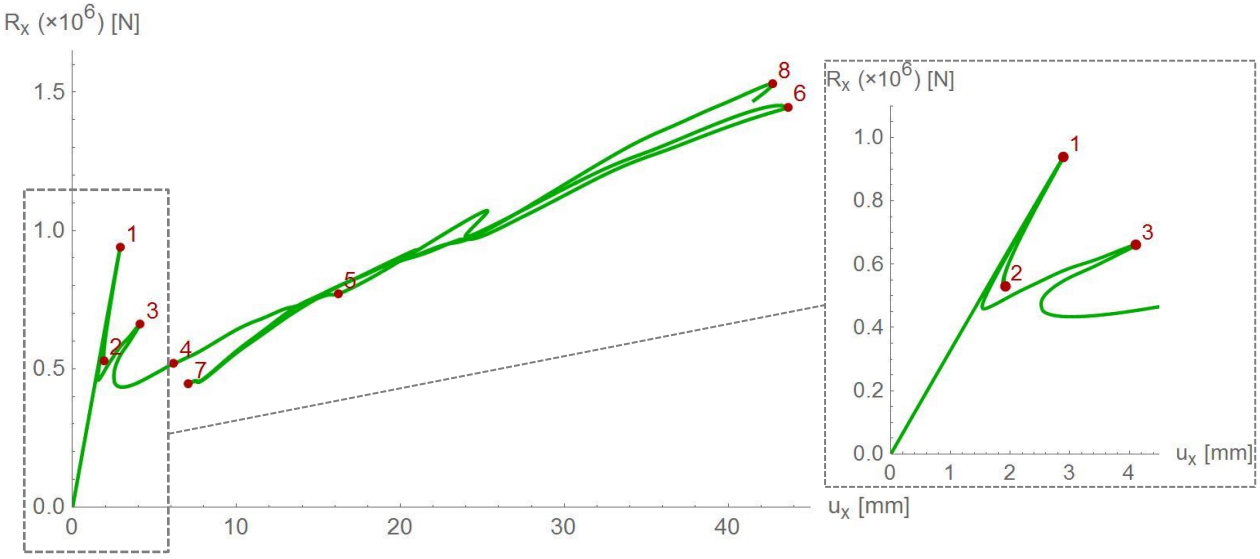

Figure 2.23: Axially loaded panel: Reaction versus imposed displacement curve for elastic analysis.

Slika 2.23: Osno obremenjen panel: Diagram reakcije v odvisnosti od predpisanega pomika pri elastični analizi.

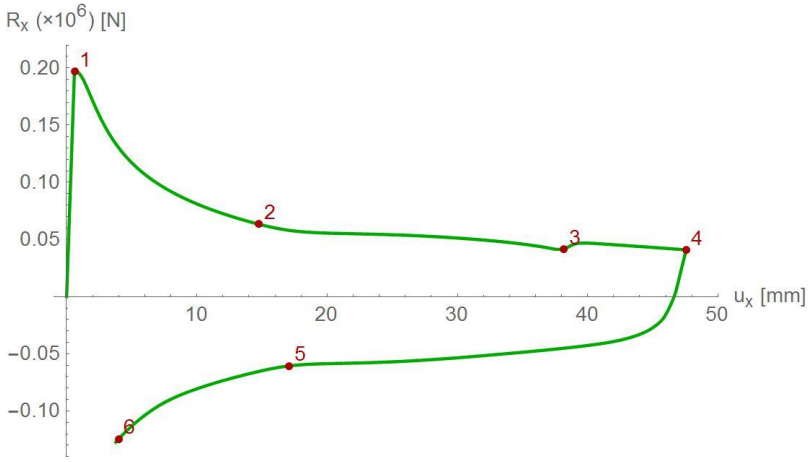

Figure 2.24: Axially loaded panel: Reaction versus imposed displacement curve for elasto-plastic analysis.

Slika 2.24: Osno obremenjen panel: Diagram reakcije v odvisnosti od predpisanega pomika pri elasto-plastični analizi.

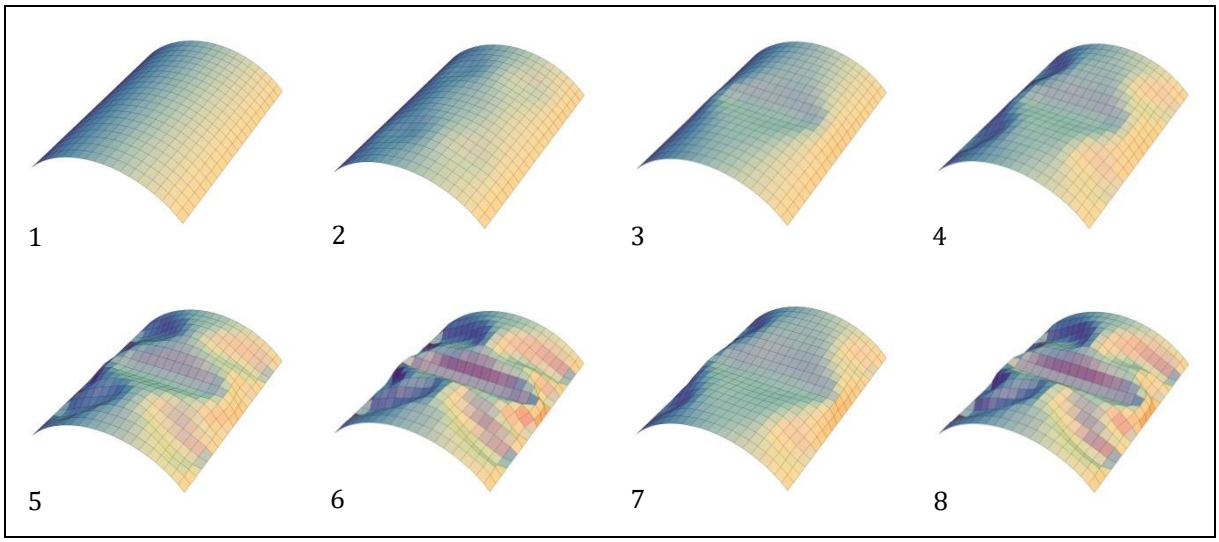

Figure 2.25: Axially loaded panel: deformed meshes for elastic analysis (the numbers correspond to Figure 2.23*).*

Slika 2.25: Osno obremenjen panel: deformirane konfiguracije mrež končnih elementov pri elastični analizi (indeks slike ustreza točkam v Slika 2.23).

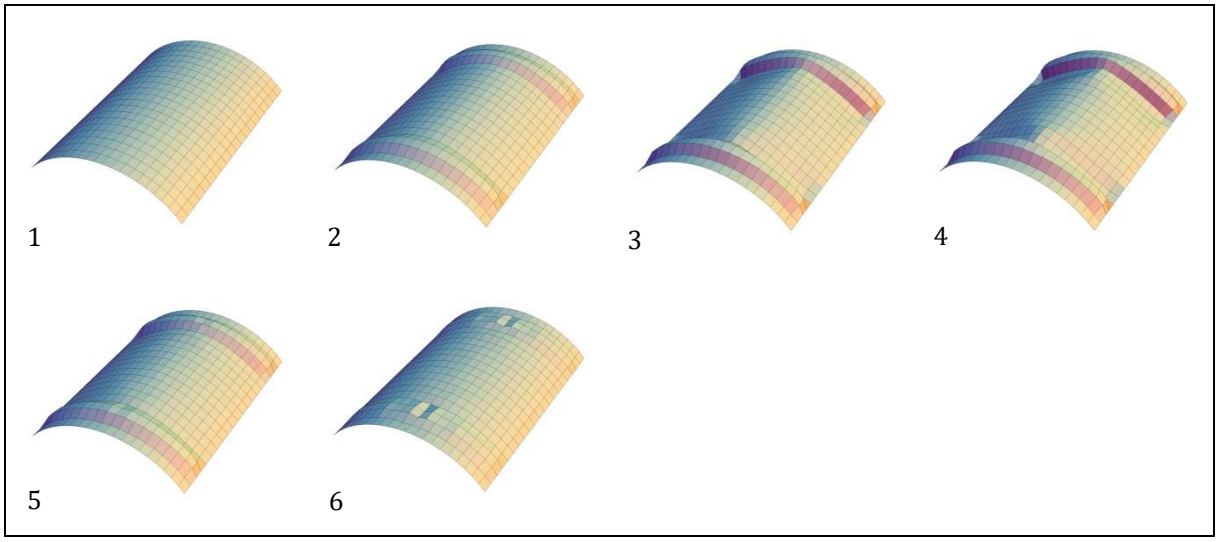

Figure 2.26: Axially loaded panel: deformed meshes for elasto-plastic analysis (the numbers correspond to Figure 2.24).

Slika 2.26: Osno obremenjen panel: deformirane konfiguracije mrež končnih elementov pri elastični analizi (indeks slike ustreza točkam v Slika 2.24).

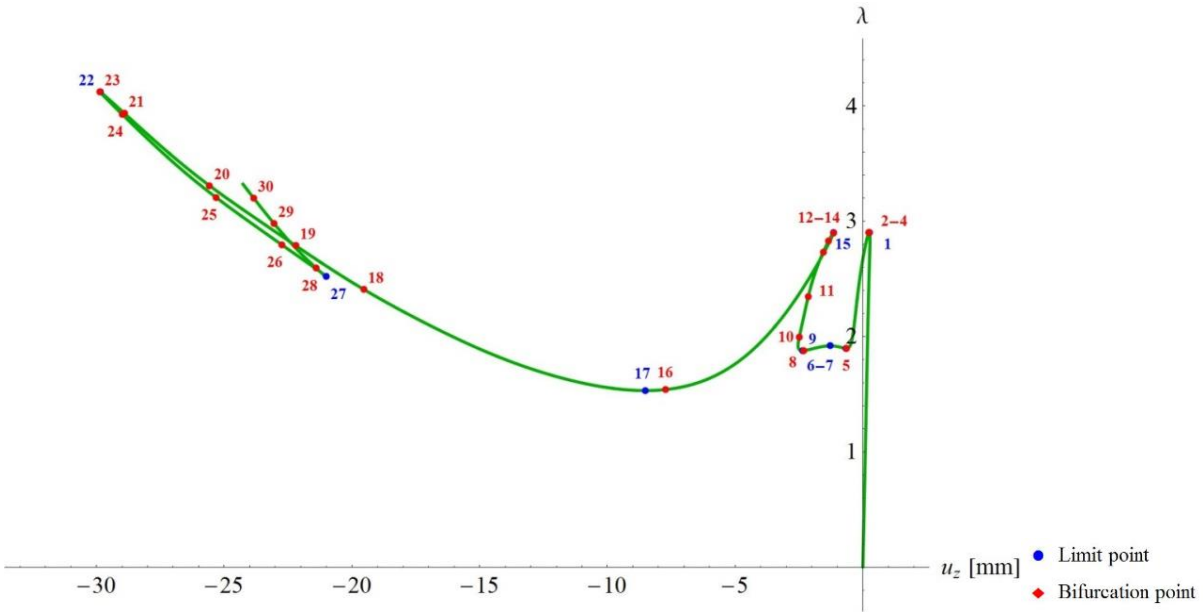

Figure 2.27: Axially loaded panel: critical points on the primary path for elastic analysis.

Slika 2.27: Osno obremenjen panel: kritične točke na primarni ravnotežni poti za elastično analizo.

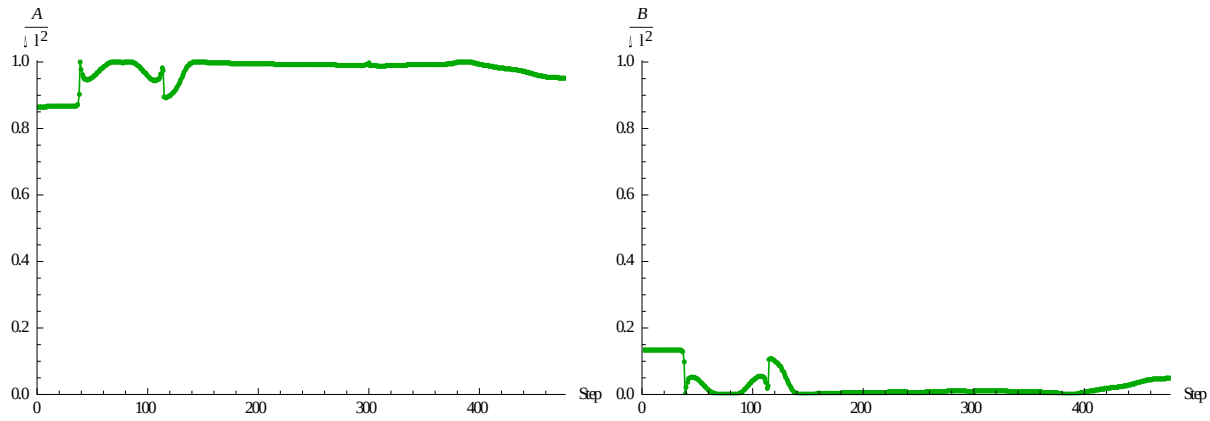

Figure 2.28: Displacement and loading parts of (2.6) at each increment: $A=(\Delta p_n)^T\,\Delta p_n$, $B=(\Delta\lambda_n)^2(p_{ref})^T p_{ref}$.

Slika 2.28: Vpliv delov vezne enačbe (2.6) zaradi pomika in obtežbe v vsakem inkrementu, $A=(\Delta p_n)^T\,\Delta p_n$, $B=(\Delta\lambda_n)^2(p_{ref})^T p_{ref}$.

2.4.7 Planar steel frame

A planar steel frame is analysed by the stress-resultant elasto-plastic geometrically linear beam Euler-Bernoulli finite element with the embedded strong discontinuity in rotation (Dujc et al., 2010), (Piculin and Brank, 2015). The later enables modelling localized failure (due to geometric and material instability) by a softening plastic hinge that dissipates the fracture energy in a mesh-independent manner. Most of the problem data, see Figure 2.29, is taken from (Rigobello et al., 2013). The Young's modulus is $E = 2.1 \cdot 10^5$ N/mm^2 and the yield stress is $\sigma_y = 235$ N/mm^2 . The yield moment of a cross-section depends on the axial force, i.e. $M_y(N) = W\left(\sigma_y - |N|/A\right)$, where W is the bending resistance cross-section modulus, A is the cross-section area and N is the axial force. Let us assume that the ultimate moment M_u is the following function of the axial force N

$$M_u(N) = \begin{cases} M_u^{ref,0}\left(1.03 + 0.85\, N/N_y\right) & \text{if} \quad N < -0.035 N_y \\ M_u^{ref,0} & \text{if} \quad N \geq -0.035 N_y \end{cases} \tag{2.44}$$

where $N_y = A\sigma_y$ and $M_u^{ref,0} = W_{pl}\sigma_y$. The data for the HEA340 are: the cross-section area $A = 12721$ mm^2, the modulus of inertia $I = 2642 \cdot 10^5$ mm^4, the plastic modulus $W_{pl} = 17.6 \cdot 10^5$ mm^3, the linear hardening modulus $K_h = 5.3 \cdot 10^{11}$ Nmm^2 and the linear softening modulus $K_s = -2 \cdot 10^9$ Nmm. The data for the HEB300 are: the cross-section area $A = 14282$ mm^2, the modulus of inertia $I = 2418 \cdot 10^5$ mm^4, the plastic modulus $W_{pl} = 17.8 \cdot 10^5$ mm^3 , the linear hardening modulus $K_h = 6.3 \cdot 10^{11}$ Nmm^2 and the linear softening modulus $K_s = -2 \cdot 10^9$ Nmm. The load consists of the horizontal force λH_0, where $H_0 = 35$ kN and two vertical forces $V = 2800$ kN that remain constant throughout the analysis. The columns and the beam are discretized as shown on Figure 2.30.

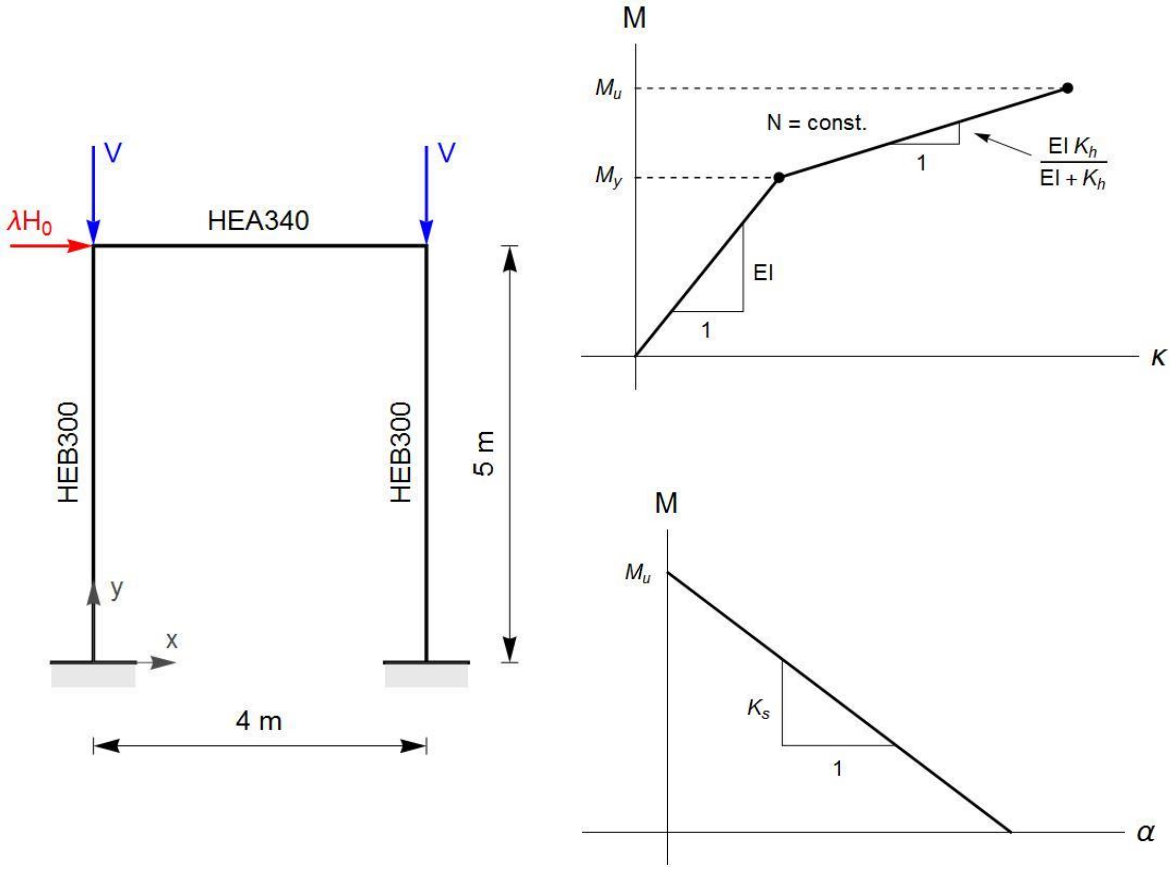

Figure 2.29: Portal frame: the problem data (left), the moment-curvature relation (right top), the moment versus jump in rotation α relation in a softening plastic hinge (right bottom).

Slika 2.29: Ravninski okvir: geometrijski podatki (levo), diagram moment v odvisnosti od ukrivljenosti (desno zgoraj), diagram moment v odvisnosti od skoka v zasuku α v plastičnem členku (desno spodaj).

For this problem, the quadratic path-following method, presented in Section 2.1, fails to converge (note curve "AL" on Figure 2.31). Therefore, at a certain increment (when the first softening plastic hinge is activated), the quadratic path-following method is replaced by the one described in Section 0. The analysis is thus performed in the following way: when there is no softening plastic hinges, we use the quadratic arc-length method; once the first softening plastic hinge is activated, we switch to the one-DOF path-following method. The data for the former are $\Delta l_0 = 1, \Delta l_{max} = 2, I_0 = 5, tol = 10^{-8}$, and the data for the latter are $\Delta \widehat{D}_0 = 10^{-5}, \Delta \widehat{D}_{max} = 10^{-4}, I_0 = 5, tol = 10^{-8}$. In the latter case, the control displacement for a current increment is chosen by using the procedure described in Section 2.2.2. The prescribed maximal value of the rotation-jump $\alpha_{n,MAX}$ is set to:

$$\alpha_{n,MAX} = min\left[\left(\frac{M_u^{ref,0}}{|K_s|}\right)^{HEA340}, \left(\frac{M_u^{ref,0}}{|K_s|}\right)^{HEB300}\right] \tag{2.45}$$

The procedure always chooses the element e6 (see Figure 2.30) as the control element Cel and one of its degrees-of-freedoms as the control parameter. In the first increment after the arc-length methods switching, the control parameter is the rotation of node 8. In the subsequent increments, the control

parameter is the horizontal displacement of node 8. Figure 2.31 shows that a complete failure response of the portal frame can be computed by the above described two-step procedure. Figure 2.32 shows how the plastic work (that is roughly the dissipated energy due to plastic deformations) changes during the analysis. We note that the same results can be computed by a simple displacement control, which, however is not applicable if there is more than one applied force that are λ dependent, as is the case of the next example.

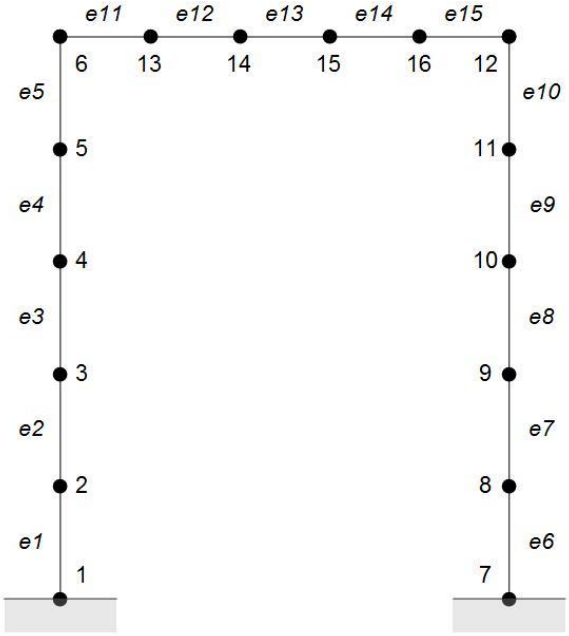

Figure 2.30: Portal frame: the finite element mesh.

Slika 2.30: Ravninski okvir: mreža končnih elementov.

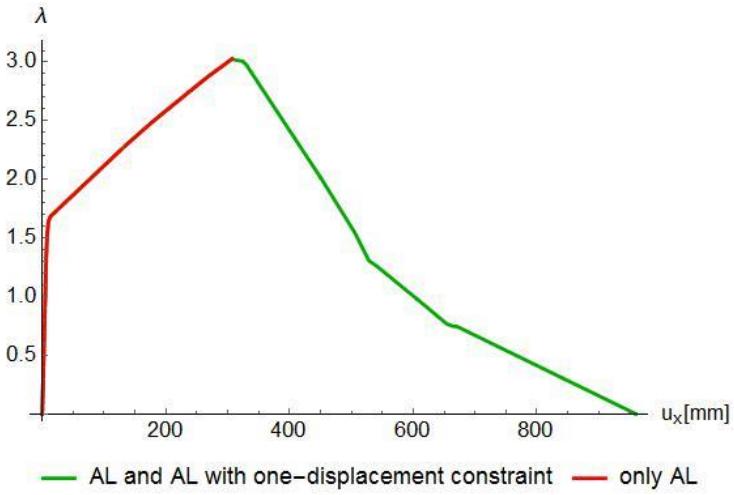

Figure 2.31: Portal frame: load-displacement curve (λ_{max} = 3.03).

Slika 2.31: Ravninski okvir: diagram obtežba-pomik (λ_{max} = 3.03).

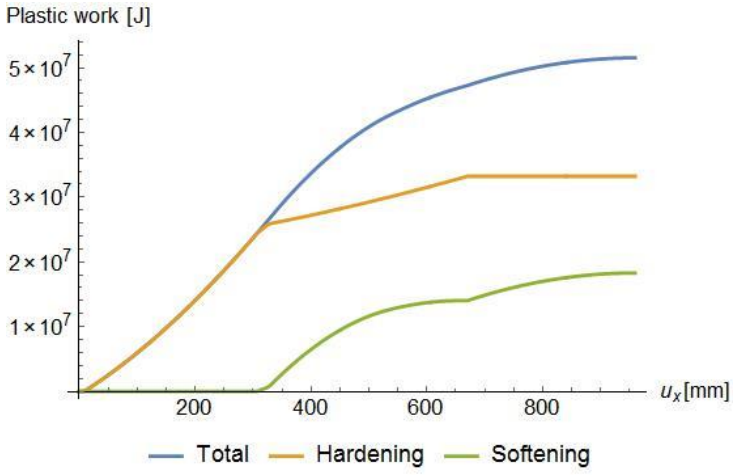

Figure 2.32: Portal frame: plastic work curves.

Slika 2.32: Ravninski okvir: diagram plastičnega dela v odvisnosti od horizontalnega pomika u_x vozlišča v zgornjem desnem vogalu.

2.4.8 Symmetric 3-storey steel frame

The 3-storey planar frame steel is considered, see Figure 2.33 for geometry, load and boundary conditions. It is composed of columns of height $H_c = 3$ m and beams of length $L_b = 4.5$ m. The columns have HEB 300 cross-section and the beams have HEA 340 cross-section. The cross-sections and the material properties are the same as in Example 2.4.7. The frame is loaded by the vertical line load $q_v = 100$ N/mm, see Figure 2.33, that remains constant during the analysis. The horizontal forces with the reference value $F_0 = 10$ kN are applied on the left side of the frame as shown on Figure 2.33. Each beam and column are meshed by 5 finite elements (the same type of beam element is used as in Example 2.4.7).

The analysis starts with the quadratic path-following method, presented in Section 2.1 (see Figure 2.34), and once the softening is triggered, we switch to the one-DOF path-following method presented in Section 0. The data for the first part of the analysis is: $\psi_1 = 1, \Delta l_0 = 10, \Delta l_{max} = 5000, I_0 = 8, tol = 10^{-8}$, and the data for the latter part of the analysis is: $\Delta\widehat{D}_0 = 10^{-2}, \Delta\widehat{D}_{max} = 0.4, I_0 = 8, tol = 10^{-8}$, with the control DOF chosen as the maximal absolute change of DOFs in the control element *Cel*, see equation (2.34). The result of the analysis is shown on Figure 2.34, where the load factor λ is shown versus the horizontal displacement u_{top} of top left corner node of the frame. Note, that the analysis based only on the quadratic path-following method, presented in Section 2.1 (denoted as "AL" on Figure 2.34), failed to compute the complete failure response of the frame. Figure 2.35 shows the deformed configuration and the distribution of softening plastic hinges, and Figure 2.36 shows the plastic work curves until complete failure of the frame.

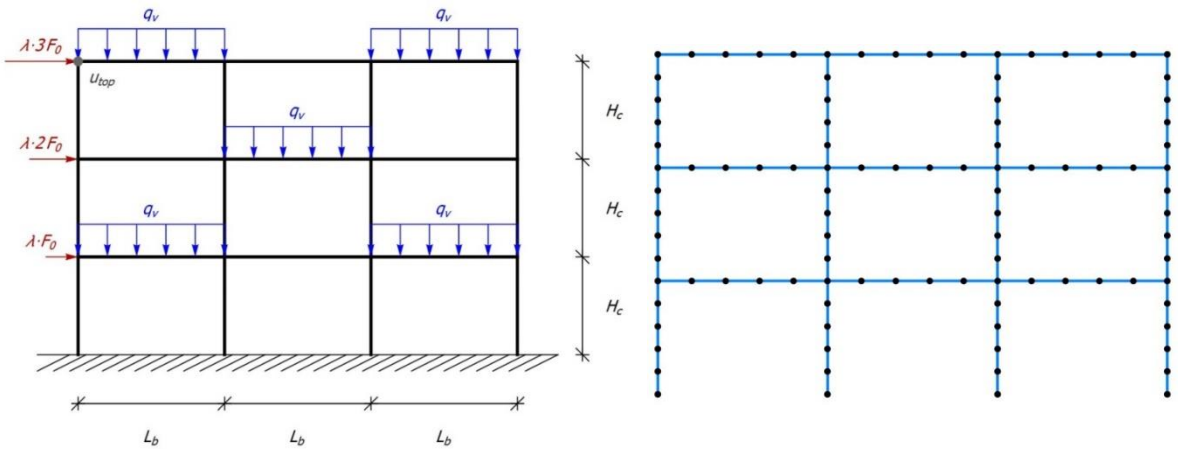

Figure 2.33: Symmetric 3-storey frame with geometry, loading and boundary conditions (left). Finite element mesh (right).

Slika 2.33: Simetrični trietažni okvir: geometrija, obtežba in robni pogoji (levo). Mreža končnih elementov (desno).

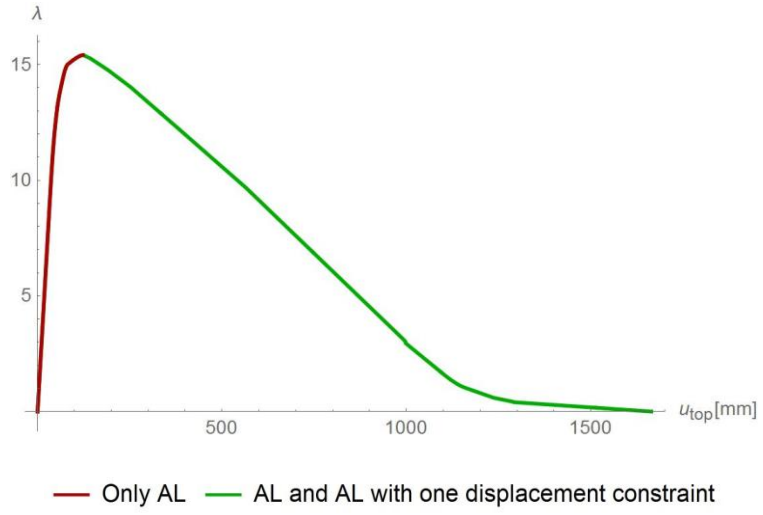

Figure 2.34: Symmetric 3-storey frame: load-displacement curve.

Slika 2.34: Simetrični trietažni okvir: Diagram obtežni faktor v odvisnosti od pomika.

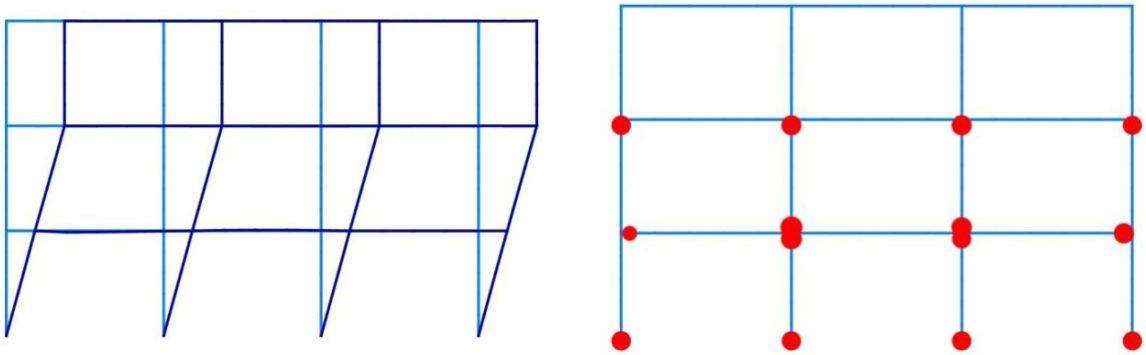

Figure 2.35: Symmetric 3-storey frame: deformed configuration (left) and state of the plastic hinges in the frame at the end of analysis.

Slika 2.35: Simetrični trietažni okvir: deformacijska konfiguracija (levo) in stanje plastičnih členkov v okvirju na koncu analize.

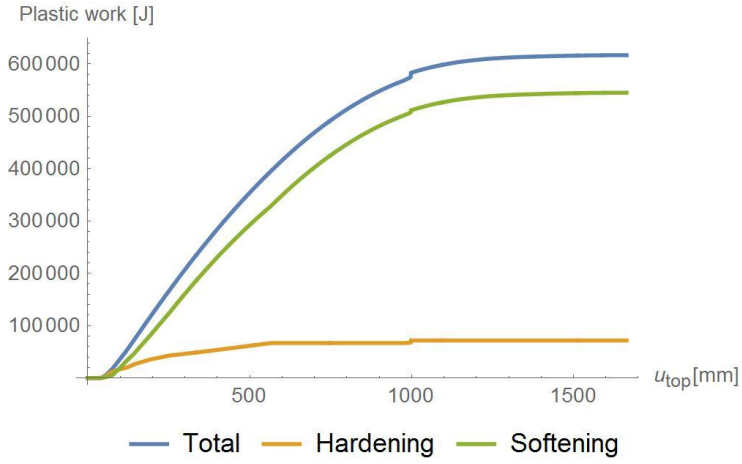

Figure 2.36: Symmetric 3-storey frame: plastic work curves.

Slika 2.36: Simetrični trietažni okvir: grafi plastičnega dela.

2.4.9 Notched concrete prism

We analyse a three point bending test of a concrete prism; the geometry is shown on Figure 2.37; the prism thickness $t = 5$ cm. The prism has a notch at the middle bottom. The material data are: Young's modulus $E = 3000$ kN/cm^2, Poisson's ratio $\nu = 0.3$ and the ultimate tensile strength $\sigma_u = 0.333$ kN/cm^2. The softening law is driven by $\bar{\bar{q}} = \sigma_u \left(1 - exp^{-\frac{\bar{\bar{\xi}}\sigma_u}{G_f}}\right)$, where the fracture energy is $G_f = 0.124 \cdot 10^{-2}$ kN/cm, and $\bar{\bar{q}}$ and $\bar{\bar{\xi}}$ are the force-like and the displacement-like inelastic constitutive variables, respectively, that control softening. The simply supported prism is subjected at its centre top to an imposed displacement $\lambda \hat{p}_{ref}$, where $\hat{p}_{ref} = 0.2$ cm. We use plane-stress ED finite elements presented in (Dujc et al 2010a). The mesh is shown on Figure 2.38.

The analysis is performed in two steps. When there is no softening, we use the quadratic path-following method; once the crack is activated, we switch to the one-DOF path-following method. The data for the former are $\Delta l_0 = 10^{-3}$, $\Delta l_{max} = 10^{-1}$, $I_0 = 5, tol = 10^{-8}$, and the data for the latter are $\Delta \widehat{D}_0 = 10^{-5}$, $\Delta \widehat{D}_{max} = 10^{-3}, I_0 = 5, tol = 10^{-8}$. The crack starts at the notch, when the tensile strength of the material is reached and propagates in the direction perpendicular to the maximum principal stress, i.e. in the mode I fashion. The control DOF was always a nodal displacement parallel to the imposed displacement $\lambda \hat{p}_{ref}$. Figure 2.39 shows the computed relation between the reaction force R_y and the imposed displacement $\lambda \hat{p}_{ref}$. Figure 2.40 shows deformed finite configuration with a crack. We note that this example can be also computed by a simple displacement control, which, however, is not applicable for several λ dependent applied forces.

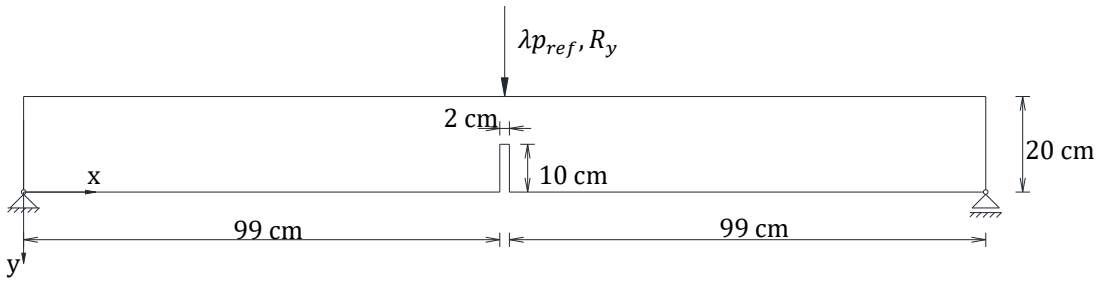

Figure 2.37: Three point bending test.

Slika 2.37: Tri-točkovni upogibni test.

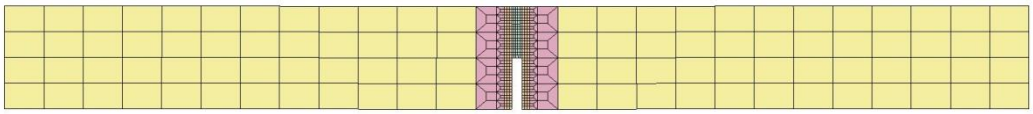

Figure 2.38: Three point bending: finite element mesh.

Slika 2.38: Tri-točkovni upogib: mreža končnih elementov.

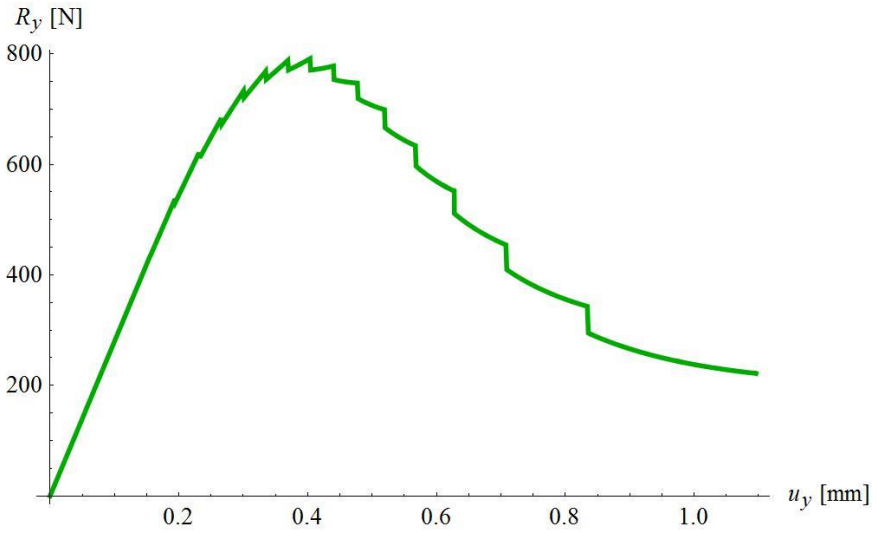

Figure 2.39: Three point bending: force-displacement curve ($R_{y,max}$ = 791.5 N*).*

Slika 2.39: Tri-točkovni upogib: diagram sila v odvisnosti od pomika ($R_{y,max}$ = 791.5 N*).*

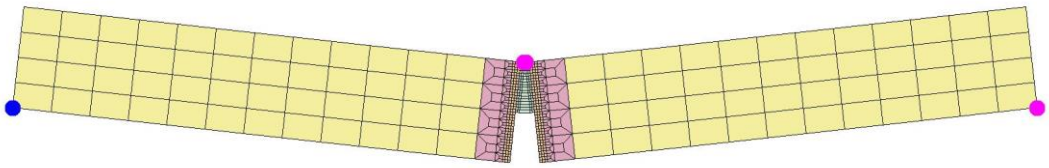

Figure 2.40: Three point bending: deformed finite element mesh at the end of the analysis (displacements are 100 times magnified).

Slika 2.40: Tri-točkovni upogib: deformacijska konfiguracija mreže končnih elementov na koncu analize (pomiki so 100-krat povečani).

2.4.10 Delamination of a beam

We reconsider delamination of a cantilever beam presented in (Manzoli and Shing, 2006), see Figure 2.41. The beam length is $L = 0.45$ cm, the thickness is $a = 0.05$ cm and the width is $b = 0.3$ cm. The elastic modulus is $E = 50$ kN/cm^2 and the Poisson ratio is $\nu = 0.3$. The beam is modeled by the plane stress embedded-discontinuity finite elements presented in (Dujc et al., 2010b). It is assumed that the delamination along the interface develops in mode I fashion only. The interface is modeled as a material line that starts opening when the ultimate tension stress $\sigma_u = 0.1$ kN/cm^2 is reached. The opening is controlled by the softening law driven by $\bar{\bar{q}} = \sigma_u \left(1 - exp^{-\frac{\bar{\bar{\xi}}\sigma_u}{G_f}}\right)$. The fracture energy is $G_f = 5 \cdot 10^{-3}$ kN/cm, and $\bar{\bar{q}}$ and $\bar{\bar{\xi}}$ are the force-like and the displacement-like inelastic constitutive variables, respectively, that control softening. The beam is subjected at its free end to a pair of prescribed displacements $\lambda \hat{p}_{ref}$, where $\hat{p}_{ref} =$ 0.2 cm (see Figure 2.41).

We perform the analysis in two steps. When there is no delamination, we use the quadratic arc-length method. Once the delamination is activated in one element of the mesh, we switch to the one-displacement path-following method. The control displacement is always chosen to be parallel to the prescribed displacements. The data for the quadratic arc-length analysis is: $l_0 = 10^{-5}$, $\Delta l_{max} = 10^{-4}$, $I_0 = 12$ and $tol = 10^{-10}$. The data for the one-constrained-displacement arc-length analysis is: $l_0 = 10^{-6}$, $\Delta l_{max} = 10^{-3}$, $I_0 = 50$ and $tol = 10^{-10}$. Figure 2.42 shows the computed relation between the reaction R_y and the imposed displacement $\lambda \hat{p}_{ref}$. The deformed finite element mesh (with no magnification) at $\lambda \hat{p}_{ref} = 1.80$ mm is presented in Figure 2.43.

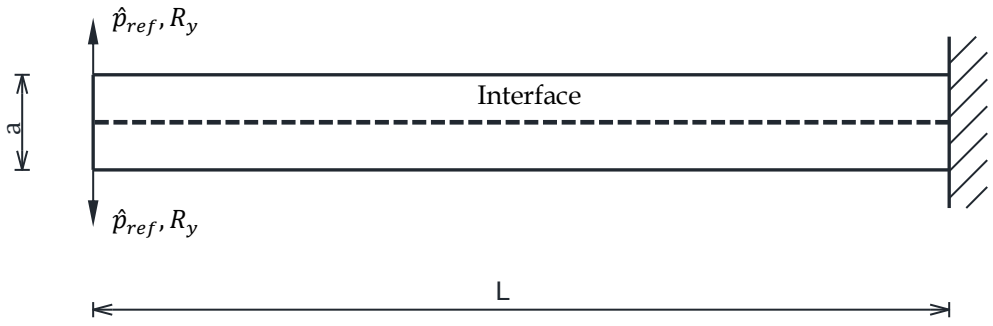

Figure 2.41: Beam delamination.

Slika 2.41: Delaminacija nosilca.

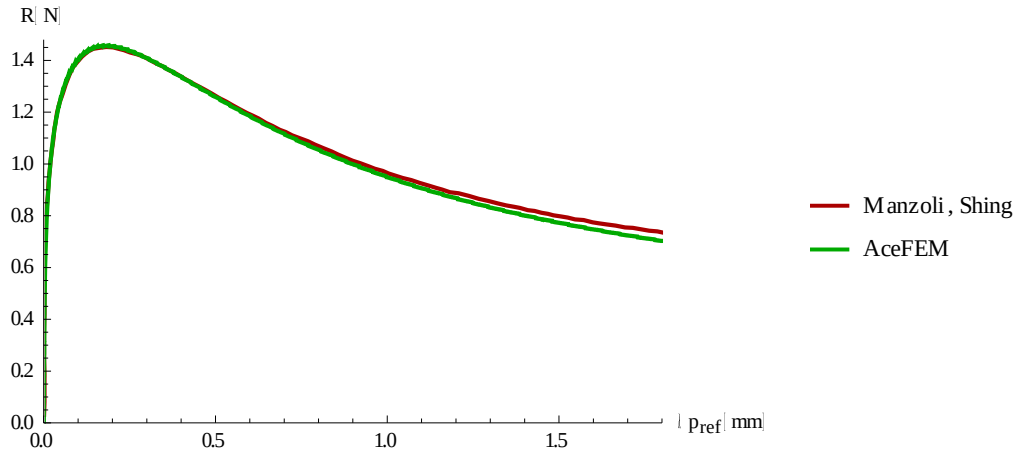

Figure 2.42: Beam delamination: reaction versus imposed displacement curve (R_{max} = 1.46 N*).*

Slika 2.42: Delaminacija nosilca: diagram reakcije v odvisnosti od pomika (R_{max} = 1.46 N*).*

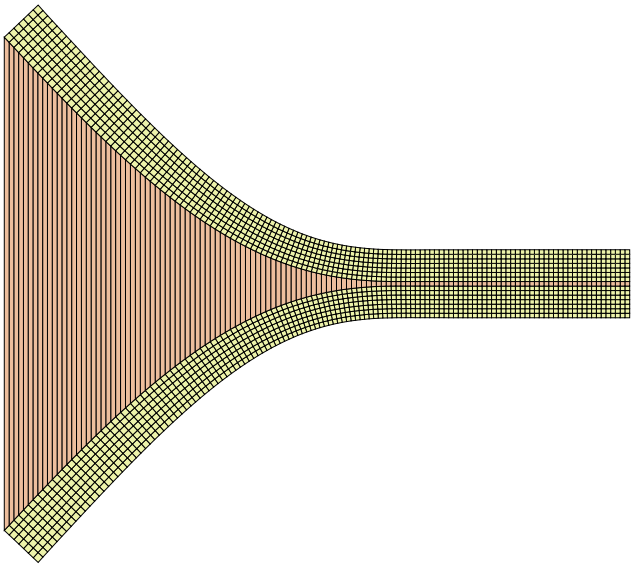

Figure 2.43: Beam delamination: deformed mesh at {λp_{ref}, R_y} = {1.8 mm*, 0.70* N*}.*

Slika 2.43: Delaminacija nosilca: deformacijska konfiguracija mreže v ravnotežni točki {λp_{ref}, R_y} = {1.8 mm*, 0.70* N*}.*

2.5 Conclusions

The consistently linearized path-following method has been revisited. We note that the term »consistently linearized« is here used in a sense that all governing equations, i.e. the equilibrium equations and the constraint equation, are linearized when searching for the solution of those equations in the framework of path-following method. The usual statement, related to the consistently linearized path-following method, is that it is less robust in the vicinity of a sharp turning point than the standard Crisfield's (cylindrical or spherical) arc-length method (see e.g. (Carrera, 1994), (Ritto-Correa and Camotim, 2008)). This is due to the fact that the latter satisfies the constraint equation at every iteration and the former shares this property only at the iterations that are related to converged configurations. The presented numerical examples illustrate that the consistently linearized path-following method is robust and very satisfying in solving many geometrically and materially nonlinear problems with sharp turning points and bifurcation points. In our view the Crisfield's arc-length method and the consistently-linearized path-following method are comparable in terms of successfulness in problem solving when it comes to (more) difficult geometrically and/or materially nonlinear problems. It has been shown that the consistently linearized path-following method can be used as a framework for a goal-oriented path-following procedure that is not based on a quadratic constraint equation. In particular, a one-DOF constraint equation has been applied, which enables computation of problems with material softening. This kind of the path-following procedure has been employed for a complete failure analysis of structures and solids by using the embedded-discontinuity finite elements.

This section illustrates that there is same theory and the same implementation procedure behind the path-following method and the direct computation of the critical points: what is changed is the structure of the

constraint equation. The solution procedure (which is related to the solution of the equilibrium equations that are extended by the constraint equation) remains the same regardless of the applied constraint equation.

In our view, there are some aspects of this work that should be emphasised: the constraint function (2.6) that takes into account the prescribed displacements and makes the path-following method more efficient for the prescribed displacement problems (see Example 2.4.6); application of a one-DOF constraint function (that changes from increment to increment) for solution of complete failure structural problems by using highly complex embedded-discontinuity frame and 2d-solid finite elements (that use softening traction-separation inelastic cohesive laws to model material failure) – to our knowledge, this combination has not been checked yet; illustration of the importance of scaling for a constraint function with the "displacement" and the "loading" parts (see Examples 2.4.2 and 2.4.6); usage of the eingenvector-free constraint function (2.36) for a direct computation of critical points in nonlinear analysis of shell structures; and usage of an automatic differentiation tool in order to obtain exact expression for the derivatives that are needed for the direct computation of critical points with an eigenvector-free constraint function.

2.6 Appendix

Table 2.7: Truss dome: critical points.

Preglednica 2.7: Palična kupola: kritične točke.

	Critical point			First three eigenvalues			B, see eq. (2.39)	
	u_z [cm]	λ	Classification	λ_1	λ_2	λ_3		
1	-0,769	0,643	LP	1,4E-14	2,12	2,12	0,98	
2	-3,028	-0,560	LP	1,1E-12	2,18	2,18	0,99	
3	-9,097	15,530	DBP	1,3E-07	1,3E-07	0,73	4,9E-09	8,3E-09
4	-10,100	17,453	BP	4,8E-12	0,22	-0,63	4,8E-08	
5	-10,513	17,668	LP	-1,4E-14	0,58	0,58	0,45	
6	-10,887	17,489	DBP	8,7E-07	9,9E-07	-0,20	1,0E-07	6,3E-09
7	-11,787	-9,513	LP	6,2E-15	-1,98	-3,20	0,99	
8	-4,645	9,434	LP	-1,2E-14	-1,98	-3,20	0,99	
9	-5,545	-17,548	DBP	-8,8E-07	-9,6E-07	-0,20	7,8E-08	1,5E-08
10	-5,919	-17,749	LP	1,3E-12	0,58	0,58	0,45	
11	-6,333	-17,555	BP	1,3E-12	0,22	-0,63	3,8E-08	
12	-7,335	-15,653	DBP	-1,1E-07	-1,1E-07	0,73	9,9E-09	2,2E-08
13	-13,404	0,479	LP	1,5E-13	2,18	2,18	0,99	
14	-15,663	-0,7266	LP	-5,4E-16	2,12	2,12	-0,98	

Table 2.8: Cylindrical panel, ¼ of the shell discretization: critical points, see Figure 2.13.

Preglednica 2.8: Cilindrični panel, model ¼ lupine: kritične točke, glej Slika 2.13.

	Critical point			First two eigenvalues		B, see eq. (2.39)
	u_z [cm]	λ	Classification	λ_1	λ_2	
1	-0,133	0,196	LP	1,4E-09	0,08	-0,034
2	-0,161	-0,128	LP	-5,8E-14	0,03	-0,008

Table 2.9: Cylindrical panel, ½ of the shell discretization along section A: the primary path critical points, see Figure 2.14 (top).

Preglednica 2.9: Cilindrični panel, model ½ lupine vzdolž prereza A: kritične točke na primarni ravnotežni poti, glej Slika 2.14 (zgoraj).

	Critical point			First two eigenvalues		B, see eq. (2.39)
	u_z [cm]	λ	Classification	λ_1	λ_2	
1	-0,1328	0,1963	LP	2,5E-8	0,01	4,9E-02
2	-0,1526	0,1763	LP	5,3E-13	-0,01	7,9E-02
3	-0,1474	-0,0804	LP	6,5E-10	0,007	-7,2E-02
4	-0,1606	-0,1282	LP	6,6E-10	0,02	-9,0E-03

Table 2.10: Cylindrical panel, ½ of the shell discretization along section B: the primary path critical points, see Figure 2.14 (bottom).

Preglednica 2.10: Cilindrični panel, model ½ lupine vzdolž prereza B: kritične točke na primarni ravnotežni poti, glej Slika 2.14 (spodaj).

	Critical point			First two eigenvalues		B, see eq. (2.39)
	u_z [cm]	λ	Classification	λ_1	λ_2	
1	-0,0974	0,1750	BP	2,8E-12	0,01	-6,9E-10
2	-0,1328	0,1963	LP	1,3E-07	-0,01	-7,3E-2
3	-0,1606	-0,1282	LP	6,3E-11	-0,02	8,7E-2
4	-0,2182	-0,0754	BP	4,4E-14	0,03	-2,0E-8

Table 2.11: Cylindrical panel, ½ of the shell discretization along section B: the secondary path critical points, see Figure 2.14 (bottom).

Preglednica 2.11: Cilindrični panel, model ½ lupine vzdolž prereza B:kritične točke na sekundarni veji, glej Slika 2.14 (spodaj).

	Critical point			First two eigenvalues		B, see eq. (2.39)
	u_z [cm]	λ	Classification	λ_1	λ_2	
1	-0,097378	0,175021	BP	2,8E-12	0,01	-6,9E-10
2	-0,097431	0,175003	LP	2,0E-05	0,01	5,0E-03
3	-0,2182	-0,0754	LP	9,3E-07	0,03	-1,9E-03

Table 2.12: Cylindrical panel, complete shell discretization: the primary path critical points, see Figure 2.15.

Preglednica 2.12: Cilindrični panel, model celotne lupine: kritične točke na primarni ravnotežni poti, glej Slika 2.15.

	Critical point			First two eigenvalues		B, see eq. (2.39)
	u_z [cm]	λ	Classification	λ_1	λ_2	
1	-0,097	0,175	LP	2,9E-09	0,01	0,03
2	-0,133	0,196	BP	2,9E-06	-0,01	1,9E-13
3	-0,153	0,176	BP	-1,0E-13	-0,01	6,4E-14
4	-0,169	0,002	LP	9,2E-12	-0,01	0,06
5	-0,147	-0,080	BP	1,6E-13	-0,004	2,2E-12
6	-0,145	-0,095	LP	5,4E-13	0,01	0,05
7	-0,161	-0,128	BP	5,5E-07	0,01	4,0E-13
8	-0,218	-0,075	LP	2,0E-11	0,02	0,03

Table 2.13: Cylindrical panel, complete shell discretization: the secondary path critical points, see Figure 2.15.

Preglednica 2.13: Cilindrični panel, model celotne lupine: kritične točke na sekundarni veji, glej Slika 2.15.

	Critical point			First two eigenvalues		B, see eq. (2.39)
	u_z [cm]	λ	Classification	λ_1	λ_2	
1	-0,097	0,175	LP	2,9E-09	0,014	-0,032
2	-0,133	0,196	BP	2,9E-06	-0,008	-1,7E-13
3	-0,153	0,176	BP	-2,0E-13	-0,011	-6,6E-13
4	-0,124	0,059	LP	-6,9E-10	-0,002	0,009
5	-0,144	0,057	BP	7,9E-07	0,005	4,3E-13
6	-0,169	0,058	BP	1,6E-07	0,008	2,7E-13
7	-0,198	0,022	LP	8,6E-12	-0,012	-0,056
8	-0,162	-0,083	LP	7,7E-07	0,001	-0,051
9	-0,159	-0,084	BP	-1,9E-07	-0,001	-1,7E-13
10	-0,147	-0,080	BP	4,3E-08	-0,004	2,4E-12

Table 2.14: Axially loaded panel: Critical points from Figure 2.27.

Preglednica 2.14: Osno obremenjen panel: kritične točke iz Slika 2.27.

	Critical point			First two eigenvalues		B, see eq. (2.39)
	u_z [cm]	λ	Classification	λ_1	λ_2	
1	0,25	2,90	LP	1,15E-06	1,619	0,0004
2	0,25	2,90	BP	6,40E-08	3,592	-6,0E-10
3	0,24	2,90	BP	-1,83E-06	1,680	-8,5E-08
4	0,23	2,90	BP	-2,49E-07	-3,55	2,1E-10
5	-0,63	1,90	BP	-3,70E-07	-4,515	-4,6E-11
6	-0,65	1,90	LP	6,03E-07	1,146	-0,003
7	-1,27	1,92	LP	6,46E-11	7,098	-0,002
8	-2,31	1,88	BP	1,15E-06	4,714	-9,7E-12
9	-2,35	1,88	LP	-0,00063	-1,350	-0,003
10	-2,49	2,00	BP	-3,80E-08	4,955	-4,6E-09
11	-2,14	2,35	BP	-2,63E-07	22,665	4,0E-12
12	-1,55	2,73	BP	-1,44E-06	33,818	-7,0E-12
13	-1,34	2,83	BP	-3,59E-07	20,919	7,4E-11
14	-1,15	2,90	BP	-1,66E-05	-4,982	3,8E-07
15	-1,15	2,90	LP	6,30E-08	5,193	-0,0005
16	-7,72	1,54	BP	4,95E-09	-4,434	-6,1E-09
17	-8,51	1,53	LP	0,00043	1,515	-0,001
18	-19,53	2,41	BP	4,94E-08	5,399	7,3E-11
19	-22,20	2,79	BP	-3,65E-07	2,692	5,4E-12
20	-25,57	3,31	BP	7,20E-08	6,171	-5,0E-11
21	-28,90	3,94	BP	5,81E-08	9,235	3,1E-08
22	-29,86	4,12	LP	0,00074	1,099	-2,8E-06
23	-29,86	4,12	BP	6,53E-07	1,094	2,3E-10
24	-29,00	3,93	BP	-9,81E-08	9,733	-4,7E-09
25	-25,32	3,21	BP	5,97E-07	5,133	2,0E-12
26	-22,74	2,80	BP	7,09E-08	1,036	-8,4E-11
27	-21,00	2,52	LP	0,00105	2,499	-0,002
28	-21,39	2,59	BP	-1,97E-06	10,441	-8,4E-12
29	-23,06	2,98	BP	1,33E-06	-7,993	9,6E-12
30	-23,85	3,20	BP	-2,41E-08	-0,949	2,3E-10

3 PATH-FOLLOWING METHOD BASED ON CONTROL OF PLASTIC DISSIPATION OR PLASTIC WORK

A path-following method that is based on controlling plastic dissipation or plastic work in an inelastic solid or structure is presented. It can be effective for highly nonlinear materially and geometrically problems. In particular, it can be applied for elasto-plastic problems where the standard path-following methods fail, or to avoid artificial and undesirable elastic unloading of a complete solid or structure during the computation. The essential ingredients, the plastic dissipation and the plastic work based constraint equations, are derived by using either explicit or implicit pseudo-time step integration. These constraint equations are valid for geometrically nonlinear small strain elasto-plasticity with hardening. The constraint function is also derived for the embedded-discontinuity finite elements. Their implementation in the framework of the path-following method is described. Several numerical examples are presented in order to illustrate very satisfying performance of the derived path-following method. It performed very well for some challenging shell problems.

The rest of the section is organized as follows. In Section 3.1, the path-following method framework is presented. In Section 3.2, several plastic dissipation based constraint equations are derived by using an explicit or implicit integration in the pseudo-time step. Section 3.3 provides illustrative numerical examples. Conclusions are drawn in Section 3.4.

3.1 The framework for the path-following methods

In the nonlinear finite element method for solids and structures, one has to solve the following system of nonlinear equations

$$\boldsymbol{R}\big(\boldsymbol{u}(t),\lambda(t)\big)=\boldsymbol{R}^{int}\big(\boldsymbol{u}(t)\big)-\boldsymbol{f}^{ext}\big(\lambda(t)\big)=\boldsymbol{0} \tag{3.1}$$

where $\boldsymbol{R}^{int}$ and $\boldsymbol{f}^{ext}$ are vectors of internal and external (equivalent) nodal forces (and moments, if they are present in the formulation), respectively, $\boldsymbol{u}$ is vector of unknown nodal displacements (and rotations, if they are present in the formulation), λ is the load factor, and $t \geq 0$ is a monotonically increasing parameter that will be called the pseudo-time. In many practical cases, the system of equations (3.1) is possible to solve only with an additional constraint equation

$$g\big(\boldsymbol{u}(t)-\boldsymbol{u}(t-\Delta t),\lambda(t)-\lambda(t-\Delta t)\big)=0 \tag{3.2}$$

where Δ represents a small (incremental) change. Solving (3.1) and (3.2) simultaneously is called the path-following method or the arc-length method if (3.2) has a cylindrical or spherical form, see e.g. (Crisfield, 1981, 1991). The solution of (3.1) and (3.2) is searched for at the discrete pseudo-time points $0 = t_0, t_1, \dots, t_n, t_{n+1}, \dots, t_{final}$. Let us assume that configuration at t_n is known (the notation $a(t_n) = a_n$ will be

used in what follows) and defined by the pair $\{\boldsymbol{u}(t_n), \lambda(t_n)\} = \{\boldsymbol{u}_n, \lambda_n\}$. At searching for the next configuration at $t_{n+1} = t_n + \Delta t_n$, we additively decompose $\boldsymbol{u}_{n+1}$ and λ_{n+1} as $\boldsymbol{u}_{n+1} = \boldsymbol{u}_n + \Delta\boldsymbol{u}_n$ and $\lambda_{n+1} = \lambda_n + \Delta\lambda_n$, where $\Delta\boldsymbol{u}_n$ and $\Delta\lambda_n$ are the increments of the displacement vector and the load vector, respectively. Equations (3.1) and (3.2) can be rewritten for t_{n+1} as

$$\begin{aligned} &\boldsymbol{R}_{n+1}(\boldsymbol{u}_n, \lambda_n; \Delta\boldsymbol{u}_n, \Delta\lambda_n) = \boldsymbol{0} \\ &g_{n+1}(\Delta\boldsymbol{u}_n, \Delta\lambda_n) = 0 \end{aligned} \tag{3.3}$$

where $\Delta\boldsymbol{u}_n$ and $\Delta\lambda_n$ are the unknowns. The solution of (3.3) is searched for iteratively by the Newton-Raphson method. At an iteration i, the following linear system has to be solved

$$\begin{bmatrix} \boldsymbol{K}_{n+1}^i & \boldsymbol{R}_{n+1,\lambda}^i \\ \left[g_{n+1,\boldsymbol{u}}^i\right]^T & g_{n+1,\lambda}^i \end{bmatrix} \begin{Bmatrix} \Delta\tilde{\boldsymbol{u}}_n^i \\ \Delta\tilde{\lambda}_n^i \end{Bmatrix} = -\begin{Bmatrix} \boldsymbol{R}_{n+1}^i \\ g_{n+1}^i \end{Bmatrix} \tag{3.4}$$

for the iterative pair $\{\Delta\tilde{\boldsymbol{u}}_n^i, \Delta\tilde{\lambda}_n^i\}$, where $(\circ)_{,\lambda}$ and $(\circ)_{,\boldsymbol{u}}$ denote the derivatives of $(\circ)$ with respect to $\Delta\lambda_n^i$ and $\Delta\boldsymbol{u}_n^i$, respectively, and $\boldsymbol{K}_{n+1}^i = \boldsymbol{R}_{n+1,\boldsymbol{u}}^i$ is the tangent stiffness matrix. New iterative guess is obtained as $\Delta\boldsymbol{u}_{n+1}^{i+1} = \Delta\boldsymbol{u}_n^i + \Delta\tilde{\boldsymbol{u}}_n^i$ and $\Delta\lambda_{n+1}^i = \Delta\lambda_n^i + \Delta\tilde{\lambda}_n^i$. System of equations (3.4) can be effectively solved by the bordering algorithm, see e.g. (Wriggers, 2008) for details. When the iteration loop ends due to fulfilment of a convergence criterion, the converged incremental values $\Delta\boldsymbol{u}_n$ and $\Delta\lambda_n$ are obtained. The configuration $\{\boldsymbol{u}_{n+1}, \lambda_{n+1}\}$ at t_{n+1} becomes known and the search for the solution at the next pseudo-time point can start.

The above framework is valid for any constraint function g_{n+1} in (3.3). However, the robustness and efficiency of the path-following method depend crucially on the specific form of this function. In what follows, we will elaborate for the case when g_{n+1} controls the incremental structural plastic dissipation when elasto-plastic or rigid-plastic material models are used, see e.g. (Crisfield, 1991), (Simo and Hughes, 2000), (Ibrahimbegovic, 2009) for such models.

3.2 Plastic dissipation constraint equation for geometrically nonlinear elasto-plasticity

In this section, we will present and discuss several possibilities for deriving the constraint equation $g_{n+1} = 0$, see (3.3), which will control incremental structural plastic dissipation. In particular, we will derive the plastic dissipation constraint equation by two different approaches (called version 1 and version 2) and we will show in Section 3.2.3 that the final results of those two approaches are equivalent.

3.2.1 Explicit form of plastic dissipation constraint equation – version 1

The rate of plastic dissipation in an elasto-plastic solid or structure can be defined as $\dot{D} = \dot{P} - \dot{\Psi}$, where $\dot{P}$ is the pseudo-time rate of the applied work, and $\dot{\Psi}$ is the pseudo-time rate of the thermodynamic (i.e. the free energy) potential for plasticity (the dot denotes the derivative with respect to the pseudo-time). For the discretized solid or structure in the framework of the geometrically nonlinear and inelastic finite element method, $\dot{P}$ can be written as

$$\dot{P} = \sum_e \int_{V^e} \boldsymbol{S}^T \dot{\boldsymbol{E}}\, dV = \boldsymbol{f}^{ext,T} \dot{\boldsymbol{u}} = \lambda \hat{\boldsymbol{f}}^{ext,T} \dot{\boldsymbol{u}} \tag{3.5}$$

where e denotes a finite element of the mesh, $\boldsymbol{S}$ and $\boldsymbol{E}$ are vectors comprising the 2nd Piola-Kirchhoff stresses and the Green-Lagrange strains, respectively, and V^e is the initial volume of the element. It was assumed in (3.5) that the external forces are conservative and can be expressed as $\boldsymbol{f}^{ext} = \lambda \hat{\boldsymbol{f}}^{ext}$, where $\hat{\boldsymbol{f}}^{ext}$ is a fixed pattern of nodal forces. The free energy potential of a solid or structure, based on the St. Venant-Kirchhoff elasticity and plasticity with linear isotropic hardening, is $\Psi = U + H$, where the stored energy due to elastic deformations is

$$U = \sum_e \int_{V^e} \frac{1}{2} \boldsymbol{E}^{el,T} \boldsymbol{D} \boldsymbol{E}^{el}\, dV = \sum_e \int_{V^e} \frac{1}{2} \boldsymbol{S}^T \boldsymbol{D}^{-1} \boldsymbol{S}\, dV \tag{3.6}$$

and the stored energy due to the material hardening is

$$H = \sum_e \int_{V^e} \frac{1}{2} \mathrm{K}_h \xi_h^2\, dV \tag{3.7}$$

Here, $\boldsymbol{E}^{el} = \boldsymbol{E} - \boldsymbol{E}^p$ is vector of elastic strains, $\boldsymbol{E}^p$ is vector of plastic strains, $\boldsymbol{D}$ is symmetric constitutive matrix that relates stresses with elastic strains $\boldsymbol{S} = \boldsymbol{D}\boldsymbol{E}^{el}$, K_h is hardening modulus, and ξ_h is strain-like variable that controls linear isotropic hardening. For any other type of hardening, H in (3.7) has to be changed accordingly. Differentiation of U with respect to the pseudo-time gives

$$\dot{U} = \sum_e \int_{V^e} \dot{\boldsymbol{E}}^{el,T} \boldsymbol{C}^{ep} \boldsymbol{D}^{-1} \boldsymbol{S}\, dV = \dot{\boldsymbol{u}}^T \mathbb{A}_e \left[\int_{V^e} \boldsymbol{B}^T \boldsymbol{C}^{ep} \boldsymbol{D}^{-1} \boldsymbol{S}\, dV \right] \tag{3.8}$$

where $\boldsymbol{C}^{ep}$ and $\boldsymbol{B}$ denote the consistent symmetric elasto-plastic tangent modulus and the strain-displacement matrix, respectively, and $\mathbb{A}$ is the finite element mesh assembly operator. The following relations were used in (3.8): $\dot{\boldsymbol{S}} = \boldsymbol{C}^{ep} \dot{\boldsymbol{E}}$, $\dot{\boldsymbol{E}} = \boldsymbol{B} \dot{\boldsymbol{u}}^e$, and $\dot{\boldsymbol{u}} = \mathbb{A}_e \dot{\boldsymbol{u}}^e$, where $\boldsymbol{u}^e$ is vector of element nodal displacements. Differentiation of H with respect to the pseudo-time gives

$$\dot{H} = \sum_e \int_{V^e} \mathrm{K}_h \xi_h \dot{\xi}_h \, dV = \sum_e \int_{V^e} \mathrm{K}_h \xi_h \left(\frac{\partial \xi_h}{\partial \boldsymbol{u}^e}\right)^T \dot{\boldsymbol{u}}^e \, dV = \dot{\boldsymbol{u}}^T \mathbb{A}_e \left[\int_{V^e} \mathrm{K}_h \xi_h \left(\frac{\partial \xi_h}{\partial \boldsymbol{u}^e}\right) dV\right] \tag{3.9}$$

Let us use the forward Euler pseudo-time step in order to express the plastic dissipation at the pseudo-time point t_{n+1}, i.e. $D_{n+1} = D_n + \dot{D}_n \Delta t_n$, where $\Delta t_n = t_{n+1} - t_n$. Let us further define the following constraint equation:

$$g_{n+1} = D_{n+1} - D_n - \tau_n = 0 \quad \Rightarrow \quad g_{n+1} = \dot{D}_n \Delta t_n - \tau_n = 0 \tag{3.10}$$

where τ_n is a predefined (required) value of plastic dissipation at pseudo-time step $[t_n, t_{n+1}]$. By concluding that $\dot{D}_n = \dot{P}_n - \dot{\Psi}_n = \dot{P}_n - \dot{\mathrm{U}}_n - \dot{H}_n$ and by using (3.5), (3.8) and (3.9), equation (3.10) can be rewritten as

$$g_{n+1} = \dot{D}_n \Delta t_n - \tau_n = \Delta \boldsymbol{u}_n^T \left(\lambda_n \hat{\boldsymbol{f}}^{ext} - \boldsymbol{f}_n^*\right) - \tau_n = 0 \tag{3.11}$$

Here, $\Delta \boldsymbol{u}_n = \dot{\boldsymbol{u}}_n \Delta t_n$ is the current iterative guess of incremental displacements (iterative index i is omitted) and

$$\boldsymbol{f}_n^* = \mathbb{A}_e \left[\int_{V^e} \boldsymbol{B}^T \boldsymbol{C}^{ep} \boldsymbol{D}^{-1} \boldsymbol{S} \, dV + \int_{V^e} \mathrm{K}_h \xi_h \left(\frac{\partial \xi_h}{\partial \boldsymbol{u}^e}\right)_n dV\right] \tag{3.12}$$

It follows from (3.11) and (3.12) that the derivatives needed in (3.4) are

$$g_{n+1,\lambda} = 0 \text{ and } g_{n+1,\boldsymbol{u}} = \lambda_n \hat{\boldsymbol{f}}^{ext} - \boldsymbol{f}_n^*, \tag{3.13}$$

since g_{n+1} is not a function of $\Delta\lambda_n$. Most of the terms of $\boldsymbol{f}_n^*$ in (3.12) are needed for the elasto-plastic analysis and can be readily used to compute (3.11) and its derivatives. An exception is $(\partial \xi_h / \partial \boldsymbol{u}^e)_n$, which can be obtained by using the elasto-plastic constitutive relations.

In practice, one has to compute $\boldsymbol{f}_n^*$ after the last iteration at t_n or before the first iteration at t_{n+1} and use it when iterating for configuration at t_{n+1} (note that $\boldsymbol{f}_n^*$ does not change during the iterations).

3.2.2 Explicit form of plastic work constraint equation – version 1

The value of the second integral on the right hand side of (3.12) should be smaller than the value of the first integral, which might be a justification for neglecting the former when computing $\boldsymbol{f}_n^*$. One can approximate $\boldsymbol{f}_n^*$ as

$$\boldsymbol{f}_n^* \;\rightarrow\; \boldsymbol{f}_n^{*,app} = \mathbb{A}_e \left[\int_{V^e} \boldsymbol{B}_n^T \boldsymbol{C}_n^{ep} \boldsymbol{D}^{-1} \boldsymbol{S}_n \, dV\right] \tag{3.14}$$

It can be seen from (3.11) and (3.12) that $\left(\dot{D}_n \Delta t_n\right)^{app}$ computed with $\boldsymbol{f}_n^{*,app}$ is larger than $\dot{D}_n \Delta t_n$ computed with $\boldsymbol{f}_n^{*}$. As explained below in Section 3.2.4, one actually controls plastic work when $\boldsymbol{f}_n^{*,app}$ is used in constraint equation (3.11).

3.2.3 Explicit form of plastic dissipation constraint equation – version 2

The rate of plastic dissipation in an elasto-plastic solid or structure can also be written as (see e.g. (Ibrahimbegovic, 2009))

$$\dot{D} = \sum_e \int_{V^e} \left(\dot{\mathbf{E}}^{p,T} \boldsymbol{S} + q \dot{\xi}_h \right) dV \tag{3.15}$$

where $q = -K_h \xi_h$ is the stress-like variable associated with the linear isotropic material hardening. Since $\dot{\boldsymbol{S}} = \boldsymbol{D} \dot{\boldsymbol{E}}^{el}$, one has $\dot{\boldsymbol{E}}^{p} = \dot{\boldsymbol{E}} - \dot{\boldsymbol{E}}^{el} = (\boldsymbol{I} - \boldsymbol{D}^{-1} \boldsymbol{C}^{ep}) \dot{\boldsymbol{E}}$ and (3.15) can be rewritten as

$$\dot{D} = \dot{\boldsymbol{u}}^T \mathbb{A}_e \left[\int_{V^e} \boldsymbol{B}^T (\boldsymbol{I} - \boldsymbol{D}^{-1} \boldsymbol{C}^{ep})^T \boldsymbol{S} \, dV \right] - \sum_e \int_{V^e} \mathrm{K}_h \xi_h \dot{\xi}_h \, dV \tag{3.16}$$

The last expression on the right hand side of (3.16) can be elaborated as in (3.9). If (3.16) is used for $\dot{D}_n$, the constraint equation is

$$g_{n+1} = \dot{D}_n \Delta t_n - \tau_n = \Delta \boldsymbol{u}_n^T \bar{\boldsymbol{f}}_n - \tau_n = 0 \tag{3.17}$$

where

$$\bar{\boldsymbol{f}}_n = \mathbb{A}_e \left[\int_{V^e} \boldsymbol{B}^T (\boldsymbol{I} - \boldsymbol{D}^{-1} \boldsymbol{C}^{ep})^T \boldsymbol{S}_n \, dV - \int_{V^e} \mathrm{K}_h \xi_{h,n} \left(\frac{\partial \xi_h}{\partial \boldsymbol{u}^e} \right)_n dV \right] \tag{3.18}$$

The derivatives of (3.17) are $g_{n+1,\lambda} = 0$ and $g_{n+1,\boldsymbol{u}} = \bar{\boldsymbol{f}}_n$.

By noting that $(\boldsymbol{I} - \boldsymbol{D}^{-1} \boldsymbol{C}^{ep})^T = \boldsymbol{I} - \boldsymbol{C}^{ep} \boldsymbol{D}^{-1}$, since $\boldsymbol{C}^{ep}$ and $\boldsymbol{D}$ are both symmetric, the comparison of (3.11) and (3.12) with (3.17) and (3.18) yields

$$\lambda_n \hat{\boldsymbol{f}}^{ext} = \mathbb{A}_e \left[\int_{V^e} \boldsymbol{B}_n^T \boldsymbol{S}_n \, dV \right] \tag{3.19}$$

Eq. (3.19) defines the equilibrium at t_n (equivalent external nodal forces equal internal nodal forces), see e.g. (Ibrahimbegovic, 2009), a condition that is accomplished at the beginning of the current pseudo-time step $[t_n, t_{n+1}]$. This leads to the conclusion that constraint equations (3.11) and (3.17) are equivalent. In other words, the version 1 and version 2 derivations produce the same final form of the constraint equation.

3.2.4 Explicit form of plastic work constraint equation – version 2

If the contribution due to material hardening is neglected in version 2, one has the following approximations for the rate of plastic dissipation (3.16) and vector $\bar{\boldsymbol{f}}_n$ in (3.19)

$$\begin{aligned} \dot{D} \;\rightarrow\; \dot{D}^{approx} &= \sum_e \int_{V^e} \dot{\boldsymbol{E}}^{p,T} \boldsymbol{S}\, dV \\ \bar{\boldsymbol{f}}_n \;\rightarrow\; \bar{\boldsymbol{f}}_n^{approx} &= \mathbb{A}_e \left[\int_{V^e} \boldsymbol{B}_n^T \left(\boldsymbol{I} - \boldsymbol{D}^{-1} \boldsymbol{C}_n^{ep} \right)^T \boldsymbol{S}_n \, dV \right] \end{aligned} \tag{3.20}$$

The first expression in (3.20) is the rate of the plastic work.

3.2.5 1d illustration of plastic dissipation and plastic work

Let us illustrate integration of the rates of plastic dissipation and plastic work for the 1d case, i.e. for the stretching/compressing of an elasto-plastic bar with homogenous stress-strain state. Figure 3.1 shows plastic yielding at a material point of a bar; σ, ε^p and σ_y denote stress, plastic strain and yield stress, respectively. Let us look at the pseudo-time increment $\left[t_y, \bar{t}\right]$, where t_y is the pseudo-time point at the outset of plastic yielding. Let the stress monotonically increase during this increment, so that the plastic strain equals the strain hardening parameter, $\varepsilon^p = \xi_h$. The plastic dissipation at a material point at the end of the increment is the grey area on Figure 3.1 (right). An integration of equation (3.16) relates to Figure 3.1 (right). The plastic work at a material point at the end of the increment is the grey area on Figure 3.1 (left). An integration of (3.20) [1] thus relates to Figure 3.1 (left).

One can conclude from the above that neglecting the energy storage due to the material hardening (either in version 1 or in version 2) leads to an approximation of the plastic dissipation with the plastic work. As illustrated in Figure 3.1, the plastic work is always larger than the plastic dissipation for elasto-plasticity with hardening. The constraint equation that corresponds to the usage of (3.14) in (3.11) for version 1 and (3.20) [2] in (3.17) for version 2 was used in (Verhoosel et al., 2009) for geometrically linear elasto-plastic problems. However, it is clear from the above derivation that the constraint equations (3.11) and (3.17) can be both used for geometrically linear as well as for geometrically nonlinear small-strain elasto-plastic problems.

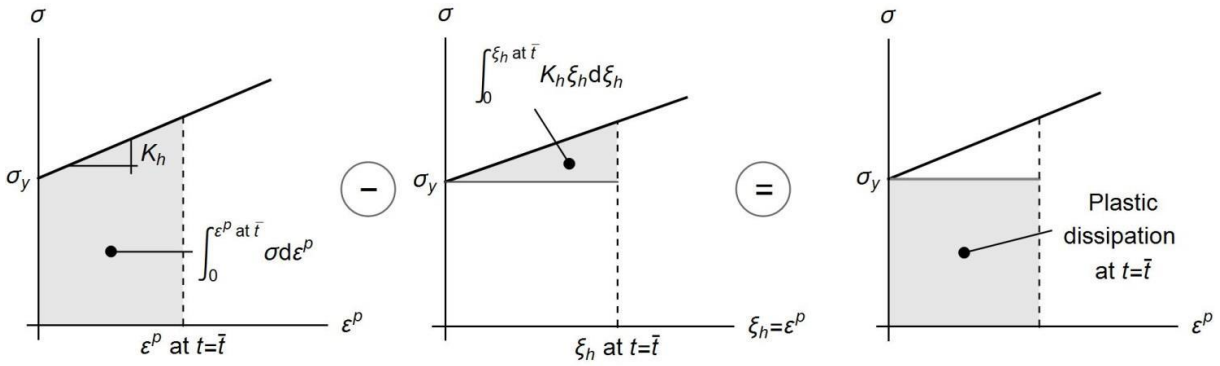

Figure 3.1: Plastic work (left) and plastic dissipation (right) at a point of an elasto-plastic material with hardening for pseudo-time increment [t_y, $\bar{t}$] and 1d case.

Slika 3.1: Plastično delo (levo) in plastična disipacija (desno) v točki v elasto-plastičnem materialu z utrjevanjem za psevdo-časovni korak [t_y, $\bar{t}$] in 1d primer.

3.2.6 Implicit forms

In this section, we present implicit counterparts of explicit formulations presented above. The backward Euler pseudo-time step can be used to compute the plastic dissipation at the pseudo-time point t_{n+1}, i.e.

$$D_{n+1} = D_n + \dot{D}_{n+1}\Delta t_n\,, \quad \Delta t_n = t_{n+1} - t_n \tag{3.21}$$

which leads to the following constraint equation (compare it with (3.16))

$$g_{n+1} = \dot{D}_{n+1}\Delta t_n - \tau_n = \Delta \boldsymbol{u}_n^T\left(\lambda_{n+1}\hat{\boldsymbol{f}}^{ext} - \boldsymbol{f}_{n+1}^*\right) - \tau_n = 0 \tag{3.22}$$

where

$$\boldsymbol{f}_{n+1}^* = \mathbb{A}_e\left[\int_{V^e} \boldsymbol{B}_{n+1}^T \boldsymbol{C}_{n+1}^{ep}\boldsymbol{D}^{-1}\boldsymbol{S}_{n+1}\,dV + \int_{V^e} \mathrm{K}_h \xi_{h,n+1}\left(\frac{\partial \xi_h}{\partial \boldsymbol{u}^e}\right)_n dV\right] \tag{3.23}$$

Note that $\Delta\boldsymbol{u}_n$ in (3.22) is redefined as $\Delta\boldsymbol{u}_n = \dot{\boldsymbol{u}}_{n+1}\Delta t_n$. Expressions for the derivatives of g_{n+1} are much more complex in comparison with (3.18) and can be written as

$$g_{n+1,\lambda} = \Delta\boldsymbol{u}_n^T\hat{\boldsymbol{f}}^{ext}\,, \quad g_{n+1,\boldsymbol{u}} = \lambda_{n+1}\hat{\boldsymbol{f}}^{ext} - \boldsymbol{f}_{n+1}^* - \left(\boldsymbol{f}_{n+1,\boldsymbol{u}}^*\right)^T\Delta\boldsymbol{u}_n \tag{3.24}$$

The problem is to derive $\boldsymbol{f}_{n+1,\boldsymbol{u}}^*$, which demands, among other derivatives, the derivative of elasto-plastic tangent modulus $\boldsymbol{C}_{n+1,\boldsymbol{u}}^{ep}$.

Alternatively to (3.22), the constraint equation can be expressed as

$$g_{n+1} = \dot{D}_{n+1}\Delta t_n - \tau_n = \Delta\boldsymbol{u}_n^T\bar{\boldsymbol{f}}_{n+1} - \tau_n = 0 \tag{3.25}$$

where

$$\bar{\boldsymbol{f}}_{n+1} = \mathbb{A}_e \left[\int_{V^e} \boldsymbol{B}_{n+1}^T \left(\boldsymbol{I} - \boldsymbol{D}^{-1} \boldsymbol{C}_{n+1}^{ep} \right)^T \boldsymbol{S}_{n+1} \, dV - \int_{V^e} \mathrm{K}_h \xi_{h,n+1} \left(\frac{\partial \xi_h}{\partial \boldsymbol{u}^e} \right)_{n+1} dV \right] \tag{3.26}$$

and

$$g_{n+1,\lambda} = 0 \,, \quad g_{n+1,\boldsymbol{u}} = \bar{\boldsymbol{f}}_{n+1} - \left(\bar{\boldsymbol{f}}_{n+1,\boldsymbol{u}} \right)^T \Delta \boldsymbol{u}_n \tag{3.27}$$

Again, $\bar{\boldsymbol{f}}_{n+1,\boldsymbol{u}}$ calls for derivative of the elasto-plastic tangent modulus $\boldsymbol{C}_{n+1,\boldsymbol{u}}^{ep}$.

It is obvious that $\boldsymbol{f}_{n+1,\boldsymbol{u}}^*$ and $\bar{\boldsymbol{f}}_{n+1,\boldsymbol{u}}$, needed in (3.24) and (3.27), respectively, are not easy to derive and compute, which renders explicit formulations much more attractive for implementation than implicit.

3.2.7 Dissipation constraint for embedded discontinuity finite elements

Let us derive the plastic dissipation constraint for a situation when the material failure in solid is modelled by the embedded-displacement-discontinuity finite element formulation and inelastic softening cohesive traction-separation law is used at the discontinuity. In what follows, we will restrict to 2-d solids with a single fracture curve (i.e. with a single discontinuity) and to frames with softening plastic hinges. Let the bulk of the 2-d solid or frame be modelled as elastic and let the cohesive stresses at the discontinuity be modelled by rigid-plasticity with linear softening.

The free energy potential (i.e. the stored energy) of the solid can be written as

$$\Psi = (U - S) + S_s \tag{3.28}$$

where the stored energy due to elastic deformations of the bulk

$$\mathrm{U} = \int_V \frac{1}{2} \boldsymbol{E}^T \boldsymbol{D} \boldsymbol{E} \, dV = \int_V \frac{1}{2} \boldsymbol{S}^T \boldsymbol{D}^{-1} \boldsymbol{S} \, dV \tag{3.29}$$

is diminished for S due to localized plastic deformations at the failure curve. Due to softening rigid-plasticity, those plastic deformations equal to kinematic variables $\boldsymbol{\alpha}$ that describe material separation along the discontinuity. The S in (3.28) is defined as

$$\mathrm{S} = \int_\Gamma \boldsymbol{\alpha}^T \boldsymbol{t} \, d\Gamma \tag{3.30}$$

where $\boldsymbol{t}$ is vector of cohesive stresses in discontinuity, and Γ is length of the discontinuity curve. The S_s in (3.28) is due to the linear softening and takes the form

$$S_s = \int_\Gamma \frac{1}{2} K_s \xi_s^2 \, d\Gamma \tag{3.31}$$

In (3.31), $K_s < 0$ is softening modulus, and ξ_s is displacement-like variable that controls softening. The pseudo-time derivatives of (3.29), (3.30) and (3.31) are

$$\dot{\mathrm{U}} = \int_{\mathrm{V}} \dot{\boldsymbol{E}}^T \boldsymbol{S}\, dV\,, \qquad \dot{\mathrm{S}} = \int_{\Gamma} \dot{\boldsymbol{\alpha}}^T \boldsymbol{t}\, d\Gamma\,, \qquad \dot{\mathrm{S}}_s = \int_{\Gamma} K_s \xi_s \dot{\xi}_s\, d\Gamma \tag{3.32}$$

The derivatives in (3.32) can be expressed by $\dot{\boldsymbol{u}}$ using $\boldsymbol{E} \dot{=} \boldsymbol{B}\dot{\boldsymbol{u}}$ and the chain rule

$$\dot{\boldsymbol{\alpha}} = \frac{\partial \boldsymbol{\alpha}}{\partial \boldsymbol{u}} \dot{\boldsymbol{u}}, \qquad \dot{\xi}_s = \left(\frac{\partial \xi_s}{\partial \boldsymbol{\alpha}}\right)^T \frac{\partial \boldsymbol{\alpha}}{\partial \boldsymbol{u}} \dot{\boldsymbol{u}} \tag{3.33}$$

The constraint equation can be defined for forward Euler pseudo-time step (according to the *Version 1* of above presented explicit formulation, see (3.11)) as

$$g_{n+1} = \dot{D}_n \Delta t_n - \tau_n = \Delta \boldsymbol{u}_n^T \left(\lambda_n \hat{\boldsymbol{f}}^{ext} - \boldsymbol{f}_n^*\right) - \tau_n = 0 \tag{3.34}$$

Where $\boldsymbol{f}_n^*$ in (3.34) is now defined as

$$\boldsymbol{f}_n^* = \int_V \boldsymbol{B}_n^T \boldsymbol{S}_n\, dV + \underbrace{\int_{\Gamma} \left(\frac{\partial \boldsymbol{\alpha}}{\partial \boldsymbol{u}}\right)_n^T \boldsymbol{t}_n\, d\Gamma + \int_{\Gamma} K_s \xi_{s,n} \left(\frac{\partial \boldsymbol{\alpha}}{\partial \boldsymbol{u}}\right)_n^T \left(\frac{\partial \xi_s}{\partial \boldsymbol{\alpha}}\right)_n d\Gamma}_{\bar{\boldsymbol{f}}_n^*} \tag{3.35}$$

The equilibrium of solid or structure at t_n demands equality of external and internal nodal forces, i.e. $\lambda_n \hat{\boldsymbol{f}}^{ext} = \int_V \boldsymbol{B}_n^T \boldsymbol{S}_n\, dV$. Thus, inserting (3.35) in (3.34) yields

$$g_{n+1} = \dot{D}_n \Delta t_n - \tau_n = \Delta \boldsymbol{u}_n^T \bar{\boldsymbol{f}}_n^* - \tau_n = 0 \tag{3.36}$$

where $\bar{\boldsymbol{f}}_n^*$ is indicated in (3.35). The derivatives of g_{n+1} are the expressions from (3.13) with $\boldsymbol{f}_n^*$ from (3.35). In the implementation of embedded-discontinuity finite elements, kinematic variables $\boldsymbol{\alpha}$ are condensed on the element level. This enables to compute $\left(\frac{\partial \boldsymbol{\alpha}}{\partial \boldsymbol{u}}\right)_n$ in (3.35) as assembly of element contributions. Since the condensation on the element level (e) yields

$$\Delta \boldsymbol{\alpha}_n^{(e)} = \left(\boldsymbol{K}^{\boldsymbol{\alpha\alpha},(e)}\right)_n^{-1} \boldsymbol{K}_n^{\boldsymbol{\alpha u},(e)} \Delta \boldsymbol{u}_n^{(e)}\,, \quad \boldsymbol{K}_n^{(e)} = \begin{bmatrix} \boldsymbol{K}^{\boldsymbol{uu}} & \boldsymbol{K}^{\boldsymbol{u\alpha}} \\ \boldsymbol{K}^{\boldsymbol{\alpha u}} & \boldsymbol{K}^{\boldsymbol{\alpha\alpha}} \end{bmatrix}_n^{(e)} \tag{3.37}$$

one has

$$\left(\frac{\partial \boldsymbol{\alpha}}{\partial \boldsymbol{u}}\right)_n^{(e)} = \left(\boldsymbol{K}^{\boldsymbol{\alpha\alpha},(e)}\right)_n^{-1} \boldsymbol{K}_n^{\boldsymbol{\alpha u},(e)} \tag{3.38}$$

where $\boldsymbol{K}_n^{(e)}$ is the element stiffness matrix at t_n, which can be decomposed as shown in (3.37). How $\left(\frac{\partial \xi_s}{\partial \boldsymbol{u}}\right)_n$ in (3.35) is computed will not be further elaborated.

The third integral on the right hand side of (3.35) might be neglected, i.e.

$$\bar{f}_n^* \;\rightarrow\; \bar{f}_n^{*,approx} = \int_\Gamma \left(\frac{\partial \boldsymbol{\alpha}}{\partial \boldsymbol{u}}\right)_n^T \boldsymbol{t}_n \, d\Gamma \tag{3.39}$$

The corresponding approximation $\left(\dot{D}_n \Delta t_n\right)^{approx}$ is smaller than $\dot{D}_n \Delta t_n$ in (3.36) since $K_s < 0$. This is illustrated for 1d case, i.e. stretching/compressing of a bar, in Figure 3.2, where plastic dissipation for a point at the discontinuity is presented. For a 1d case integration of (3.36) relates to Figure 3.2 (right), and integration of (3.36) by using (3.39) relates to Figure 3.2 (left). In Figure 3.2, f is cohesive stress, f_f is material failure stress at which softening begins, and α is separation. The plastic dissipation at the end of the pseudo-time increment $\left[t_f, \bar{t}\right]$ is shown, where t_f is pseudo-time point at material failure. Since the cohesive stress monotonically decreases during this increment, $\alpha = \xi_s$. Plastic dissipation at a material point at $t = \bar{t}$ is the grey area on Figure 3.2 (right). When material softening is neglected, an approximation of plastic dissipation at $t = \bar{t}$ is obtained, which is smaller than the plastic dissipation and corresponds to the grey area on Figure 3.2 (left).

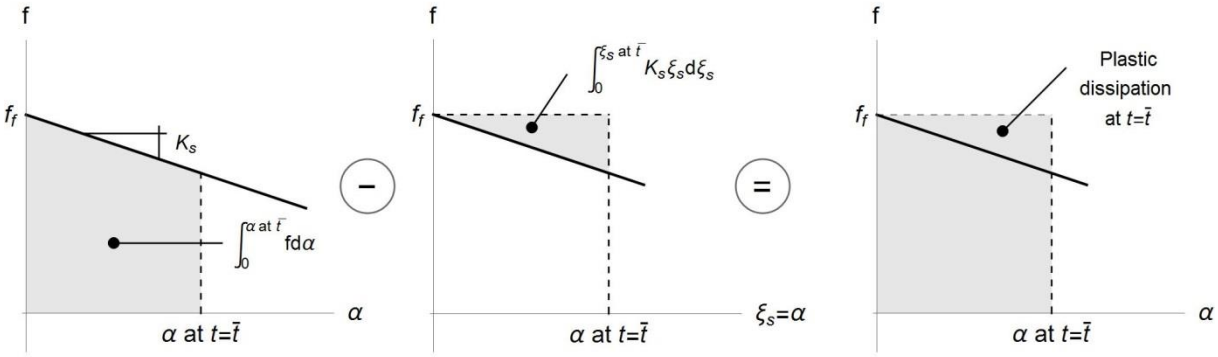

Figure 3.2: Plastic dissipation at discontinuity point for rigid-plastic material with linear softening for pseudo-time increment [t_y, $\bar{t}$] and 1d case.

Slika 3.2:Plastična disipacija v točki nezveznosti za togo-plastičen material z linearnim mehčanjem za psevdo-časovni inkrement [t_y, $\bar{t}$] in 1d primer.

The above derivation is the embedded-discontinuity softening-rigid-plasticity counterpart of the concepts introduced above in Section 3.2.1 (“Explicit form of plastic dissipation constraint equation – version 1”). If one wants to exploit the concepts from Section 3.2.3 (“Explicit form of plastic dissipation constraint equation – version 2”), the rate of plastic dissipation has to be considered, which is defined as (since the plastic dissipation takes place only at the discontinuity curve)

$$\dot{D} = \int_\Gamma \left(\dot{\boldsymbol{\alpha}}^T \boldsymbol{t} + \dot{\xi}_s q_s\right) d\Gamma \tag{3.40}$$

where $q_s = -K_s \xi_s$. It is straightforward to show that the constraint equations related to (3.40) is (3.36). The corresponding implicit formulation will not be considered here.

When dealing with frames with elastic bulk and softening plastic hinges, the integral over the discontinuity curve in the expressions above is replaced with the sum over discontinuity points (i.e. the sum over softening plastic hinges). For example, in such a case, (3.30) transforms to

$$S = \sum_{i=1}^{n_p} \boldsymbol{\alpha}_i^T \boldsymbol{t}_i \tag{3.41}$$

Where n_p is number of discontinuity points in the frame, and $\boldsymbol{\alpha}_i$ and $\boldsymbol{t}_i$ are vectors comprising jumps in displacements and rotations and cohesive forces and moments, respectively at i-th softening plastic hinge.

3.3 Numerical examples

In this section, we present several numerical examples related to plastic collapse of elasto-plastic shells. The 4-node assumed natural strain (ANS) shell element, e.g. (Brank et al., 1995), with the stress-resultant Ilyushin-Shapiro elasto-plasticity, e.g. (Dujc and Brank, 2012), was used to compute the examples. We note that the Ilyushin-Shapiro elasto-plasticity is the shell stress-resultant counterpart of the shell plasticity with hardening and von Mises yield criterion, see e.g. (Brank et al., 1997).

In what follows, we will call the standard arc-length method the "arc-length" (AL). The AL used in the numerical examples is the cylindrical Crisfield arc-length, see e.g. (Crisfield, 1991), with the constraint equation

$$g_{n+1} = \Delta \boldsymbol{u}_n^T \, \Delta \boldsymbol{u}_n - \Delta l_n^2 = 0 \tag{3.42}$$

The path direction in the predictor phase of the AL was chosen according to the suggestion of (Feng et al., 1996). The prescribed value τ_n in (3.42) was allowed to change from increment to increment in accordance with the actual and desired number of incremental iterations. The details of the AL implementation are provided in (Stanić et al., 2016).

We will call in what follows the path-following methods, derived in Section 3.2, as the "arc-length with the dissipation constraint" (AL-D). In particular, the AL-D with the constraint equation (3.11) of version 1 was implemented. In this respect we note that the versions 1 and 2 implementations are equivalent as explained in Section 3.2.3. For the initial part of the AL-D computations, when the material was still elastic, the AL was used. We note that for problems with hardening the implemented AL-D provided the same results for $\boldsymbol{f}_n^*$ from (3.12) and $\boldsymbol{f}_n^{*,app}$ from (3.14).

The shell finite element, the AL and the AL-D were implemented into the computer code AceFEM, see (Korelc, 2015). Both path-following methods consider different type of control parameters: Δl_n for AL (3.42) and τ_n for AL-D (see (3.11), (3.17), (3.25), (3.34)). In what follows, we will use $\hat{\tau}_n$ for both control parameters.

3.3.1 Cylindrical panels

We analyse axially loaded thin cylindrical panels. We consider two examples, A and B, which illustrate that for "regular" elasto-plastic problems the AL and the AL-D provide the same results.

3.3.1.1 Problem A

The basic information for this problem is presented in Figure 3.3 (u_x, u_y and u_z are the mid-surface displacements in x, y and z directions, respectively, and ϕ_y is the shell-director rotation around y axis). The geometry is defined by panel's length $L = 2000$ mm, radius $R = 1000$ mm, opening angle $\theta = 1$ rad, and thickness $t = 5$ mm. The material data are: modulus of elasticity $E = 210000$ N/mm^2, Poisson's ratio $\nu = 0.30$, yield stress $\sigma_y = 235$ N/mm^2 and plastic hardening modulus $K_h = 0$. The displacement/rotation boundary conditions are indicated in Figure 3.3. The mesh consists of 24×24 shell finite elements. The point and the line load are applied. The point load λV_0 (where $V_0 = 10\ N$) acts at $\{x, y, z\} = \{0, L/8, R\}$. The line load is approximated by equal horizontal point forces λH_0 (where $H_0 = 1$ kN) applied at each node of the free curved edge at $x = 0$. The input data for the AL and the AL-D solution methods are given in Table 3.1.

The results are presented in Figure 3.4 and Figure 3.5. It can be seen from Figure 3.4 that the cylinder buckled at $\lambda = 16.8$. Both the AL and the AL-D methods can compute this example nicely and they provide the same results.

Table 3.1: Cylindrical panel A: data for used path-following methods.
Preglednica 3.1: Cilindrični panel A: vhodni podatki za uporabljeni metodi sledenja ravnotežne poti.

Method	Initial value for $\hat{\tau}_n$	Maximal allowed value for $\hat{\tau}_n$	Desired number of iterations	Convergence tolerance
AL	0.8	10	7	10^{-8}
AL-D	10^2 Nmm	$5 \cdot 10^4$ Nmm	8	10^{-8}

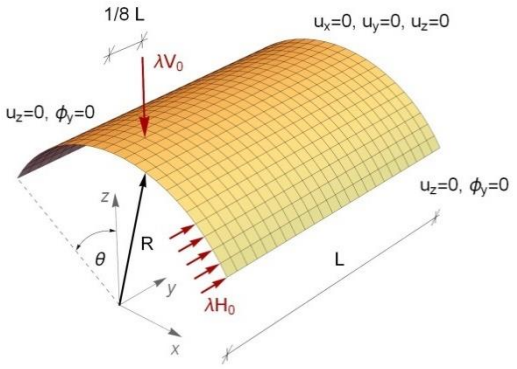

Figure 3.3: Cylindrical panel A: geometry, loading and boundary conditions.
Slika 3.3: Cilindrični panel A: geometrija, obtežba in robni pogoji.

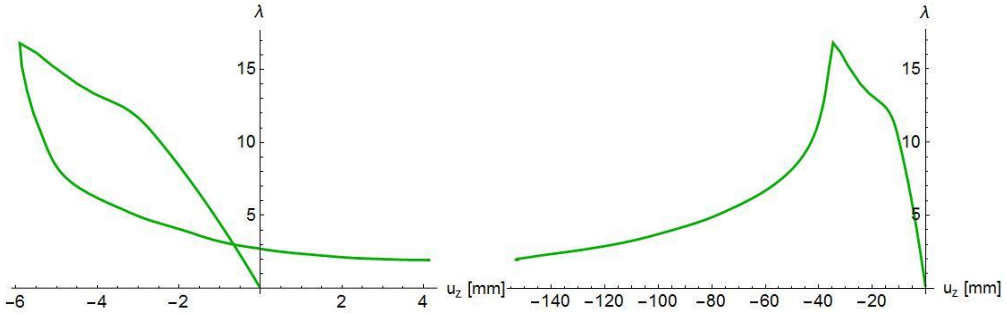

Figure 3.4: Cylindrical panel A: load factor versus displacement curves for the node {x, y, z}={0, L/2, R} and the node {x, y, z}={0, L/8, R}, respectively.

Slika 3.4: Cilindrični panel A: diagram obtežni faktor v odvisnosti od pomika vozlišča {x, y, z}={0, L/2, R} (levo) in vozlišča {x, y, z}={0, L/8, R} (desno).

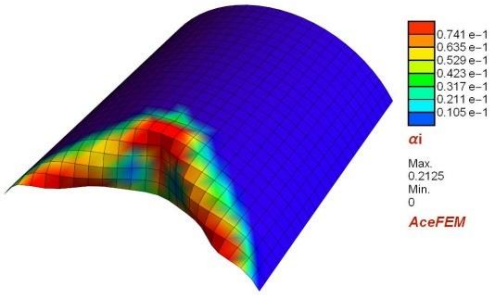

Figure 3.5: Cylindrical panel A: deformed mesh configuration with distribution of equivalent plastic strain at final stage of computation at λ = 1.94.

Slika 3.5: Cilindrični panel A: deformacijska konfiguracija mreže končnih elementov s prikazom porazdelitve plastične deformacije na koncu analize (λ = 1.94).

3.3.1.2 Problem B

Figure 3.6 illustrates the geometry and boundary conditions for the second cylindrical panel with thickness $t = 2$ mm. One curved edge is fully clamped and at the other curved edge only the axial displacement u_y is allowed. The latter edge is subjected to an axial, compressive, uniform line load λh_0 (where $h_0 = 56.98$ N/mm). The finite element mesh consists of 24 finite elements per edge. The material is the same as for the Problem A. Table 3.2 presents the input data for both used solution methods.

The results are presented in Figure 3.7 and Figure 3.8. Figure 3.7 shows the load factor λ versus horizontal displacement curve for the node at $\{x, y, z\} = \{0, 0, R\}$. Both methods compute the same solution curve.

Table 3.2: Cylindrical panel B: data for used path-following methods.

Preglednica 3.2: Cilindrični panel B: vhodni podatki za uporabljeni metodi sledenja poti.

Method	Initial value for $\hat{\tau}_n$	Maximal allowed value for $\hat{\tau}_n$	Desired number of iterations	Convergence tolerance
AL	0.5	1	8	10^{-8}
AL-D	10^2 Nmm	10^4 Nmm	8	10^{-8}

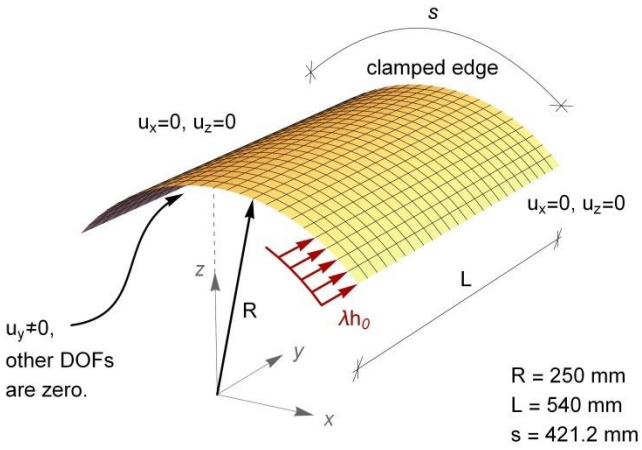

Figure 3.6: Cylindrical panel B: geometry and boundary conditions.

Slika 3.6: Cilindrični panel B: geometrija in robni pogoji.

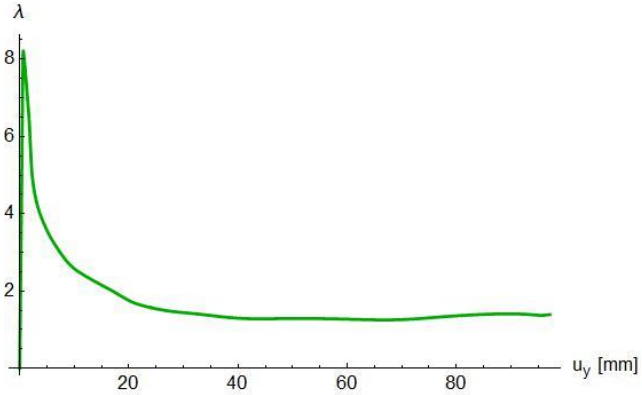

Figure 3.7: Cylindrical panel B: load factor λ versus horizontal displacement curve.

Slika 3.7: Cilindrični panel B: diagram obtežni faktor λ v odvisnosti od horizontalnega pomika.

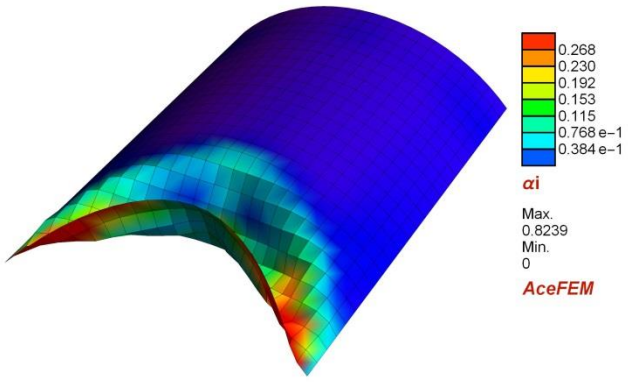

Figure 3.8: Cylindrical panel B: deformed mesh configuration with distribution of equivalent plastic strain at final stage of computation at {u_y, λ} = {97.11 mm*, 1.39}.*

Slika 3.8: Cilindrični panel B: deformacijska konfiguracija mreže končnih elementov s porazdelitvijo ekvivalentne plastične deformacije na koncu analize {u_y, λ} = {97.11 mm*, 1.39}.*

3.3.2 Half of a sphere

This example illustrates that the AL-D can be superior to the AL and can find a solution even when the AL fails. Figure 3.9 shows the example problem: one half of a sphere with thickness $t = 1$ mm and radius $R = 1000$ mm. Displacements u_x, u_y and u_z are set to 0 at the plane $z = 0$. The shell is loaded by a conservative surface pressure λp_{ref}, where $p_{ref} = 0.1$ N/mm^2. The material data is the same as for the cylindrical panels in Section 3.3.1. The path-following methods data are shown in the Table 3.3. The mesh consists of 2700 elements.

Figure 3.10 – Figure 3.12 present results. Figure 3.10 and Figure 3.11 show the factor load λ versus the vertical displacement u_z of the top of the shell. It seems that at point 1 (see Figure 3.10), where $\{u_z, \lambda\} = \{-0.55\text{ mm}, 21.70\}$, the axial symmetry somehow changes to the one plane symmetry. The AL unloads elastically from the point 1 along the already computed path and it thus fails to compute the spread of the plastic zones around the hemisphere. On the contrary, the AL-D enables computation of the evolution of plastic zones and it is therefore successful in solving the problem. It can be seen from Figure 3.11 that the AL-D also unloads from point 1, however with the solution path running along the elastic loading path and a continuous growth of plastic deformations (see Figure 3.12). Figure 3.12 shows deformed finite element configurations, marked with 1–4 in Figure 3.10.

Table 3.3: Half of a sphere: data for used path-following methods.

Preglednica 3.3: Polovica sfere: vhodni podatki za uporabljeni metodi sledenja ravnotežne poti.

Method	Initial value for $\hat{\tau}_n$	Maximal allowed value for $\hat{\tau}_n$	Desired number of iterations	Convergence tolerance
AL	10^{-3}	0.5	10	10^{-9}
AL-D	1 Nmm	$5 \cdot 10^5$ Nmm	10	10^{-8}

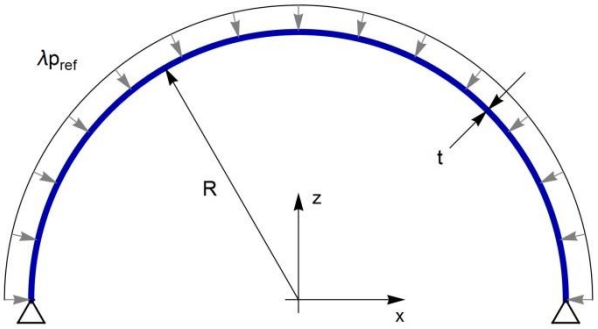

Figure 3.9: Half of a sphere: geometry, loading and boundary conditions.

Slika 3.9: Polovica sfere: geometrija, obtežba in robni pogoji.

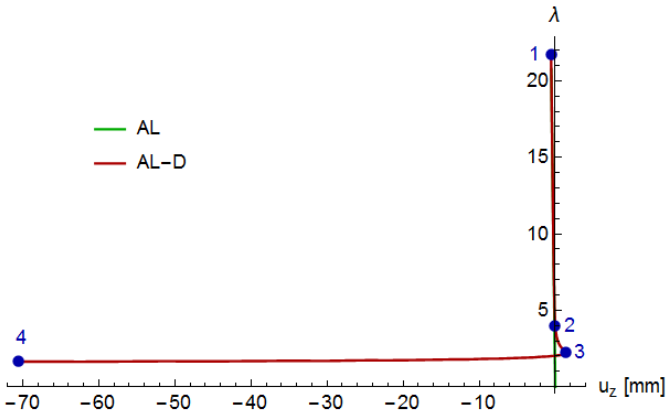

Figure 3.10: Half of a sphere: load factor λ versus vertical displacement curve for a node at the top of the model {x, y, z} = {0, 0, R}.

Slika 3.10: Polovica sfere: diagram obtežni faktor λ v odvisnosti od vertikalnega pomika za vozlišče na vrhu modela {x, y, z} = {0, 0, R}.

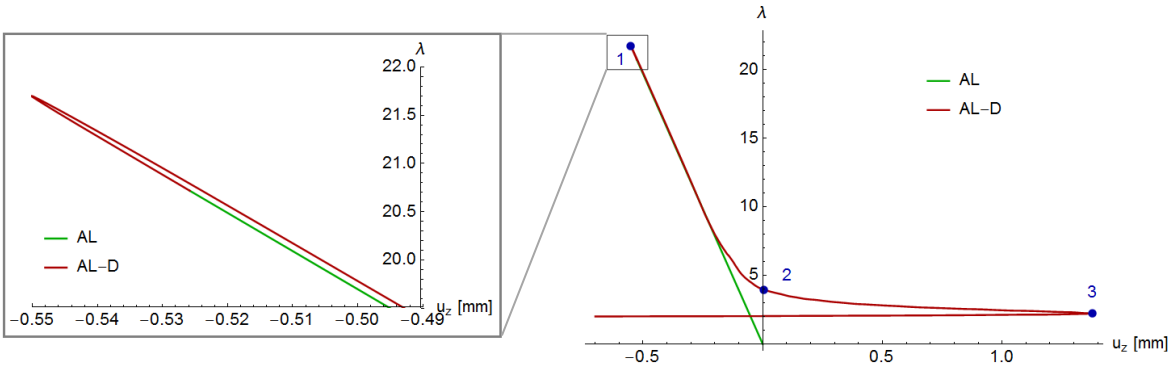

Figure 3.11: The same graph as in Figure 3.10. Left: Area around the equilibrium point 1. Right: Graph area that includes the equilibrium points 1, 2 and 3..

Slika 3.11: Isti graf kot na Slika 3.10. Levo: Prikaz grafa v območju ravnotežne točke 1. Desno: Prikaz grafa v območju ravnotežnih točk 1, 2 in 3.

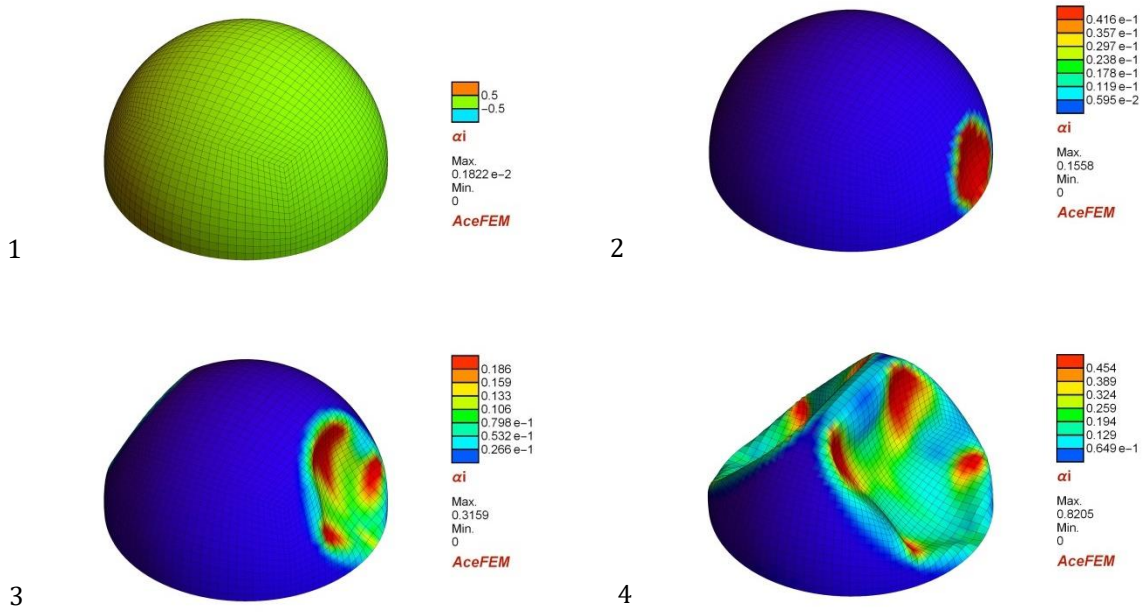

Figure 3.12: Half of a sphere: deformed mesh at solution points marked on Figure 3.10 with the distribution of equivalent plastic strain.

Slika 3.12: Polovica sfere: deformacijske konfiguracije mrež končnih elementov v izbranih ravnotežnih točkah (glej Figure 3.10) s porazdelitvijo ekvivalentne plastične deformacije.

3.3.3 Pinched cylinder

This example illustrates that the AL-D avoids undesirable (artificial) elastic unloading of the whole structure, which is a solution commonly provided by the AL for a difficult elasto-plastic problem. A popular shell benchmark, see e.g. (Dujc and Brank, 2012), is slightly modified. A short cylinder is bounded with rigid diaphragms at its both ends and subjected to several point forces (see Figure 3.13). Two forces λF_1, where $F_1 = 4000$ kN, act at its middle section. Additional point forces λF_2, where $F_2 = 1000$ kN, act parallel to the x axis. Due to the triple symmetry, only one eighth of the cylinder is considered for the analysis by taking into account the symmetrical boundary conditions. Figure 3.13 presents geometry, loading and boundary conditions: $a = 300$ cm, e1 denotes the edge with the rigid diaphragm, while e2, e3 and e4 denote the edges with the symmetrical boundary conditions. On the edge e1 $u_x = u_z = 0$, on the edge e2 $u_x = 0$, $\phi_y = 0$, on the edge e3 $u_y = 0$, $\phi_x = 0$, and on the edge e4 $u_z = 0$, $\phi_y = 0$. The shell thickness is $t = 3$ cm. The material has the following properties: Young's modulus $E = 3000$ kN/cm^2, Poisson's ratio $\nu = 0.30$ and yield stress $\sigma_y = 24.3$ kN/cm^2. The plastic response is characterized by linear isotropic hardening response with stress-resultant hardening modulus $K_h = 300$ kN/cm^2 (Dujc and Brank, 2012). The finite element mesh consists of 32×32 elements. Table 3.4 presents the input data for used solution methods.

Figure 3.14 presents the load factor λ versus the vertical displacement under the force F_1. It can be seen from Figure 3.14 that the AL at a certain point chose an undesirable (artificial) solution path that was related to structural elastic unloading. This was not the case with the AL-D, which continued to compute configurations with growing plastic deformations, thus providing the desired solution. It can be seen from

Figure 3.14 that the load displacement curve at the final stage of computation is not smooth. This might be due to an artificial buckling already noticed in (Crisfield and Peng, 1996) and (Brank, 2008) in nonlinear shell analysis with not very fine meshes. Deformed mesh at the final stage of the AL-D analysis is shown on Figure 3.15.

Table 3.4: Pinched cylinder: Data for used path-following methods.

Preglednica 3.4: Vpeti cilinder: Vhodni podatki za uporabljeni metodi sledenja ravnotežnih poti.

Method	Initial value for $\hat{\tau}_n$	Maximal allowed value for $\hat{\tau}_n$	Desired number of iterations	Convergence tolerance
AL	0.1	10	8	10^{-8}
AL-D	10 kNcm	2000 kNcm	8	10^{-8}

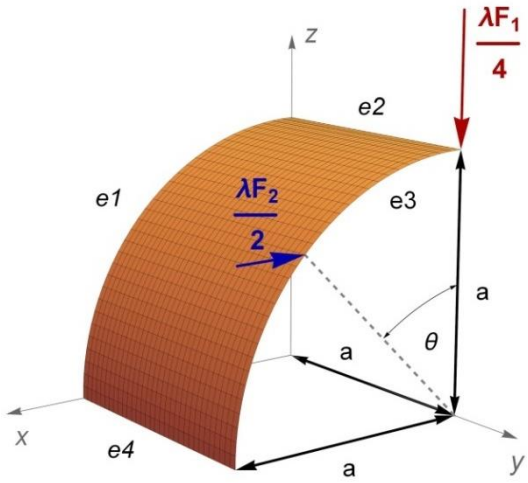

Figure 3.13: Pinched cylinder: geometry, loading and boundary conditions.

Slika 3.13: Vpeti cilinder: geometrija, obtežba in robni pogoji.

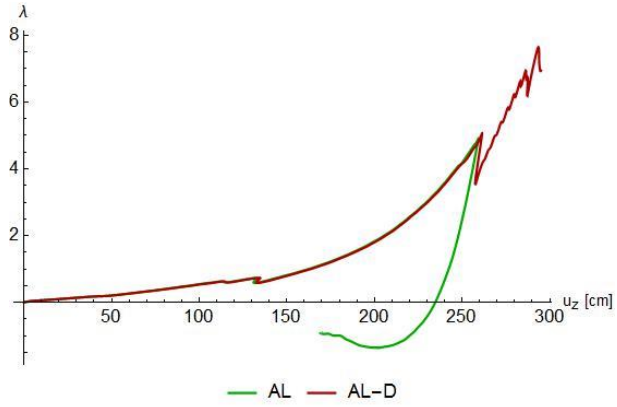

Figure 3.14: Pinched cylinder: load factor versus vertical displacement under the vertical force.

Slika 3.14: Vpeti cilinder: diagram obtežni faktor v odvisnosti od vertikalnega pomika prijemališča vertikalne sile.

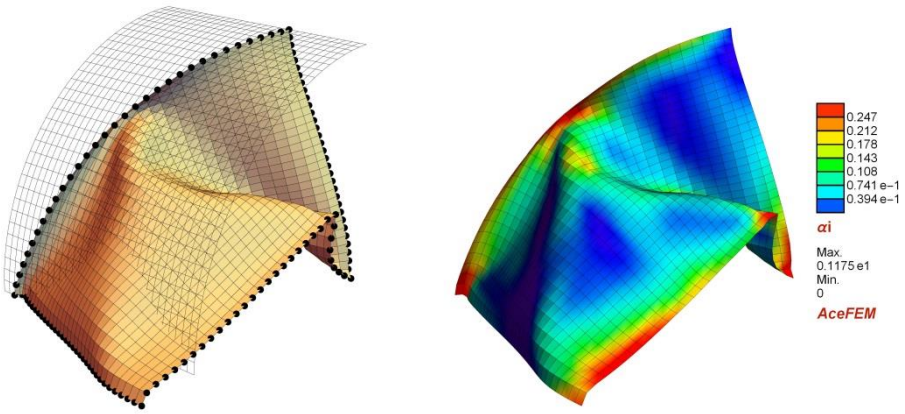

Figure 3.15: Pinched cylinder: deformed finite element configuration at vertical displacement under the vertical force $u_z = 295$ cm*. Left: initial mesh. Right: the distribution of equivalent plastic strain.*

Slika 3.15: Vpeti cilinder: deformacijska konfiguracija mreže končnih elementov, ko je vertikalni pomik prijemališča vertikalne sile $u_z = 295$ cm*. Levo: Začetna konfiguracija mreže končnih elementov. Desno: porazdelitev ekvivalentne plastične deformacije.*

3.3.4 Failure of steel frame

The planar steel frame from Section 2.4.7 (Figure 2.29 – Figure 2.30) is analysed with the stress-resultant elasto-plastic geometrically linear beam Euler-Bernoulli finite element with the embedded strong discontinuity in rotation, see e.g. (Dujc et al., 2010). This time, the same numerical model from Section 2.4.7 is computed by the standard arc-length method (AL) and the path-following method with dissipation control (AL-D).

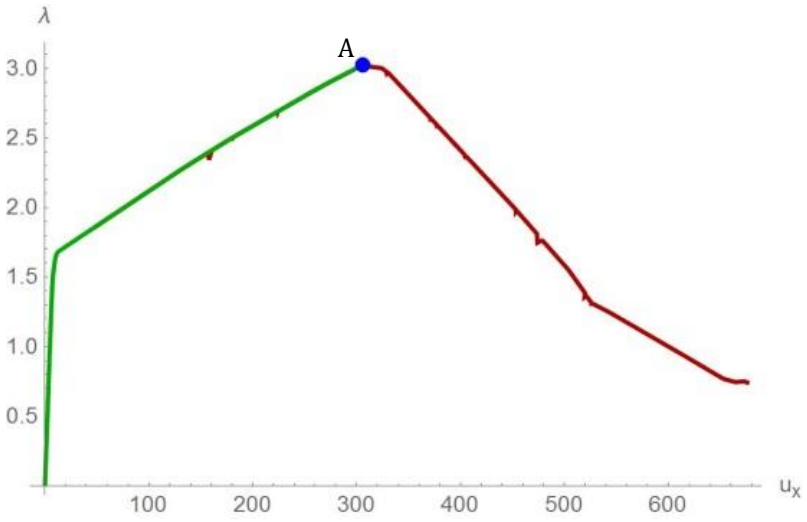

Figure 3.16: Load factor versus horizontal displacement of the upper left corner of the frame.

Slika 3.16: Diagram obtežni faktor v odvisnosti od horizontalnega pomika zgornjega levega vogala v okvirju.

The AL (see Table 3.5) failed to converge at point A on Figure 3.16. If we replaced it by the AL-D (see Table 3.5) after the activation of first plastic hinge, complete failure was computed. Figure 3.17 (left) shows

deformed configuration at point marked with circle on Figure 3.16. The values of plastic rotation at softening plastic hinges at that configuration are presented in Figure 3.17 (right).

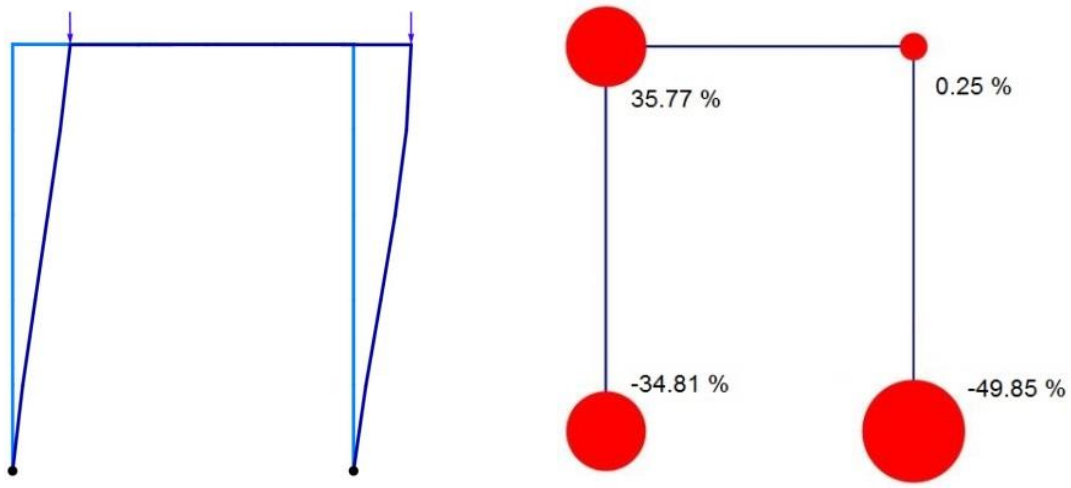

Figure 3.17: Deformed configuration. Plastic hinges and corresponding ratio of plastic rotation α/α_s (in percent).

Slika 3.17: Deformacijska konfiguracija: Plastični členki in pripadajoče razmerje plastične rotacije α/α_s (v odstotkih).

Table 3.5: Planar steel frame: data for used path-following methods.

Preglednica 3.5: Ravninski jekleni okvir: Vhodni podatki za uporabljeni metodi sledenja ravnotežnih poti.

Method	Initial value for $\hat{\tau}_n$	Maximal allowed value for $\hat{\tau}_n$	Desired number of iterations	Convergence tolerance
AL	500	500	5	10^{-10}
AL-D	1 Nmm	10^5 Nmm	5	10^{-10}

3.4 Conclusions

In this section, we studied in detail the equations that may be used to constrain incremental plastic dissipation in geometrically nonlinear elasto-plastic solid and structural problems. The derived constraint equations were employed to govern a dissipation-based path-following method for geometrically nonlinear elasto-plasticity with hardening. This is an extension of the work presented in (Verhoosel et al., 2009), which was restricted to geometrically linear elasto-plastic problems without hardening. It turned out that the resulting, plastic dissipation based path-following method is in some cases superior to the standard path-following methods, e.g. the very popular Crisfield's (cylindrical) arc-length (Crisfield, 1991, 1997). One of the reasons for such a conclusion is that the standard path-following methods allow for unrealistic, spurious elastic unloading of complete structure (see e.g. (Pohl et al., 2014)), while the here derived path-following method does not. Also, as shown by one of the presented example, the derived plastic dissipation

based path-following method can find solution for a difficult structural problem where the standard path-following method fails.

Explicit and implicit forms of the incremental plastic dissipation constraint equation were proposed. The performed numerical tests show that the usage of an explicit form can lead to a very satisfying and robust path-following method, which suggested that dealing with the demanding derivation and implementation of an implicit form is not mandatory.

It has been shown that neglecting hardening terms in the constraint equation leads to the control of plastic work rather than to the control of plastic dissipation. However, the performed numerical tests suggest that the control of plastic work is very efficient also for the elasto-plastic problems with hardening. Thus, the constraint that neglects hardening can be efficiently used for problems with and without plastic hardening.

The constraint dissipation function is also derived for 2-d solid (but not tested) and plane-frame embedded-discontinuity finite elements that represent the cohesive stresses in the discontinuity by rigid-plasticity with softening. It is suitable for computation of complete failure of solids and structures by using embedded-discontinuity finite elements. We performed test for beam finite element with embedded discontinuity (see steel frame in section 3.3.4). It should be also very robust for any other finite element formulation involving material softening.

4 EMBEDDED STRONG DISCONTINUITY QUADRILATERALS FOR 2D SOLIDS

Several formulations related to the plane stress and plane strain quadrilateral finite element with embedded strong discontinuity in displacements are presented and studied. The formulations are based either on classical, displacement-based element or on element with incompatible displacements. Two possibilities are chosen for deriving the operators in the equilibrium equations that are responsible for relating the bulk stresses with the tractions in the crack opening. The major-principle-stress criterion is used for the crack embedment, which is suitable for the quasi brittle materials. The normal and tangential cohesions in the crack are described by two uncoupled, non-associative damage-softening constitutive relations. A crack tracing algorithm is used for computation of crack propagation through the mesh. It allows for crack propagation through several elements in a single solution increment. Results of a set of numerical examples (see Sections 5 and 6) are provided in order to assess the derived formulations.

4.1 Introduction

In this chapter, we present ED-FEM formulations with strong discontinuity for 2d problems, i.e. for plane stress and plane strain structures. We restrict ourselves to quasi-brittle materials, such as concrete, masonry and stone. The concept of crack modeling in quasi-brittle materials is shown in Figure 4.1. There are three areas in Figure 4.1 that relate to the crack: (a) the area of fully open macro-crack, (b) the area where the macro-crack orientation and formation is already indicated, but there is still (normal and shear) cohesion between the two opening sides of the crack; (c) the area where the material is micro-damaged with the micro-cracks. In the area (a) there has already been a complete failure of the material. In the areas (b) and (c), the material failure is still ongoing, with the macro-crack being already well indicated in the area (b), but not in the area (c). The areas (a) and (b) are modeled with a strong-discontinuity in displacements. In the area (b), an inelastic cohesion law is applied, which relates (normal and shear) cohesion tractions with the (mode I normal, and mode II tangential) crack opening. The cohesion law for this area needs to be calibrated. At elongation of fully-open crack, the cohesive law should dissipate the specified amount of the fracture energy per newly open crack surface (i.e. the specific fracture energy), which is material characteristic. In the area (c), for quasi-brittle materials, elasto-damage constitutive relations are very often used, the main feature of which is to reduce the material stiffness due to micro-damage. When the crack propagates, all three areas are expanded, with the area (b) dissipating the energy due to the material failure, and the area (c) dissipating the energy due to micro-damage of the material.

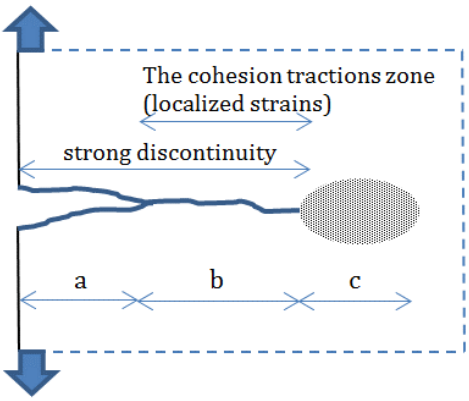

Figure 4.1: The concept of the embedded strong discontinuity.

Slika 4.1: Ilustracija koncepta vgrajene močne nezveznosti (ED-FEM).

4.2 Displacement-based embedded-strong-discontinuity quadrilateral

In this section, we derive displacement-based embedded-strong-discontinuity quadrilateral finite element, which can be used for plane stress problems. The formulation allows for linear crack opening in both mode I and mode II.

4.2.1 Kinematics

Let us consider a quadrilateral finite element occupying domain $\Omega^e \subset \mathbb{R}^2$, see Figure 4.2. The element is divided into two subdomains Ω^{e+} and Ω^{e-}, with $\Omega^e = \Omega^{e+} \cup \Omega^{e-}$ and $\Omega^{e+} \cap \Omega^{e-} = \emptyset$, by the line Γ^e representing crack. The geometry of the element is defined by the bi-linear mapping $\boldsymbol{\xi} \rightarrow \boldsymbol{x}$

$$\boldsymbol{x}(\boldsymbol{\xi}) = \sum_{a=1}^{4} N_a(\boldsymbol{\xi})\, \boldsymbol{x}_a, \qquad \boldsymbol{x}_a = [x_a, y_a]^T \tag{4.1}$$

where $\boldsymbol{x} = [x, y]^T \in \Omega^e$, $\boldsymbol{\xi} = (\xi, \eta) \in [-1,1] \times [-1,1]$, $\boldsymbol{x}_a$ are coordinates of node a, and

$$N_a(\xi, \eta) = \frac{1}{4}(1 + \xi_a \xi)(1 + \eta_a \eta), \tag{4.2}$$

a	1	2	3	4
ξ_a	-1	1	1	-1
η_a	-1	-1	1	1

are Lagrange interpolation functions over the bi-unit square.

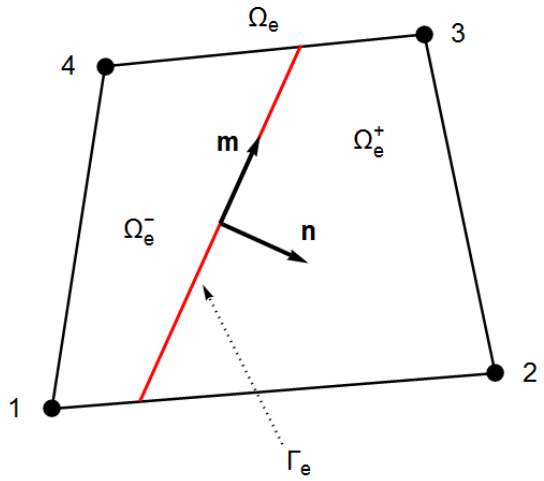

Figure 4.2: Quadrilateral finite element divided by line Γ^e representing crack.
Slika 4.2: Štirikotni končni element razdeljen z linijo Γ^e, ki predstavlja razpoko.

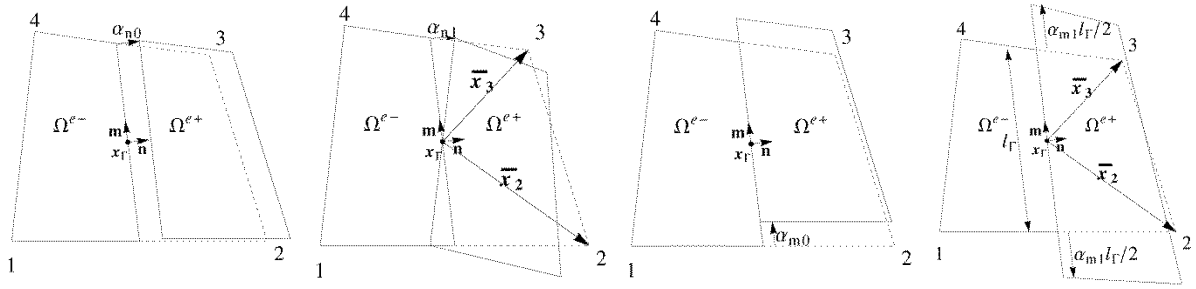

Figure 4.3: Four basic separation modes for positive α_m ($\alpha_1 = \alpha_{n0}$, $\alpha_2 = \alpha_{n1}$, $\alpha_3 = \alpha_{m0}$, $\alpha_4 = \alpha_{m1}$).
Slika 4.3: Štiri osnovni načini širjenja razpoke za pozitivne α_m ($\alpha_1 = \alpha_{n0}$, $\alpha_2 = \alpha_{n1}$, $\alpha_3 = \alpha_{m0}$, $\alpha_4 = \alpha_{m1}$).

In order to model the opening between Ω^{e-} and Ω^{e+}, the parameters α_m, $m = 1, \dots, 4$, are introduced. They are associated with the four basic separation modes shown in Figure 4.3, which define four basic positions of Ω^{e+} with respect to Ω^{e-}. The first two basic separation modes, $m = 1$ and $m = 2$, relate to the mode I (i.e. normal) opening (of the crack), and the last two basic separation modes, $m = 3$ and $m = 4$, relate to the mode II (i.e. tangential) opening (of the crack). Each of the first three basic separation modes displaces Ω^{e+} from Ω^{e-} in a rigid-body manner. The fourth basic separation mode displaces Ω^{e+} from Ω^{e-} via linear stretching of Ω^{e+} along Γ^e. A linear combination of the basic separation modes describes kinematics of Ω^{e+} with respect to Ω^{e-}, or in other words, the opening (of the crack) between Ω^{e-} and Ω^{e+}.

The displacements across the finite element are approximated as:

$$\boldsymbol{u}(\boldsymbol{\xi}, \Gamma^e) = \sum_{a=1}^{4} N_a(\boldsymbol{\xi})\, \boldsymbol{d}_a + \sum_{m=1}^{4} \boldsymbol{p}_m(\boldsymbol{\xi}, \Gamma^e)\, \alpha_m, \tag{4.3}$$

where $\boldsymbol{u} = [u_x, u_y]^T$, $\boldsymbol{d}_a = [u_{xa}, u_{ya}]^T$ are displacements of node a, and $\boldsymbol{p}_m = [p_{mx}, p_{my}]^T$ is vector of interpolation functions associated with parameter α_m and basic separation mode m. It is derived from the following condition: Ω^{e-} remains un-deformed when Ω^{e+} is displaced for basic separation mode m. Let $\boldsymbol{u}_m = \boldsymbol{u}_m(\boldsymbol{\xi}, \Gamma^e)$ denote element displacements due to the basic separation mode. It can be concluded from (4.3) that it consists of two parts

$$\boldsymbol{u}_m = \boldsymbol{u}_{d,m} + \boldsymbol{u}_{\alpha,m,} \quad \boldsymbol{u}_{d,m} = \sum_{a=1}^{4} N_a \, \boldsymbol{d}_{a,m}, \qquad \boldsymbol{u}_{\alpha,m} = \boldsymbol{p}_m \alpha_m, \tag{4.4}$$

where $\boldsymbol{d}_{a,m}$ are nodal displacements. It follows from (4.4) that

$$\boldsymbol{p}_m = \frac{\boldsymbol{u}_m - \boldsymbol{u}_{d,m}}{\alpha_m} \tag{4.5}$$

Displacements $\boldsymbol{u}_m$ and $\boldsymbol{u}_{d,m}$ can be obtained straightforwardly, due to well defined positions of Ω^{e+} and Ω^{e-} for each basic separation mode. Recall that Ω^{e+} displaces from Ω^{e-} in a rigid body manner for $m =$ 1,2,3, and stretches uniformly along Γ^e for $m = 4$. Explicit expressions for $\boldsymbol{u}_m$ and $\boldsymbol{u}_{d,m}$ are provided in (Dujc et al., 2010). By using them in (4.5), the following interpolation functions follow (Dujc et al., 2010)

$$\boldsymbol{p}_1 = \left(H_\Gamma - \sum_{a \in \Omega^{e+}} N_a \right) \boldsymbol{n} \tag{4.6}$$

$$\boldsymbol{p}_2 = H_\Gamma \hat{\boldsymbol{I}} \bar{\boldsymbol{x}} - \sum_{a \in \Omega^{e+}} N_a \hat{\boldsymbol{I}} \bar{\boldsymbol{x}}_a \tag{4.7}$$

$$\boldsymbol{p}_3 = \left(H_\Gamma - \sum_{a \in \Omega^{e+}} N_a \right) \boldsymbol{m} \tag{4.8}$$

$$\boldsymbol{p}_4 = \left((\boldsymbol{m} \cdot \bar{\boldsymbol{x}}) \, H_\Gamma - \sum_{a \in \Omega^{e+}} (\boldsymbol{m} \cdot \bar{\boldsymbol{x}}) \, N_a \right) \boldsymbol{m} \tag{4.9}$$

where $\boldsymbol{n} = [n_x, n_y]^T$ and $\boldsymbol{m} = [m_x, m_y]^T = [-n_y, n_x]^T$ are unit normal and unit tangent to Γ^e, respectively, $\bar{\boldsymbol{x}} = \boldsymbol{x} - \boldsymbol{x}_\Gamma$, dot denotes scalar product of two vectors, $\boldsymbol{x}_\Gamma$ are coordinates of the middle point of Γ^e, $\bar{\boldsymbol{x}}_a = \boldsymbol{x}_a - \boldsymbol{x}_\Gamma$, and $\hat{\boldsymbol{I}} = [[0, -1]^T, [1,0]^T]$. The normal $\boldsymbol{n}$ is pointing from Ω^{e-} to Ω^{e+}, see Figure 4.3. The Heaviside function with the unit step at Γ^e was introduced in (4.6)-(4.9)

$$H_\Gamma(\boldsymbol{x}) = \begin{cases} 1 & \text{for} \boldsymbol{x}, \boldsymbol{x} \in \Omega^{e+} \\ 0 & \text{otherwise} \end{cases} \tag{4.10}$$

Due to H_Γ in (4.6) - (4.9), the element displacements have a strong discontinuity (i.e. a step) at Γ^e, which is the reason for the terminology “embedded-(strong)-discontinuity finite element”.

4.2.2 Strains

The tensor of small strains for the plane stress and plane strain is defined as $\nabla^s \boldsymbol{u} = \frac{1}{2}(\nabla \otimes \boldsymbol{u} + \boldsymbol{u} \otimes \nabla)$, where $\nabla = \left[\frac{\partial}{\partial x}, \frac{\partial}{\partial y}\right]^T$ and $\otimes$ is tensor product (for plane stress there exists an additional strain, which can be computed by post-processing). The terms of the symmetric strain tensor can be collected in a vector as

$$\boldsymbol{\epsilon} = \left[\frac{\partial u_x}{\partial x}, \frac{\partial u_y}{\partial y}, \frac{\partial u_x}{\partial y} + \frac{\partial u_y}{\partial x}\right]^T = \left[\epsilon_{xx}, \epsilon_{yy}, \gamma_{xy}\right]^T \tag{4.11}$$

Strain vector can be expressed with nodal displacements and opening parameters as

$$\boldsymbol{\epsilon}(\boldsymbol{\xi}, \Gamma^e) = \sum_{a=1}^{4} \boldsymbol{B}_a(\boldsymbol{\xi}) \boldsymbol{d}_a + \sum_{m=1}^{4} \boldsymbol{G}_m(\boldsymbol{\xi}, \Gamma^e) \alpha_m \tag{4.12}$$

where $\boldsymbol{G}_m = \left[\frac{\partial p_{mx}}{\partial x}, \frac{\partial p_{my}}{\partial y}, \frac{\partial p_{mx}}{\partial y} + \frac{\partial p_{my}}{\partial x}\right]^T$. Explicit expressions are

$$\boldsymbol{G}_1 = \underbrace{-\sum_{a \in \Omega^{e+}} \boldsymbol{B}_a \boldsymbol{n}}_{\bar{\boldsymbol{G}}_1} + \underbrace{\delta_\Gamma \boldsymbol{B}_n \boldsymbol{n}}_{\bar{\bar{\boldsymbol{G}}}_1} \tag{4.13}$$

$$\boldsymbol{G}_2 = \underbrace{-\sum_{a \in \Omega^{e+}} \boldsymbol{B}_a \hat{\boldsymbol{I}} \bar{\boldsymbol{x}}_a}_{\bar{\boldsymbol{G}}_2} + \underbrace{\delta_\Gamma [\boldsymbol{B}_n \boldsymbol{n} \xi_\Gamma - \boldsymbol{B}_n \boldsymbol{m} (\boldsymbol{n} \cdot \bar{\boldsymbol{x}})]}_{\bar{\bar{\boldsymbol{G}}}_2} \tag{4.14}$$

$$\boldsymbol{G}_3 = \underbrace{-\sum_{a \in \Omega^{e+}} \boldsymbol{B}_a \boldsymbol{m}}_{\bar{\boldsymbol{G}}_3} + \underbrace{\delta_\Gamma \boldsymbol{B}_n \boldsymbol{m}}_{\bar{\bar{\boldsymbol{G}}}_3} \tag{4.15}$$

$$\boldsymbol{G}_4 = \underbrace{H_\Gamma \boldsymbol{B}_m \boldsymbol{m} - \sum_{a \in \Omega^{e+}} \boldsymbol{B}_a \boldsymbol{m} (\boldsymbol{m} \cdot \bar{\boldsymbol{x}}_a)}_{\bar{\boldsymbol{G}}_4} + \underbrace{\delta_\Gamma \boldsymbol{B}_n \boldsymbol{m}\, \xi_\Gamma}_{\bar{\bar{\boldsymbol{G}}}_4} \tag{4.16}$$

Here, $\xi_\Gamma = \boldsymbol{m} \cdot \bar{\boldsymbol{x}} \in \left[-\frac{l_\Gamma}{2}, \frac{l_\Gamma}{2}\right]$ is coordinate along line Γ^e, which has the length l_Γ. The coordinate ξ_Γ has origin at $\boldsymbol{x}_\Gamma$ and is positive in $\boldsymbol{m}$ direction. When deriving (4.14), the identity $\boldsymbol{I} = \boldsymbol{n} \otimes \boldsymbol{n} + \boldsymbol{m} \otimes \boldsymbol{m}$ was used. The matrices, introduced in (4.12) - (4.16), have the following forms

$$\boldsymbol{B}_a = \left[\left[\frac{\partial N_a}{\partial x}, 0, \frac{\partial N_a}{\partial y}\right]^T, \left[0, \frac{\partial N_a}{\partial y}, \frac{\partial N_a}{\partial x}\right]^T\right]$$

$$\boldsymbol{B}_n = \left[\left[n_x, 0, n_y\right]^T, \left[0, n_y, n_x\right]^T\right], \qquad \boldsymbol{B}_m = \left[\left[m_x, 0, m_y\right]^T, \left[0, m_y, m_x\right]^T\right]$$

where derivatives of interpolation functions (4.2) with respect to x and y are obtained in the standard manner of isoparametric elements, see e.g. (Ibrahimbegovic, 2009).

Expressions (4.13)-(4.16) include derivatives of the Heaviside function (4.10), which are by definition, see e.g. (Mosler, 2004)

$$\frac{\partial H_\Gamma(\boldsymbol{x})}{\partial x} = \delta_\Gamma(\boldsymbol{x}) n_x \qquad \frac{\partial H_\Gamma(\boldsymbol{x})}{\partial y} = \delta_\Gamma(\boldsymbol{x}) n_y \tag{4.17}$$

with δ_Γ being defined as

$$\delta_\Gamma(\boldsymbol{x}) = \begin{cases} \infty & \text{for } \boldsymbol{x}, \boldsymbol{x} \in \Gamma^e \\ 0 & \text{otherwise} \end{cases} \tag{4.18}$$

Let us evaluate the integral of (4.17) over the element. Mathematica (Wolfram, 2016) provides

$$\int_{\Omega^e} \frac{\partial H_\Gamma}{\partial x_i} d\Omega = n_{x_i} l_\Gamma, \quad i = 1,2, \qquad x_1 = x, \qquad x_2 = y \tag{4.19}$$

One can get the result (4.19) also by an additional intermediate step

$$\int_{\Omega^e} \frac{\partial H_\Gamma}{\partial x_i} d\Omega = n_{x_i} \int_{\Omega^e} \delta_\Gamma d\Omega = n_{x_i} \int_{\Gamma^e} d\Gamma = n_{x_i} l_\Gamma, \quad i = 1,2, \qquad x_1 = x, \qquad x_2 = y \tag{4.20}$$

which implies the relation

$$\int_{\Omega^e} \delta_\Gamma d\Omega = \int_{\Gamma^e} d\Gamma \tag{4.21}$$

Furthermore, (4.21) implies that integration of a function $f(\boldsymbol{x})$ multiplied by $\delta_\Gamma(\boldsymbol{x})$ over Ω^e is

$$\int_{\Omega^e} \delta_\Gamma(\boldsymbol{x}) f(\boldsymbol{x})\, d\Omega = \int_{\Gamma^e} f(\boldsymbol{x})|_{x \in \Gamma^e} d\Gamma = \int_{\Gamma^e} f(\xi_\Gamma) d\Gamma \tag{4.22}$$

We will use relations (4.21) and (4.22) later on.

It can be concluded from (4.1)-(4.16) that $\boldsymbol{G}_m$ consists of two parts

$$\boldsymbol{G}_m = \overline{\boldsymbol{G}}_m + \overline{\overline{\boldsymbol{G}}}_m \tag{4.23}$$

where $\overline{\boldsymbol{G}}_m$ is bounded (i.e. regular) and $\overline{\overline{\boldsymbol{G}}}_m$ is unbounded (i.e. singular) due to δ_Γ. With this in mind, one can divide the strain vector $\boldsymbol{\epsilon}$ into the bounded (i.e. regular) and unbounded (i.e. singular) parts, $\bar{\boldsymbol{\epsilon}}$ and $\overline{\bar{\boldsymbol{\epsilon}}}$, respectively, in the following manner

$$\boldsymbol{\epsilon} = \underbrace{\sum_{a=1}^{4} \boldsymbol{B}_a \boldsymbol{d}_a + \sum_{m=1}^{4} \overline{\boldsymbol{G}}_m \alpha_m}_{\bar{\boldsymbol{\epsilon}}} + \underbrace{\sum_{m=1}^{4} \overline{\overline{\boldsymbol{G}}}_m \alpha_m}_{\overline{\bar{\boldsymbol{\epsilon}}}} \tag{4.24}$$

4.2.3 Virtual strains

The embedded-strong-discontinuity finite elements, derived in this work, will be based on Petrov-Galerkin approximation, which uses different interpolations for real strains and virtual strains. Such approximation is best suited for the embedded-strong-discontinuity finite elements, as shown by e.g. (Jirasek, 2000), who named them “SKON formulations”.

The vector of virtual strains consists of two parts

$$\hat{\boldsymbol{\epsilon}}(\boldsymbol{\xi},\Gamma^{e}) = \sum_{a=1}^{4} \boldsymbol{B}_a(\boldsymbol{\xi})\hat{\boldsymbol{d}}_a + \sum_{m=1}^{4} \widehat{\boldsymbol{G}}_m(\boldsymbol{\xi},\Gamma^{e})\hat{\alpha}_m \tag{4.25}$$

In (4.25), $\hat{\boldsymbol{d}}_a$ are virtual displacements of node a, $\hat{\alpha}_m$ is virtual counterpart of α_m, and $\widehat{\boldsymbol{G}}_m$ needs to be defined. In what follows, we will summarize two different concepts for defining $\widehat{\boldsymbol{G}}_m$. The first one was introduced in (Dujc et al, 2010), while the second one was proposed in (Linder and Armero, 2007).

4.2.3.1 Defining $\widehat{\boldsymbol{G}}_m$ by modifying of $\boldsymbol{G}_m$ in the spirit of incompatible modes

The virtual strains (4.25) are the sum of: (i) the compatible virtual strains due to compatible virtual nodal displacements, and (ii) the incompatible virtual strains due to virtual basic separation modes, which are incompatible between neighbouring elements. (Dujc et al., 2010) suggested that in case of constant element stress state, the internal virtual work due to incompatible virtual strains should be zero (the reason for this demand will become obvious in Section 4.2.4). The demand can be accomplished by designing $\widehat{\boldsymbol{G}}_m$ in such a way that the integral of $\widehat{\boldsymbol{G}}_m$ over the element is zero.

To this end, the following procedure is applied: the modification of interpolation $\boldsymbol{G}_m$, see (4.13)-(4.16), is performed by submitting its area-average from $\boldsymbol{G}_m$, which yields

$$\widehat{\boldsymbol{G}}_m = \boldsymbol{G}_m - \frac{1}{A_{\Omega^e}}\int_{\Omega^e} \boldsymbol{G}_m \, d\Omega \tag{4.26}$$

where A_{Ω^e} is area of the finite element. The area integral of $\widehat{\boldsymbol{G}}_m$ from (4.26) is indeed zero

$$\int_{\Omega^e} \widehat{\boldsymbol{G}}_m \, d\Omega = \boldsymbol{0} \tag{4.27}$$

After performing (4.26) for each basic separation mode, the following expressions are obtained

$$\widehat{\boldsymbol{G}}_1 = \underbrace{\overline{\boldsymbol{G}}_1 - \frac{1}{A_{\Omega^e}}\int_{\Omega^e} \overline{\boldsymbol{G}}_1 \, d\Omega - \frac{l_\Gamma}{A_{\Omega^e}}\boldsymbol{B}_n\boldsymbol{n}}_{\overline{\overline{\boldsymbol{G}}}_1} + \underbrace{\delta_\Gamma \boldsymbol{B}_n\boldsymbol{n}}_{\overline{\overline{\boldsymbol{G}}}_1} \tag{4.28}$$

$$\widehat{\boldsymbol{G}}_2 = \underbrace{\overline{\boldsymbol{G}}_2 - \frac{1}{A_{\Omega^e}}\int_{\Omega^e} \overline{\boldsymbol{G}}_2 \, d\Omega}_{\overline{\overline{\boldsymbol{G}}}_2} + \underbrace{\delta_\Gamma[\boldsymbol{B}_n\boldsymbol{n}\xi_\Gamma(\boldsymbol{x}) - \boldsymbol{B}_n\boldsymbol{m}(\boldsymbol{n}\cdot\overline{\boldsymbol{x}})]}_{\overline{\overline{\boldsymbol{G}}}_2} \tag{4.29}$$

$$\widehat{\boldsymbol{G}}_3 = \underbrace{\overline{\boldsymbol{G}}_3 - \frac{1}{A_{\Omega^e}}\int_{\Omega^e} \overline{\boldsymbol{G}}_3 \, d\Omega - \frac{l_\Gamma}{A_{\Omega^e}}\boldsymbol{B}_n\boldsymbol{m}}_{\overline{\overline{\boldsymbol{G}}}_3} + \underbrace{\delta_\Gamma \boldsymbol{B}_n\boldsymbol{m}}_{\overline{\overline{\boldsymbol{G}}}_3} \tag{4.30}$$

$$\widehat{\boldsymbol{G}}_4 = \underbrace{\overline{\boldsymbol{G}}_4 - \frac{1}{A_{\Omega^e}}\int_{\Omega^e} \overline{\boldsymbol{G}}_4 \, d\Omega}_{\overline{\overline{\boldsymbol{G}}}_4} + \underbrace{\delta_\Gamma \boldsymbol{B}_n\boldsymbol{m}\xi_\Gamma}_{\overline{\overline{\boldsymbol{G}}}_4} \tag{4.31}$$

To obtain (4.28)-(4.31), relation (4.21) was used, and relation (4.22) was applied in the following forms

$$\int_{\Omega^e} \delta_\Gamma \xi_\Gamma d\Omega = \int_{\Gamma^e} \xi_\Gamma d\Gamma = 0, \qquad \int_{\Omega^e} \delta_\Gamma (\boldsymbol{n} \cdot \overline{\boldsymbol{x}}) d\Omega = \int_{\Gamma^e} (\boldsymbol{n} \cdot \overline{\boldsymbol{x}}) d\Gamma = 0 \tag{4.32}$$

Note, that the first integral in (4.32) is zero, because the coordinate ξ_Γ has origin at the middle point of Γ^e, and the second integral in (4.32) is zero, because $\overline{\boldsymbol{x}}$ is perpendicular to $\boldsymbol{n}$ for any point on Γ^e.

It can be concluded from (4.28)-(4.31) that $\widehat{\boldsymbol{G}}_m$ consists of two parts

$$\widehat{\boldsymbol{G}}_m = \overline{\widehat{\boldsymbol{G}}}_m + \overline{\overline{\widehat{\boldsymbol{G}}}}_m \tag{4.33}$$

where $\overline{\widehat{\boldsymbol{G}}}_m$ is bounded (regular) and $\overline{\overline{\widehat{\boldsymbol{G}}}}_m$ is unbounded (singular) due to δ_Γ. It can be also checked that integration of (4.28)-(4.31) over the element indeed yields zero. The above modification of $\boldsymbol{G}_m$ to get $\widehat{\boldsymbol{G}}_m$, see (4.26), is borrowed from the classical method of incompatible modes, see e.g. (Ibrahimbegovic, 2009). For this reason, it is sometimes stated, see e.g. (Dujc et al., 2010), that the above derivation of $\widehat{\boldsymbol{G}}_m$ is performed in the spirit of the incompatible modes. We note however, that in the classical incompatible modes concept, $\widehat{\boldsymbol{G}}_m$ interpolation is used for both virtual and real strains, which is not the case here. Due to the usage of $\boldsymbol{G}_m$ for real strains and $\widehat{\boldsymbol{G}}_m$ for virtual strains, the stiffness matrices of the here derived embedded-strong-discontinuity finite elements are non-symmetric as will be shown below.

4.2.3.2 Deriving $\widehat{\boldsymbol{G}}_m$ by stress projection function

Another way of defining $\widehat{\boldsymbol{G}}_m$ was proposed in (Linder and Armero, 2007). (Linder and Armero, 2007) also choose to decompose $\widehat{\boldsymbol{G}}_m$ into two parts as $\widehat{\boldsymbol{G}}_m = \overline{\widehat{\boldsymbol{G}}}_m + \overline{\overline{\widehat{\boldsymbol{G}}}}_m$, see (4.33), where $\overline{\widehat{\boldsymbol{G}}}_m$ is bounded (regular) and $\overline{\overline{\widehat{\boldsymbol{G}}}}_m$ is unbounded (singular). The structure of $\overline{\overline{\widehat{\boldsymbol{G}}}}_m$ is the same as already presented in Section 4.2.3.1, see (4.28)-(4.31), but the structure of $\overline{\widehat{\boldsymbol{G}}}_m$ is different. (Linder and Armero, 2007) chose to design $\overline{\widehat{\boldsymbol{G}}}_m$ as

$$\overline{\widehat{\boldsymbol{G}}}_{nk} = -\frac{l_\Gamma}{A_{\Omega^e}} g_e^{\langle k \rangle}(\tilde{x}, \tilde{y}) \boldsymbol{B}_n \boldsymbol{n}, \quad k = 0{,}1 \tag{4.34}$$

$$\overline{\widehat{\boldsymbol{G}}}_{mk} = -\frac{l_\Gamma}{A_{\Omega^e}} g_e^{\langle k \rangle}(\tilde{x}, \tilde{y}) \boldsymbol{B}_n \boldsymbol{m}, \quad k = 0{,}1 \tag{4.35}$$

where $\tilde{x}, \tilde{y}$ are Cartesian coordinates with origin at the element center (and with the orientations of x, y, respectively), and $g_e^{\langle k \rangle}$ is yet undefined function.

The motivation for the choice (4.34)-(4.35) can be explained on the local set of equilibrium equations, derived below in Section 4.2.4, see equations (4.68)-(4.71). For the sake of clarity, we present those equations also here, but we write them in a more compact form

$$t^e \int_{\Omega^e} \bar{\bar{\boldsymbol{G}}}_{nk}^T \boldsymbol{\sigma}\, d\Omega + t^e \int_{\Gamma^e} t_n\, (\xi_\Gamma)^k d\Gamma = 0, \qquad k = 0{,}1 \tag{4.36}$$

$$t^e \int_{\Omega^e} \bar{\bar{\boldsymbol{G}}}_{mk}^T \boldsymbol{\sigma}\, d\Omega + t^e \int_{\Gamma^e} t_m (\xi_\Gamma)^k d\Gamma = 0\,, \qquad k = 0{,}1 \tag{4.37}$$

The following notation is used in (4.36)-(4.37): $\bar{\bar{\boldsymbol{G}}}_{n0}^T = \bar{\bar{\boldsymbol{G}}}_1^T$, $\bar{\bar{\boldsymbol{G}}}_{n1}^T = \bar{\bar{\boldsymbol{G}}}_2^T$, $\bar{\bar{\boldsymbol{G}}}_{m0}^T = \bar{\bar{\boldsymbol{G}}}_3^T$, $\bar{\bar{\boldsymbol{G}}}_{m1}^T = \bar{\bar{\boldsymbol{G}}}_4^T$, t^e is (constant) element thickness, $\boldsymbol{\sigma} = \left[\sigma_{xx}, \sigma_{yy}, \sigma_{xy}\right]^T$ is vector of stresses with respect to x and y coordinates, and t_n and t_m are normal and shear cohesive tractions in the crack. By using the stress transformation $\boldsymbol{n}^T \boldsymbol{B}_n^T\, \boldsymbol{\sigma} = \sigma_{nn}$, $\boldsymbol{m}^T \boldsymbol{B}_n^T\, \boldsymbol{\sigma} = \sigma_{nm}$ (see also equation (4.59) below), and (4.34)-(4.35), the equations (4.36)-(4.37) can be rewritten as

$$-t^e \frac{l_\Gamma}{A_{\Omega^e}} \int_{\Omega^e} g_e^{\langle k \rangle}(\tilde{x}, \tilde{y}) \sigma_{nn}\, d\Omega + t^e \int_{\Gamma^e} t_n (\xi_\Gamma)^k d\Gamma = 0, \qquad k = 0{,}1 \tag{4.38}$$

$$-t^e \frac{l_\Gamma}{A_{\Omega^e}} \int_{\Omega^e} g_e^{\langle k \rangle}(\tilde{x}, \tilde{y}) \sigma_{nm}\, d\Omega + t^e \int_{\Gamma^e} t_m (\xi_\Gamma)^k d\Gamma = 0\,, \qquad k = 0{,}1 \tag{4.39}$$

In case of constant bulk stress state (the bulk is defined as Ω^e/Γ^e), one has $t_n = \sigma_{nn}$ and $t_m = \sigma_{nm}$. The situation happens in a limit of very fine mesh, and in any mesh under special loading conditions. The crack normal and shear tractions t_n and t_m equal to the bulk stresses at the crack edge, which are σ_{nn} (normal stress) and σ_{nm} (shear stress). Due to the constant bulk stress state, σ_{nn} and σ_{nm} are constant throughout the bulk. For the case of constant bulk stress state, four equations in (4.38)-(4.39) reduce to two equations (since two pairs of identical equations are obtained)

$$-\frac{l_\Gamma}{A_{\Omega^e}} \int_{\Omega^e} g_e^{\langle k \rangle}(\tilde{x}, \tilde{y})\, d\Omega + \int_{\Gamma^e} (\xi_\Gamma)^k d\Gamma = 0, \qquad k = 0{,}1\ ; \qquad \int_{\Gamma^e} (\xi_\Gamma)^k d\Gamma = \begin{cases} l_\Gamma, & k = 0 \\ 0, & k = 1 \end{cases} \tag{4.40}$$

Equation (4.40) shows that the choice (4.34)-(4.35) is completely valid from the view of local equilibrium equations (4.36)-(4.37). However, the structure of function $g_e^{\langle k \rangle}$ is restricted with condition (4.40).

It is natural to assume $g_e^{\langle k \rangle}$ as a bi-linear function

$$g_e^{\langle k \rangle}(\tilde{x}, \tilde{y}) = a_k + b_k \tilde{x} + c_k \tilde{y}, \quad k = 0{,}1 \tag{4.41}$$

where a_k, b_k and c_k are unknown constants. The total number of constants for $g_e^{\langle 0 \rangle}$ and $g_e^{\langle 1 \rangle}$ is six. In order to get additional four equations, besides two in (4.40), for computing six constants, the following is performed. Both functions under integrals in (4.40) are multiplied by $\tilde{x} = \tilde{x}_1$ and $\tilde{y} = \tilde{y}_2$ to get

$$-\frac{l_\Gamma}{A_{\Omega^e}} \int_{\Omega^e} g_e^{\langle k \rangle}(\tilde{x}, \tilde{y}) \bar{x}_i\, d\Omega + \int_{\Gamma^e} (\xi_\Gamma)^k \tilde{x}_i\, d\Gamma = 0, \qquad k = 0{,}1 \quad i = 1{,}2 \tag{4.42}$$

With (4.40) and (4.42), one has two systems of three equations for computing six constants a_k, b_k and c_k. These two systems can be written in a compact form as

$$\begin{bmatrix} a_k \\ b_k \\ c_k \end{bmatrix} = \left(\frac{1}{A_{\Omega^e}} \int_{\Omega^e} \begin{bmatrix} 1 & \tilde{x} & \tilde{y} \\ \tilde{x} & \tilde{x}^2 & \tilde{x}\tilde{y} \\ \tilde{y} & \tilde{x}\tilde{y} & \tilde{y}^2 \end{bmatrix} d\Omega \right)^{-1} \left(\frac{1}{l_\Gamma} \int_{\Gamma_e} \begin{Bmatrix} (\xi_\Gamma)^k \\ (\xi_\Gamma)^k \tilde{x} \\ (\xi_\Gamma)^k \tilde{y} \end{Bmatrix} d\Gamma \right), \quad k = 0,1 \tag{4.43}$$

With the element constants a_k, b_k and c_k in hand, $\widehat{\boldsymbol{G}}_m$ is completely defined, see (4.34)-(4.35). Moreover, for a constant element stress state, the local element equilibrium equations (4.36)-(4.37) are identically satisfied, since all four equations yield $0 = 0$. This is due to choice of constants a_k, b_k and c_k according to (4.40) and (4.42).

For the sake of completeness, let us write the explicit forms

$$\bar{\bar{\widehat{\boldsymbol{G}}}}_1 = -\frac{l_\Gamma}{A_{\Omega^e}} (a_0 + b_0\tilde{x} + c_0\tilde{y}) \boldsymbol{B}_n \boldsymbol{n} \tag{4.44}$$

$$\bar{\bar{\widehat{\boldsymbol{G}}}}_2 = -\frac{l_\Gamma}{A_{\Omega^e}} (a_1 + b_1\tilde{x} + c_1\tilde{y}) \boldsymbol{B}_n \boldsymbol{n} \tag{4.45}$$

$$\bar{\bar{\widehat{\boldsymbol{G}}}}_3 = -\frac{l_\Gamma}{A_{\Omega^e}} (a_0 + b_0\tilde{x} + c_0\tilde{y}) \boldsymbol{B}_n \boldsymbol{m} \tag{4.46}$$

$$\bar{\bar{\widehat{\boldsymbol{G}}}}_4 = -\frac{l_\Gamma}{A_{\Omega^e}} (a_1 + b_1\tilde{x} + c_1\tilde{y}) \boldsymbol{B}_n \boldsymbol{m} \tag{4.47}$$

4.2.4 Equilibrium equations

Let the 2d body under consideration be discretized by N_e embedded discontinuity quadrilaterals. The principal of virtual work (i.e. the weak form of equilibrium equations) can be written for the discretized body as

$$\mathbb{A}_{e=1}^{N_e} (G^{int,e} - G^{ext,e}) = 0 \tag{4.48}$$

where $\mathbb{A}$ is the finite element assembly operator, $G^{ext,e}$ is virtual work of external forces that act on element, and $G^{int,e}$ is internal virtual work. The latter is defined as

$$G^{int,e} = t^e \int_{\Omega^e} \hat{\boldsymbol{\epsilon}}(\boldsymbol{\xi}, \Gamma^e) \cdot \boldsymbol{\sigma}(\boldsymbol{\xi}) \, d\Omega \tag{4.49}$$

where t^e is (constant) element thickness, $\boldsymbol{\sigma} = \left[\sigma_{xx}, \sigma_{yy}, \sigma_{xy}\right]^T$ is vector of stresses, and $\hat{\boldsymbol{\epsilon}}$ is vector of virtual strains (4.25). Due to (4.25), equation (4.49) can be rewritten as

$$G^{int,e} = t^e \int_{\Omega^e} \hat{\boldsymbol{\epsilon}} \cdot \boldsymbol{\sigma} \, d\Omega = \sum_{a=1}^{4} t^e \int_{\Omega^e} \widehat{\boldsymbol{d}}_a^T \boldsymbol{B}_a^T \boldsymbol{\sigma} \, d\Omega + \sum_{m=1}^{4} t^e \int_{\Omega^e} \hat{\alpha}_m \widehat{\boldsymbol{G}}_m^T \boldsymbol{\sigma} \, d\Omega \tag{4.50}$$

Let us write the first sum in (4.50) as

$$\sum_{a=1}^{4} t^e \int_{\Omega^e} \widehat{\boldsymbol{d}}_a^T \boldsymbol{B}_a^T \boldsymbol{\sigma}\, d\Omega = \sum_{a=1}^{4} \widehat{\boldsymbol{d}}_a^T \boldsymbol{f}_a^{int,e} \tag{4.51}$$

where $\boldsymbol{f}_a^{int,e}$ is part of the vector of element internal nodal forces $\boldsymbol{f}^{int,e} = \left[\boldsymbol{f}_a^{int,e,T}\right]^T$. The vector of element external nodal forces $\boldsymbol{f}^{ext,e}$, which represents equivalent nodal loading due to external loadings acting on the element, is $\boldsymbol{f}^{ext,e} = \left[\boldsymbol{f}_a^{ext,e,T}\right]^T$, where $\boldsymbol{f}_a^{ext,e}$ follows from the element virtual work of external forces $G^{ext,e} = \sum_{a=1}^{4} \widehat{\boldsymbol{d}}_a^T \boldsymbol{f}_a^{ext,e}$. With the above, one can rewrite (4.48) as

$$\mathbb{A}_{e=1}^{N_e} \left(\sum_{a=1}^{4} \widehat{\boldsymbol{d}}_a^T \left(\boldsymbol{f}_a^{int,e} - \boldsymbol{f}_a^{ext,e} \right) \right) + \mathbb{A}_{e=1}^{N_e} \left(\sum_{m=1}^{4} t^e \int_{\Omega^e} \hat{\alpha}_m \widehat{\boldsymbol{G}}_m^T \boldsymbol{\sigma}\, d\Omega \right) = 0 \tag{4.52}$$

Since the components of vector $\widehat{\boldsymbol{d}}_a$ are arbitrary (yet kinematically admissible), the first part of eq. (4.52) yields the following set of equations

$$\mathbb{A}_{e=1}^{N_e} \underbrace{\left(\boldsymbol{f}^{int,e} - \boldsymbol{f}^{ext,e} \right)}_{\boldsymbol{R}_d^e} = \boldsymbol{0} \tag{4.53}$$

where $\mathbb{A}$ is the finite element assembly operator that also takes into account displacement boundary conditions.

The second part of eq. (4.52) yields the following equations due to arbitrariness of $\hat{\alpha}_m$

$$t^e \int_{\Omega^e} \widehat{\boldsymbol{G}}_m^T \boldsymbol{\sigma}\, d\Omega = 0 \quad \text{for } \forall\, m = 1, \cdots, 4 \text{ and } \forall\, e = 1, \cdots, N_e \tag{4.54}$$

Equations (4.53) and (4.54) are two sets of equilibrium equations for the embedded discontinuity quadrilateral. The equations (4.53) can be seen as a set of global equilibrium equations, and the equations (4.54) can be seen as a set of local (i.e. element) equilibrium equations.

4.2.4.1 Local equilibrium equations with $\widehat{\boldsymbol{G}}_m$

Let us further elaborate on equations (4.54). To that end, let us consider $\widehat{\boldsymbol{G}}_m$ from Section 4.2.3.1. By inserting (4.28)-(4.31) into (4.54), one gets

$$t^e \int_{\Omega^e} \overline{\widehat{\boldsymbol{G}}}_1^T \boldsymbol{\sigma}\, d\Omega + t^e \int_{\Omega^e} \delta_\Gamma \boldsymbol{n}^T \boldsymbol{B}_n^T\, \boldsymbol{\sigma}\, d\Omega = 0 \tag{4.55}$$

$$t^e \int_{\Omega^e} \overline{\widehat{\boldsymbol{G}}}_2^T \boldsymbol{\sigma}\, d\Omega + t^e \int_{\Omega^e} \delta_\Gamma [\boldsymbol{n}^T \boldsymbol{B}_n^T\, \xi_\Gamma(\boldsymbol{x}) - \boldsymbol{m}^T \boldsymbol{B}_n^T\, (\boldsymbol{n} \cdot \overline{\boldsymbol{x}})] \boldsymbol{\sigma}\, d\Omega = 0 \tag{4.56}$$

$$t^e \int_{\Omega^e} \overline{\widehat{\boldsymbol{G}}}_3^T \boldsymbol{\sigma}\, d\Omega + t^e \int_{\Omega^e} \delta_\Gamma \boldsymbol{m}^T \boldsymbol{B}_n^T\, \boldsymbol{\sigma}\, d\Omega = \tag{4.57}$$

$$t^e \int_{\Omega^e} \overline{\widehat{\boldsymbol{G}}}_4^T \boldsymbol{\sigma}\, d\Omega + t^e \int_{\Omega^e} \delta_\Gamma \boldsymbol{m}^T \boldsymbol{B}_n^T\, \xi_\Gamma\, \boldsymbol{\sigma}\, d\Omega = 0 \tag{4.58}$$

Note, that some of the products in the above integrals are standard expressions for the transformation of stresses, i.e.

$$\boldsymbol{n}^T \boldsymbol{B}_n^T \boldsymbol{\sigma} = \boldsymbol{n}^T \boldsymbol{S}\boldsymbol{n}, \quad \boldsymbol{m}^T \boldsymbol{B}_n^T \boldsymbol{\sigma} = \boldsymbol{m}^T \boldsymbol{S}\boldsymbol{n}, \quad \boldsymbol{S} = \begin{bmatrix} \sigma_{xx} & \sigma_{xy} \\ \sigma_{xy} & \sigma_{yy} \end{bmatrix} \tag{4.59}$$

By applying (4.21) and (4.22) in (4.55)-(4.58), one can get the following expressions

$$t^e \int_{\Omega^e} \overline{\widehat{\boldsymbol{G}}}_1^T \boldsymbol{\sigma}\, d\Omega + t^e \int_{\Gamma^e} \boldsymbol{n}^T \boldsymbol{B}_n^T \boldsymbol{\sigma}\; d\Gamma = 0 \tag{4.60}$$

$$t^e \int_{\Omega^e} \overline{\widehat{\boldsymbol{G}}}_2^T \boldsymbol{\sigma}\, d\Omega + t^e \int_{\Gamma^e} \boldsymbol{n}^T \boldsymbol{B}_n^T \boldsymbol{\sigma}\, \xi_\Gamma\, d\Gamma = 0 \tag{4.61}$$

$$t^e \int_{\Omega^e} \overline{\widehat{\boldsymbol{G}}}_3^T \boldsymbol{\sigma}\, d\Omega + t^e \int_{\Gamma^e} \boldsymbol{m}^T \boldsymbol{B}_n^T \boldsymbol{\sigma}\, d\Gamma = 0 \tag{4.62}$$

$$t^e \int_{\Omega^e} \overline{\widehat{\boldsymbol{G}}}_4^T \boldsymbol{\sigma}\, d\Omega + t^e \int_{\Gamma^e} \boldsymbol{m}^T \boldsymbol{B}_n^T \boldsymbol{\sigma} \xi_\Gamma\, d\Gamma = 0 \tag{4.63}$$

Let us now turn attention to the bulk normal and shear stresses at the edge of Ω^{e-}, which has unit normal $\boldsymbol{n}$ and unit tangent $\boldsymbol{m}$. They are defined as (see also (4.59))

$$\sigma_{nn}|_{\Omega^{e-}edge} = \boldsymbol{n}^T \boldsymbol{S}\boldsymbol{n} = \boldsymbol{n}^T \boldsymbol{B}_n^T \boldsymbol{\sigma}\,, \quad \sigma_{nm}|_{\Omega^{e-}edge} = \boldsymbol{m}^T \boldsymbol{S}\boldsymbol{n} = \boldsymbol{m}^T \boldsymbol{B}_n^T \boldsymbol{\sigma} \tag{4.64}$$

They are equal to the boundary tractions t_n^- and t_m^- acting on the considered edge of Ω^{e-}

$$t_n^- = \sigma_{nn}|_{\Omega^{e-}edge}, \quad t_m^- = \sigma_{nm}|_{\Omega^{e-}edge} \tag{4.65}$$

Similarly, the bulk normal and shear stresses at the edge of Ω^{e+}, which has unit normal $\breve{\boldsymbol{n}} = -\boldsymbol{n}$ and unit tangent $\breve{\boldsymbol{m}} = -\boldsymbol{m}$, equal to the boundary tractions at that edge

$$t_n^+ = \sigma_{\breve{n}\breve{n}}|_{\Omega^{e+}edge} = (-\boldsymbol{n}^T)(-\boldsymbol{B}_n^T)\,\boldsymbol{\sigma}, \quad t_m^+ = \sigma_{\breve{n}\breve{m}}|_{\Omega^{e+}edge} = (-\boldsymbol{m}^T)(-\boldsymbol{B}_n^T)\,\boldsymbol{\sigma} \tag{4.66}$$

The tractions (4.66) have the opposite directions from those in (4.65). The tractions at both sides of the opening are due to the cohesion between Ω^{e-} and Ω^{e+}. It is thus reasonable to assume that they are of equal values. It is also reasonable to use the same notation for (4.65) and (4.66). In what follows, the notation t_n and t_m will be used to denote the normal and shear tractions in the crack opening

$$t_n = t_n^- = t_n^+, \quad t_m = t_m^- = t_m^+ \tag{4.67}$$

By taking into account relations (4.64)-(4.67), the local equilibrium equations (4.60)-(4.63) can be expressed by crack tractions as

$$\underbrace{t^e \int_{\Omega^e} \overline{\widehat{\boldsymbol{G}}}_1^T \boldsymbol{\sigma}\, d\Omega + t^e \int_{\Gamma^e} t_n\, d\Gamma}_{h_1} = 0 \tag{4.68}$$

$$\underbrace{t^e \int_{\Omega^e} \overline{\widehat{\boldsymbol{G}}}_2^T \boldsymbol{\sigma}\, d\Omega + t^e \int_{\Gamma^e} t_n \xi_\Gamma\, d\Gamma}_{h_2} = 0 \tag{4.69}$$

$$\underbrace{t^e \int_{\Omega^e} \overline{\widehat{\boldsymbol{G}}}_3^T \boldsymbol{\sigma}\, d\Omega + t^e \int_{\Gamma^e} t_m\, d\Gamma}_{h_3} = 0 \tag{4.70}$$

$$\underbrace{t^e \int_{\Omega^e} \overline{\widehat{\boldsymbol{G}}}_4^T \boldsymbol{\sigma}\, d\Omega + t^e \int_{\Gamma^e} t_m \xi_\Gamma\, d\Gamma}_{h_4} = 0 \tag{4.71}$$

It can be seen from (4.68)-(4.71) that $\overline{\widehat{\boldsymbol{G}}}_m$ has the role of the operator that "projects" element stresses to the normal or shear traction (or to its moment). The structure of $\overline{\widehat{\boldsymbol{G}}}_m$ is given in Section 4.2.3.1, see (4.28)-(4.31). Equations (4.68)-(4.71) provide the final form of local equilibrium equations (4.54).

Let us now check the equations (4.68)-(4.71) for a special stress state. Let bulk stresses $\boldsymbol{\sigma}$ be constant, which implies constant tractions t_n and t_m along the crack line. In such case, the following relations follow from (4.68)-(4.71)

$$t^e \left(\int_{\Omega^e} \overline{\widehat{\boldsymbol{G}}}_1^T\, d\Omega \right) \boldsymbol{\sigma} + t^e t_n \int_{\Gamma^e} d\Gamma = 0 \tag{4.72}$$

$$t^e \left(\int_{\Omega^e} \overline{\widehat{\boldsymbol{G}}}_2^T\, d\Omega \right) \boldsymbol{\sigma} + t^e t_n \int_{\Gamma^e} \xi_\Gamma\, d\Gamma = 0 \tag{4.73}$$

$$t^e \left(\int_{\Omega^e} \overline{\widehat{\boldsymbol{G}}}_3^T\, d\Omega \right) \boldsymbol{\sigma} + t^e t_m \int_{\Gamma^e} d\Gamma = 0 \tag{4.74}$$

$$t^e \left(\int_{\Omega^e} \overline{\widehat{\boldsymbol{G}}}_4^T\, d\Omega \right) \boldsymbol{\sigma} + t^e t_m \int_{\Gamma^e} \xi_\Gamma\, d\Gamma = 0 \tag{4.75}$$

All four equations (4.72)-(4.75) are satisfied identically for constant stress state, since they deliver $0 = 0$. This can be concluded from the structure of $\overline{\widehat{\boldsymbol{G}}}_m,\ m = 1, \cdots, 4$, in (4.28)-(4.31) and relations (4.64)-(4.67). The conclusion advocates that for the case of element constant stress state the interpolations $\widehat{\boldsymbol{G}}_m, m = 1, \cdots, 4$, from Section 4.2.3.1 satisfy the element local equilibrium equations identically. We note, however,

that the opening parameters for such an element are still part of the global equation (4.52). The situation is similar in the method of incompatible modes, see e.g. (Ibrahimbegovic, 2009).

The equations (4.68)-(4.71) are valid also for $\widehat{\boldsymbol{G}}_m$ from Section 4.2.3.2. In fact, they were already employed in that section for defining the appropriate structure of $\widehat{\boldsymbol{G}}_m$, which yields identical satisfaction of element local equilibrium equations for element constant stress state.

4.2.5 Constitutive equations

4.2.5.1 Elastic constitutive equations for the bulk

For the bulk, we use linear elastic material law

$$\boldsymbol{\sigma} = \boldsymbol{C}\bar{\boldsymbol{\epsilon}} \tag{4.76}$$

For the plane stress, $\boldsymbol{C}$ equals to

$$\boldsymbol{C} = \frac{E}{1-\nu^2}\begin{bmatrix} 1 & \nu & 0 \\ \nu & 1 & 0 \\ 0 & 0 & \dfrac{1-\nu}{2} \end{bmatrix} \tag{4.77}$$

where E is elastic modulus and ν is Poisson's ratio.

For the displacement-based quadrilateral, which is the background of the embedded-strong-discontinuity quadrilateral derived in Section 4.2, one should use only the plane stress constitutive relations. It is well known that for the plane strain problems, the displacement-based quadrilateral exhibits volumetric locking. The embedded discontinuity quadrilateral for the plain strain problems should be based on a mixed, assumed strain or incompatible modes formulations. An example of such element is described in Section 4.3.

Inelastic bulk constitutive equations, like elasto-plastic with hardening, see e.g. (Dujc et al., 2010), or elasto-damage with hardening, see e.g. (Brancherie and Ibrahimbegovic, 2009), will not be considered in this work.

4.2.5.2 Uncoupled elasto-damage cohesion with softening for the crack

To describe tractions in the opening, we use two uncoupled damage traction-separation laws: one in the $\boldsymbol{n}$ direction describing normal traction t_n due the mode I opening, and the other one in the $\boldsymbol{m}$ direction describing shear traction t_m due to the mode II opening.

In $\boldsymbol{n}$ direction, only tension traction is considered, i.e. $t_n \geq 0$. The non-associative softening damage (Bude, 2015) is formulated. The Helmholtz free energy is

$$\psi_n\left(\bar{\bar{u}}_n, \bar{\bar{\xi}}_n\right) = \frac{1}{2}\bar{\bar{Q}}_n^{-1}\bar{\bar{u}}_n^2 + \Xi\left(\bar{\bar{\xi}}_n\right) \tag{4.78}$$

where $\bar{\bar{Q}}_n^{-1} \in [E, 0]$ is inverse of compliance modulus and $\bar{\bar{u}}_n$ is opening in normal direction defined as $\bar{\bar{u}}_n = \alpha_1 + \xi_\Gamma \alpha_2$. The failure function is

$$\bar{\bar{\phi}}_n(t_n, \bar{\bar{q}}_n) = t_n - (\sigma_{un} - \bar{\bar{q}}_n) \leq 0 \tag{4.79}$$

where σ_{un} is material failure stress, and $\bar{\bar{q}}_n$ is traction-like softening force. For the softening law we choose an exponential form

$$\bar{\bar{q}}_n(\bar{\bar{\xi}}_n) = \sigma_{un}\left(1 - e^{-\frac{\sigma_{un}}{G_{fn}}\bar{\bar{\xi}}_n}\right) \tag{4.80}$$

where $\bar{\bar{\xi}}_n$ is displacement-like parameter that controls softening, and G_{fn} is the mode I fracture energy (the energy needed to propagate a crack in mode I for a unit surface), which is material characteristic.

From the principle of maximum dissipation the following relations follow:

$$t_n = \bar{\bar{Q}}_n^{-1}\bar{\bar{u}}_n \tag{4.81}$$

and evolution equations

$$\dot{\bar{\bar{\xi}}}_n = \dot{\bar{\bar{\gamma}}}_n \frac{\partial F_n}{\partial \bar{\bar{q}}_n} = \dot{\bar{\bar{\gamma}}}_n \tag{4.82}$$

$$\dot{\bar{\bar{Q}}}_n = \dot{\bar{\bar{\gamma}}}_n \frac{\partial F_n}{\partial \bar{\bar{Y}}_n} = \dot{\bar{\bar{\gamma}}}_n \frac{\partial F_n}{\partial t_n}\frac{\partial t_n}{\partial \bar{\bar{Y}}_n} = \frac{\dot{\bar{\bar{\gamma}}}_n}{t_n}\left(1 + \frac{\sigma_{un}}{G_{fn}}\bar{\bar{\xi}}_n\right) \tag{4.83}$$

where $\dot{\bar{\bar{\gamma}}}_n$ is damage multiplier, the dissipation potential F_n and damage associated variable $\bar{\bar{Y}}_n$ are:

$$F_n\left(t_n, \bar{\bar{q}}_n(\bar{\bar{\xi}}_n)\right) = |t_n|\left(2 - \ln\left[\frac{|t_n|}{\sigma_{un}}\right]\right) - \left(\sigma_{un} - \bar{\bar{q}}_n(\bar{\bar{\xi}}_n)\right) \tag{4.84}$$

$$\bar{\bar{Y}}_n = -\frac{\partial \bar{\bar{\psi}}_n}{\partial \bar{\bar{Q}}_n} = \frac{1}{2}t_n^2 \tag{4.85}$$

taking into account the Kuhn-Tucker optimality conditions and consistency equation

$$\dot{\bar{\bar{\gamma}}}_n \bar{\bar{\phi}}_n = 0, \quad \dot{\bar{\bar{\gamma}}}_n \dot{\bar{\bar{\phi}}}_n = 0, \quad \dot{\bar{\bar{\gamma}}}_n \geq 0, \quad \bar{\bar{\phi}}_n \leq 0 \tag{4.86}$$

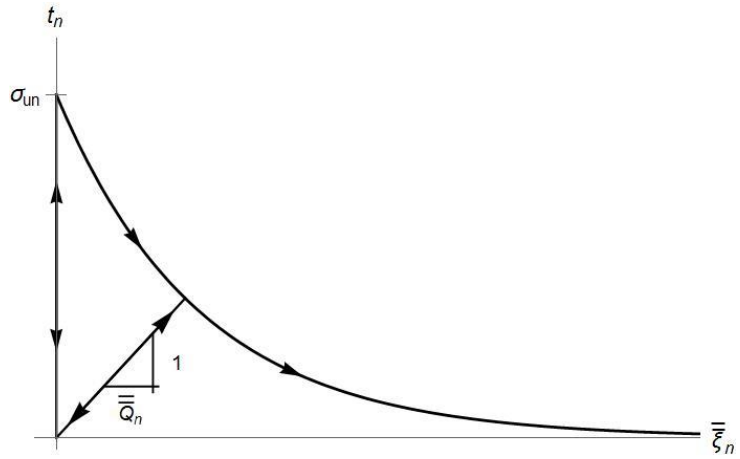

*Figure 4.4: Rigid-damage exponential softening law $t_n(\bar{\bar{\xi}}_n)$ in normal direction **n**.*

*Slika 4.4: Togo-poškodbeni eksponentni zakon mehčanja $t_n(\bar{\bar{\xi}}_n)$ v smeri normale **n**.*

In tangent direction, only shear traction t_m due to the mode II opening is considered. The failure function is:

$$\bar{\bar{\phi}}_m(t_m, \bar{\bar{q}}_m) = |t_m| - (\sigma_{um} - \bar{\bar{q}}_m) \leq 0, \tag{4.87}$$

where σ_{um} is material failure shear stress, and $\bar{\bar{q}}_m$ is traction-like softening force in tangential direction. For the softening law we choose the non-associative exponential form

$$\bar{\bar{q}}_m(\bar{\bar{\xi}}_m) = \sigma_{um}\left(1 - e^{-\frac{\sigma_{um}}{G_{fm}}\bar{\bar{\xi}}_m}\right), \tag{4.88}$$

where $\bar{\bar{\xi}}_m$ is displacement-like parameter that controls softening in tangent direction, and G_{fm} is mode II fracture energy. The corresponding evolution equations are derivated in the same way as in case of mode I (see equations (4.78) - (4.86)).

Furthermore, when it is needed the tangential traction stress t_m is replaced by the simple linear relation (Linder and Armero, 2007):

$$t_m(\bar{\bar{v}}_m) = k_m \bar{\bar{v}}_m\,, \tag{4.89}$$

where $\bar{\bar{v}}_m(\xi_\Gamma) = \alpha_3 + \xi_\Gamma \alpha_4$ (see Figure 4.3) is a jump-in-displacement in tangent direction and k_m is the tangent coefficient.

4.3 Incompatible displacements enhancement

The "in-plane" bending of isoparametric, displacement-based quadrilateral, usually denoted as Q4, can be improved by application of incompatible displacements in the framework of the incompatible modes method. The Q4 displacements are enhanced by incompatible displacements by using two additional interpolation functions $M_b, b = 1,2$, on the top of four interpolation functions $N_a, a = 1, \cdots, 4$. Such element will be denoted as Q6.

The theoretical background of the incompatible modes method can be nicely explained with the following four steps, see e.g. (Ibrahimbegovic, 2009) for details. (i) The Hu-Washizu functional, with displacements, strains and stresses as the unknown fields, is taken as the starting point. (ii) The strains of Q6 are assumed to be additively decomposed into (iia) Q4 strains and (iib) enhanced assumed strains (EAS) due to incompatible displacements. (iii) By employing (ii) in (i), one obtains the EAS-modified Hu-Washizu functional. (iv) The requirement for element-wise orthogonality of stresses and EAS strains (i.e. the strains due to incompatible displacements) is used, which is in practice enforced only for the constant stress state over the element. The application of the above four steps yields only two equations for the stationary point of EAS-modified Hu-Washizu functional for Q6 element.

The Q4 element was the background for the embedded-strong-discontinuity element derived in Section 4.2. In this section, we will derive embedded-strong-discontinuity element with the Q6 as the background.

4.3.1 Displacements and strains

Let us write the interpolation of displacements over the element by taking into account the incompatible displacements

$$\boldsymbol{u}(\boldsymbol{\xi}, \Gamma^{\mathrm{e}}) = \sum_{a=1}^{4} N_a(\boldsymbol{\xi})\, \boldsymbol{d}_a + \sum_{b=1}^{2} M_b(\boldsymbol{\xi})\, \boldsymbol{\rho}_b + \sum_{m=1}^{4} \boldsymbol{p}_m(\boldsymbol{\xi}, \Gamma^{\mathrm{e}})\, \alpha_m, \tag{4.90}$$

where the second sum relates to the incompatible displacements, $M_1(\xi) = 1 - \xi^2$ and $M_2(\eta) = 1 - \eta^2$ are interpolation functions (note that $N_a \cap M_b = \emptyset$ for $\forall\, a, b$, i.e. they do not belong to the same space), and $\boldsymbol{\rho}_1 = [\rho_{11}, \rho_{12}]^T$, $\boldsymbol{\rho}_2 = [\rho_{21}, \rho_{22}]^T$ are the parameters of the element incompatible displacements. Derivation (4.11) of displacements (4.90) yields strains

$$\boldsymbol{\epsilon}(\boldsymbol{\xi}, \Gamma^{\mathrm{e}}) = \sum_{a=1}^{4} \boldsymbol{B}_a(\boldsymbol{\xi}) \boldsymbol{d}_a + \sum_{b=1}^{2} \widetilde{\boldsymbol{G}}_b(\boldsymbol{\xi})\, \boldsymbol{\rho}_b + \sum_{m=1}^{4} \boldsymbol{G}_m(\boldsymbol{\xi}, \Gamma^{\mathrm{e}}) \alpha_m \tag{4.91}$$

with $\widetilde{\boldsymbol{G}}_b$ being modified $\boldsymbol{G}_b$ as

$$\widetilde{\boldsymbol{G}}_b = \boldsymbol{G}_b - \frac{1}{A_{\Omega^e}} \int_{\Omega^e} \boldsymbol{G}_b \, d\Omega, \quad \boldsymbol{G}_b = \left[\left[\frac{\partial M_b}{\partial x}, 0, \frac{\partial M_b}{\partial y} \right]^T, \left[0, \frac{\partial M_b}{\partial y}, \frac{\partial M_b}{\partial x} \right]^T \right] \tag{4.92}$$

so that

$$\int_{\Omega^e} \widetilde{\boldsymbol{G}}_b \, d\Omega = \boldsymbol{0} \tag{4.93}$$

The above modification makes sure that in case of constant stress state in the bulk, the stresses are orthogonal to the EAS strains (i.e. the strains due to the incompatible displacements), i.e. the above modification ensures requirement (iv) for constant stresses. Because of the additive decomposition of $\boldsymbol{G}_m$, see (4.23), the strains (4.91) can be rewritten as

$$\boldsymbol{\epsilon} = \underbrace{\sum_{a=1}^{4} \boldsymbol{B}_a \boldsymbol{d}_a + \sum_{b=1}^{2} \widetilde{\boldsymbol{G}}_b \, \boldsymbol{\rho}_b + \sum_{m=1}^{4} \overline{\boldsymbol{G}}_m \alpha_m}_{\bar{\boldsymbol{\epsilon}}} + \underbrace{\sum_{m=1}^{4} \overline{\overline{\boldsymbol{G}}}_m \alpha_m}_{\bar{\bar{\boldsymbol{\epsilon}}}} \tag{4.94}$$

where $\bar{\boldsymbol{\epsilon}}(\boldsymbol{\xi})$ are bounded strains over the bulk Ω^e/Γ^e and $\bar{\bar{\boldsymbol{\epsilon}}}$ are unbounded strains at Γ^e.

By comparing strains (4.94) with strains (4.24), and checking the form of virtual strains (4.25), one can conclude that the strain variation (the term virtual strains will be used further on for the strain variations) for the present formulation are

$$\hat{\boldsymbol{\epsilon}}(\boldsymbol{\xi}, \Gamma^e) = \underbrace{\sum_{a=1}^{4} \boldsymbol{B}_a(\boldsymbol{\xi}) \hat{\boldsymbol{d}}_a}_{\hat{\bar{\boldsymbol{\epsilon}}}^d} + \underbrace{\sum_{b=1}^{2} \widetilde{\boldsymbol{G}}_b(\boldsymbol{\xi}) \, \hat{\boldsymbol{\rho}}_b + \sum_{m=1}^{4} \widehat{\boldsymbol{G}}_m(\boldsymbol{\xi}, \Gamma^e) \hat{\alpha}_m}_{\hat{\bar{\boldsymbol{\epsilon}}}^\beta} \tag{4.95}$$

where $\hat{\bar{\boldsymbol{\epsilon}}}^d(\boldsymbol{\xi})$ are virtual strains due to virtual nodal displacements and $\hat{\bar{\boldsymbol{\epsilon}}}^\beta(\boldsymbol{\xi})$ are virtual strains due to all introduced additional parameters, i.e. incompatible displacements parameters and crack opening parameters. We note that the interpolation of real strains is different to the interpolation of virtual strains, in the spirit of Petrov-Galerkin approximation, which has been recognized as the most suitable for embedded-discontinuity finite elements.

4.3.2 Equilibrium equations

As mentioned above, the element equations, related to the stationary point of EAS-modified Hu-Washizu functional, are two. In the following they will be called equilibrium equations. The derivation of these two equations can be performed by performing the steps (i) to (iv) mentioned above. However, this derivation will be omitted here, see e.g. (Ibrahimbegovic, 2009). Only the results of the derivation (i.e. two equilibrium equations) will be presented and further elaborated.

The first element equilibrium equation can be written as

$$G^{int,e,1} - G^{ext,e} = 0, \tag{4.96}$$

where $G^{ext,e} = \sum_{a=1}^{4} \hat{\boldsymbol{d}}_a^T \boldsymbol{f}_a^{ext,e}$ can be seen as the virtual work of external loading acting on the element. It is related only to nodal virtual displacements and will not be further elaborated. Note that neither the incompatible displacement parameters nor the crack opening parameters contribute to the virtual work of external loading. The $G^{int,e,1}$ is defined as

$$G^{int,e,1} = t^e \int_{\Omega^e} \hat{\bar{\boldsymbol{\epsilon}}}^d \cdot \boldsymbol{C}\bar{\boldsymbol{\epsilon}}\, d\Omega, \tag{4.97}$$

where $\hat{\bar{\boldsymbol{\epsilon}}}^d$ and $\bar{\boldsymbol{\epsilon}}$ are given in (4.94) and (4.95), respectively. The quadrilateral, which is under derivation in Section 4.3, will be suitable for analysis of both plane stress and plane strain problems. Thus, $\boldsymbol{C}$ in (4.97) can be either in plane stress or plane strain form. For the plane stress, $\boldsymbol{C}$ is given in (4.77), and for the plane strain, $\boldsymbol{C}$ is

$$\boldsymbol{C} = \frac{E}{(1+\nu)(1-2\nu)} \begin{bmatrix} 1-\nu & \nu & 0 \\ \nu & 1-\nu & 0 \\ 0 & 0 & \dfrac{1-2\nu}{2} \end{bmatrix} \tag{4.98}$$

With (4.94) and (4.95), equation (4.97) can be rewritten as

$$G^{int,e,1} = t^e \int_{\Omega^e} \left(\sum_{a=1}^{4} \boldsymbol{B}_a \hat{\boldsymbol{d}}_a \right)^T \boldsymbol{C} \left(\sum_{c=1}^{4} \boldsymbol{B}_c \boldsymbol{d}_c + \sum_{b=1}^{2} \widetilde{\boldsymbol{G}}_b \boldsymbol{\rho}_b + \sum_{m=1}^{4} \overline{\boldsymbol{G}}_m \alpha_m \right) d\Omega \tag{4.99}$$

and yet as

$$G^{int,e,1} = \sum_{a=1}^{4} \hat{\boldsymbol{d}}_a^T \boldsymbol{f}_a^{int,e,1} \tag{4.100}$$

where

$$\boldsymbol{f}_a^{int,e,1} = t^e \int_{\Omega^e} \boldsymbol{B}_a^T \boldsymbol{C} \left(\sum_{c=1}^{4} \boldsymbol{B}_c \boldsymbol{d}_c + \sum_{b=1}^{2} \widetilde{\boldsymbol{G}}_b \boldsymbol{\rho}_b + \sum_{m=1}^{4} \overline{\boldsymbol{G}}_m \alpha_m \right) d\Omega \tag{4.101}$$

With the above, one can make element-by-element mesh-assembly of equation (4.96) for discretized 2d solid with N_e elements. The assembly produces the global set of equations

$$\mathbb{A}_{e=1}^{N_e} \underbrace{\left(\boldsymbol{f}^{int,e,1} - \boldsymbol{f}^{ext,e} \right)}_{\boldsymbol{R}_d^e} = \boldsymbol{0} \tag{4.102}$$

where $\boldsymbol{f}^{int,e,1} = \left[\boldsymbol{f}_a^{int,e,1,T} \right]^T$, $\boldsymbol{f}^{ext,e} = \left[\boldsymbol{f}_a^{ext,e,T} \right]^T$, and $\mathbb{A}$ is the finite element assembly operator that also takes into account displacement boundary conditions.

Let us now turn to the second element equilibrium equation, which is defined as

$$G^{int,e,2} = t^e \int_{\Omega^e} \hat{\bar{\boldsymbol{\epsilon}}}^\beta \cdot \boldsymbol{C}\bar{\boldsymbol{\epsilon}}\, d\Omega = 0 \tag{4.103}$$

where $\hat{\bar{\boldsymbol{\epsilon}}}^\beta$ and $\bar{\boldsymbol{\epsilon}}$ are given in (4.94) and (4.95), respectively. With (4.94), (4.95) and decomposition (4.33), equation (4.103) can be rewritten as

$$G^{int,e,2} = t^e \int_{\Omega^e} \left(\sum_{b=1}^{2} \widetilde{\boldsymbol{G}}_b \, \widehat{\boldsymbol{\rho}}_b + \sum_{m=1}^{4} \left(\overline{\widehat{\boldsymbol{G}}}_m + \overline{\overline{\widehat{\boldsymbol{G}}}}_m \right) \hat{\alpha}_m \right) \cdot \boldsymbol{C} \left(\sum_{c=1}^{4} \boldsymbol{B}_c \boldsymbol{d}_c + \sum_{b=1}^{2} \widetilde{\boldsymbol{G}}_b \, \boldsymbol{\rho}_b + \sum_{m=1}^{4} \overline{\boldsymbol{G}}_m \alpha_m \right) d\Omega = 0 \tag{4.104}$$

In the EAS-modified Hu Washizu functional, the stresses vanish from the formulation at step (iv). However, it is usually assumed that the element stresses $\boldsymbol{\sigma}(\boldsymbol{\xi})$ can be computed as

$$\boldsymbol{\sigma} = \underbrace{\boldsymbol{C} \left(\sum_{c=1}^{4} \boldsymbol{B}_c \boldsymbol{d}_c + \sum_{b=1}^{2} \widetilde{\boldsymbol{G}}_b \, \boldsymbol{\rho}_b + \sum_{m=1}^{4} \overline{\boldsymbol{G}}_m \alpha_m \right)}_{\boldsymbol{C}\bar{\boldsymbol{\epsilon}}} \tag{4.105}$$

With (4.105) in hand, equation (4.104) can be rewritten as

$$G^{int,e,2} = t^e \int_{\Omega^e} \left(\sum_{b=1}^{2} \widetilde{\boldsymbol{G}}_b \, \widehat{\boldsymbol{\rho}}_b + \sum_{m=1}^{4} \left(\overline{\widehat{\boldsymbol{G}}}_m + \overline{\overline{\widehat{\boldsymbol{G}}}}_m \right) \hat{\alpha}_m \right) \cdot \boldsymbol{\sigma} \, d\Omega = 0 \tag{4.106}$$

Note that $G^{int,e,1} + G^{int,e,2} = G^{ext,e}$, with $G^{int,e,1}$ from (4.97), $G^{int,e,2}$ from (4.103), and $\boldsymbol{\sigma} = \boldsymbol{C}\bar{\boldsymbol{\epsilon}}$, see (4.105), resembles the virtual work equation. By considering manipulations in Section 4.2.3.1, equation (4.106) yields the following four element equations

$$\underbrace{t^e \int_{\Omega^e} \overline{\widehat{\boldsymbol{G}}}_1^T \boldsymbol{\sigma} \, d\Omega + t^e \int_{\Gamma^e} t_n \, d\Gamma}_{h_1} = 0 \tag{4.107}$$

$$\underbrace{t^e \int_{\Omega^e} \overline{\widehat{\boldsymbol{G}}}_2^T \boldsymbol{\sigma} \, d\Omega + t^e \int_{\Gamma^e} t_n \xi_\Gamma \, d\Gamma}_{h_2} = 0 \tag{4.108}$$

$$\underbrace{t^e \int_{\Omega^e} \overline{\widehat{\boldsymbol{G}}}_3^T \boldsymbol{\sigma} \, d\Omega + t^e \int_{\Gamma^e} t_m \, d\Gamma}_{h_3} = 0 \tag{4.109}$$

$$\underbrace{t^e \int_{\Omega^e} \overline{\widehat{\boldsymbol{G}}}_4^T \boldsymbol{\sigma} \, d\Omega + t^e \int_{\Gamma^e} t_m \xi_\Gamma \, d\Gamma}_{h_4} = 0 \tag{4.110}$$

which are identical to (4.68)-(4.71), except that $\boldsymbol{\sigma}$ is now defined with (4.105). Moreover, equation (4.106) yields additional equations

$$\underbrace{t^e \int_{\Omega^e} \widetilde{\boldsymbol{G}}_b^T \boldsymbol{\sigma} \, d\Omega}_{\boldsymbol{R}_{\rho,b}} = \boldsymbol{0}, \qquad b = 1,2 \tag{4.111}$$

For the later use, we will collect (4.111) as

$$\boldsymbol{R}_\rho^e = \left[\boldsymbol{R}_{\rho,1}^T, \boldsymbol{R}_{\rho,2}^T \right]^T \tag{4.112}$$

4.4 Crack tracing

4.4.1 Criterion for crack embedding

The criterion for the crack embedding is based on the maximal principal stress. When the maximal principle element stress exceeds or equals the material tension strength

$$\sigma_1 \geq \sigma_{un} \tag{4.113}$$

the crack is embedded. The σ_1 is computed as

$$\sigma_1 = \mathrm{Max}\left[\sigma_{p1}, \sigma_{p2}\right] \quad , \quad \sigma_{p1/p2} = \frac{\bar{\sigma}_{xx} + \bar{\sigma}_{yy}}{2} \pm \sqrt{\left(\frac{\bar{\sigma}_{xx} - \bar{\sigma}_{yy}}{2}\right)^2 + \left(\bar{\sigma}_{xy}\right)^2} \tag{4.114}$$

where $\bar{\sigma}_{xx}$, $\bar{\sigma}_{yy}$ and $\bar{\sigma}_{xy}$ are the components of the average stress vector $\bar{\boldsymbol{\sigma}}$ in the element's center. The average stress vector $\bar{\boldsymbol{\sigma}}$ is computed as

$$\bar{\boldsymbol{\sigma}} = \left[\bar{\sigma}_{xx}, \bar{\sigma}_{yy}, \bar{\sigma}_{xy}\right]^T = \frac{1}{4} \sum_{bip=1}^{4} \boldsymbol{\sigma}|_{bip} \, , \tag{4.115}$$

where $\boldsymbol{\sigma}|_{bip}$ is the stress state in the corresponding bulk integration point bip.

4.4.2 Crack tracing algorithm

The most straightforward strategy to analyse cracking in a 2d solid is to allow each element of the mesh to develop a crack when the crack embedment criterion (4.113) is fulfilled for that element. Unfortunately, such a strategy does not provide reasonable results as illustrated by numerical examples in Section 6.

The second possibility is to use a crack tracing algorithm, which traces one crack in a predefined domain of the mesh. With this algorithm, only the crack-front element is allowed to develop a crack. The crack-front element is the element at which edge the crack stopped, see Figure 4.5.

The crack tracing algorithm used in this work is presented in Figure 4.6. The algorithm changes crack configuration within the solution increment $[\tau_n, \tau_{n+1}]$, until the stress state in the crack-front element indicates no need for crack embedding in that element. For each change of crack configuration during the solution increment, the current pseudo-time point is re-computed with the rest of the data taken from the beginning of the solution increment τ_n. Thus, one, two, three or even more crack-front elements can develop a crack in single solution increment $[\tau_n, \tau_{n+1}]$.

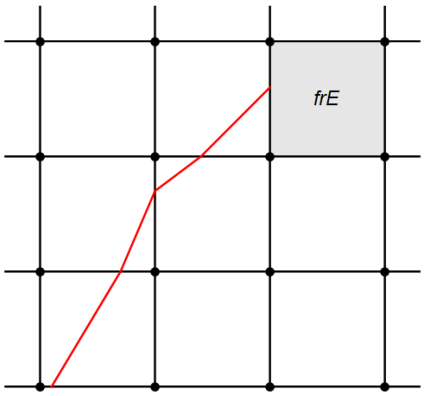

Figure 4.5: The crack-front element frE.

Slika 4.5: Prednji končni element frE, v katerem se bo aktivirala razpoka.

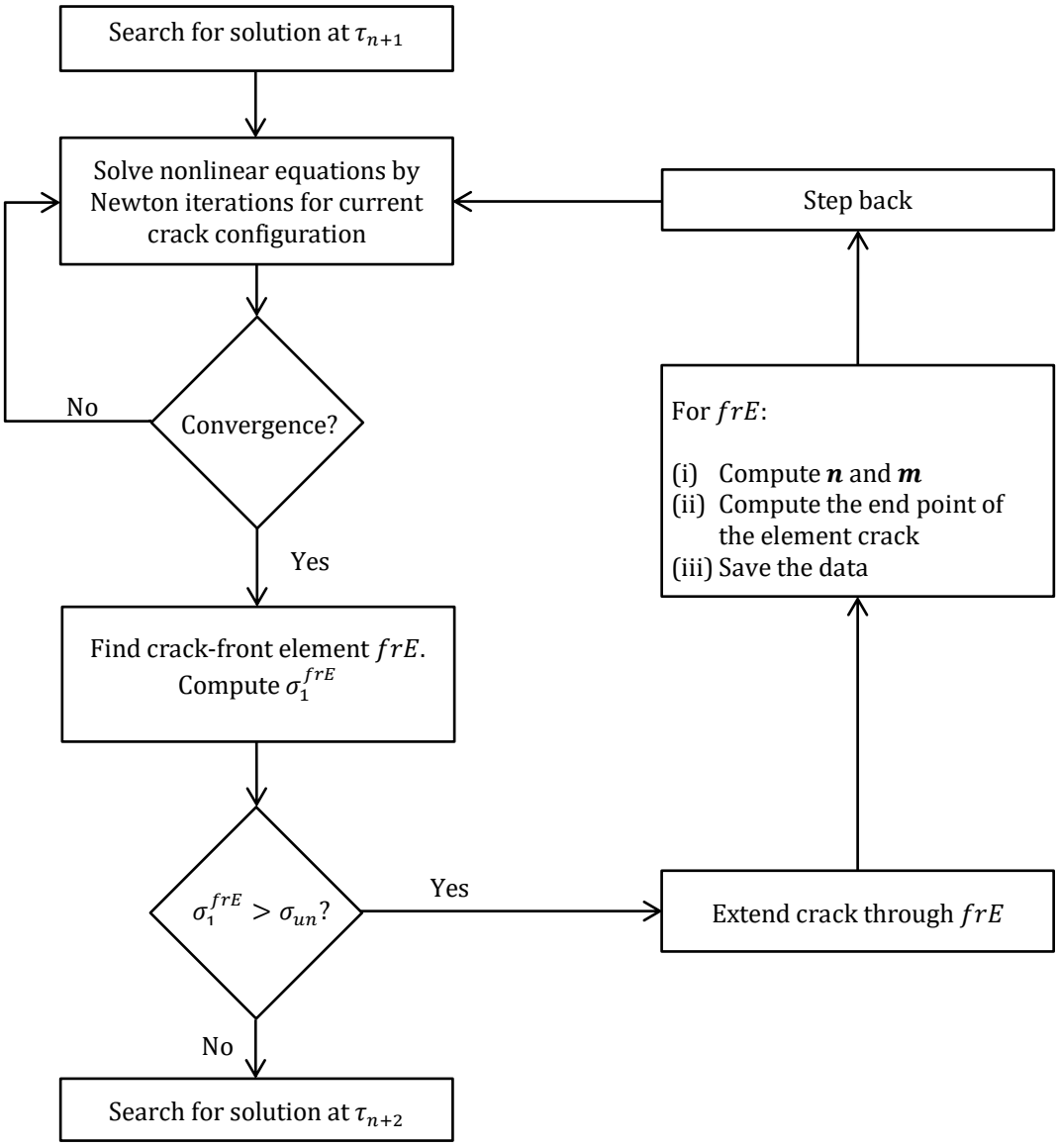

Figure 4.6: Crack tracing algorithm.

Slika 4.6: Algoritem sledenja razpoki.

4.5 Computational procedures

In this section, the solution of nonlinear equations is presented. The solution is searched at discrete pseudo-time points $0, \tau_1, \cdots, \tau_n, \tau_{n+1}, \cdots, T$. Either the standard incremental-iterative Newton method or the path-following method is used to that end. In both cases the linearization of nonlinear equations is needed.

Let us illustrate below the iteration i when searching for the solution at pseudo-time point τ_{n+1} in the framework of Newton method.

4.5.1 Solution of equations for Q4 embedded-discontinuity formulation

When there is no crack in the mesh of N_e elements, the following system of equations needs to be solved for iterative nodal displacements

$$\mathbb{A}_{e=1}^{N_e}\left(\boldsymbol{K}_{dd,n+1}^{e,i}\Delta\boldsymbol{d}_{n+1}^{e,i}\right) = \mathbb{A}_{e=1}^{N_e}\left(-\boldsymbol{R}_{d,n+1}^{e,i}\right) \tag{4.116}$$

where

$$\boldsymbol{K}_{dd,n+1}^{e,i} = \left.\frac{\partial \boldsymbol{R}_d^e}{\partial \boldsymbol{d}^e}\right|_{n+1}^{i}, \qquad \boldsymbol{R}_{d,n+1}^{e,i} = \left(\boldsymbol{f}^{int,e} - \boldsymbol{f}^{ext,e}\right)_{n+1}^{i} \tag{4.117}$$

and $\boldsymbol{d}^e = \left[\boldsymbol{d}_a^{e,T}\right]^T$. The $\boldsymbol{R}_d^e$ is the one from (4.53) with $\alpha_m = 0$. The solution of (4.116) for $\Delta\boldsymbol{d}_{n+1}^{e,i}$ is used to get iterative value of element total displacements as

$$\boldsymbol{d}_{n+1}^{e,i} = \boldsymbol{d}_{n+1}^{e,i-1} + \Delta\boldsymbol{d}_{n+1}^{e,i} \tag{4.118}$$

If the convergence tolerance is reached, (4.118) are indeed element displacements at τ_{n+1}, and the solution procedure can switch to computation of solution at pseudo-time point τ_{n+2}. If the convergence tolerance is not reached, another iteration is performed by setting $i + 1 \rightarrow i$.

When there are one or more elements with the crack in the mesh, the following system of equations needs to be solved for iterative nodal displacements

$$\mathbb{A}_{e=1}^{N_e}\left(\boldsymbol{K}_{cond,n+1}^{e,i}\Delta\boldsymbol{d}_{n+1}^{e,i}\right) = \mathbb{A}_{e=1}^{N_e}\left(-\boldsymbol{R}_{cond,n+1}^{e,i}\right) \tag{4.119}$$

For the elements without crack

$$\boldsymbol{K}_{cond,n+1}^{e,i} = \boldsymbol{K}_{dd,n+1}^{e,i}, \quad \boldsymbol{R}_{cond,n+1}^{e,i} = \boldsymbol{R}_{d,n+1}^{e,i} \tag{4.120}$$

where $\boldsymbol{K}_{dd,n+1}^{e,i}$ and $\boldsymbol{R}_{d,n+1}^{e,i}$ are defined in (4.117). For the element with a crack, static condensation of the following element system of equations is performed

$$\begin{bmatrix} \boldsymbol{K}_{dd}^{e} & \boldsymbol{K}_{d\alpha}^{e} \\ \boldsymbol{K}_{\alpha d}^{e} & \boldsymbol{K}_{\alpha\alpha}^{e} \end{bmatrix}_{n+1}^{i} \begin{Bmatrix} \Delta \boldsymbol{d}_{n+1}^{e,i} \\ \Delta \boldsymbol{\alpha}_{n+1}^{e,i} \end{Bmatrix} = \begin{Bmatrix} -\boldsymbol{R}_{d,n+1}^{e,i} \\ -\boldsymbol{h}_{n+1}^{e,i} \end{Bmatrix} \tag{4.121}$$

where $\boldsymbol{K}_{dd,n+1}^{e,i}$ remains as in (4.117), and

$$\begin{aligned} &\boldsymbol{K}_{d\alpha,n+1}^{e,i} = \left.\frac{\partial \boldsymbol{R}_{d}^{e}}{\partial \boldsymbol{\alpha}^{e}}\right|_{n+1}^{i}, \qquad \boldsymbol{K}_{\alpha d,n+1}^{e,i} = \left.\frac{\partial \boldsymbol{h}^{e}}{\partial \boldsymbol{d}^{e}}\right|_{n+1}^{i}, \\ &\boldsymbol{K}_{\alpha\alpha,n+1}^{e,i} = \left.\frac{\partial \boldsymbol{h}^{e}}{\partial \boldsymbol{\alpha}^{e}}\right|_{n+1}^{i}, \qquad \boldsymbol{\alpha}^{e} = [\alpha_1, \alpha_2, \alpha_3, \alpha_4]^T \end{aligned} \tag{4.122}$$

The $\boldsymbol{R}_{d}^{e}$ is the one from (4.53), and

$$\boldsymbol{h}_{n+1}^{e,i} = [h_1, h_2, h_3, h_4]^T|_{n+1}^{i} \tag{4.123}$$

with expressions $h_m, m = 1, \cdots, 4$, given in (4.68)-(4.71). The opening parameters will be condensed in the following way. From the second equation in (4.121), one can express $\Delta \boldsymbol{\alpha}_{n+1}^{e,i}$ in terms of $\Delta \boldsymbol{d}_{n+1}^{e,i}$ as

$$\Delta \boldsymbol{\alpha}_{n+1}^{e,i} = -\left[\boldsymbol{K}_{\alpha\alpha,n+1}^{e,i}\right]^{-1}\left(-\boldsymbol{h}_{\alpha,n+1}^{e,i} - \boldsymbol{K}_{\alpha d,n+1}^{e,i}\, \Delta \boldsymbol{d}_{n+1}^{e,i}\right) \tag{4.124}$$

By inserting this relation in the first element equation in (4.121), one gets

$$\boldsymbol{K}_{cond,n+1}^{e,i} \Delta \boldsymbol{d}_{n+1}^{e,i} = -\boldsymbol{R}_{cond,n+1}^{e,i} \tag{4.125}$$

where

$$\boldsymbol{K}_{cond,n+1}^{e,i} = \boldsymbol{K}_{dd,n+1}^{e,i} - \boldsymbol{K}_{d\alpha,n+1}^{e,i}\left[\boldsymbol{K}_{\alpha\alpha,n+1}^{e,i}\right]^{-1} \boldsymbol{K}_{\alpha d,n+1}^{e,i} \tag{4.126}$$

and

$$\boldsymbol{R}_{cond,n+1}^{e,i} = \boldsymbol{R}_{d,n+1}^{e,i} - \boldsymbol{K}_{d\alpha,n+1}^{e,i}\left[\boldsymbol{K}_{\alpha\alpha,n+1}^{e,i}\right]^{-1} \boldsymbol{h}_{n+1}^{e,i} \tag{4.127}$$

Thus, for the element with the crack, (4.126) and (4.127) enter (4.119). The solution of the system of equations (4.119) for $\Delta \boldsymbol{d}_{n+1}^{e,i}$ and element-by-element post-computation of (4.124) to get $\Delta \boldsymbol{\alpha}_{n+1}^{e,i}$, for $e = 1, \cdots, N^e$, provide new iterative values of element total displacements and opening parameters

$$\boldsymbol{d}_{n+1}^{e,i} = \boldsymbol{d}_{n+1}^{e,i-1} + \Delta \boldsymbol{d}_{n+1}^{e,i}, \quad \boldsymbol{\alpha}_{n+1}^{e,i} = \boldsymbol{\alpha}_{n+1}^{e,i-1} + \Delta \boldsymbol{\alpha}_{n+1}^{e,i} \tag{4.128}$$

If the convergence tolerance is reached, (4.128) are indeed element nodal displacements and crack parameters at τ_{n+1}, and the solution procedure will switch to computation of solution at pseudo-time point τ_{n+2}. If the convergence tolerance is not reached, another iteration will be performed by setting $i + 1 \rightarrow i$.

4.5.2 Solution of equations for Q6 embedded-discontinuity formulation

When there is no crack in the mesh of N_e elements, the following system of equations needs to be solved for iterative nodal displacements and iterative incompatible parameters

$$\mathbb{A}_{e=1}^{N_e}\left(\begin{bmatrix}\boldsymbol{K}_{dd}^{e} & \boldsymbol{K}_{d\rho}^{e}\\ \boldsymbol{K}_{\rho d}^{e} & \boldsymbol{K}_{\rho\rho}^{e}\end{bmatrix}_{n+1}^{i}\begin{Bmatrix}\Delta\boldsymbol{d}_{n+1}^{e,i}\\ \Delta\boldsymbol{\rho}_{n+1}^{e,i}\end{Bmatrix}\right)=\mathbb{A}_{e=1}^{N_e}\left(\begin{Bmatrix}-\boldsymbol{R}_{d,n+1}^{e,i}\\ -\boldsymbol{R}_{\rho,n+1}^{e,i}\end{Bmatrix}\right) \tag{4.129}$$

where

$$\begin{aligned}\boldsymbol{K}_{dd,n+1}^{e,i}&=\left.\frac{\partial\boldsymbol{R}_{d}^{e}}{\partial\boldsymbol{d}^{e}}\right|_{n+1}^{i}, \qquad \boldsymbol{K}_{d\rho,n+1}^{e,i}=\left.\frac{\partial\boldsymbol{R}_{d}^{e}}{\partial\boldsymbol{\rho}^{e}}\right|_{n+1}^{i},\\ \boldsymbol{K}_{\rho d,n+1}^{e,i}&=\left.\frac{\partial\boldsymbol{R}_{\rho}^{e}}{\partial\boldsymbol{d}^{e}}\right|_{n+1}^{i}, \qquad \boldsymbol{K}_{\rho\rho,n+1}^{e,i}=\left.\frac{\partial\boldsymbol{R}_{\rho}^{e}}{\partial\boldsymbol{\rho}^{e}}\right|_{n+1}^{i}\end{aligned} \tag{4.130}$$

and $\boldsymbol{\rho}^{e}=[\rho_{11},\rho_{12},\rho_{21},\rho_{22}]^{T}$. The $\boldsymbol{R}_{d}^{e}$ and $\boldsymbol{R}_{\rho}^{e}$ are those from (4.102) and (4.112), respectively, with $\alpha_m=0$. The system (4.129) simplifies, because the static condensation of incompatible modes parameters is performed on the element level. The following relations are obtained for an element

$$\Delta\boldsymbol{\rho}_{n+1}^{e,i}=-\left[\boldsymbol{K}_{\rho\rho,n+1}^{e,i}\right]^{-1}\left(-\boldsymbol{R}_{\rho,n+1}^{e,i}-\boldsymbol{K}_{\rho d,n+1}^{e,i}\Delta\boldsymbol{d}_{n+1}^{e,i}\right) \tag{4.131}$$

and

$$\begin{aligned}\boldsymbol{K}_{cond,n+1}^{e,i}&=\boldsymbol{K}_{dd,n+1}^{e,i}-\boldsymbol{K}_{d\rho,n+1}^{e,i}\left[\boldsymbol{K}_{\rho\rho,n+1}^{e,i}\right]^{-1}\boldsymbol{K}_{\rho d,n+1}^{e,i}\\ \boldsymbol{R}_{cond,n+1}^{e,i}&=\boldsymbol{R}_{d,n+1}^{e,i}-\boldsymbol{K}_{d\rho,n+1}^{e,i}\left[\boldsymbol{K}_{\rho\rho,n+1}^{e,i}\right]^{-1}\boldsymbol{R}_{\rho,n+1}^{e,i}\end{aligned} \tag{4.132}$$

Due to element-wise static condensation of incompatible modes parameters, the system of equations (4.129) is replaced by

$$\mathbb{A}_{e=1}^{N_e}\left(\boldsymbol{K}_{cond,n+1}^{e,i}\Delta\boldsymbol{d}_{n+1}^{e,i}\right)=\mathbb{A}_{e=1}^{N_e}\left(-\boldsymbol{R}_{cond,n+1}^{e,i}\right) \tag{4.133}$$

and (4.131). After solving (4.133) for $\Delta\boldsymbol{d}_{n+1}^{e,i}$, and performing post-computation of $\Delta\boldsymbol{\rho}_{n+1}^{e,i}$ with (4.131) for $e=1,\cdots,N^{e}$, new iterative values of element total displacements and incompatible modes parameters can be obtained as

$$\boldsymbol{d}_{n+1}^{e,i}=\boldsymbol{d}_{n+1}^{e,i-1}+\Delta\boldsymbol{d}_{n+1}^{e,i}, \qquad \boldsymbol{\rho}_{n+1}^{e,i}=\boldsymbol{\rho}_{n+1}^{e,i-1}+\Delta\boldsymbol{\rho}_{n+1}^{e,i} \tag{4.134}$$

If the convergence tolerance is reached, (4.134) are indeed element nodal displacements and incompatible modes parameters at τ_{n+1}, and the solution procedure will switch to computation of solution at pseudo-time point τ_{n+2}. If the convergence tolerance is not reached, another iteration will be performed by setting $i+1\rightarrow i$.

When there are one or more elements with the crack in the mesh, the following system of equations needs to be solved for iterative nodal displacements

$$\mathbb{A}_{e=1}^{N_e}\left(\boldsymbol{K}_{cond,n+1}^{e,i}\Delta\boldsymbol{d}_{n+1}^{e,i}\right)=\mathbb{A}_{e=1}^{N_e}\left(-\boldsymbol{R}_{cond,n+1}^{e,i}\right) \tag{4.135}$$

For element with no crack, $\boldsymbol{K}_{cond,n+1}^{e,i}$ and $\boldsymbol{R}_{cond,n+1}^{e,i}$ contributions are those from (4.132). For element with the crack, they are obtained by performing static condensation of the incompatible mode parameters as well as of the crack opening parameters. The following element equations are considered

$$\begin{bmatrix}\boldsymbol{K}_{dd}^{e} & \boldsymbol{K}_{d\rho}^{e} & \boldsymbol{K}_{d\alpha}^{e}\\ \boldsymbol{K}_{\rho d}^{e} & \boldsymbol{K}_{\rho\rho}^{e} & \boldsymbol{K}_{\rho\alpha}^{e}\\ \boldsymbol{K}_{\alpha d}^{e} & \boldsymbol{K}_{\alpha\rho}^{e} & \boldsymbol{K}_{\alpha\alpha}^{e}\end{bmatrix}_{n+1}^{i}\begin{Bmatrix}\Delta\boldsymbol{d}_{n+1}^{e,i}\\ \Delta\boldsymbol{\rho}_{n+1}^{e,i}\\ \Delta\boldsymbol{\alpha}_{n+1}^{e,i}\end{Bmatrix}=\begin{Bmatrix}-\boldsymbol{R}_{d,n+1}^{e,i}\\ -\boldsymbol{R}_{\rho,n+1}^{e,i}\\ -\boldsymbol{h}_{n+1}^{e,i}\end{Bmatrix} \tag{4.136}$$

where some of the terms are already defined in (4.130), and

$$\begin{aligned}&\boldsymbol{K}_{d\alpha,n+1}^{e,i}=\left.\frac{\partial\boldsymbol{R}_{d}^{e}}{\partial\boldsymbol{\alpha}^{e}}\right|_{n+1}^{i},\qquad \boldsymbol{K}_{\rho\alpha,n+1}^{e,i}=\left.\frac{\partial\boldsymbol{R}_{\rho}^{e}}{\partial\boldsymbol{\alpha}^{e}}\right|_{n+1}^{i}\\ &\boldsymbol{K}_{\alpha d,n+1}^{e,i}=\left.\frac{\partial\boldsymbol{h}^{e}}{\partial\boldsymbol{d}^{e}}\right|_{n+1}^{i},\qquad \boldsymbol{K}_{\alpha\rho,n+1}^{e,i}=\left.\frac{\partial\boldsymbol{h}^{e}}{\partial\boldsymbol{\rho}^{e}}\right|_{n+1}^{i},\qquad \boldsymbol{K}_{\alpha\alpha,n+1}^{e,i}=\left.\frac{\partial\boldsymbol{h}^{e}}{\partial\boldsymbol{\alpha}^{e}}\right|_{n+1}^{i}\end{aligned} \tag{4.137}$$

The $\boldsymbol{R}_{d}^{e}$ and $\boldsymbol{R}_{\rho}^{e}$ are given in (4.102) and (4.112), respectively, and $h_m, m=1,\cdots,4$, in $\boldsymbol{h}_{n+1}^{e,i}=[h_1,h_2,h_3,h_4]^T|_{n+1}^{i}$ are given in (4.107)-(4.110). For the sake of brevity, let us rewrite (4.136) as

$$\begin{bmatrix}\boldsymbol{K}_{dd}^{e} & \boldsymbol{K}_{d\beta}^{e}\\ \boldsymbol{K}_{\beta d}^{e} & \boldsymbol{K}_{\beta\beta}^{e}\end{bmatrix}_{n+1}^{i}\begin{Bmatrix}\Delta\boldsymbol{d}_{n+1}^{e,i}\\ \Delta\boldsymbol{\beta}_{n+1}^{e,i}\end{Bmatrix}=-\begin{Bmatrix}\boldsymbol{R}_{d,n+1}^{e,i}\\ \boldsymbol{R}_{\beta,n+1}^{e,i}\end{Bmatrix} \tag{4.138}$$

where

$$\boldsymbol{K}_{\beta\beta,n+1}^{e,i}=\begin{bmatrix}\boldsymbol{K}_{\rho\rho}^{e} & \boldsymbol{K}_{\rho\alpha}^{e}\\ \boldsymbol{K}_{\alpha\rho}^{e} & \boldsymbol{K}_{\alpha\alpha}^{e}\end{bmatrix}_{n+1}^{i}\qquad \boldsymbol{K}_{d\beta,n+1}^{e,i}=\begin{bmatrix}\boldsymbol{K}_{d\rho}^{e} & \boldsymbol{K}_{d\alpha}^{e}\end{bmatrix}_{n+1}^{i}\qquad \boldsymbol{K}_{\beta d,n+1}^{e,i}=\begin{bmatrix}\boldsymbol{K}_{\rho d}^{e}\\ \boldsymbol{K}_{\alpha d}^{e}\end{bmatrix}_{n+1}^{i}$$

and

$$\Delta\boldsymbol{\beta}_{n+1}^{e,i}=\begin{Bmatrix}\Delta\boldsymbol{\rho}_{n+1}^{e,i}\\ \Delta\boldsymbol{\alpha}_{n+1}^{e,i}\end{Bmatrix}\qquad \boldsymbol{R}_{\beta,n+1}^{e,i}=\begin{Bmatrix}\boldsymbol{R}_{\rho,n+1}^{e,i}\\ \boldsymbol{h}_{n+1}^{e,i}\end{Bmatrix}$$

The static condensation of (4.138) yields the following equations

$$\Delta\boldsymbol{\beta}_{n+1}^{e,i}=-\left[\boldsymbol{K}_{\beta\beta,n+1}^{e,i}\right]^{-1}\left(-\boldsymbol{R}_{\beta,n+1}^{e,i}-\boldsymbol{K}_{\beta d,n+1}^{e,i}\Delta\boldsymbol{d}_{n+1}^{e,i}\right) \tag{4.139}$$

and

$$\begin{aligned}\boldsymbol{K}_{cond,n+1}^{e,i}&=\boldsymbol{K}_{dd,n+1}^{e,i}-\boldsymbol{K}_{d\beta,n+1}^{e,i}\left[\boldsymbol{K}_{\beta\beta,n+1}^{e,i}\right]^{-1}\boldsymbol{K}_{\beta d,n+1}^{e,i}\\ \boldsymbol{R}_{cond,n+1}^{e,i}&=\boldsymbol{R}_{d,n+1}^{e,i}-\boldsymbol{K}_{d\beta,n+1}^{e,i}\left[\boldsymbol{K}_{\beta\beta,n+1}^{e,i}\right]^{-1}\boldsymbol{R}_{\beta,n+1}^{e,i}\end{aligned} \tag{4.140}$$

For element with the crack, (4.140) are used in (4.135). By solving (4.135) for $\Delta \boldsymbol{d}_{n+1}^{e,i}$ and by performing post-computations (4.139) to get $\Delta \boldsymbol{\rho}_{n+1}^{e,i}$ and $\Delta \boldsymbol{\alpha}_{n+1}^{e,i}$, new iterative value of element total displacements, incompatible modes parameters, and opening parameters can be obtained

$$\boldsymbol{d}_{n+1}^{e,i} = \boldsymbol{d}_{n+1}^{e,i-1} + \Delta \boldsymbol{d}_{n+1}^{e,i}, \;\; \boldsymbol{\rho}_{n+1}^{e,i} = \boldsymbol{\rho}_{n+1}^{e,i-1} + \Delta \boldsymbol{\rho}_{n+1}^{e,i}, \;\; \boldsymbol{\alpha}_{n+1}^{e,i} = \boldsymbol{\alpha}_{n+1}^{e,i-1} + \Delta \boldsymbol{\alpha}_{n+1}^{e,i} \tag{4.141}$$

If the convergence tolerance is reached, (4.141) are indeed element nodal displacements, incompatible modes parameters and crack opening parameters at τ_{n+1}, and the solution procedure will switch to computation of solution at pseudo-time point τ_{n+2}. If the convergence tolerance is not reached, another iteration will be performed by setting $i + 1 \rightarrow i$.

4.5.3 Tangent operator for cohesion

In order to compute $\boldsymbol{K}_{\alpha\alpha,n+1}^{e,i} = \left.\frac{\partial \boldsymbol{h}^e}{\partial \boldsymbol{\alpha}^e}\right|_{n+1}^{i}$, which is part of the set of equations, see (4.121) and (4.136), one needs to derive

$$\left.\frac{\partial \boldsymbol{t}}{\partial \boldsymbol{\alpha}}\right|_{n+1}^{i} = \left.\frac{\partial \boldsymbol{t}}{\partial \bar{\bar{\boldsymbol{u}}}} \frac{\partial \bar{\bar{\boldsymbol{u}}}}{\partial \boldsymbol{\alpha}}\right|_{n+1}^{i} \tag{4.142}$$

where $\boldsymbol{t} = [t_n, t_m]^T$ is the vector of traction stresses and $\boldsymbol{\alpha} = [\alpha_1, \alpha_2, \alpha_3, \alpha_4]^{\boldsymbol{T}}$ is the vector of parameters associated with the crack separation modes (see Figure 4.3). Jump in displacements $\bar{\bar{\boldsymbol{u}}} = [\bar{\bar{u}}, \bar{\bar{v}}]^T$ has two components: $\bar{\bar{u}} = \bar{\bar{u}}(\xi_\Gamma) = \alpha_1 + \xi_\Gamma \alpha_2$ and $\bar{\bar{v}} = \bar{\bar{v}}(\xi_\Gamma) = \alpha_3 + \xi_\Gamma \alpha_4$.

We use two uncoupled-softening laws for $\bar{\bar{q}}_n(\bar{\bar{\xi}}_n)$ and $\bar{\bar{q}}_m(\bar{\bar{\xi}}_m)$, therefore the failure functions $\bar{\bar{\phi}}_n(\bar{\bar{t}}_n, \bar{\bar{q}}_n)$ and $\bar{\bar{\phi}}_m(\bar{\bar{t}}_m, \bar{\bar{q}}_m)$ (see (4.79), (4.87)) are independent. Now, we can split equation (4.142) into two parts as:

$$\left.\frac{\partial t_n}{\partial [\alpha_1, \alpha_2]}\right|_{n+1}^{i} = \left.\frac{\partial t_n}{\partial \bar{\bar{u}}} \frac{\partial \bar{\bar{u}}}{\partial [\alpha_1, \alpha_2]}\right|_{n+1}^{i} \tag{4.143}$$

$$\left.\frac{\partial t_m}{\partial [\alpha_3, \alpha_4]}\right|_{n+1}^{i} = \left.\frac{\partial t_m}{\partial \bar{\bar{v}}} \frac{\partial \bar{\bar{v}}}{\partial [\alpha_3, \alpha_4]}\right|_{n+1}^{i} \tag{4.144}$$

In (4.143) and (4.144) we apply $\left.\frac{\partial \bar{\bar{u}}}{\partial [\alpha_1, \alpha_2]}\right|_{n+1}^{i} = [1, \xi_\Gamma]^T$ and $\left.\frac{\partial \bar{\bar{v}}}{\partial [\alpha_3, \alpha_4]}\right|_{n+1}^{i} = [1, \xi_\Gamma]^T$. The terms $\left.\frac{\partial t_n}{\partial \bar{\bar{u}}}\right|_{n+1}^{i}$ and $\left.\frac{\partial t_m}{\partial \bar{\bar{v}}}\right|_{n+1}^{i}$ are obtained by using the chain rule:

$$\left.\frac{\partial \boldsymbol{t}}{\partial \bar{\bar{\boldsymbol{u}}}}\right|_{n+1}^{i} = \frac{\partial \boldsymbol{t}}{\partial \bar{\bar{\gamma}}} \otimes \left.\frac{\partial \bar{\bar{\gamma}}}{\partial \bar{\bar{\boldsymbol{u}}}}\right|_{n+1}^{i} \tag{4.145}$$

Equation (4.145) can be rewritten for both directions $\boldsymbol{n}$ and $\boldsymbol{m}$ separately:

$$\left.\frac{\partial t_n}{\partial \bar{\bar{u}}}\right|_{n+1}^{i} = \left.\frac{\partial t_n}{\partial \bar{\bar{\gamma}}_n} \cdot \frac{\partial \bar{\bar{\gamma}}_n}{\partial \bar{\bar{u}}}\right|_{n+1}^{i} \tag{4.146}$$

$$\left.\frac{\partial t_m}{\partial \bar{\bar{v}}}\right|_{n+1}^{i} = \left.\frac{\partial t_m}{\partial \bar{\bar{\gamma}}_m} \cdot \frac{\partial \bar{\bar{\gamma}}_m}{\partial \bar{\bar{v}}}\right|_{n+1}^{i} \tag{4.147}$$

The failure functions $\bar{\bar{\phi}}_n$ in normal direction $\boldsymbol{n}$ (4.79) and $\bar{\bar{\phi}}_m$ in tangential direction $\boldsymbol{m}$ (4.87) have similar forms. The failure function $\bar{\bar{\phi}}_m$ for Mode II contains the absolute value, for this reason we present the derivation of the corresponding tangent operator $\left.\frac{\partial t_m}{\partial \bar{\bar{v}}}\right|_{n+1}^{i}$. We bear in mind the following equations and relations (some of them are introduced in Section 4.2.5.2):

$$\bar{\bar{\phi}}_m\left(t_{m,n+1}^{i}, \bar{\bar{\xi}}_{m,n+1}^{i}\right) = \left|t_{m,n+1}^{i}\right| - \left(\sigma_{um} - \bar{\bar{q}}_m\left(\bar{\bar{\xi}}_{m,n+1}^{i}\right)\right) = 0 \tag{4.148}$$

$$t_{m,n+1}^{i} = \left.\frac{\partial \bar{\bar{v}}}{\partial \bar{\bar{Q}}_m}\right|_{n+1}^{i} \tag{4.149}$$

$$\bar{\bar{q}}_{m,n+1}^{i} = \bar{\bar{q}}_m\left(\bar{\bar{\xi}}_{m,n+1}^{i}\right) = \sigma_{um}\left(1 - e^{-\frac{\sigma_{um}}{G_{fm}}\bar{\bar{\xi}}_{m,n+1}^{i}}\right) \tag{4.150}$$

$$\bar{\bar{\xi}}_{m,n+1}^{i} = \bar{\bar{\xi}}_{m,n} + \bar{\bar{\gamma}}_{m,n+1}^{i} \tag{4.151}$$

$$\bar{\bar{Q}}_{m,n+1}^{i} = \bar{\bar{Q}}_{m,n} + \frac{\bar{\bar{\gamma}}_{m,n+1}^{i}}{\left|t_{m,n+1}^{i}\right|}\left(1 + \frac{\sigma_{um}}{G_{fm}}\,\bar{\bar{\xi}}_{m,n+1}^{i}\right) \tag{4.152}$$

The term $\left.\frac{\partial \bar{\bar{\gamma}}_m}{\partial \bar{\bar{v}}}\right|_{n+1}^{i}$ in (4.147) is obtained from the consistency conditions $\dot{\bar{\bar{\gamma}}}_m \dot{\bar{\bar{\phi}}}_m\Big|_{n+1}^{i} = 0$.

Since $\bar{\bar{\gamma}}_{m,n+1}^{i} = \dot{\bar{\bar{\gamma}}}_{m,n+1}^{i}(\tau_{n+1} - \tau_n) \neq 0$, one considers:

$$\dot{\bar{\bar{\phi}}}_{m,n+1}^{i} = \left[\frac{\partial \bar{\bar{\phi}}_m}{\partial t_m} \cdot \frac{\partial t_m}{\partial \bar{\bar{v}}} + \frac{\partial \bar{\bar{\phi}}_m}{\partial \bar{\bar{q}}_m} \cdot \frac{\partial \bar{\bar{q}}_m}{\partial \bar{\bar{\gamma}}_m} \cdot \frac{\partial \bar{\bar{\gamma}}_m}{\partial \bar{\bar{v}}}\right]_{n+1}^{i} \dot{\bar{\bar{v}}}_{n+1}^{i} = 0 \tag{4.153}$$

Since $\dot{\bar{\bar{v}}}_{n+1}^{i} \neq 0$, we solve first part of $\dot{\bar{\bar{\phi}}}_{m,n+1}^{i} = 0$ for unknown $\left.\frac{\partial \bar{\bar{\gamma}}_m}{\partial \bar{\bar{v}}}\right|_{n+1}^{i}$.

Using the (4.148)-(4.152), we get the following relations:

$$\left.\frac{\partial \bar{\bar{\phi}}_m}{\partial t_m}\right|_{n+1}^{i} = sign\left[t_{m,n+1}^{i}\right], \quad \left.\frac{\partial \bar{\bar{\phi}}_m}{\partial \bar{\bar{q}}_m}\right|_{n+1}^{i} = 1 \tag{4.154}$$

$$\left.\frac{\partial t_m}{\partial \bar{\bar{v}}}\right|_{n+1}^{i} = \left.\frac{\partial}{\partial \bar{\bar{v}}}\left[\frac{\bar{\bar{v}}}{\bar{\bar{Q}}_m}\right]\right|_{n+1}^{i} = \left[\left(\bar{\bar{Q}}_m\right)^{-1} + \bar{\bar{v}} \cdot \frac{\partial\left(\bar{\bar{Q}}_m\right)^{-1}}{\partial \bar{\bar{\gamma}}_m} \cdot \frac{\partial \bar{\bar{\gamma}}_m}{\partial \bar{\bar{v}}}\right]_{n+1}^{i} \tag{4.155}$$

Using (4.154) and (4.155), the first part of the (4.153) can be rewritten as:

$$\left[\frac{\partial\bar{\bar{\phi}}_m}{\partial t_m}\cdot\frac{\partial t_m}{\partial\bar{\bar{v}}}+\frac{\partial\bar{\bar{\phi}}_m}{\partial\bar{\bar{q}}_m}\cdot\frac{\partial\bar{\bar{q}}_m}{\partial\bar{\bar{\gamma}}_m}\cdot\frac{\partial\bar{\bar{\gamma}}_m}{\partial\bar{\bar{v}}}\right]_{n+1}^{i}=0 \tag{4.156}$$

$$\left[sign[t_m]\left(\left(\bar{\bar{Q}}_m\right)^{-1}+\bar{\bar{v}}\cdot\frac{\partial\left(\bar{\bar{Q}}_m\right)^{-1}}{\partial\bar{\bar{\gamma}}_m}\cdot\frac{\partial\bar{\bar{\gamma}}_m}{\partial\bar{\bar{v}}}\right)+\frac{\partial\bar{\bar{q}}_m}{\partial\bar{\bar{\gamma}}_m}\cdot\frac{\partial\bar{\bar{\gamma}}_m}{\partial\bar{\bar{v}}}\right]_{n+1}^{i}=0 \tag{4.157}$$

We can express $\left.\frac{\partial\bar{\bar{\gamma}}_m}{\partial\bar{\bar{v}}}\right|_{n+1}^{i}$ from (4.157):

$$\left.\frac{\partial\bar{\bar{\gamma}}_m}{\partial\bar{\bar{v}}}\right|_{n+1}^{i}=\left[\frac{-sign[t_m]\left(\bar{\bar{Q}}_m\right)^{-1}}{sign[t_m]\cdot\bar{\bar{v}}\cdot\frac{\partial\left(\bar{\bar{Q}}_m\right)^{-1}}{\partial\bar{\bar{\gamma}}_m}+\frac{\partial\bar{\bar{q}}_m}{\partial\bar{\bar{\gamma}}_m}}\right]_{n+1}^{i} \tag{4.158}$$

Further, we need to develop the term $\left.\frac{\partial t_m}{\partial\bar{\bar{\gamma}}_m}\right|_{n+1}^{i}$:

$$\left.\frac{\partial t_m}{\partial\bar{\bar{\gamma}}_m}\right|_{n+1}^{i}=\frac{\partial}{\partial\bar{\bar{\gamma}}_{m,n+1}^{i}}\left[sign\left[t_{m,n+1}^{i}\right]\cdot\left(\sigma_{um}-\bar{\bar{q}}_{m,n+1}^{i}\right)\right]=-sign\left[t_{m,n+1}^{i}\right]\cdot\frac{\partial\bar{\bar{q}}_{m,n+1}^{i}}{\partial\bar{\bar{\gamma}}_{m,n+1}^{i}} \tag{4.159}$$

Finally, using the expressions (4.158) and (4.159), the tangent operator $\left.\frac{\partial t_m}{\partial\bar{\bar{v}}}\right|_{n+1}^{i}$ for loading softening phase in tangent direction is:

$$\left.\frac{\partial t_m}{\partial\bar{\bar{v}}}\right|_{n+1}^{i}=\frac{\partial t_m}{\partial\bar{\bar{\gamma}}_m}\cdot\left.\frac{\partial\bar{\bar{\gamma}}_m}{\partial\bar{\bar{v}}}\right|_{n+1}^{i}=\left[\frac{\frac{\partial\bar{\bar{q}}_m}{\partial\bar{\bar{\gamma}}_m}}{\bar{\bar{Q}}_m\cdot\left(sign\left[t_{m,n+1}^{i}\right]\cdot\bar{\bar{v}}\cdot\frac{\partial\left(\bar{\bar{Q}}_m\right)^{-1}}{\partial\bar{\bar{\gamma}}_m}+\frac{\partial\bar{\bar{q}}_m}{\partial\bar{\bar{\gamma}}_m}\right)}\right]_{n+1}^{i} \tag{4.160}$$

The consistent tangent operator $\left.\frac{\partial t_n}{\partial\bar{\bar{u}}}\right|_{n+1}^{i}$ for loading softening phase in normal direction (Mode I) can be derived in the same way as in case of direction $\boldsymbol{m}$. Using steps from (4.148) to (4.160) and $sign\left[t_{n,n+1}^{i}\right]=1$, we get:

$$\left.\frac{\partial t_n}{\partial\bar{\bar{u}}}\right|_{n+1}^{i}=\frac{\partial t_n}{\partial\bar{\bar{\gamma}}_n}\cdot\left.\frac{\partial\bar{\bar{\gamma}}_n}{\partial\bar{\bar{u}}}\right|_{n+1}^{i}=\left[\frac{\frac{\partial\bar{\bar{q}}_n}{\partial\bar{\bar{\gamma}}_n}}{\bar{\bar{Q}}_n\cdot\left(\bar{\bar{u}}\cdot\frac{\partial\left(\bar{\bar{Q}}_n\right)^{-1}}{\partial\bar{\bar{\gamma}}_n}+\frac{\partial\bar{\bar{q}}_n}{\partial\bar{\bar{\gamma}}_n}\right)}\right]_{n+1}^{i} \tag{4.161}$$

4.6 Comparison of G operators

When the discontinuity is embedded, the local equilibrium equations (4.54) should be solved. The G operators have the important role in the equilibrium equations; they compare the bulk's stresses with the traction stresses at the discontinuity. In section 4.2, the $\boldsymbol{G}_m$ for real strains and $\widehat{\boldsymbol{G}}_m$ for virtual strains are introduced. Furthermore, two different concepts for defining $\widehat{\boldsymbol{G}}_m$ are presented. The first one was [G-Dujc] introduced in section 4.2.3.1, while the second one [G-Linder] was proposed in section 4.2.3.2. In the following sections, we perform the comparison between both groups of $\widehat{\boldsymbol{G}}_m$. The aim of this section is to review the distribution of the G-operators over the element domain Ω^e. The considered operators are vectors of three components:

$$\bar{\boldsymbol{G}}_m = \begin{Bmatrix} \bar{G}_m^1 \\ \bar{G}_m^2 \\ \bar{G}_m^3 \end{Bmatrix} \text{ and } \bar{\bar{\boldsymbol{G}}}_m = \begin{Bmatrix} \bar{\bar{G}}_m^1 \\ \bar{\bar{G}}_m^2 \\ \bar{\bar{G}}_m^3 \end{Bmatrix}, \; m = 1,2,3,4 \tag{4.162}$$

The following notation will be also used. The subscripts 1, 2, 3 and 4 will be sometimes replaced with $n0, n1, m0, m1$, respectively.

We take a simple square block with $a = 2$, see Figure 4.7. It was modelled by a quadrilateral embedded discontinuity finite element, where the local coordinate system (ξ, η) coincides with the global coordinate system (x, y). We look at two examples, that have different crack line (different start point P_1 and end point P_2). One example considers the crack line that crosses opposite sides (see Figure 4.7, left) and the second one, where the crack line crosses the adjacent sides of the finite element, i.e. single node separation (see Figure 4.7, right).

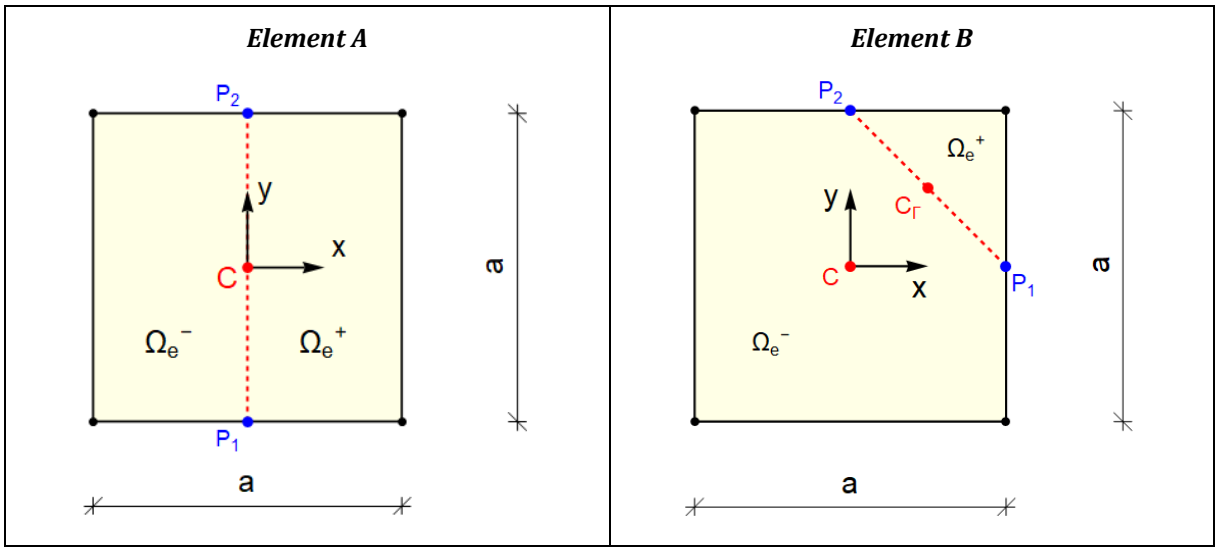

Figure 4.7: A square element. Left: Element A with vertical crack line. Right: Element B with single node separation.

Slika 4.7: Kvadratni element z razpoko, ki gre vertikalno čez center (levo) ali seka sosednja robova (desno).

4.6.1 Square element with vertical crack

We evaluate the G-operators for the Element A (Figure 4.7, left). Table 4.1 and Table 4.2 present the examined values of the real $\overline{\mathbf{G}}_{\mathrm{m}}$ operators over the elements. Table 4.1 collects the numerical values of each component for all separation modes. Table 4.2 graphically presents the values from Table 4.1. The green graph presents the embedded discontinuity zone.

Table 4.3 and Table 4.4 show comparison of $\overline{\widehat{\boldsymbol{G}}}_m$ for virtual strains between [G-Dujc] and [G-Linder]. For constant separation modes ($n0$ and $m0$), the [G-Dujc] and [G-Linder] provide the same interpolations over the element's domain Ω^e. On the other side, the components of $\overline{\widehat{\boldsymbol{G}}}_m$ for linear separation modes ($n1$ and $m1$) are different. Namely, the [G-Dujc] and [G-Linder]

Table 4.1: Components of $\overline{\boldsymbol{G}}_m$ operators for the Element A (Figure 4.7).
Preglednica 4.1: Komponente $\overline{\boldsymbol{G}}_m$ operatorja za Element A (Slika 4.7).

Component Separation mode m	$\bar{G}_m^1$	$\bar{G}_m^2$	$\bar{G}_m^3$
$n0$	-0.5	0	0
$n1$	$-0.5\ y$	0	$-0.5\ x$
$m0$	0	0	-0.5
$m1$	0	$-0.5 - 0.5\ x + H_\Gamma(\{1+y, x\})$	$-0.5\ y$

Table 4.2: Graphical illustration of components of $\bar{\boldsymbol{G}}_m$ operators for the Element A (Figure 4.7).

Preglednica 4.2: Grafična ilustracija komponent $\bar{\boldsymbol{G}}_m$ operatorja po območju Elementa A (Slika 4.7).

Component / Separation mode m	$\bar{G}_m^1$	$\bar{G}_m^2$	$\bar{G}_m^3$
$n0$	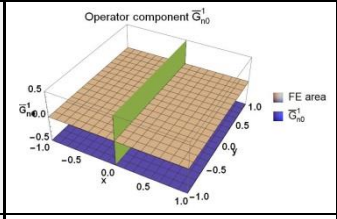	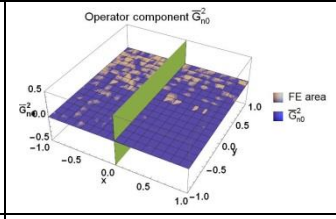	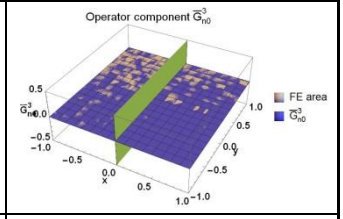
$n1$	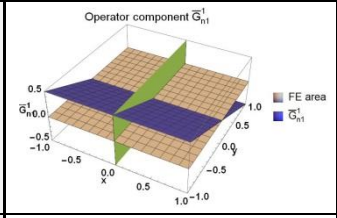	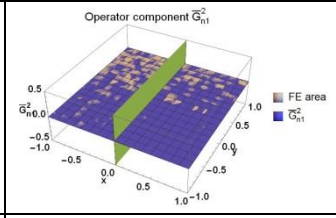	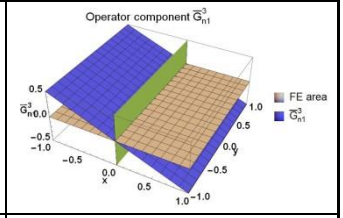
$m0$	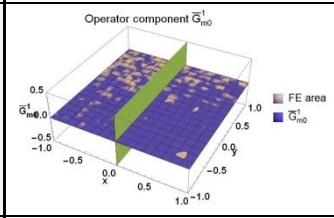	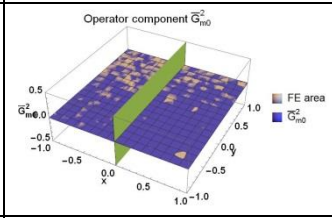	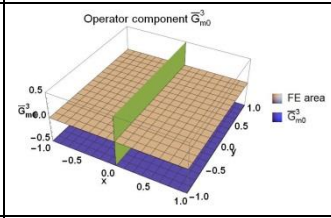
$m1$	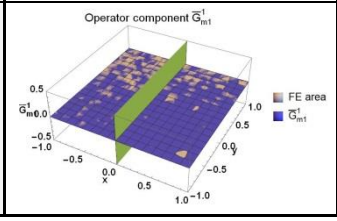	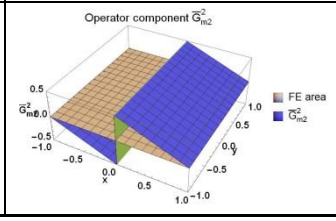	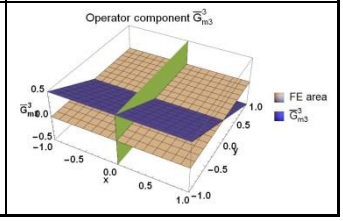

Table 4.3: Components of $\bar{\bar{\boldsymbol{G}}}_m$ operators for the Element A (Figure 4.7). Comparison of the operators [G-Dujc] and [G-Linder].

Preglednica 4.3: Komponente $\bar{\bar{\boldsymbol{G}}}_m$ operatorja za Element A (Slika 4.7). Primerjava operatorjev [G-Dujc] in [G-Linder].

Component / Separation mode m	$\bar{\bar{G}}_m^1$	$\bar{\bar{G}}_m^2$	$\bar{\bar{G}}_m^3$
$n0$ [$\bar{\bar{G}}_1$ −Dujc]	-0.5	0	0
$n0$ [$\bar{\bar{G}}_1$ −Linder]			
$n1$ [$\bar{\bar{G}}_2$ −Dujc]	$-0.5\ y$	0	$-0.5\ x$
$n1$ [$\bar{\bar{G}}_2$ −Linder]			0
$m0$ [$\bar{\bar{G}}_3$ −Dujc]	0	0	-0.5
$m0$ [$\bar{\bar{G}}_3$ −Linder]			
$m1$ [$\bar{\bar{G}}_4$-Dujc]	0	$-0.5 - 0.5\ x + H_\Gamma(\{1+y, x\})$	$-0.5\ y$
$m1$ [$\bar{\bar{G}}_4$ −Linder]		0	

Table 4.4: Graphical illustration of components of $\bar{\bar{\boldsymbol{G}}}_m$ operators for the Element A (Figure 4.7). Comparison of the operators [G-Dujc] and [G-Linder].

Preglednica 4.4: Grafična ilustracija komponent $\bar{\bar{\boldsymbol{G}}}_m$ operatorja po območju Elementa A (Slika 4.7). Primerjava operatorjev iz [G-Dujc] in [G-Linder].

Component separation mode m	$\bar{\bar{G}}_m^1$	$\bar{\bar{G}}_m^2$	$\bar{\bar{G}}_m^3$
$n0$	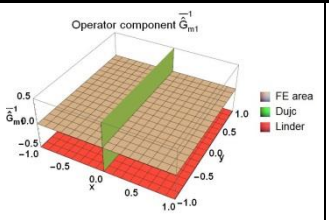	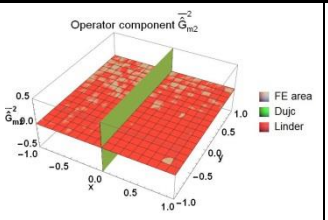	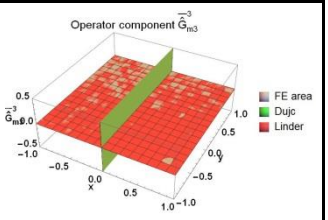
$n1$	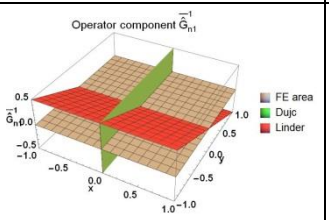	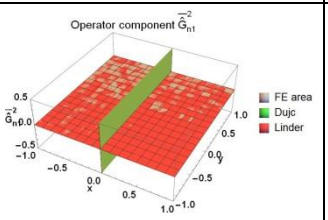	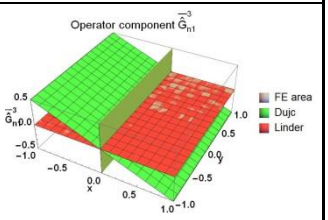
$m0$	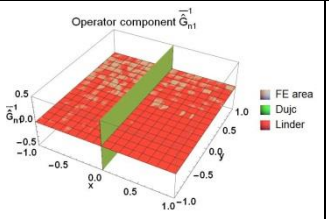	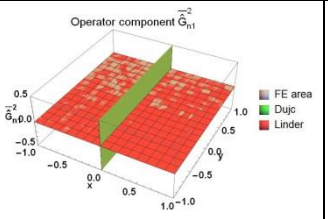	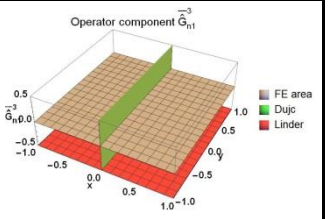
$m1$	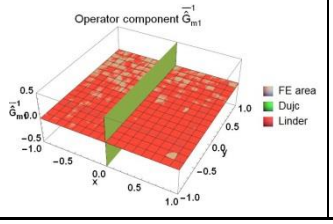	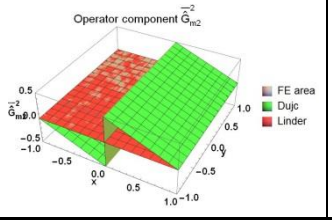	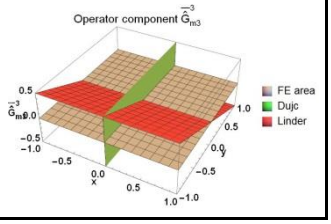

4.6.2 Square element with single node separation

We evaluate the G-operators for the Element B (Figure 4.7, right). Table 4.5 and Table 4.6 present the examined values of the real $\bar{\mathbf{G}}_{\mathrm{m}}$ operators over the elements. Table 4.5 collects the numerical values of each component for all separation modes. Table 4.6 graphically presents the values from Table 4.5. The vertical graph presents the embedded discontinuity zone.

Table 4.7 and Table 4.8 show comparison of $\bar{\bar{\boldsymbol{G}}}_m$ for virtual strains between [G-Dujc] and [G-Linder]. One can see that [G-Dujc] and [G-Linder] provide different interpolations over the element's domain Ω^e for all components.

Table 4.5: Components of $\bar{\boldsymbol{G}}_m$ operators for the Element B (Figure 4.7).

Preglednica 4.5: Komponente $\bar{\boldsymbol{G}}_m$ operatorja za Element B (Slika 4.7).

Component / Separation mode	$\bar{G}_m^1$	$\bar{G}_m^2$	$\bar{G}_m^3$
$n0$	$-\frac{1+y}{4\sqrt{2}}$	$-\frac{1+x}{4\sqrt{2}}$	$-\frac{2+x+y}{4\sqrt{2}}$
$n1$	$-\frac{1+y}{8}$	$\frac{1+x}{8}$	$-\frac{x-y}{8}$
$m0$	$\frac{1+y}{4\sqrt{2}}$	$-\frac{1+x}{4\sqrt{2}}$	$\frac{x-y}{4\sqrt{2}}$
$m1$	$0.5\, H_\Gamma(\{1+y, x+y-1\})$	$0.5\, H_\Gamma(\{1+y, x+y-1\})$	$-H_\Gamma(\{1+y, x+y-1\})$

Table 4.6: Graphical illustration of components of $\bar{\boldsymbol{G}}_m$ operators for the Element B (Figure 4.7).

Preglednica 4.6: Grafična ilustracija komponent $\bar{\boldsymbol{G}}_m$ operatorja po območju Elementa B (Slika 4.7).

Component / Separation mode	$\bar{G}_m^1$	$\bar{G}_m^2$	$\bar{G}_m^3$
$n0$	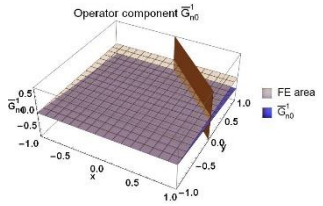	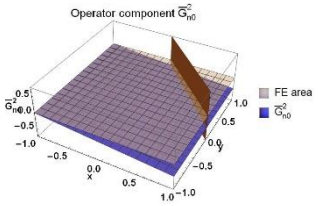	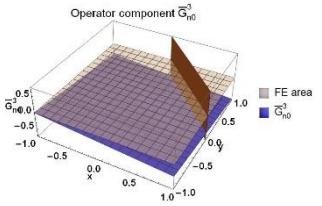
$n1$	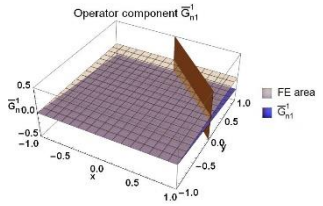	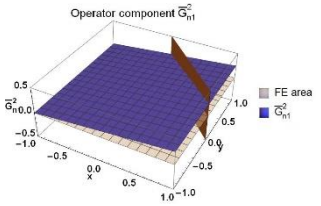	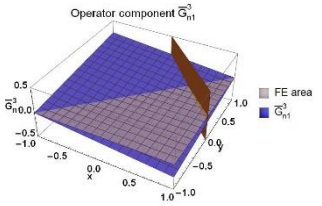
$m0$	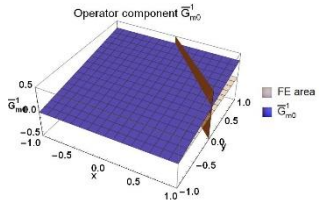	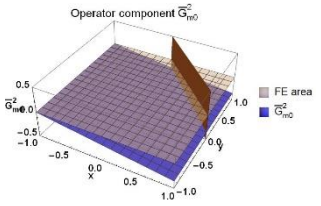	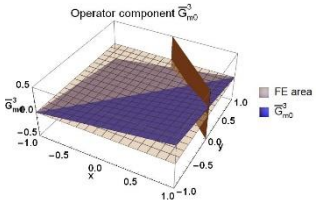
$m1$	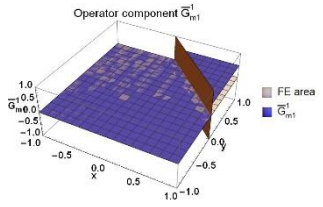	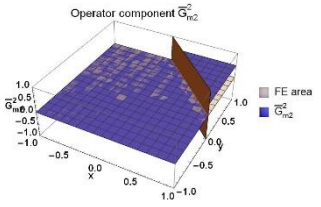	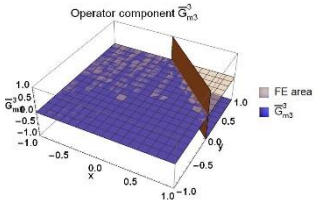

Table 4.7: Components of $\bar{\bar{\boldsymbol{G}}}_m$ operators for the Element B (Figure 4.7). Comparison of the operators [G-Dujc] and [G-Linder].

Preglednica 4.7: Komponente $\bar{\bar{\boldsymbol{G}}}_m$ operatorja za Element B (Slika 4.7). Primerjava operatorjev [G-Dujc] in [G-Linder].

Component Separation mode m	$\bar{\bar{G}}_m^1$	$\bar{\bar{G}}_m^2$	$\bar{\bar{G}}_m^3$
$n0$ [$\bar{\bar{G}}_1$ −Dujc]	$-\frac{1+y}{4\sqrt{2}}$	$-\frac{1+x}{4\sqrt{2}}$	$-\frac{2+x+y}{4\sqrt{2}}$
$n0$ [$\bar{\bar{G}}_1$ −Linder]	$-\frac{1+1.5\cdot(x+y)}{4\sqrt{2}}$	$-\frac{1+1.5\cdot(x+y)}{4\sqrt{2}}$	$-\frac{1+1.5\cdot(x+y)}{2\sqrt{2}}$
$n1$ [$\bar{\bar{G}}_2$ −Dujc]	$-0.25\,y$	$0.25\,x$	$-0.25\,(x-y)$
$n1$ [$\bar{\bar{G}}_2$ −Linder]	$0.0625\cdot(x-y)$	$0.0625\cdot(x-y)$	$0.1250\cdot(x-y)$
$m0$ [$\bar{\bar{G}}_3$ −Dujc]	$\frac{1+y}{4\sqrt{2}}$	$-\frac{1+x}{4\sqrt{2}}$	$\frac{x-y}{4\sqrt{2}}$
$m0$ [$\bar{\bar{G}}_3$ −Linder]	$\frac{1+1.5\cdot(x+y)}{4\sqrt{2}}$	$-\frac{1+1.5\cdot(x+y)}{4\sqrt{2}}$	0
$m1$ [$\bar{\bar{G}}_4$-Dujc]	$-0.0625 +$ $0.5\,H_\Gamma(\{1+y, x+y-1\})$	$-0.0625+$ $0.5\,H_\Gamma(\{1+y, x+y-1\})$	$0.125 -$ $H_\Gamma(\{1+y, x+y-1\})$
$m1$ [$\bar{\bar{G}}_4$ −Linder]	$0.0625\cdot(x-y)$	$0.0625\cdot(x-y)$	0

Table 4.8: Graphical illustration of components of $\overline{\widehat{\boldsymbol{G}}}_m$ operators for the Element B (Figure 4.7). Comparison of the operators [G-Dujc] and [G-Linder].

Preglednica 4.8: Grafična ilustracija komponent $\overline{\widehat{\boldsymbol{G}}}_m$ operatorja po območju Elementa B (Slika 4.7). Primerjava operatorjev [G-Dujc] in [G-Linder].

Component separation mode m	$\bar{\widehat{G}}_m^1$	$\bar{\widehat{G}}_m^2$	$\bar{\widehat{G}}_m^3$
$n0$	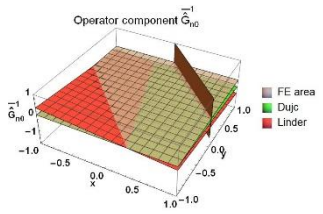	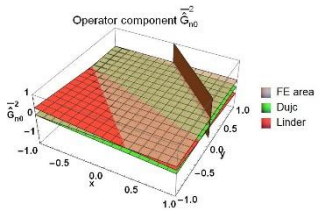	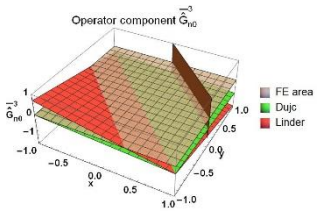
$n1$	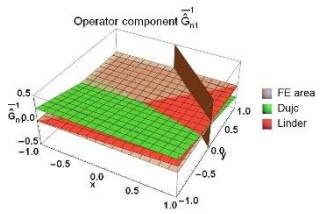	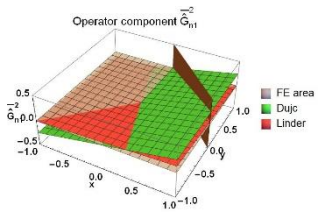	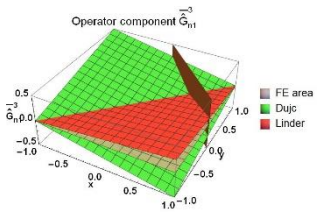
$m0$	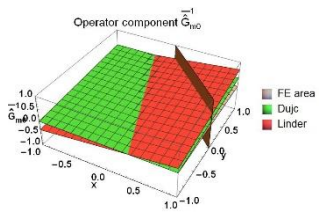	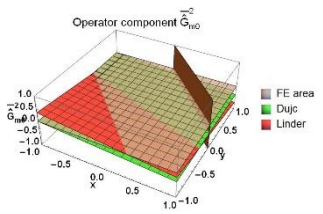	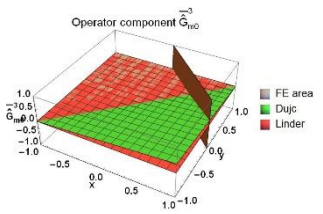
$m1$	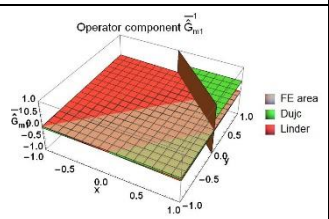	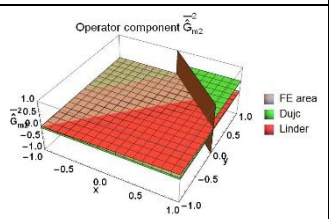	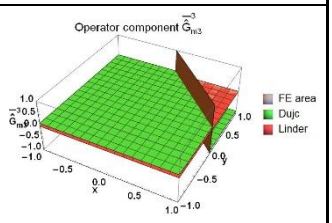

4.6.3 Conclusion

In section 4.2.3, we introduce two different concepts for G-operators ([G-Dujc] and [G-Linder]) that play role in the local equilibrium equation (4.54). They are dependent on the failure line direction and the geometry of the Ω_e^+ area. Namely, A failure line may cross quadrilateral finite element in a two different ways: it crosses the opposite sides of the finite element or the adjacent sides (see Figure 4.7). In this section, the comparison of G-operators is done for both crack situations.

When a crack crosses the opposite sides of the element (see Figure 4.7, Element A), [G-Dujc] and [G-Linder] are the same functions for constant separation modes (n0 and m0). For the linear separation modes (n1 and m1), the operators are not equal. [G-Dujc] take into account more stress components than [G-Linder]. In case of single node separation (see Figure 4.7, Element B), [G-Dujc] and [G-Linder] consider stress components completely different for all separation modes. The comparison clearly shows that G-operators are equal only for constant separation modes (n0 and m0) in Element A, otherwise they differ. In the next section, small tests are presented to assess the effectiveness for both G-operators.

5 ONE- AND TWO-ELEMENT TESTS WITH STRONG DISCONTINUITY QUADRILATERALS

We present the results of extended numerical investigation of the new designed finite elements for failure analysis. The aim of this investigation is to check the effectiveness of the embedded discontinuity model, when softening is active. Therefore the tests are limited to simple numerical models – one or two finite element mesh. Some tests are taken from (Linder and Armero, 2007) and (Dujc et al., 2010).

We are interested in: (1) the performance of Q4 or Q6 in combination with the embedded discontinuity (ED) and (2) the G-operators that are applied in the ED-FEM.

Furthermore, we want to check the single node separation problem when the exponential softening law is set and the linear separation modes are active ($\alpha_{n1} \neq 0$ and/or $\alpha_{m1} \neq 0$).

5.1 Used elements

We use a quadrilateral plane-stress finite element with embedded discontinuity. The small tests are performed for different finite element formulations. We set 2x2 integration scheme over bulk area, 2-points integration along the crack line and exponential softening law (4.80), by default. The name of the numerical model indicates the items of the used finite element formulation. We can combine the following properties:

(i) Quadrilateral formulations: Q4 or Q6
(ii) G-operators for virtual strains: [G-Dujc] or [G-Linder]
(iii) The traction-separation law in direction $\boldsymbol{m}$ (Mode II): the exponential law (4.88) or the linear relation with k_m (4.89).

When the linear relation (4.89) is used for Mode II, the tangent coefficient is $k_m = 0.3$ Mpa/mm (Linder and Armero, 2007).

***Remark 5.1**: Name "Q4+km [G-Linder]" means that the finite element with the embedded discontinuity is based on the standard quadrilateral formulation (Q4), G-operators are [G-Linder] and the traction-separation law in the tangential direction is modelled by the linear relation with k_m (4.89).*

Name "Q6 [G-Dujc]" denotes that the finite element with the embedded discontinuity is based on the standard quadrilateral formulation enhanced with the incompatible mode parameters (Q6), G-operators are [G-Dujc] and the traction-separation law in the tangential direction is modelled by the exponential softening law (4.88).

***Remark 5.2**: (Linder and Armero, 2007) presents finite element designs with 5-point integration scheme along the discontinuity line – the reason for using 5-point integration is unknown. The tests that are presented in the following sections were performed with the same finite elements (Q4 or Q6) that have 5 integration points along failure line. The results were the same as when 2-point integration scheme is set.*

Definition says that the crack opening parameters $\alpha_m, m = 1, \dots, 4$ are constant along the discontinuity line. Smaller number of the integration points decreases the computational time. Therefore, we take 2-point integration scheme.

***Remark 5.3**: Integration points along discontinuity line (dip) are considered individually. It allows a situation when one integration point is in loading phase of softening and the second one in unloading phase.*

***Remark 5.4**: Some authors deal with the finite elements that enable certain crack separation modes, i.e. only linear Mode I (n0 + n1) or constant separation modes (n0 + m0), to ensure the analysis convergence. In this section we use the finite element that enables all separation modes (n0 + n1 + m0 + m1).*

***Remark 5.5**: (Linder and Armero, 2007) proposes a stabilization parameter κ to improve numerical simulation. The authors report that the quadrilateral finite element with [G-Linder] operators is prone to instabilities if a crack line crosses the adjacent sides (single node separation). When full softening state is achieved (the resistance at the failure line is zero), the [G-Linder] operators become linearly dependent. For this reason they propose to use a stabilization parameter κ in set of local equilibrium equations (4.68) - (4.71):*

$$\begin{Bmatrix} h_1 \\ h_2 \\ h_3 \\ h_4 \end{Bmatrix} + \kappa \begin{Bmatrix} 0 \\ \alpha_2 \\ 0 \\ \alpha_4 \end{Bmatrix} = \mathbf{0} \tag{5.1}$$

which leads to a stabilized tangent matrix (see (4.122)):

$$\boldsymbol{K}^e_{\alpha\alpha} + \kappa \begin{bmatrix} 0 & 0 & 0 & 0 \\ 0 & 1 & 0 & 0 \\ 0 & 0 & 0 & 0 \\ 0 & 0 & 0 & 1 \end{bmatrix} \tag{5.2}$$

***Remark 5.6**: Once the embedded discontinuity is activated, the first iteration of each incremental step is forced to be elastic (no evolution of softening variables). Proof: Failure functions $\bar{\bar{\phi}}_n(\bar{\bar{u}})$ and $\bar{\bar{\phi}}_m(\bar{\bar{v}})$ are zero for the crack opening parameters $\alpha_m, m = 1, \dots, 4$ in the first iteration of each increment. Namely, the first iteration originates from the last converged state, where failure functions are satisfied.*

5.2 Tension test

5.2.1 Loading/unloading cycle

This example verifies the implementation of the non-associative rigid-damage law with exponential softening. A rectangular block with length $a = 200$ mm and thickness 1 mm is subjected to a simple tension. Figure 5.1 (left) illustrates the geometry and boundary conditions. The left edge of the block is fully supported; the free edge is subjected to the imposed horizontal displacement $u_x = \lambda p_0$, with $p_0 = 0.1$ mm. The material data are: Young's modulus $E = 30000$ MPa , Poisson's ratio $\nu = 0.2$, and tensile

strength $\sigma_{un} = 3$ MPa. The mode I and mode II crack openings are controlled by σ_{un} and $\sigma_{um} = 3$ MPa, respectively, and the fracture energies $G_{fn} = G_{fm} = 0.1$ N/mm, respectively. We note that only mode I opening is activated in the test. One loading cycle is considered. The imposed displacement is increased to λ=0.4, decreased to $\lambda = 0$ and increased again to $\lambda = 1.6$. The crack line is predefined.

All the considered elements (Q4 [G-Dujc], Q4 [G-Linder], Q6 [G-Dujc], Q6 [G-Linder]) give the same response. Only α_{n0} parameter is non-zero, the other parameters are zero. The reaction force versus imposed displacement curve is presented in Figure 5.1 (right). Figure 5.2 shows evolution of internal variables during the computation. While the reaction force decreases to zero, the accumulated jump-in-displacement parameter $\bar{\bar{\xi}}_n$ is constant and α_{n0} decreases simultaneously.

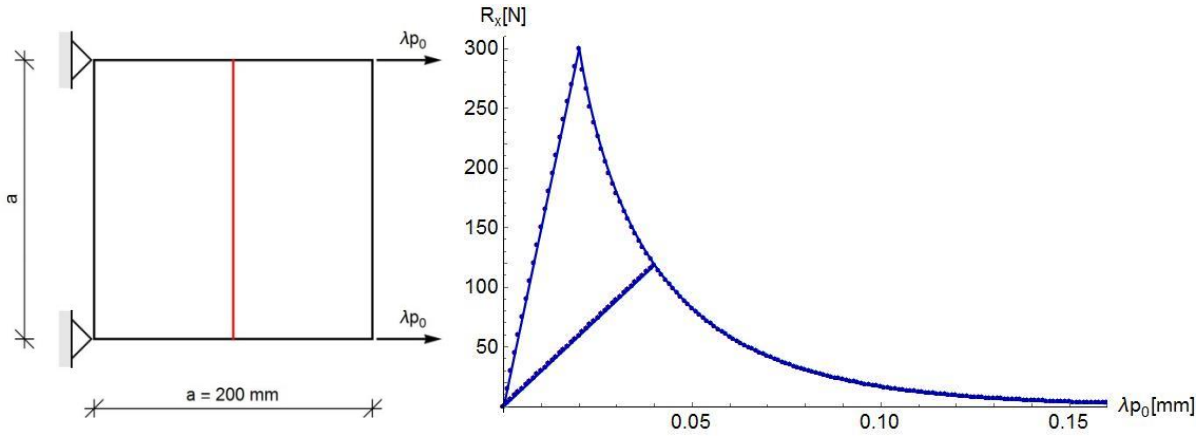

Figure 5.1: Left: The geometry, boundary conditions, imposed displacement and crack line position. Right: Reaction R_x versus imposed displacement curve.

Slika 5.1: Levo: Geometrija, robni pogoji, obtežba in pozicija razpoke. Desno: Diagram reakcija R_x v odvisnosti od vsiljenega pomika.

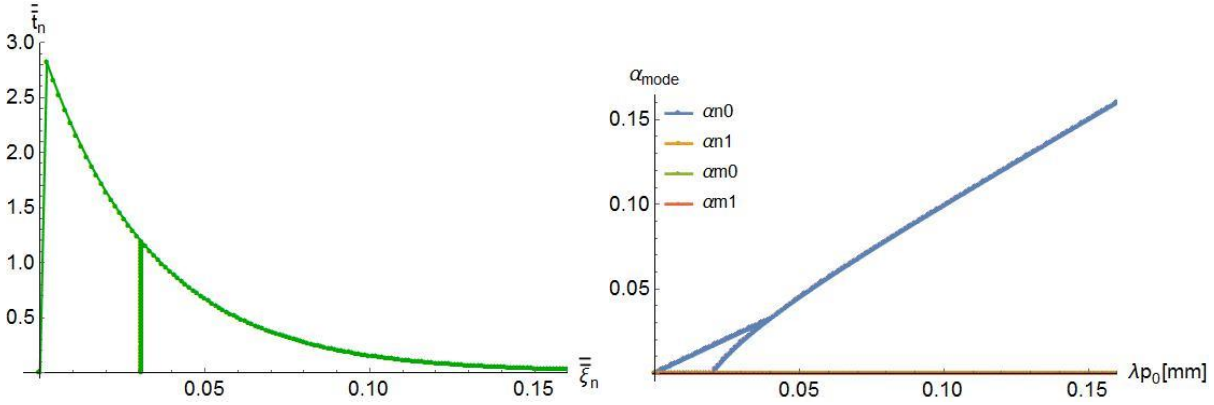

Figure 5.2: Left: Traction stress t_n in normal direction versus accumulated softening $\bar{\bar{\xi}}_n$ curve; Right: Crack opening parameters through the loading program.

Slika 5.2: Levo: Graf kohezijske normalne napetosti t_n v odvisnosti od akumulacije mehčanja $\bar{\bar{\xi}}_n$. Desno: Graf parametrov širjenja razpoke v odvisnosti od obtežbe.

5.2.2 Monotonic tension test

The concrete block from Section 5.2.1 is subjected to imposed displacement $p_{Hor} = \lambda p_0$ with $p_0 = 0.01$ mm (see Figure 5.3, left). The geometry and material data are the same as in Section 5.2.1. Figure 5.3 illustrates geometry and boundary conditions. The test was presented in (Linder and Armero, 2007) for checking the invariance of $\overline{\overline{\boldsymbol{G}}}$ operators with respect to the choice of the fixed Cartesian coordinate system. Firstly, we analyse one finite-element in horizontal and rotated configurations. The start and end points of the crack line are predefined. Secondly, we analyse a mesh with two distorted elements (see Figure 5.4) and imposed vertical crack passing through the center of the square block. The crack separates single node in both elements. The two element mesh is also tested for horizontal and rotated configurations.

All considered elements (Q4 [G-Dujc], Q4 [G-Linder], Q6 [G-Dujc], Q6 [G-Linder]) produce the same response, since the $\overline{\overline{\boldsymbol{G}}}_{\boldsymbol{m}}$ operators from (Dujc et al, 2010) and (Linder and Armero, 2007) are the same for mode n0. The reaction force versus imposed displacement curve is presented in Figure 5.5.

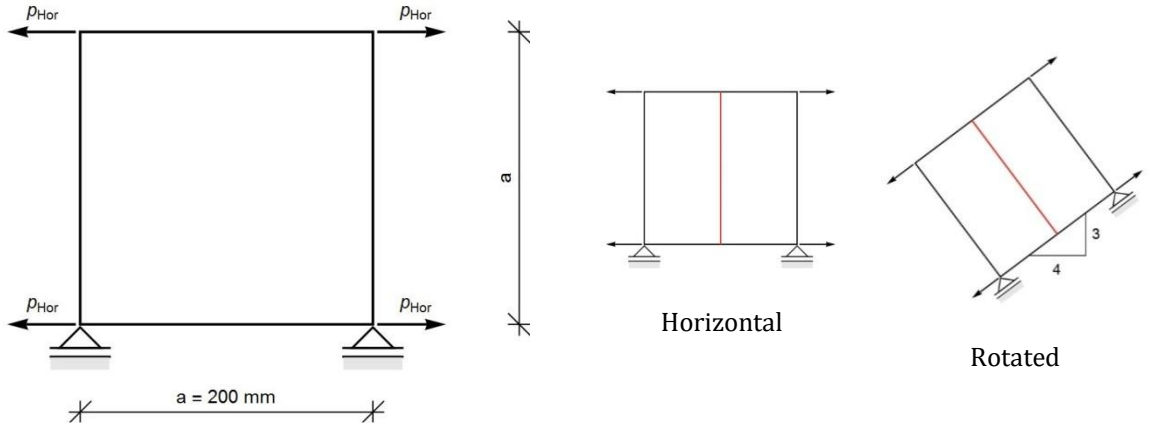

Figure 5.3: Left: Geometry, supports and load data for the one-element-tension test. Right: Horizontal and rotated configurations.

Slika 5.3: Levo: Geometrija, robni pogoji in obtežba. Desno: Horizontalen in zasukan model.

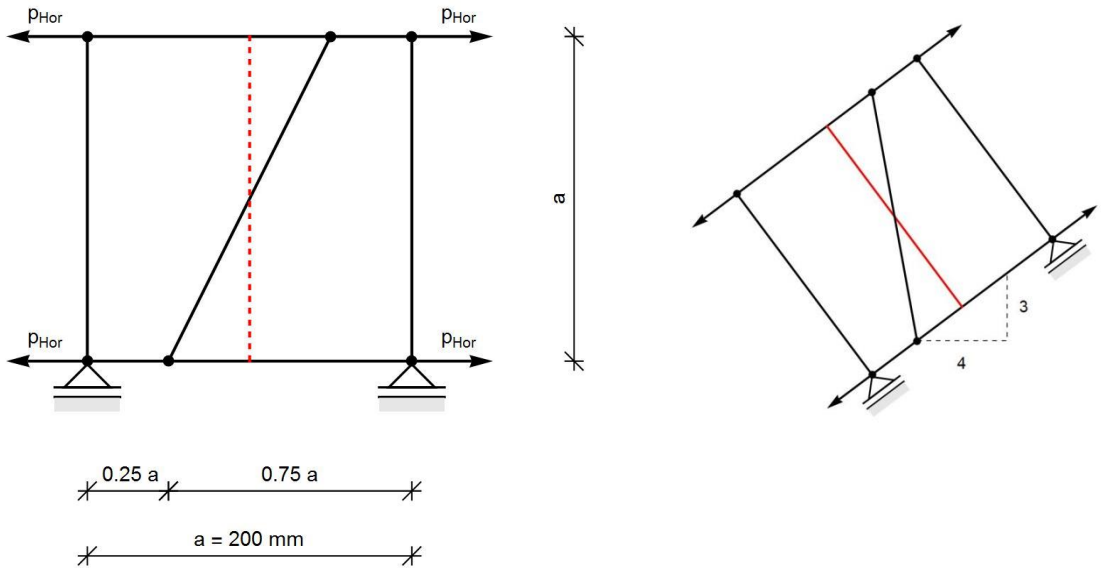

Figure 5.4: Two-elements test. Left: Geometry, boundary conditions and load for single-node-separation tension test (red line is the embedded discontinuity line). Right: Rotated configuration.

Slika 5.4: Test na dveh elementih. Levo: Geometrija, robni pogoji in obtežba. Rdeča linija je vgrajena nezveznost. Desno: Zasukan model.

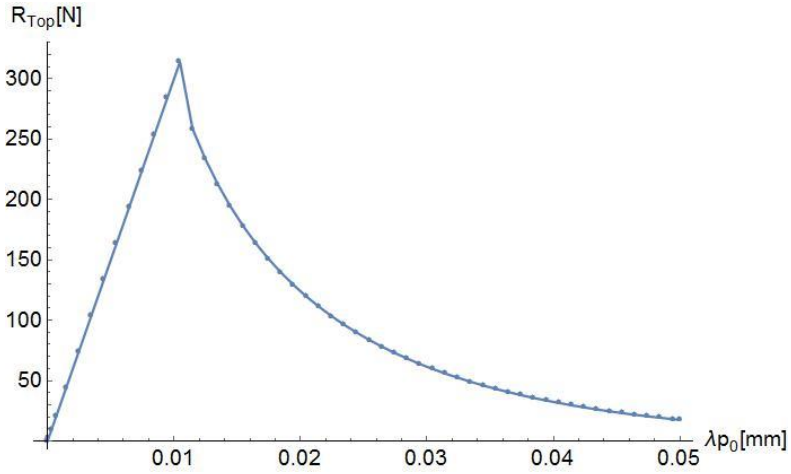

Figure 5.5: Reaction force R_y versus imposed displacement curve u_y. The curves for the horizontal and rotated configurations are identical.

Slika 5.5: Diagram reakcijska sila R_y v odvisnosti od vsiljenega pomika u_y. Grafi so enaki tako za horizontalen kot za zasukan model.

5.3 Bending test

We take the concrete block from section 5.2.1 with the same geometrical and material data. We perform the bending test from (Linder and Armero, 2007), see Figure 5.6. The bending loading condition is established by two horizontal imposed displacements: $p_{Bot}(\lambda) = p_{Init} + \lambda p_{Bot,0}$ and $p_{Top}(\lambda) = p_{Init} + \lambda p_{Top,0}$, where $p_{Init} = 0.01$ mm, $p_{Bot,0} = 0.02$ mm and $p_{Top,0} = 0.01$ mm. The crack line is predefined and runs vertically

through the block's center. The bending test is performed for the following elements: Q4 [G-Dujc], Q4 [G-Linder], Q6 [G-Dujc], Q6 [G-Linder], Q4+km [G-Dujc], Q4+km [G-Linder], Q6+km [G-Dujc] and Q6+km [G-Linder].

The one-element test gives practically the same response for all finite elements and for both configurations (see Figure 5.7). As expected, only Mode I is activated. Two Mode I jump-in-displacement parameters α_{n0} and α_{n1} are not zero and the jump-in-displacements parameters for Mode II (α_{m0} and α_{m1}) remain zero.

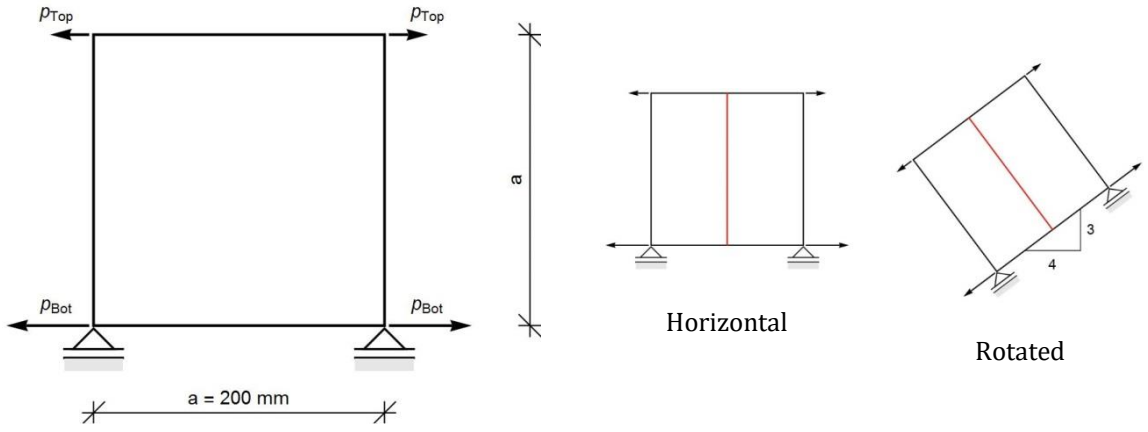

Figure 5.6: One-element bending test. Left: Geometry, supports and load data. Right: Horizontal and rotated configurations.

Slika 5.6: Upogibni test na enem elementu: Levo: Geometrija, robni pogoji in obtežba. Desno: Horizontalen in zasukan model.

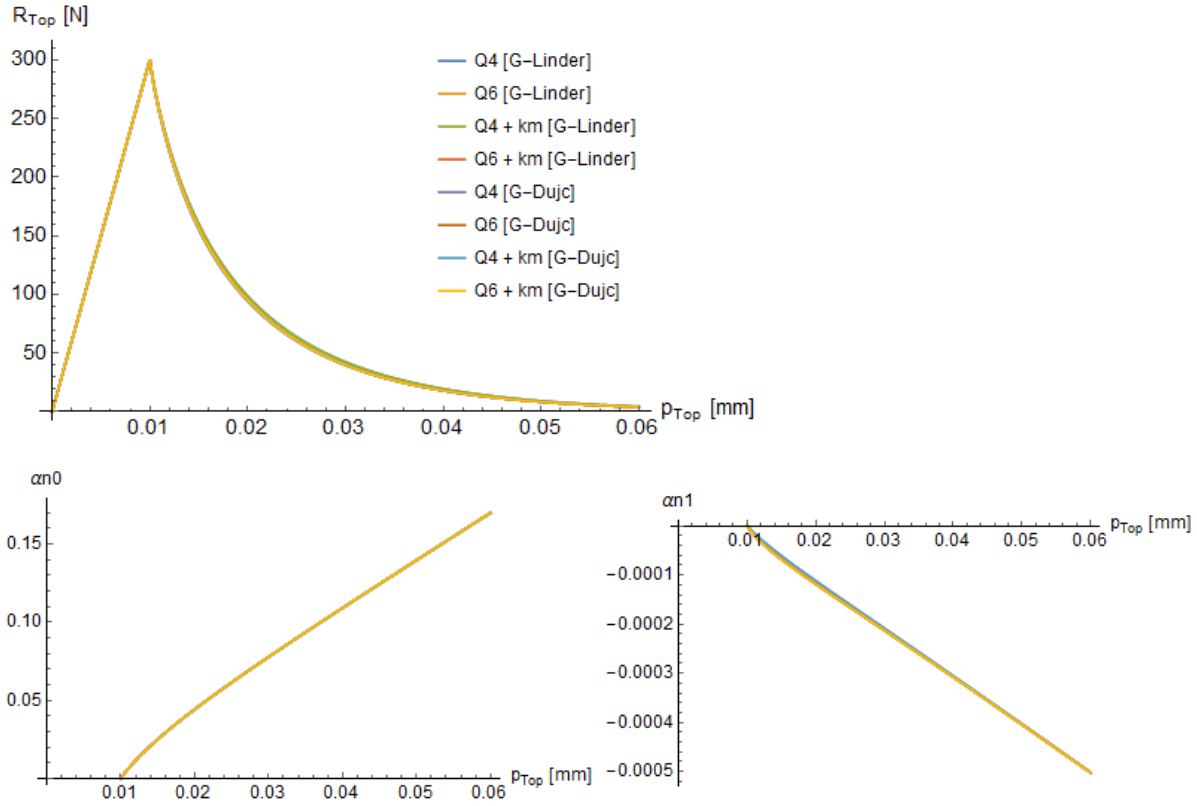

Figure 5.7: One-element bending test. Top: Reaction force R_y – imposed displacement p_{Top} in the top node curves. Bottom left: Jump-in-displacement parameter α_{n0} – the displacement p_{Top} curves. Bottom right: Jump-in-displacement parameter α_{n1} – the displacement p_{Top} curves.

Slika 5.7: Upogibni test na enem elementu: Zgoraj: Grafi reakcije R_y v odvisnosti od pomika zgornjega vozlišča p_{Top}. Spodaj levo: Grafi parametra širjenja razpoke α_{n0} v odvisnosti od pomika p_{Top}. Spodaj desno: Grafi parametra širjenja razpoke α_{n1} v odvisnosti od pomika p_{Top}.

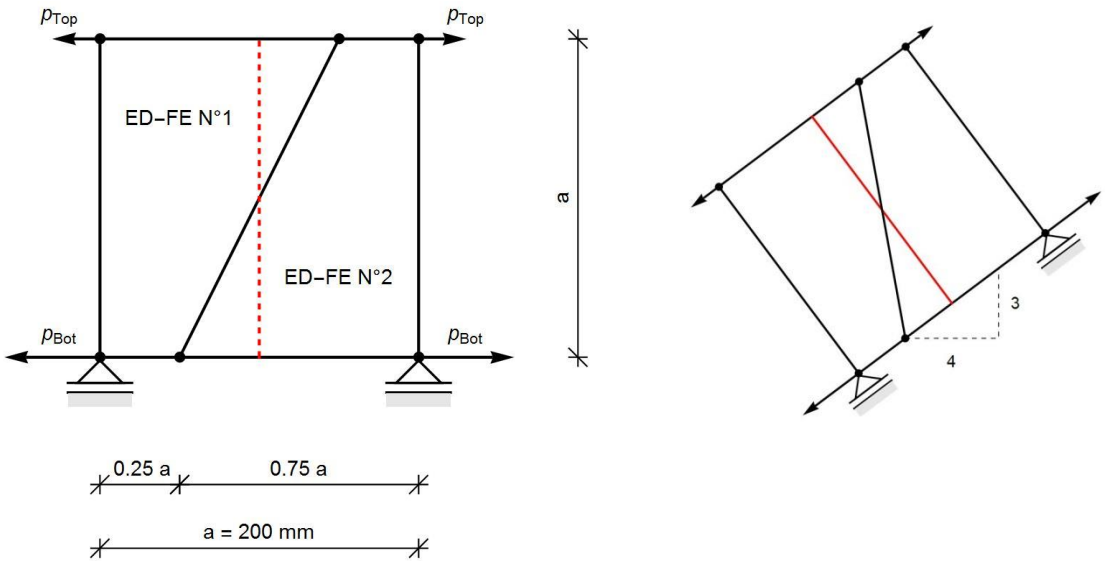

Figure 5.8: Geometry, supports and load data for single-node-separation bending test (two element mesh). Dashed line represents discontinuity line.

Slika 5.8: Geometrija, robni pogoji in obtežba za upogibni test na mreži dveh elementov. Rdeča črta predstavlja potek razpoke.

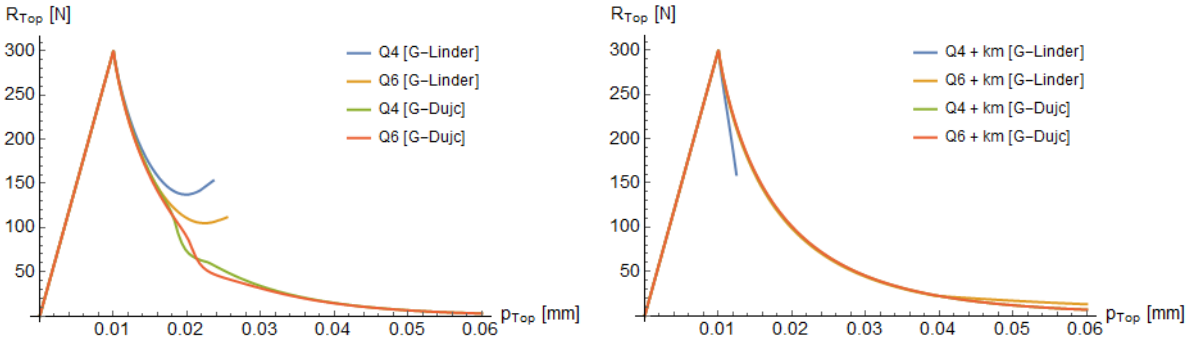

Figure 5.9: Two-elements-mesh. Left: The reaction-displacement curves for exponential softening law for Mode II. Right: The reaction-displacement curves for linear law for Mode II.

Slika 5.9: Diagram reakcijska sila R_{Top} v odvisnosti od pomika zgornjega vozlišča u_{Top}. Levo: Za Mode II uporabimo eksponentni zakon mehčanja. Desno: Za Mode II uporabimo linearno relacijo.

Figure 5.8 illustrates the geometry and boundary conditions for the mesh of two distorted elements. The elements are named ED-FE N°1 and ED-FE N°2. Recall, that the vertical crack is predefined in the middle of the block. The single node separation occurs in both elements. The crack separates element in such a way that a single node exists on either Ω_e^+ or Ω_e^-. (Manzoli and Shing, 2006) reported that no stress locking occurs in case of single-node-separations in quadrilateral elements. In (Linder and Armero, 2007), the authors reports the single-node-separation is prone to instabilities. The test is performed for the following elements: Q4 [G-Dujc], Q4 [G-Linder], Q6 [G-Dujc], Q6 [G-Linder], Q4+km [G-Dujc], Q4+km [G-Linder], Q6+km [G-Dujc] and Q6+km [G-Linder]. Results for the mesh of two distorted elements are presented in Figure 5.9 – Figure 5.13.

Figure 5.9 shows reaction-displacement curves for all elements. One can see that the models with the [G-Dujc] operators converge in all cases. On the other hand, for good results with the [G-Linder] operators we had to include incompatible modes (Q6) and simplified linear relation (4.89) for Mode II tractions.

ED-FE with exponential softening law for Mode II

Let us take a look at the results for the ED-FEs that use exponential softening law (4.88) for Mode II. The graphs of the reaction force R_{Top} versus imposed displacement p_{Top} are shown in Figure 5.9 (left). We note that only ED-FEs with the [G-Dujc] operators successfully converge. Only Mode I is active. Since the failure function $\bar{\bar{\phi}}_m(t_m)$ is negative during the computation, the Mode II remains silent, i.e. the opening parameters for Mode II are zero. Figure 5.10 shows the graphs of jump-parameters α_{n0} and α_{n1} versus imposed displacement at the top node p_{Top} for the ED-FE N°1 (first row) and the ED-FE N°2 (bottom row). The graphs in Figure 5.10 show the following:

- Constant jump-parameter α_{n0} increases during the analysis for all cases.
- When $p_{Top} \cong 0.02$ mm, the linear jump-parameter α_{n1} starts decreasing – the subdomain Ω_e^+ changes the direction of rotation.

- When $p_{Top} \cong 0.025$ mm, the elements with [G-Linder] fail to converge (the top FE: $\alpha_{n1} \approx 0$, the bottom FE: α_{n1} still increases).

- When $p_{Top} \cong 0.025$ mm, the elements with [G-Dujc] behave as follows: the bottom FE: α_{n1} decreases toward the zero, the top FE: α_{n1} still increases).

- After $p_{Top} \geq 0.025$ mm the linear jump-parameter α_{n1} increases again – now, the embedded discontinuity behaves in accordance with the external load.

We can conclude the following:

- Regarding the loading conditions, it is expected that only Mode I is active. One would expect α_{n0} and α_{n1} to monotonically increase as in one-element test. The decreasing of α_{n1} in the middle of analysis is unexpected.

- The models with the [G-Linder] operators fail to compute the bending test.

- The models with the [G-Dujc] operators can find a way out of the critical area (0.02 mm $< p_{Top} <$ 0.025 mm).

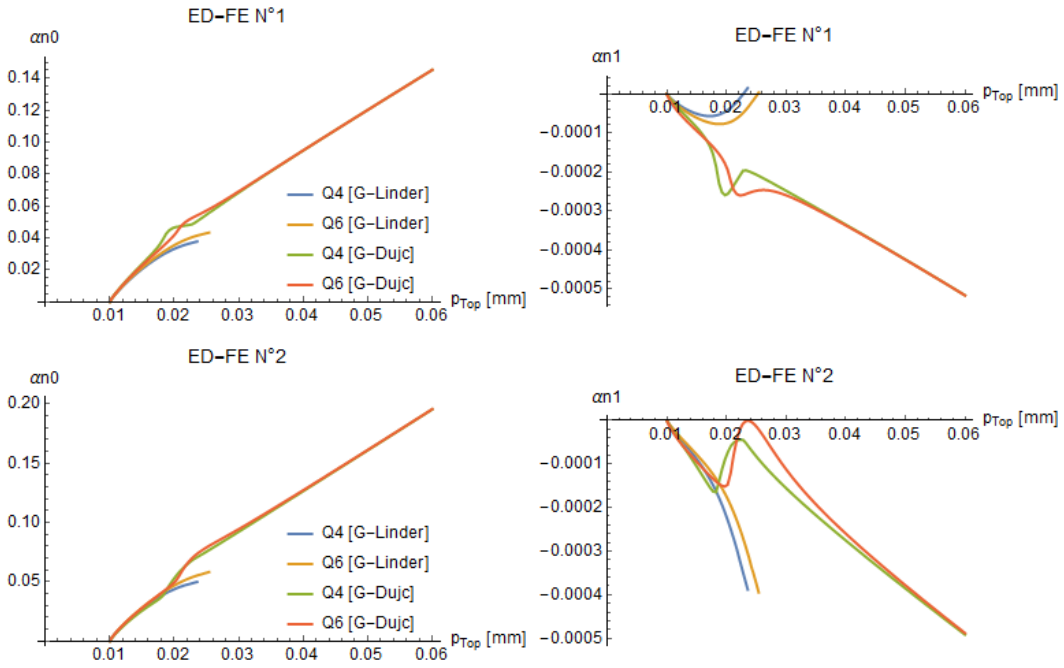

Figure 5.10: Two-elements-mesh with the exponential law for Mode II. Top: Crack opening parameters for Mode I in ED-FE N°1. Bottom: Crack opening parameters for Mode I in ED-FE N°2.

Slika 5.10: Mreža dveh elementov z eksponentnim zakonom mehčanja za Mode II. Zgoraj: Diagrami parametrov širjenja razpoke (α_{n0}, α_{n1}) v elementu ED-FE N°1. Spodaj: Diagrami parametrov širjenja razpoke (α_{n0}, α_{n1}) v elementu ED-FE N°2.

ED-FE with linear relation ($\mathbf{t_m = k_m \bar{\bar{v}}}$) for Mode II

Figure 5.9 (right) shows the graphs of the reaction force R_{Top} versus imposed displacement p_{Top} at the top node. Using linear relation $t_m = k_m \bar{\bar{v}}$ significantly improves the results, since reaction force R_{Top} continuously decreases. Only the ED-FE Q4 with the [G-Linder] operators fails to converge. Figure 5.11 and Figure 5.12 give insight into the evolution of the jump-in-displacements parameters α_m during the analysis. It can be noticed that all parameters α_m are active. Unlike the failure function $\bar{\bar{\phi}}_m$ (4.87), the linear relation (4.89) doesn't check whether the material failure shear stress σ_{um} is exceeded. Consequently, when the shear traction t_m are non-zero, the parameters for Mode II are activated. Figure 5.11 illustrates the graphs of the parameters for Mode I (α_{n0} and α_{n1}) in each elements separately. Figure 5.12 presents the graphs of the parameters for Mode II (α_{m0} and α_{m1}) versus imposed displacement at the top node p_{Top}.

It can be noticed from the diagrams that the models with the [G-Dujc] operators perform well. The corresponding graphs are similar. The parameters for Mode I (α_{n0} and α_{n1}) monotonically increase, the constant parameter α_{m0} evolves and the linear parameter $\alpha_{m1}$is around zero ($\cong 10^{-6}$).

If the [G-Linder] is set, the model converges only in combination with the linear relation (4.89) for Mode II and the incompatible mode parameters ("Q6+km [G-Linder]"). At $p_{Top} = 0.04$ mm, the parameter α_{n1} starts decreasing and it changes its direction. The separation Mode II is fully active.

We can conclude the following:

- In case of bending loading, the element formulations with the [G-Linder] operators have to be combined with incompatible mode method and linear relation for Mode II.

- The "single-node-separation" could become difficult when crack spreads in linear separation modes (α_{n1}, α_{m1}). The linear relation makes that Mode II is activated, which numerically improve the global model response (reaction force).

- The [G-Dujc] operators show well performance in bending test of all models.

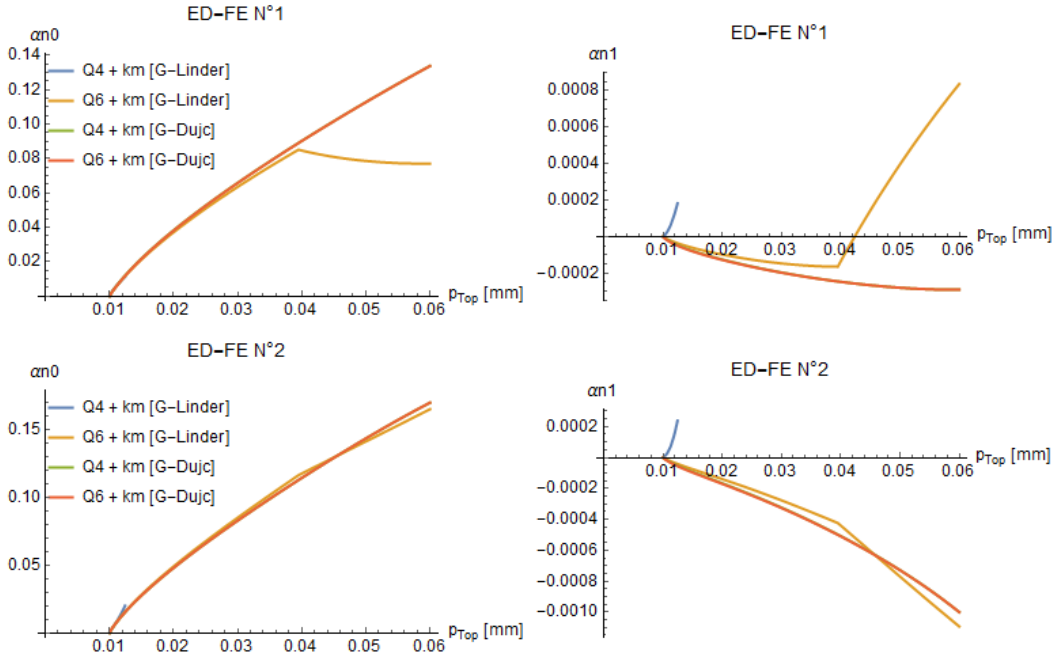

Figure 5.11: Two-elements-mesh with the linear relation for Mode II. Top: Crack opening parameters for Mode I in ED-FE N°1. Bottom: Crack opening parameters for Mode I in ED-FE N°2.

Slika 5.11: Mreža dveh elementov. Uporabimo linearno relacijo za Mode II. Zgoraj: Parametri širjenja razpoke v smeri normale v ED-FE N°1. Spodaj: Parametri širjenja razpoke v smeri normale v ED-FE N°2.

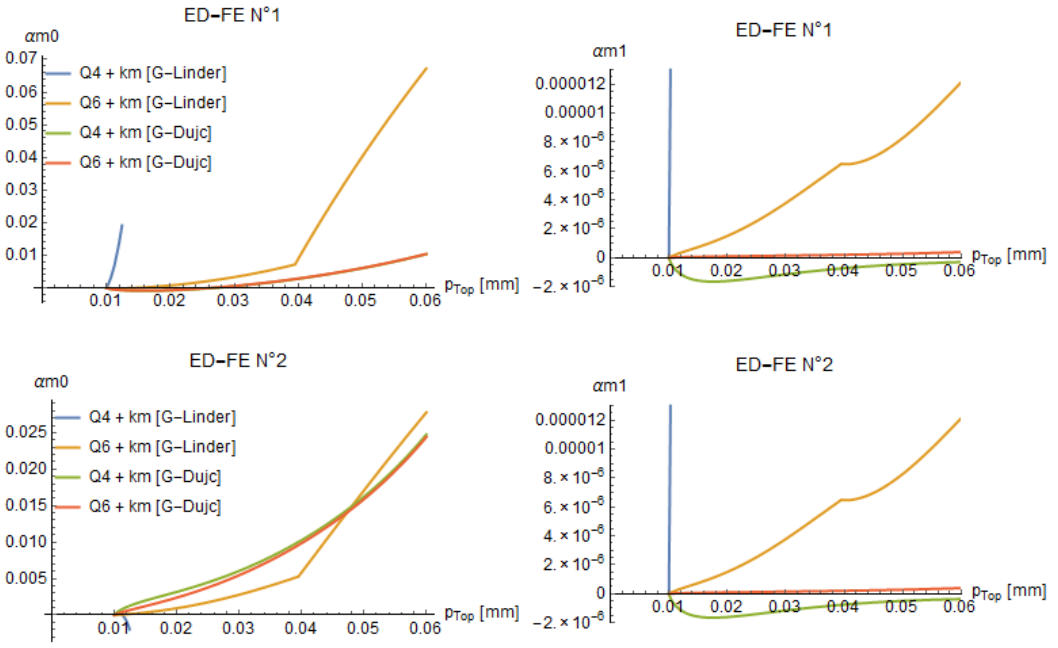

Figure 5.12: Two-elements-mesh configuration. The linear law for Mode II. Top: Crack opening parameters for Mode II in ED-FE N°1. Bottom: Opening parameters for Mode II in ED-FE N°2.

Slika 5.12: Mreža dveh končnih elementov, kjer uporabimo linearno relacijo za Mode II. Zgoraj: Parametri širjenja razpoke v smeri tangente v ED-FE N°1. Spodaj: Parametri širjenja razpoke v smeri tangente v ED-FE N°2.

Conclusions about the bending tests

When the one-element mesh is subjected to the bending loading conditions, the crack expands in separation mode I. We recognize very well performance of all models.

The mesh of two distorted elements results in a demanding problem. Namely, the crack lines cross the adjacent element's sides (i.e. single node separation), which makes difficult to describe the linear part of crack separation modes. Beside the separation Mode I, the Mode II is needed to capture the correct global response of the concrete block subjected to the bending load. The models with the [G-Dujc] operators successfully converge. The [G-Linder] operators are effective only in a combination with the incompatible mode parameters and the linear relation (4.89) for Mode II.

Based on the results for the bending test, we suggest using the [G-Dujc] operators for linear Mode I. Figure 5.13 draws a comparison between the results $R_{Top}(p_{Top})$ of the one-element mesh and the two-element mesh model.

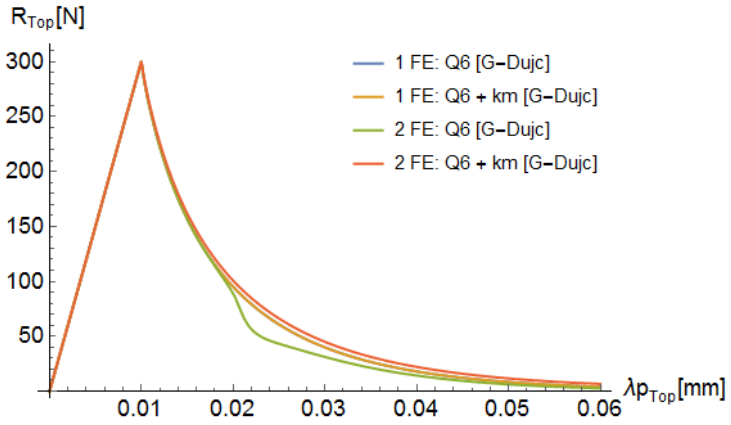

Figure 5.13: Reaction force $R_{x,Top}$ versus imposed displacement p_{Top} graph in top node.
Slika 5.13: Reakcijska sila $R_{x,Top}$ v odvisnosti od vsiljenega pomika p_{Top} v zgornjem vozlišču.

5.4 Shear test

With this test we investigate behaviour of the ED elements in shear mode (Mode II). We consider a square-like 2d solid with length $a = 200$ mm and thickness 1 mm. The material data are Young's modulus $E = 30000$ N/mm^2 and Poisson's ratio $\nu = 0$. The cohesive forces in the embedded discontinuity are described by the exponential softening law in normal direction (Mode I) and the linear relation $t_m = k_m \bar{\bar{v}}$ in tangential direction (Mode II). The aim of the shear test is to check the crack opening in Mode II. Therefore, the numerical simulations are performed on an element with a pre-existed discontinuity with no resistance, i.e. the ultimate tensile strength is $\sigma_{un} = 0$ and $k_m = 0$.

Four versions of the shear test were prepared (see Figure 5.14 and Figure 5.15). The *Model A* has discontinuity between the opposite sides of the element. The *Model B* has the single-node-separation. The numerical models are tested for the following variations of ED-FEs: Q4+km [G-Dujc], Q4+km [G-Linder], Q6+km [G-Dujc] and Q6+km [G-Linder].

5.4.1 Shear test for the constant Mode II (α_{m0})

The test provides an insight into constant separation Mode II. Only the parameter α_{m0} is expected to evolve. Figure 5.14 illustrates the considered numerical examples.

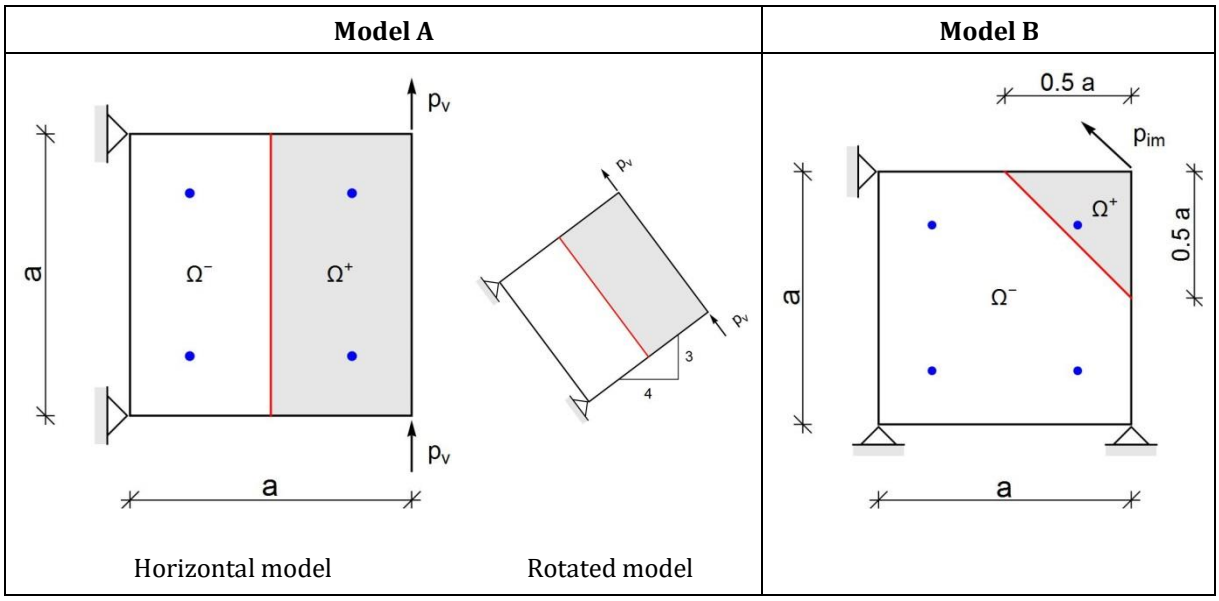

Figure 5.14: The geometry, the boundary conditions and the loading for two shear tests for the constant Mode II. The blue points represent the bulk integration points.

Slika 5.14: Strižni test za konstanten način širjenja razpoke v tangentni smeri: Geometrija, robni pogoji in obtežba za dva strižna testa za linearen Mode II. Modre pike so integracijske točke po elementu.

Model A

One finite element is fully supported on the left side. The pre-existed crack line without the resistance runs vertically through the element center. The right side of the element is subjected to a pair of imposed vertical displacements $p_v = \lambda p_0$, with $p_0 = 1$ mm. The analysis is performed for $\lambda_{max} = 30$, i.e. $p_v = 30$ mm. We consider the horizontal and the rotated configuration of the *Model A*.

Since the crack does not exhibit any resistance, the constant separation Mode II is expected to evolve (at $p_v = 30$ mm , one should have $\alpha_{m0} = 30$ and $\alpha_{m1} = 0$) and the stresses should be zero over the element's domain. The results meet the expectations for both configurations of the *Model A*. In case of the [Q6+ G-Linder], the stabilization parameter $\kappa = 1$ from (Linder and Armero, 2007) (see *Remark 5.5*) is used to establish the analysis convergence.

Table 5.1: Results for the shear test for the constant Mode II, Model A (the horizontal and the rotated configurations provide the same results).

Preglednica 5.1: Rezultati strižnega testa za konstantni Mode II, Model A (za horizontalen in zasukan model dobimo enake rezultate).

ED-FE		$\lambda_{max} = 30$	
Q4+km [G-Linder]	OK	$\alpha_{m0} = 30$ and $\alpha_{m1} = 0$	$\boldsymbol{\sigma} = \mathbf{0}$
Q4+km [G-Dujc]	OK	$\alpha_{m0} = 30$ and $\alpha_{m1} = 0$	$\boldsymbol{\sigma} = \mathbf{0}$
Q6+km [G-Linder]	If $\kappa = 1$, then OK	$\alpha_{m0} = 30$ and $\alpha_{m1} = 0$	$\boldsymbol{\sigma} = \mathbf{0}$
Q6+km [G-Dujc]	OK	$\alpha_{m0} = 30$ and $\alpha_{m1} = 0$	$\boldsymbol{\sigma} = \mathbf{0}$

Model B (single-node-separation)

One element is fully supported in three nodes. The fourth node is subjected to the imposed displacement $p_{im} = \lambda p_0$, with $p_0 = 1$ mm. The imposed displacement direction is parallel to the pre-existed crack line direction. Figure 5.14 (right) shows the geometry and boundary conditions of the Model B. The analysis is performed for $\lambda_{max} = 30$, i.e. $p_v = 30$ mm.

We got the same results as for Model A, i.e. at $p_{imp} = 30$ mm the jump-parameters for Mode II are $\alpha_{m0} = 30$ and $\alpha_{m1} = 0$ and the stresses are zero over the element's domain area. In case of ED-FE with the [G-Linder] operators, the stabilization parameter κ from (Linder and Armero, 2007) must be set $\kappa = 1$ to establish the analysis convergence. In (Linder and Armero, 2007), it is reported that the "single-node-separation" is prone to computational sensitivity. In case of ED-FE with the [G-Linder] operators, all crack separation modes and fully softened state (stiffness is zero), the singularity of the $\boldsymbol{K}^e_{\alpha\alpha}$ can appear. They recommend using the stabilization parameter $\kappa > 0$ (see *Remark 5.5*). Here, the shear test confirms that using $\kappa = 1$ significantly improves computation convergence.

Table 5.2: Results for the shear test for the constant Mode II, Model B.

Preglednica 5.2: Rezultati strižnega testa za konstantni Mode II, Model B.

ED-FE		$\lambda_{max} = 30$	
Q4+km [G-Linder]	If $\kappa = 1$, then OK	$\alpha_{m0} = 30$ and $\alpha_{m1} = 0$	$\boldsymbol{\sigma} = \mathbf{0}$
Q4+km [G-Dujc]	OK	$\alpha_{m0} = 30$ and $\alpha_{m1} = 0$	$\boldsymbol{\sigma} = \mathbf{0}$
Q6+km [G-Linder]	If $\kappa = 1$, then OK	$\alpha_{m0} = 30$ and $\alpha_{m1} = 0$	$\boldsymbol{\sigma} = \mathbf{0}$
Q6+km [G-Dujc]	OK	$\alpha_{m0} = 30$ and $\alpha_{m1} = 0$	$\boldsymbol{\sigma} = \mathbf{0}$

5.4.2 Shear test for the linear Mode II (α_{m1})

The element is subjected to tension load that causes the development of the jump-parameter α_{m1}. Figure 5.15 illustrates the considered configurations.

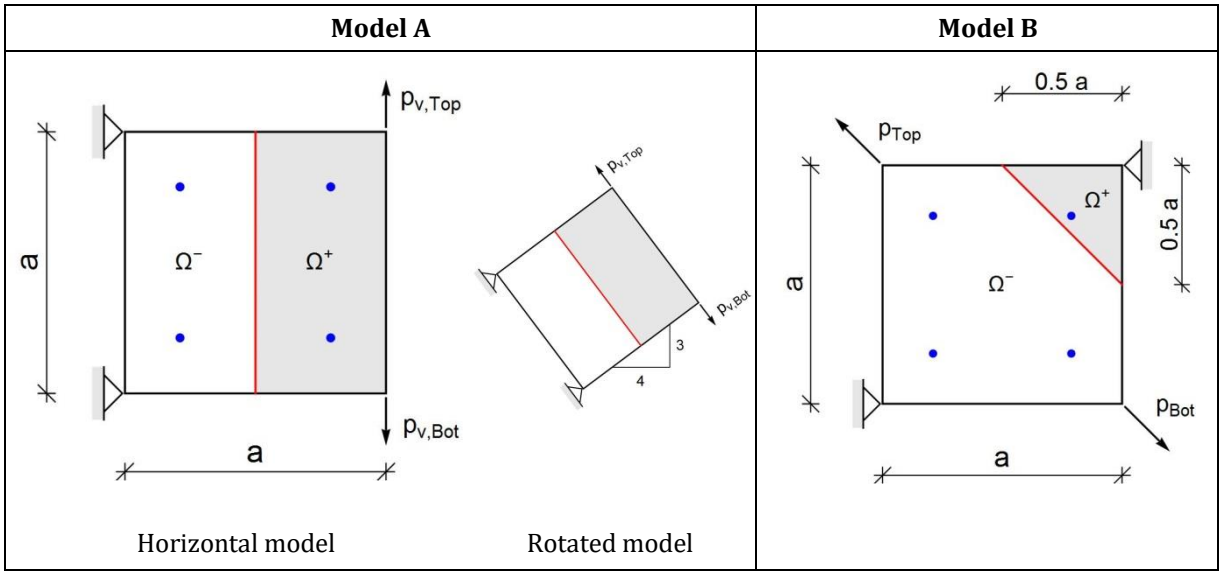

Figure 5.15: The geometry, the boundary conditions and the loadings for two shear tests for the linear Mode II. The blue points represent the bulk integration points.

Slika 5.15: Strižni test za linearen način širjenja razpoke v tangentni smeri: Geometrija, robni pogoji in obtežba za dva strižna testa za linearen Mode II. Modre pike so integracijske točke po elementu.

Model A

The test is taken from (Linder and Armero, 2007). The element is fully supported on the left side. The pre-existing crack line without the resistance runs vertically through the elements center. The right side of the element is subjected to a pair of opposite imposed vertical displacements $p_{v,Top} = -p_{v,Bot} = \lambda p_0$, with $p_0 =$ 1 mm. The analysis is performed for $\lambda_{max} = 30$. We consider the horizontal and the rotated configurations (Figure 5.15).

Since the crack does not exhibit any resistance, the linear separation Mode II is expected to evolve (at $\lambda =$ 30, we expect $\alpha_{m0} = 0$ and $\alpha_{m1} = 0.30$). Consequently, the stress component σ_{yy} should be constant over the Ω_e^+ domain area and the stress field of the Ω_e^- domain area should remain zero.

The horizontal and the rotated configurations return the same results. Only the [Q4+G-Linder] meets the expected behaviour. The model [Q4+G-Dujc] clearly shows that the [G-Dujc] operators are not reliable when linear shear mode II is active. In this test, the ED-FE [Q4+G-Dujc] returns negative parameter α_{m1}, which indicates contraction along the failure line. This does not fit the tension stress state in the subdomain Ω_e^+. The computed responses get even worse when the incompatible displacements are included.

Table 5.3: Results for the shear test for the linear Mode II, Model A (the horizontal and the rotated configurations provide the same results).

Preglednica 5.3: Rezultati strižnega testa za linearen Mode II, Model A (Za horizontalen in zasukan model dobimo enake rezultate).

ED-FE		$\lambda_{max} = 30$	
Q4+km [G-Linder]	OK	$\alpha_{m0} = 0$ $\alpha_{m1} = 0.30$	$\boldsymbol{\sigma}\|_{\Omega^-} = \mathbf{0}$, $\boldsymbol{\sigma}\|_{\Omega^+} = \{0 \quad \sigma_{yy}^+ \quad 0\}^T$ $\sigma_{yy}^+ = 9000$ MPa
Q4+km [G-Dujc]	NOT OK	$\alpha_{m0} = 0$ $\alpha_{m1} = -0.067$	$\boldsymbol{\sigma}\|_{\Omega^- Top} = \{0 \quad 2328 \quad 1590\}^T$ MPa $\boldsymbol{\sigma}\|_{\Omega^- Bot} = \{0 \quad 2328 \quad -1590\}^T$ MPa $\boldsymbol{\sigma}\|_{\Omega^+ Top} = \{0 \quad 6672 \quad 1590\}^T$ MPa $\boldsymbol{\sigma}\|_{\Omega^+ Bot} = \{0 \quad 6672 \quad -1590\}^T$ MPa
Q6+km [G-Linder]	$\kappa = 1$, NOT OK	$\alpha_{m0} = 0$ $\alpha_{m1} = 0$	$\boldsymbol{\sigma}\|_{\Omega^-} = \{0 \quad 1902 \quad 0\}^T$ MPa $\boldsymbol{\sigma}\|_{\Omega^+} = \{0 \quad 7098 \quad 0\}^T$ MPa
Q6+km [G-Dujc]	NOT OK	$\alpha_{m0} = 0$ $\alpha_{m1} = -0.410$	Constant stress field over the element domain Ω $\boldsymbol{\sigma} = \{0 \quad 4500 \quad 0\}^T$ MPa

Model B (single-node-separation)

Figure 5.15 (right) shows the geometry and the boundary conditions of Model B. A pair of non-adjacent nodes is fully supported, the other nodes are subjected to a pair of opposite imposed displacements $p_{Top} = -p_{Bot} = \lambda p_0$, with $p_0 = 1$ mm. The imposed displacement direction is parallel to the pre-existed crack line direction (see Figure 5.15, right). The analysis is performed for $\lambda_{max} = 30$, i.e. $p_{Top} = -p_{Bot} = 30$ mm.

Since the crack does not exhibit any resistance, the linear separation Mode II is expected to evolve (at $\lambda = 30$, one expects $\alpha_{m0} = 0$ and $\alpha_{m1} > 0$). None of the elements could describe crack opening in linear Mode II ($\alpha_{m1} > 0$). In case of the [G-Linder] operators, the stabilization parameter κ from (Linder and Armero, 2007) (see *Remark 5.5*) must be set $\kappa \geq 1$ to establish the analysis convergence.

Conclusions about the shear tests

- The shear tests for constant Mode II show that all models meet the expected behaviour.
- The element with the [G-Dujc] operators for linear Mode II does not return the correct results.
- The ED-FE with [G-Dujc] operators does not need the stabilization parameter κ. Additionally, the element with [G-Dujc] operators converges well in combination with the incompatible mode method, while it is not true for [G-Linder] operators.
- In case of shear test for linear Mode II, the incompatible modes ruin behaviour of ED-FE. The numerical simulations return wrong stresses and consequently, false results for jump-in-displacements parameters.
- In case of shear test for linear Mode II and single node separation, none of the elements response correct. The linear Mode II needs to be further investigated.

- At last, we suggest setting the [G-Linder] operator for the linear Mode II.

Table 5.4: Results for the shear test for the linear Mode II, Model B.

Preglednica 5.4: Rezultati strižnega testa za linearen Mode II, Model B.

ED-FE		$\lambda_{max} = 30$	
Q4+km [G-Linder]	$\kappa = 10^5$, NOT OK	$\alpha_{m0} = 0$ $\alpha_{m1} = 0$	Constant stress field over the element domain Ω $\boldsymbol{\sigma} = \{3182 \quad 3182 \quad -3182\}^T$ MPa
Q4+km [G-Dujc]	NOT OK	$\alpha_{m0} = 0$ $\alpha_{m1} = -0.121$	$\boldsymbol{\sigma}\|_{\Omega^-} = \{3181 \quad 3181 \quad -3181\}^T$ MPa $\boldsymbol{\sigma}\|_{\Omega^+} = \{1364 \quad 1364 \quad -1364\}^T$ MPa
Q6+km [G-Linder]	$\kappa = 1$, NOT OK	$\alpha_{m0} = 0$ $\alpha_{m1} = 0$	Constant stress field over the element domain Ω $\boldsymbol{\sigma} = \{3182 \quad 3182 \quad -3182\}^T$ MPa
Q6+km [G-Dujc]	NOT OK	$\alpha_{m0} = 0$ $\alpha_{m1} = -0.283$	$\boldsymbol{\sigma}\|_{\Omega^+} = \{1061 \quad 1061 \quad -1061\}^T$ MPa $\boldsymbol{\sigma}\|_{\Omega^- Bot,Right} = \{3182 \quad 3182 \quad -3182\}^T$ MPa $\boldsymbol{\sigma}\|_{\Omega^- Top,Left} = \{3182 \quad 3182 \quad -3182\}^T$ MPa $\boldsymbol{\sigma}\|_{\Omega^- Bot,Left} = \{1061 \quad 1061 \quad -1061\}^T$ MPa

5.5 Conclusions

We conducted a set of simple tests to check the effectiveness of the embedded discontinuity model, when softening is active. We were interested in: the performance of Q4 and Q6 element formulation in combination with the embedded discontinuity and the G-operators that are applied in the embedded discontinuity finite element. Three different tests are performed for horizontal and rotated mesh configuration: tension test, bending test and shear test.

The results confirms the invariance of both groups of the G-operators ([G-Dujc] and [G-Linder]) with respect to the choice of the coordinate system, since the horizontal and the rotated model configurations have the same response. If only the constant separation modes (n0 and m0) are active, both G-operators ([G-Dujc] and [G-Linder]) perform well.

In case of bending tests, the [G-Dujc] operators perform well in all models. The incompatible mode method significantly improves the behaviour of finite elements with embedded-discontinuity (ED-FE) in bending problems. The elements with the [G-Linder] operators are better, when the linear relation ($t_m = k_m \bar{\bar{v}}$) for Mode II is used.

In case of shear test for linear Mode II, only the model "Q4 + [G-Linder]" meets the expected behaviour. The computed results get worse, when the incompatible displacements are included (Q6).

When a failure line crosses the adjacent element's sides (i.e. single node separation), it makes difficult to describe the linear part of crack separation modes (α_{n1} and α_{m1}). We demonstrated that none finite elements with the single node separation do not pass the shear test for linear Mode II. It needs to be further investigated.

Based on the results for the one- or two-element tests, we recommend setting the [G-Dujc] operators for all separation modes except for linear Mode II. For linear Mode II, the [G-Linder] operator is suggested. However, the sliding Mode II needs to be further investigated

6 NUMERICAL EXAMPLES WITH STRONG DISCONTINUITY QUADRILATERALS

Three numerical examples are presented in this section. Two types of analysis were performed for each example: (a) by using the crack tracing algorithm (Figure 4.6), and (b) without any crack tracing algorithm.

Let us recall that the crack is embedded in the finite element when the major principal tensile stress at "the center of the element" σ_1 is larger or equal to the material tensile strength σ_{un} (4.113). The normal on the crack $\boldsymbol{n}$ coincides with the direction of the major principal stress at crack appearance.

To describe the bulk behavior, linearly elastic constitutive relations are used in all examples. The cohesion in the crack is described by two uncoupled, 1d, non-associative, elasto-damage traction-separation laws with exponential softening. One is used for the normal direction $\boldsymbol{n}$ (i.e for the mode I opening), and the other one for the tangent (shear) direction $\boldsymbol{m}$ (i.e for the mode II opening). For mode I, the damage law describes: (1) inelastic decrease of normal traction t_n when normal crack opening $\bar{\bar{u}}_n$ increases, i.e. inelastic unloading, and (2) elastic unloading when normal crack opening $\bar{\bar{u}}_n$ is decreasing. We note that for the case (2), no special requirements are introduced when $\bar{\bar{u}}_n \to 0$. In fact, the situation $\bar{\bar{u}}_n < 0$ and $t_n < 0$ is not prevented. Thus, the case (2) calls for an improvement. However, in the computed examples, the element cracks are not closing, and the implemented version of case (2) does not produce any problems. The details of the considered softening elasto-damage laws are given in Section 4.2.5.2.

The presented results were obtained by 2x2 bulk Gauss integration points and 2 Gauss integration points along the discontinuity line (i.e. crack). At these 2 points, the tractions t_n and t_m were computed.

Let us also briefly describe the crack tracing algorithm from Figure 4.6 that is used for analyses (a). Once the converged configuration at pseudo time τ_n is reached for the load factor λ_n, the stresses in the crack-front element are checked. If the crack embedding criteria is fulfilled at the crack-front element, the following is done: (i) the crack is embedded in the crack-front element, (ii) its normal $\boldsymbol{n}$ is computed and set fixed for further computations, and (iii) the step back in analysis is performed in order to re-compute for the load factor λ_n with the new crack configuration that takes into account its propagation for one more element. The procedure (i)-(iii) is repeated for load level λ_n, until the stress state in the current crack-front-element suggests no crack embedding. Only then the algorithm proceeds to seek solution at the next pseudo-time step τ_{n+1}. Thus, the crack can propagate for more than one element in the solution increment $[\tau_{n-1}, \tau_n]$. This algorithm, presented also in Figure 4.6, is similar to the one proposed in (Wu et al., 2015).

The used crack tracing algorithm enforces the continuous geometry of the crack. In other words, the crack line is continuous across element edge. Of course, the crack opening parameters are not continuous across element edge, since they are condensed on the element level, and the continuity of α_m is not required, but the crack line is continuous. However, it may happen that the continuity of the crack line is not enforced. Such a situation is shown in Figure 6.1, where the computed orientation of the last front-crack element does not allow for a continuation of the crack. This might sometimes happen at the last crack-front element, just

before the crack would completely separate the structure in two disconnected parts. In such a case, the crack tracing algorithm does not embed the crack for $\sigma_1^e \geq \sigma_{un}$.

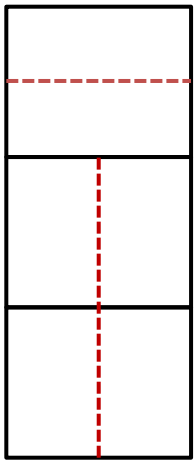

Figure 6.1: Rotation of the potential crack for approximately 90° in the crack-front element with respect to the existing vertical crack. The crack in the crack-front element is not embedded in such case.

Slika 6.1: Zasuk potencialne razpoke za približno 90°v prednjem elementu za razpoko glede na obstoječo vertikalno razpoko. V tem primeru se razpoka ne umesti v prednji element.

For computing the examples, the following elements were used: (A) displacement-based embedded-discontinuity quadrilateral derived in Section 4.2 that will be denoted as Q4 below, and (B) incompatible-displacements-based embedded-discontinuity quadrilateral derived in Section 4.3 that will be denoted as Q6 below. The elements use two types of $\overline{\widehat{\boldsymbol{G}}}_m, m = 1, \cdots, 4$ operators. In what follows, the $\overline{\widehat{\boldsymbol{G}}}_m$ operators from Section 4.2.3.1 will be referred to as those from (Dujc et al., 2010), since they were first presented there. The $\overline{\widehat{\boldsymbol{G}}}_m$ operators from Section 4.2.3.2 will be referred to as those from (Linder and Armero, 2007), since they were first presented there.

The examples were computed for different combinations of element basic separation modes. The following notation will be used:

- combination of all four basic separation modes will be denoted as “Mode I + Mode II” or yet as “Mode I+II”
- combination of mode I basic separation modes, $m = 1$ and $m = 2$, will be denoted as “Mode I”
- combination of mode II basic separation modes, $m = 3$ and $m = 4$, will be denoted as “Mode II”
- combination of constant parts of mode I and mode II basic separation modes, $m = 1$ and $m = 3$, will be denoted as “n0 + m0”.

The Newton's incremental-iterative method was applied to compute the examples. The incremental value of the load factor was changing as $\Delta\lambda_n = B(I_o, I_{n-1})\,\Delta\lambda_{n-1}$, $\Delta\lambda_n \in [\Delta\lambda_{min}, \Delta\lambda_{max}]$ The adjustable factor B is

a function of two parameters: I_0, which is a desired number of incremental iterations, and I_{n-1}, which represents a number of iterations in the last performed incremental computation (Korelc, 2016)

$$B = \begin{cases} 2 - \left(\frac{I_{n-1} - 1}{I_o - 1}\right)^2, & I_{n-1} < I_o \\ 1 - \frac{1}{2}\left(\frac{I_{n-1} - I_o}{N - I_o}\right)^2, & I_{n-1} \geq I_o \end{cases} \tag{6.1}$$

In (6.1), N is the maximum allowed number of iterations. When the Newton's incremental-iterative method was not applicable, the arc-length method of (Pohl et al., 2014) and (Stanić et al., 2016) was used.

6.1 Three-point bending test

We consider a simply supported concrete beam (Figure 6.2) of length L = 200 cm, height h = 20 cm and thickness t = 5 cm. At its half-length it has a notch of dimensions a = 0.4 cm and b = 10 cm. The beam is loaded at the middle of the span, on the upper edge, with imposed vertical displacement λp_0, where $p_0 =$ 0.1 cm, and λ is the load factor. The Q4 element, which was used for computing this example, has $\bar{\bar{\boldsymbol{G}}}_1$, $\bar{\bar{\boldsymbol{G}}}_2$ from (Dujc et al., 2010) and $\bar{\bar{\boldsymbol{G}}}_3$, $\bar{\bar{\boldsymbol{G}}}_4$ from (Linder and Armero, 2007). The bulk data are (Linder and Armero, 2007): elastic modulus E = 3000 kN/cm², Poisson ratio ν = 0.2, and tensile strength $\sigma_{un} = 0.333$ kN/cm². The used Q4 element allows crack opening in mode I and crack sliding in mode II, although, due to the nature of the considered problem, only mode I was activated in the analysis. The crack starts to open in mode I and mode II when the corresponding tractions are equal to or greater to σ_{un} and σ_{um}, respectively. The values for σ_{un} and σ_{um} are 0.333 kN/cm² and the fracture energies G_{fn} and G_{fm} for mode I and mode II, respectively, are 0.115 10^{-2} kN/cm (Petersson, 1981). Figure 6.3 shows the used finite element mesh, which is much refined in the region where the crack is expected to occur and propagate.

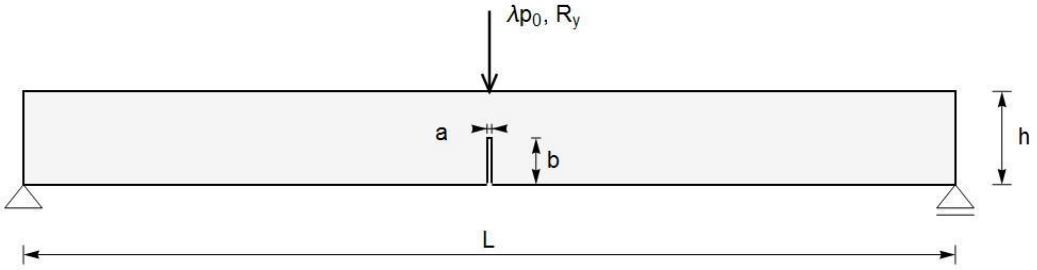

Figure 6.2: Three point bending test: geometry, boundary conditions and loading.

Slika 6.2: Tri-točkovni upogibni test: geometrija, robni pogoji in obtežba.

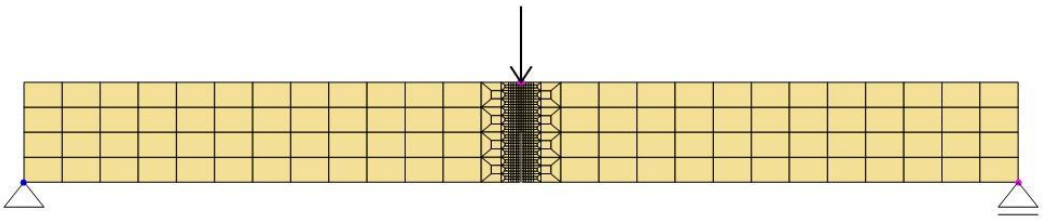

Figure 6.3: Finite element mesh.

Slika 6.3: Mreža končnih elementov.

6.1.1 Analysis with crack tracing algorithm

The results obtained by using the crack tracing algorithm (Figure 4.6) are presented in Figure 6.4 and Figure 6.5, which show dependence of the force R_y on the imposed displacement $u_y = \lambda p_0$. Figure 6.4 illustrates nice matching of the computed results with the range of experimental data presented in (Petersson, 1981). In Figure 6.5, a comparison of the results with respect to prescribed maximal load factor $\Delta\lambda_{max}$ is shown. The choice of $\Delta\lambda_{max}$ has influence on the size of load increment $\Delta\lambda$: the smaller $\Delta\lambda_{max}$ the smaller $\Delta\lambda$ and vice versa. Figure 6.5 illustrates that the shapes of $R_y(u_y)$ curves depend only slightly on $\Delta\lambda_{max}$, however, the convergence is considerably better for smaller $\Delta\lambda$ (allowed by smaller $\Delta\lambda_{max}$). For larger $\Delta\lambda$ (allowed by larger $\Delta\lambda_{max}$), up to three elements develop a crack in a single load increment, which is worsening the convergence. For larger $\Delta\lambda_{max}$ the analysis fails after several softening steps, and for smaller $\Delta\lambda_{max}$ the analysis proceeds until $R_y \approx 0$, more precisely, until only one element resists to the final beam collapse, see Figure 6.6. The situation in the last resisting element is the one shown in Figure 6.1. The convergence is illustrated in Table 6.1 and Table 6.2. Force-displacement curves obtained with smaller $\Delta\lambda$ exhibit jumps, see Figure 6.4 and Figure 6.5. At jump, the crack propagated for one more element and the cohesion softening was triggered in that element. For larger $\Delta\lambda$ the jumps are smoothed.

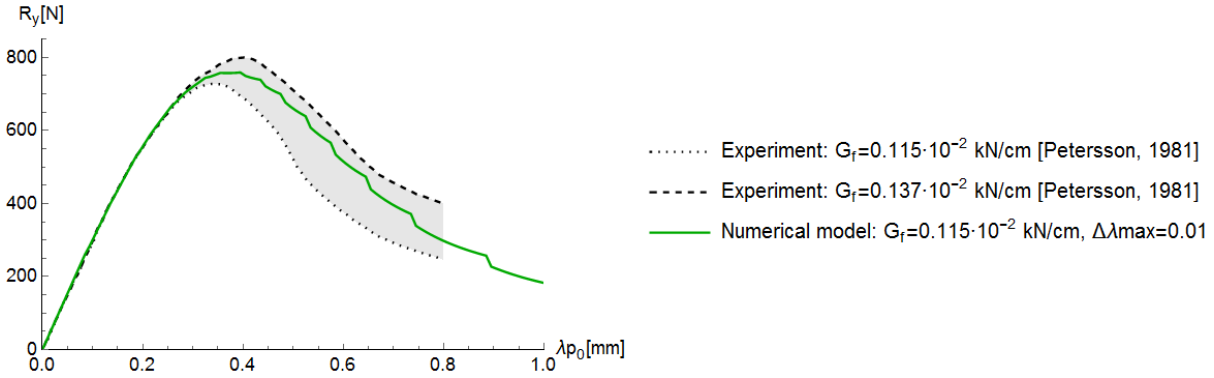

Figure 6.4: Force R_y versus imposed displacement u_y and comparison with the experimental results.

Slika 6.4: Diagram reakcija R_y v odvisnosti od vsiljenega pomika u_y in primerjava z rezultati eksperimenta.

The crack propagates along the mesh in mode I, triggering only two basic forms of element separation, $m = 1$ and $m = 2$, and leaving the other two basic forms, $m = 3$ and $m = 4$, silent. This is also evident from Figure 6.6, where final, deformed configuration of the mesh is presented. No problem with the crack orientation in the crack-front-element was observed during analysis. This is in contrast with reports in e.g. (Wu et al., 2015) stating that at some level of λ the crack-front-element developed horizontal crack instead of "logical" vertical crack, which caused analysis failure. The crack was approximately half way to the upper edge when crack rotation occurred. In (Dujc et al., 2010), the analysis was performed with predefined direction of $\boldsymbol{n}$ for all elements with crack in order to avoid such kind of problem. It seems that the applied crack tracing algorithm (Figure 4.6), which includes computation of the crack orientation in the crack-front-element before the step back, successfully overcomes the problem of physically unreasonable crack orientation in the crack-front-element at some load level.

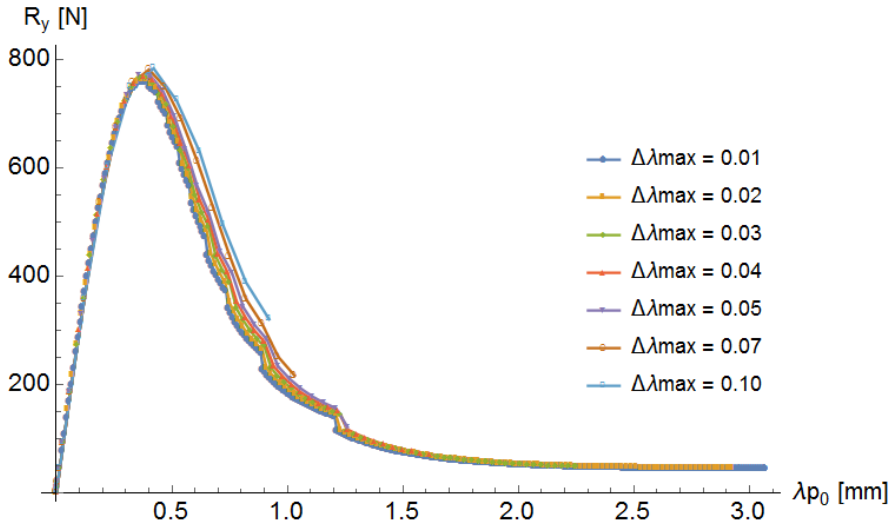

Figure 6.5: Force R_y versus imposed displacement u_y for different$\Delta\lambda_{max}$.

Slika 6.5: Diagram reakcija R_y v odvisnosti od vsiljenega pomika u_y za različne $\Delta\lambda_{max}$.

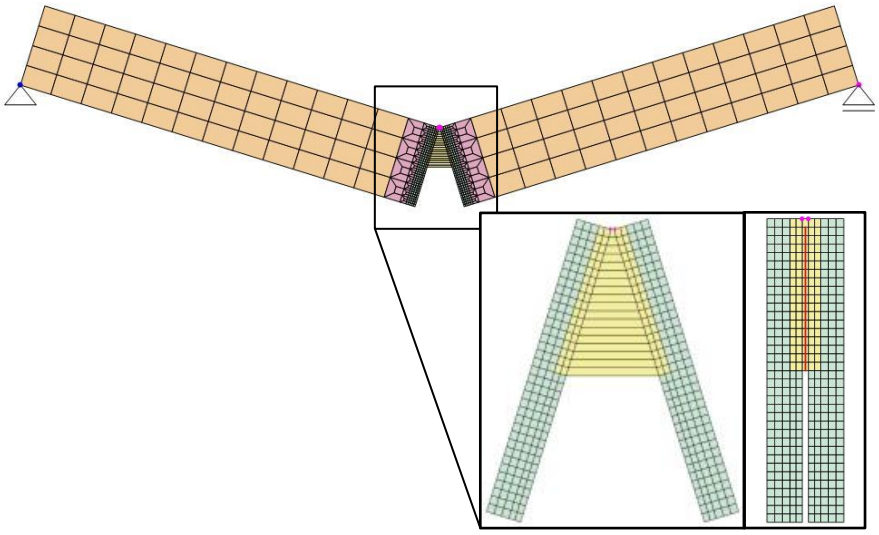

Figure 6.6: Deformed mesh at λ=3.07 (100-times scaled).

Slika 6.6: Deformacijska konfiguracija mreže končnih elementov pri λ=3.07 (100-times scaled).

Table 6.1: Convergence for 22nd solution increment, with crack in three elements, $\Delta\lambda_{max}$ = 0.01.

Preglednica 6.1: Konvergenca za 22. inkrement, z razpokami v treh elementih, $\Delta\lambda_{max}$ = 0.01.

Iteration *i*	$\|\Delta \boldsymbol{u}_{22}^{i}\|$	$\|\Delta \boldsymbol{R}_{22}^{i}\|$
1	6.72 E-03	362.94
2	1.07 E-04	5.79
3	6.77 E-06	1.00
4	1.72 E-09	8.74 E-05
5	1.72 E-09	2.77 E-11

Table 6.2: Convergence for 8th solution increment, with crack in three elements, $\Delta\lambda_{max}$ = 0.1.

Preglednica 6.2: Konvergenca za 8. inkrement, z razpokami v treh elementih, $\Delta\lambda_{max}$ = 0.1.

Iteration *i*	$\|\Delta \boldsymbol{u}_{8}^{i}\|$	$\|\Delta \boldsymbol{R}_{8}^{i}\|$
1	6.72 E-02	3629.38
2	5.61 E-04	28.19
3	1.24 E-04	13.18
4	5.74 E-05	8.26
5	9.47 E-08	5.49 E-03
6	2.15 E-13	8.42 E-09

6.1.2 Analysis without crack tracing algorithm

Analysis without the crack tracing algorithm was also performed in order to check results for such kind of analysis. The embedded-discontinuity elements were used only for the part of the mesh, which is coloured yellow in Figure 6.9. The crack was activated at the element when the criterion (4.113) was fulfilled. It was positioned to cross the center of the element.

The results are presented in Figure 6.7 – Figure 6.9. Figure 6.7 shows that this kind of modelling does not produce reasonable results for the softening part of the load versus imposed displacement curve. Namely, after certain number of elements with the crack, the $R_y(u_y)$ curve develops an upwards tendency, indicating that the structure becomes stiffer, which is obviously wrong. Note that "Q4: Mode I+II" and "Q6: Mode I+II" analyses failed at the beginning of softening. The element crack distribution throughout the mesh (i.e. the crack pattern) and their orientations, see Figure 6.8, seems to be such that the structural cracking mechanism cannot manifest in a clear way, see Figure 6.9, which results in a very stiff response after certain number of elements with the crack. Figure 6.8 and Figure 6.9 present crack patterns and the corresponding deformed mesh configurations at the end of analyses. Note that four analyses ("Q4: n0 + m0", "Q6: n0 + m0", "Q4: Mode I" and "Q6: Mode I") were performed up to imposed displacement $u_y = 2$ mm, and two analyses ("Q4: Mode I+II" and "Q6: Mode I+II") failed at the beginning of softening. Figure 6.8 shows that some of the elements developed horizontal cracks and Figure 6.9 shows that those horizontal cracks were actually the reason for the beginning of the increasing (i.e. wrong) structural stiffness.

More refined procedure for determination of orientation of element crack normal, see e.g. (Wu et al., 2015), would most probably help to get better results. Also, the use of inelastic, i.e. elasto-damage material model for the bulk, would most probably help to get better results, since such bulk material model would act as a precursor for element crack orientation and also for the distribution of cracks throughout the mesh.

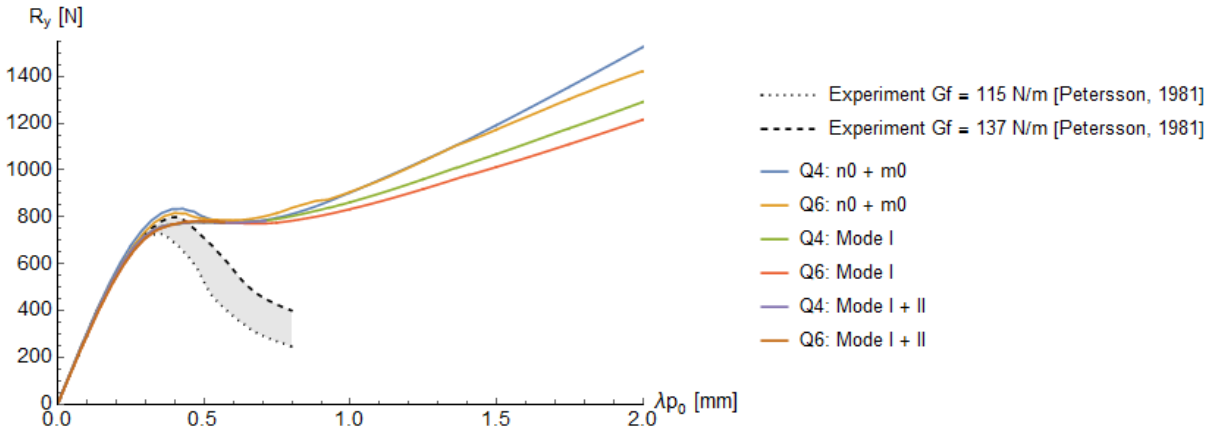

Figure 6.7: Reaction-displacement curves in comparison with the experimental results.

Slika 6.7: Diagram reakcije v odvisnosti od pomika in primerjava z rezultati eksperimenta.

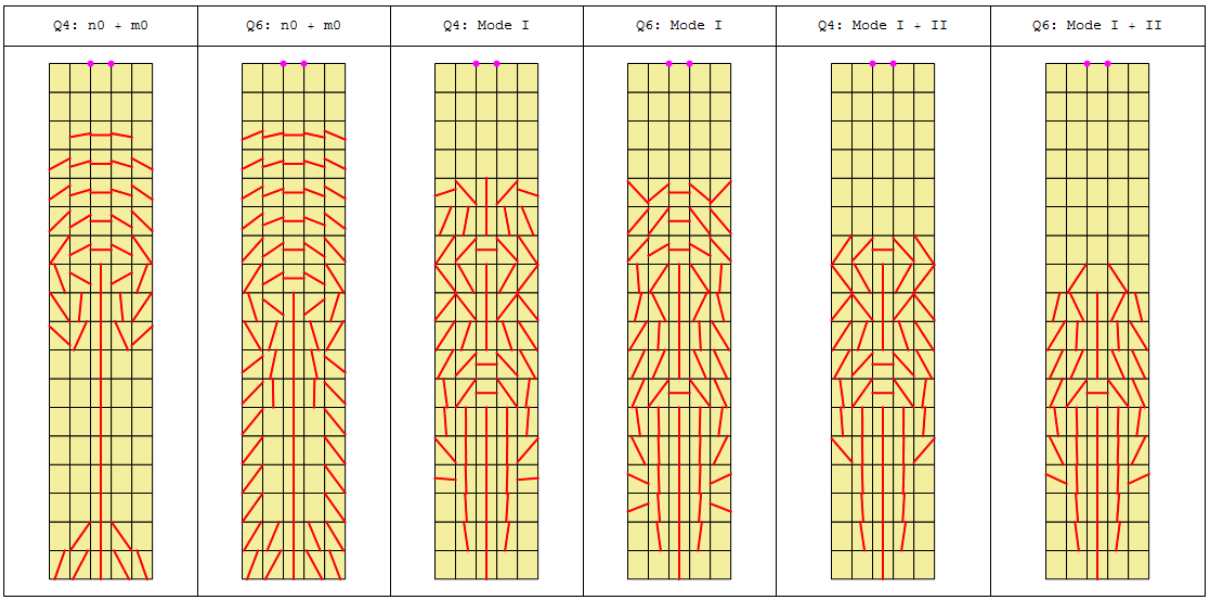

Figure 6.8: Final crack patterns.

Slika 6.8: Vzorci razpok na koncu analize.

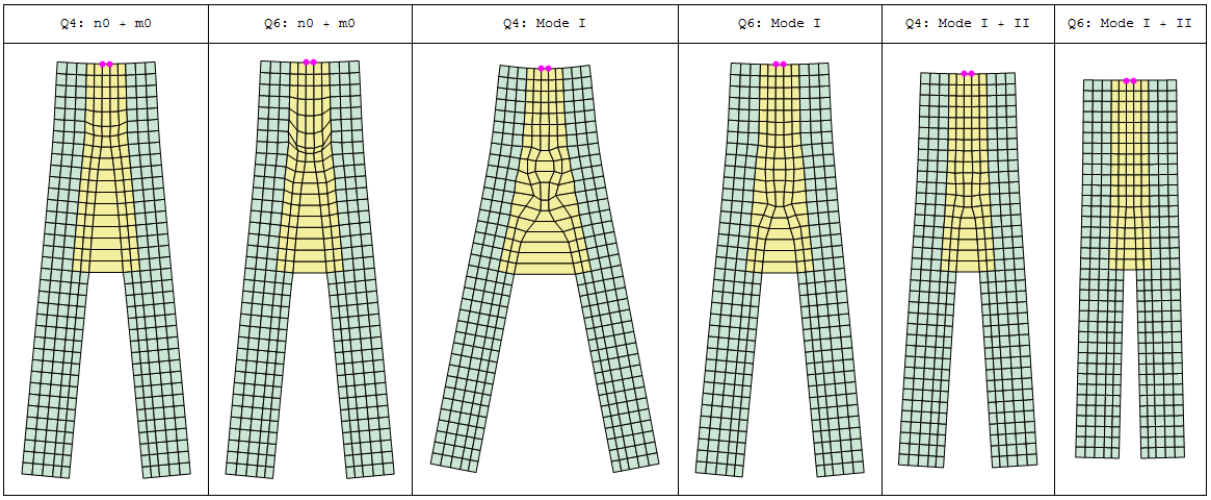

Figure 6.9: Final deformed meshes.

Slika 6.9: Deformacijske konfiguracije mrež končnih elementov na koncu analize.

6.2 Four-point bending test

We consider a simply supported concrete beam (Figure 6.10) of length L = 132.2 cm, height h = 30.6 cm, and thickness t = 15.6 cm, with the thin notch at its half-length. The loading consists of two vertical forces $0.13P_y$ and P_y, where $P_y = \lambda P_0$, $P_0 = 1$ N, and λ is load factor. The Q4 and Q6 elements that were used in this example have $\overline{\boldsymbol{G}}_1$, $\overline{\boldsymbol{G}}_2$ from (Dujc et al., 2010) and $\overline{\boldsymbol{G}}_3$, $\overline{\boldsymbol{G}}_4$ from (Linder and Armero, 2007). The non-standard arc-length method, which controls a single constantly increasing/decreasing degree of freedom,

see e.g. (Pohl et al., 2014), (Stanić et al., 2016), was applied to solve nonlinear equations. The chosen degree of freedom was vertical displacement at the crack mouth. The following data was used for the arc-length analysis: the convergence tolerance $tol = 10^{-8}$, the initial arc-length $l_0 = 10^{-5}$, the minimal arc-length $\Delta l_{min} = 10^{-6}$ and the maximal arc-length $\Delta l_{max} = 10^{-3}$. Figure 6.11 shows the finite element mesh, which is much refined in the region where the crack is expected to occur and propagate. The loading forces and the reactions are not introduced into the beam point-wise, but through small stiff devices that are modelled as elastic with elastic modulus $E = 28800$ kN/cm^2 and Poisson ratio $\nu = 0.2$.

The beam material data are (Linder and Armero, 2007): elastic modulus $E = 2880$ kN/cm^2, Poisson ratio $\nu = 0.18$, and tensile strength $\sigma_{un} = 0.28$ kN/cm^2. The used Q4 and Q6 elements allow crack opening in mode I and crack sliding in mode II. Activation of both modes (i.e. the combined mode) is expected to occur for this example, with predominant role of mode I though. The crack starts to open in mode I and mode II when the corresponding tractions are equal to or greater to σ_{un} and σ_{um}, respectively. The values of σ_{un} and σ_{um} are 0.28 kN/cm^2. Fracture energies G_{fn} and G_{fm} for mode I and mode II, respectively, are $0.1 \cdot 10^{-2}$ kN/cm (Linder and Armero, 2007). Generaly, the term mixed-mode damage refers to problems with one damage paramater and active separation mode I and mode II (Alfano and Crisfield, 2001). Since we use uncoupled constitutive law (see section 4.2.5.2) for the crack, we have two damage parameters. Therefore, in this section we will use term “combined mode” for problems with active mode I and mode II.

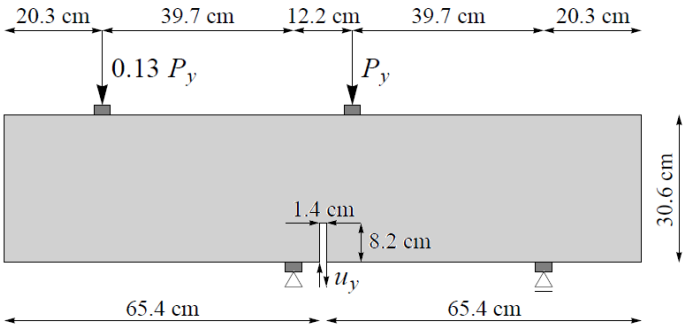

Figure 6.10: Four point bending test: geometry, boundary conditions and loading.

Slika 6.10: Štiri-točkovni upogibni test: geometrija, robni pogoji in obtežba.

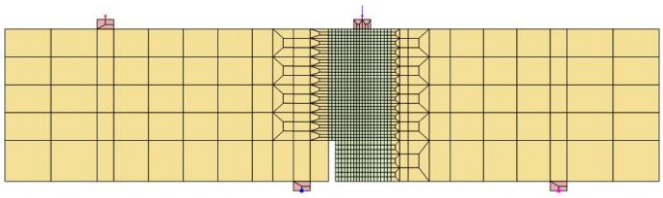

Figure 6.11: Finite element mesh.

Slika 6.11: Mreža končnih elementov.

6.2.1 Analysis with crack tracing algorithm

The results obtained by using the crack tracing algorithm (Figure 4.6) are presented in Figure 6.12 – Figure 6.15. Figure 6.12 shows the dependence of the load factor λ on the vertical crack mouth opening Δu, see Figure 6.10, and illustrates nice matching of the computed results with the range of experimental data presented in (Arrea and Ingraffea, 1982). Figure 6.12 shows results for elements that have only two constant basic separation modes. This combination gives the best results among several tested combinations, as shown in Figure 6.13. The other combinations give much poorer results due the convergence failures of analyses at $\Delta u \approx 0.1$ mm. The dot in Figure 6.13 shows location of the last element crack embedding before the convergence failure.

In this example, the crack propagates in combined type, which is a combination of type I normal crack opening and type II crack sliding. It is thus understandable that "Mode I" combination does not perform well. Why the element behavior is problematic for combined crack opening "Mode I + Mode II" combination of basic separation modes, still needs to be investigated.

Let us note that the 4-points bending test example was computed by embedded-strong-discontinuity quadrilaterals also in (Linder and Armero, 2007), with combination "Mode I + Mode II". The extremely fine mesh was used in the region of crack propagation, so that the element stress state in that region was close to the constant one. It is reasonable to assume that at constant stress state the constant parts of basic separation modes, i.e. $m = 1$ and $m = 3$ become predominant, and that the other two modes, i.e. $m = 2$ and $m = 3$ become negligible. This was probably the case in (Linder and Armero, 2007). It seems that (Linder and Armero, 2007) "Mode I + Mode II" analysis was very close to "n0 + m0" analysis due to the extremely fine mesh used. The same example was computed also in (Manzoli in Shing, 2006) by "Q4+Stress hybrid" embedded-weak-discontinuity quadrilateral. Their analyses were successful for "n0 + m0" and "Mode I + Mode II" formulations. One can conclude from the above that the robustness of the derived embedded-discontinuity quadrilaterals for the combined type opening of the crack is still not optimal.

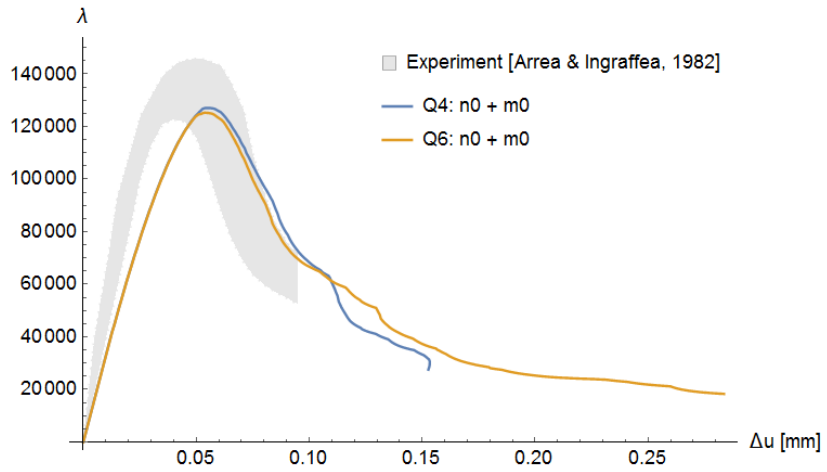

Figure 6.12: Load factor λ versus vertical crack mouth opening for combinationof constant separation modes.

Slika 6.12: Diagram faktor obtežbe λ v odvisnosti od vertikalnega relativnega pomika na ustju razpoke za kombinaciji konstantnih načinov širjenja razpoke.

The crack paths in the finite element mesh are shown in Figure 6.14. The location of crack beginning (at the top of the notch) does not result from computations but it was rather chosen before the analysis. Figure 6.14 shows that all the crack paths are practically on the top of each other. However, the crack path lengths differ for different combinations of basic forms of element separation. Figure 6.12 and Figure 6.14 show that Q6 allows to compute larger Δu than Q4 for "n0 + m0" combination. The Q6 crack propagates two more elements than the Q4 crack before the analysis fails. On the other hand, the Q6 with "Mode I + Mode II" combination computes the shortest Δu. This suggests that the convergence ability does not depend only on the background formulation, which is either Q4 or Q6. Furthermore, Figure 6.13 shows that "Q4: n0 + m0", "Q6: n0 + m0" and "Q4: Mode I + Mode II" results have one tendency in the softening, while the other three formulations tend to behave stiffer in the softening. Figure 6.15 shows deformed finite element configuration.

The above presented analyses were performed with the 1d non-associative, softening elasto-damage constitutive relations. Those relations were used to describe crack cohesion for both mode I crack opening and mode II crack sliding. The mode I and mode II constitutive relations were uncoupled, i.e. the 1d relations for mode I were not coupled with 1d relations for mode II. Let us mention that we also implemented the following uncoupled 1d constitutive relations: the above mentioned softening elasto-damage model for mode I opening, and simple linear elastic relation $t_m = k_m \bar{\bar{u}}_m$, with $k_m = 2.88\ \frac{\text{MPa}}{\text{mm}}$, for mode II sliding. The same mode II relation was used in (Linder and Armero, 2007) for all computed examples in that reference. With this approach, all the analyses (with different combinations of basic separation modes) failed very quickly.

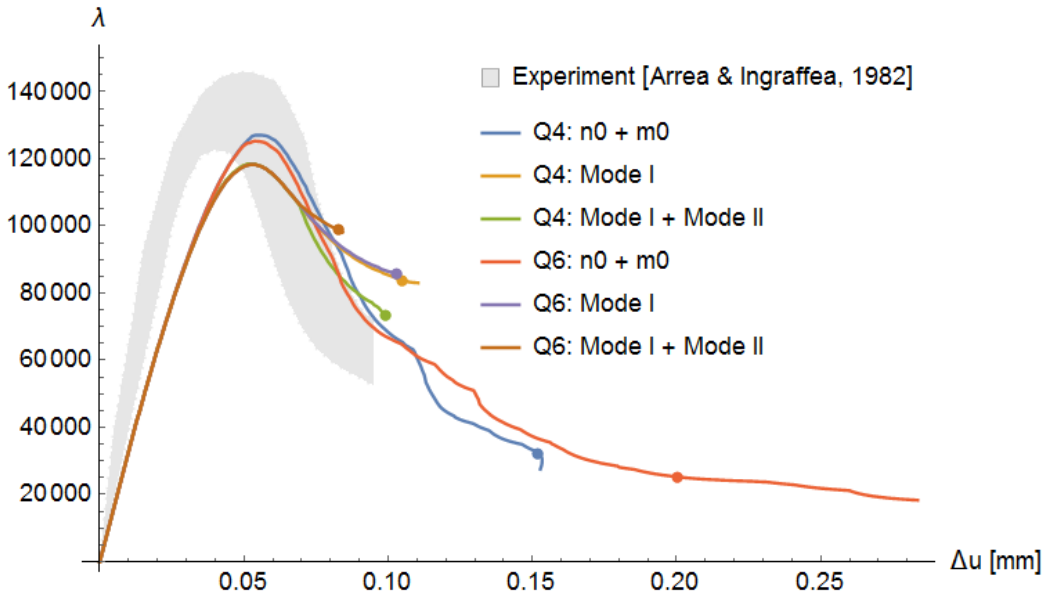

Figure 6.13: Load factor λ versus vertical crack mouth opening. The dot represents the last change of crack configuration.

Slika 6.13: Diagram faktor obtežbe λ v odvisnosti od relativnega razmika na ustju razpoke. Točka prestavlja zadnjo spremembo v konfiguraciji razpok.

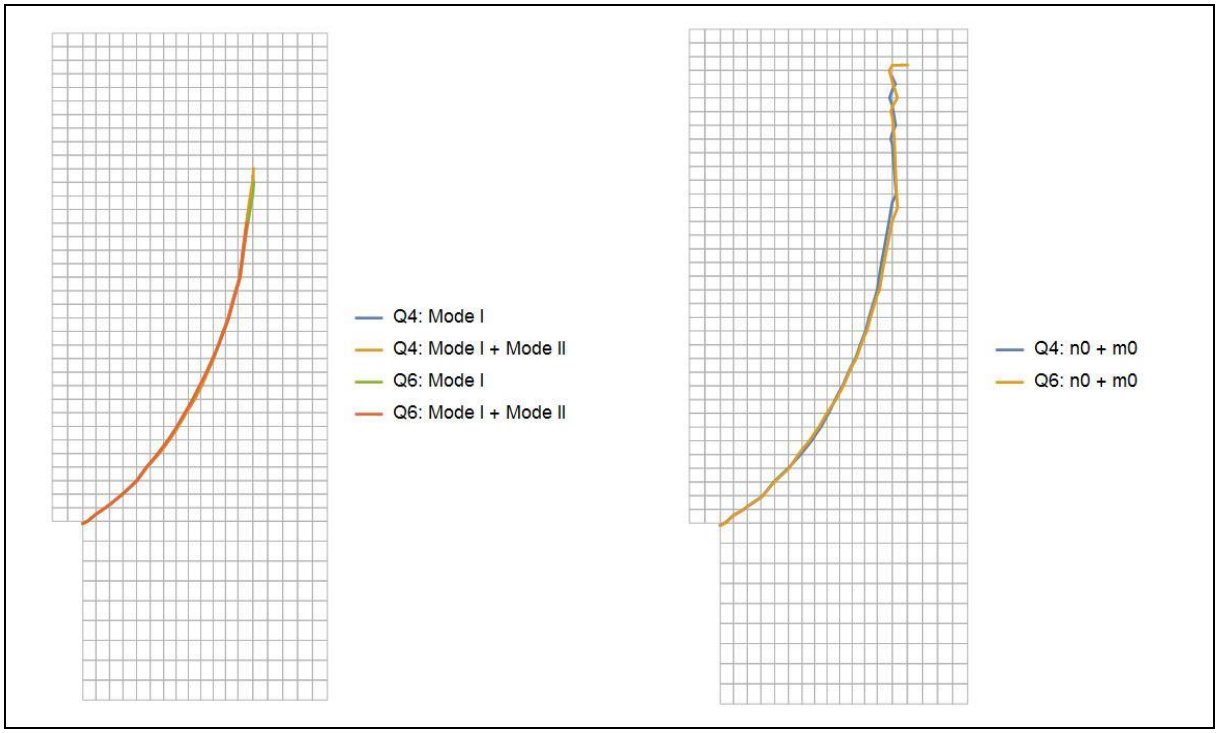

Figure 6.14: The crack paths.

Slika 6.14: Poti razpoke.

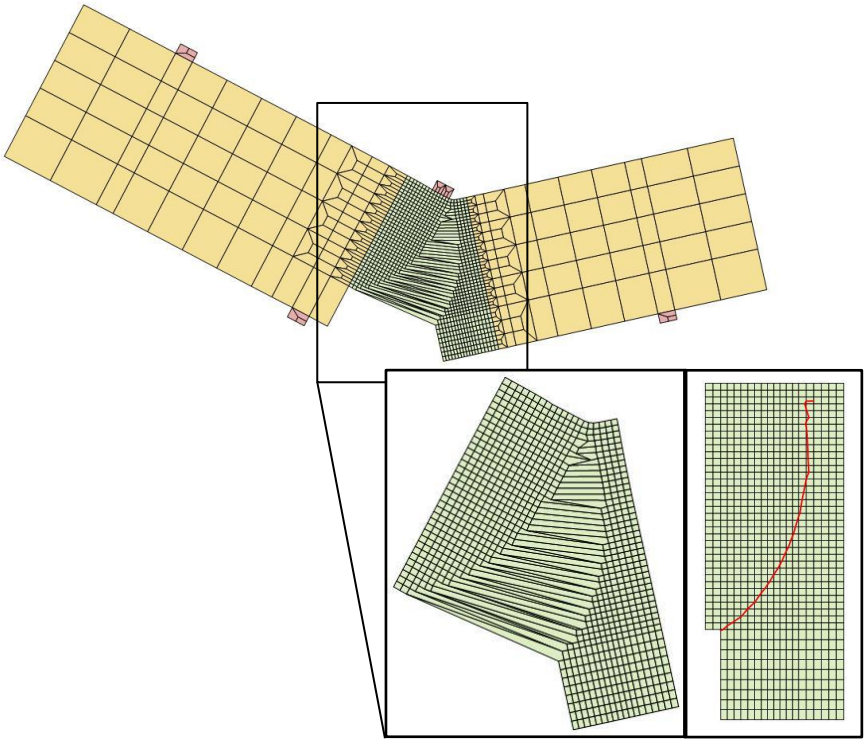

Figure 6.15: Deformed finite element mesh at the end of "Q6: n0+m0" analysis (the deformations are 100 times magnified).

Slika 6.15: Deformirana mreža končnih elementov ob koncu analize za Q6 (deformacije so 250-krat povečane).

6.2.2 Analysis without crack tracing algorithm

The same example was recomputed without the crack tracing algorithm in order to check results of such analysis. The embedded-discontinuity elements were used only for the part of the mesh, which is presented in Figure 6.17 and Figure 6.18. The crack was embedded at the element when the criterion (4.113) was fulfilled in such a way that it crossed the center of the element.

The results are presented in Figure 6.16 – Figure 6.18. Figure 6.16 shows the dependence of the load factor λ on the vertical crack mouth opening Δu. The bigger limit loads are computed as in the case of continuous crack analysis. The analyses fail soon after they pass the limit-load point, except "Q6: Mode I", who runs up to $\Delta u \approx 0.11$ mm. The elements "Q4: Mode I" and "Q6: Mode I" provide the longest $\lambda(\Delta u)$ curves. We note that "Q4: n0 + m0" and "Q6: n0 + m0" results are similar to each other, but they show considerably stiffer response in comparison with the continuous crack results for the same combinations of basic separation modes. The crack patterns are shown in Figure 6.17. Figure 6.17 shows that the most realistic crack pattern is obtained for "Q4: Mode I + Mode II" and "Q6: Mode I + Mode II", although these analyses fail fairly soon. This is also confirmed in Figure 6.18, where deformed mesh configurations at the end of analyses are shown.

We can see the influence of incompatible displacements in curves in Figure 6.16, however, this influence is much less pronounced in Figure 6.17 and Figure 6.18. The crack pattern and the deformed configurations for "n0 + m0" formulations are completely different from the continuous crack solution.

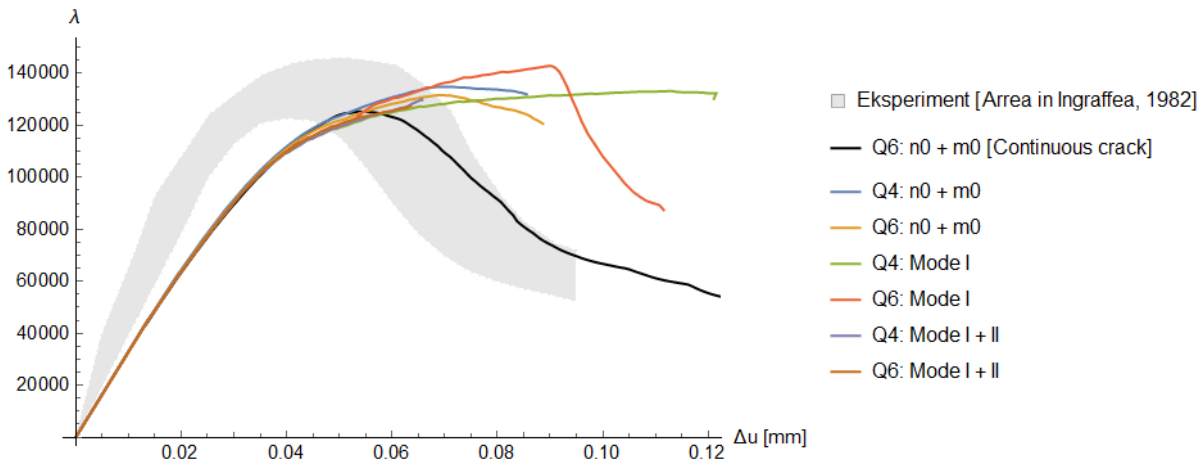

Figure 6.16: Load factor λ versus vertical crack mouth opening curves.

Slika 6.16: Diagram faktor obtežbe λ v odvisnosti od relativnega vertikalnega razmika na ustju razpoke.

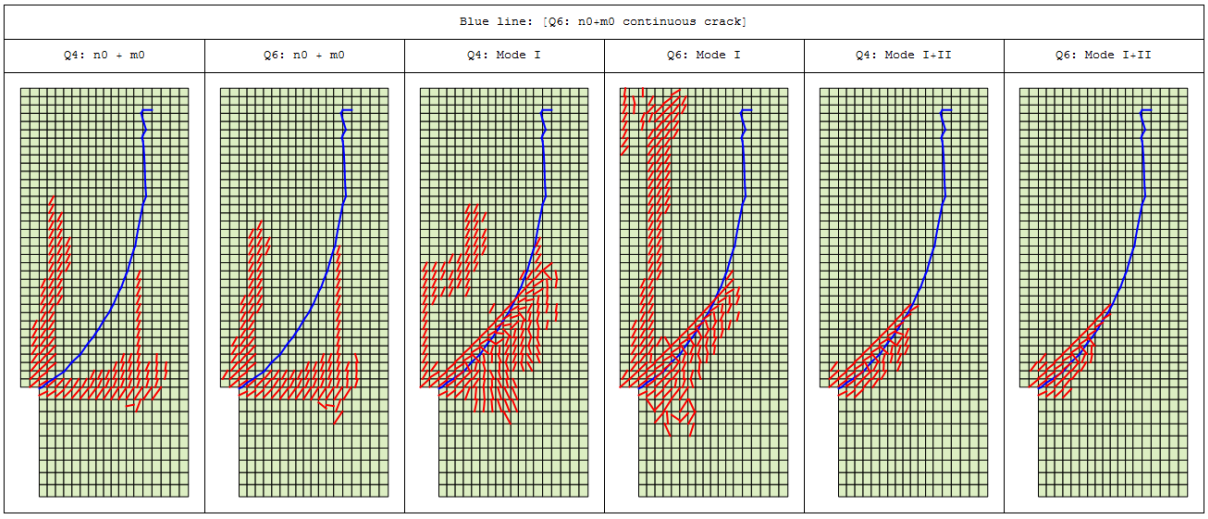

Figure 6.17: The crack patterns in comparison with the continuous crack solution "Q6: n0 + m0".

Slika 6.17: Vzorci razpokanosti v modelih v primerjavi z rešitvijo za zvezno razpoko "Q6: n0 + m0".

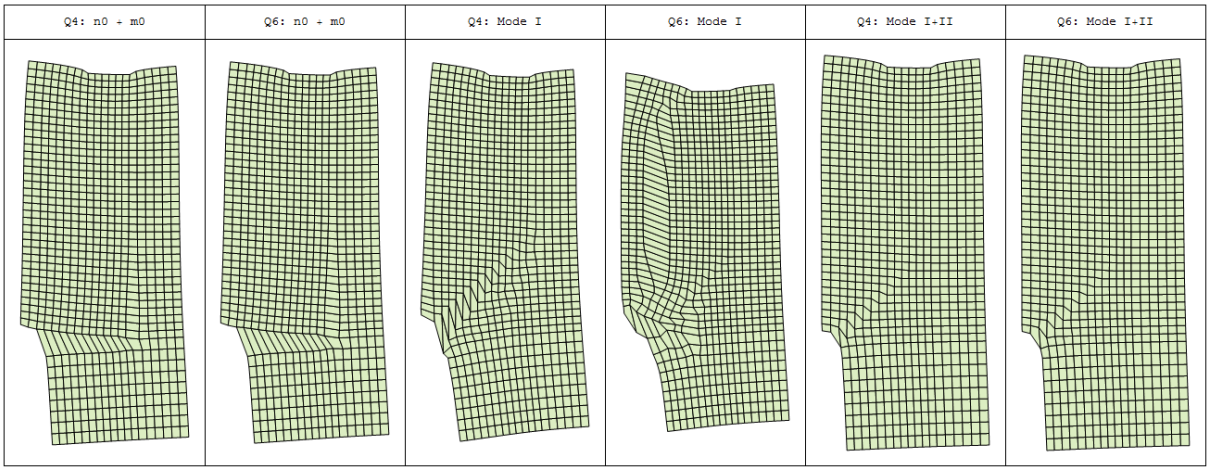

Figure 6.18: Deformed mesh configurations at the end of computation (scaled 250-times).

Slika 6.18: Deformacijske konfiguracije mrež končnih elementov na koncu analize (povečano 250-krat).

6.3 Nooru-Mohamed's test

We consider a tensile-shear test from (Nooru-Mohamed, 1992), called there "load path 4b (46-05)". Figure 6.19 presents geometry, loading, displacement boundary conditions, and finite element mesh. The square-like concrete specimen with thickness $d = 50$ mm and side length $L = 200$ mm has two notches. The notches $a \times b \times d = 25$ mm $\times$ 5 mm $\times$ 50 mm are positioned on two sides of the specimen (see Figure 6.19). The black lines around the specimen in Figure 6.19 represent loading frame that was used in the test to homogenise loading and displacement boundary conditions along the edge or part of the edge. The loading was performed in the following way. First, a horizontal force $P = 10$ kN was applied. Next, the

displacement $u_y = \lambda u_0$ ($u_0 = 1$ mm), where λ is loading factor, was imposed along the top edge of the loading frame (see Figure 6.19). The material properties for the concrete are (Wu et al., 2015): Young's modulus $E = 3 \cdot 10^5$ MPa, Poisson's coefficient $\nu = 0.2$, and tensile strength $\sigma_{un} = 3\ \mathrm{N/mm^2}$. The exponential softening law ((4.80) and (4.88)), for both normal and tangential directions, was used to describe cohesive tractions during the crack opening. The crack starts to open in mode I and slide in mode II when the corresponding tractions are equal to or greater to σ_{un} and σ_{um}, respectively. The values of σ_{un} and σ_{um} are: $\sigma_{un} = 3\ \mathrm{N/mm^2}$ (Wu et al., 2015) and $\sigma_{um} = 0.3\ \mathrm{N/mm^2}$ (Brancherie and Ibrahimbegovic, 2009). The mode I and mode II fracture energy are $G_{fn} = 0.11\ \mathrm{N/mm^2}$ (Wu et al., 2015) and $G_{fm} = 0.011\ \mathrm{N/mm^2}$ (Brancherie and Ibrahimbegovic, 2009). For the loading frame, the following material data is assumed $E = 3 \cdot 10^{10}$ MPa and Poisson's coefficient $\nu = 0.2$.

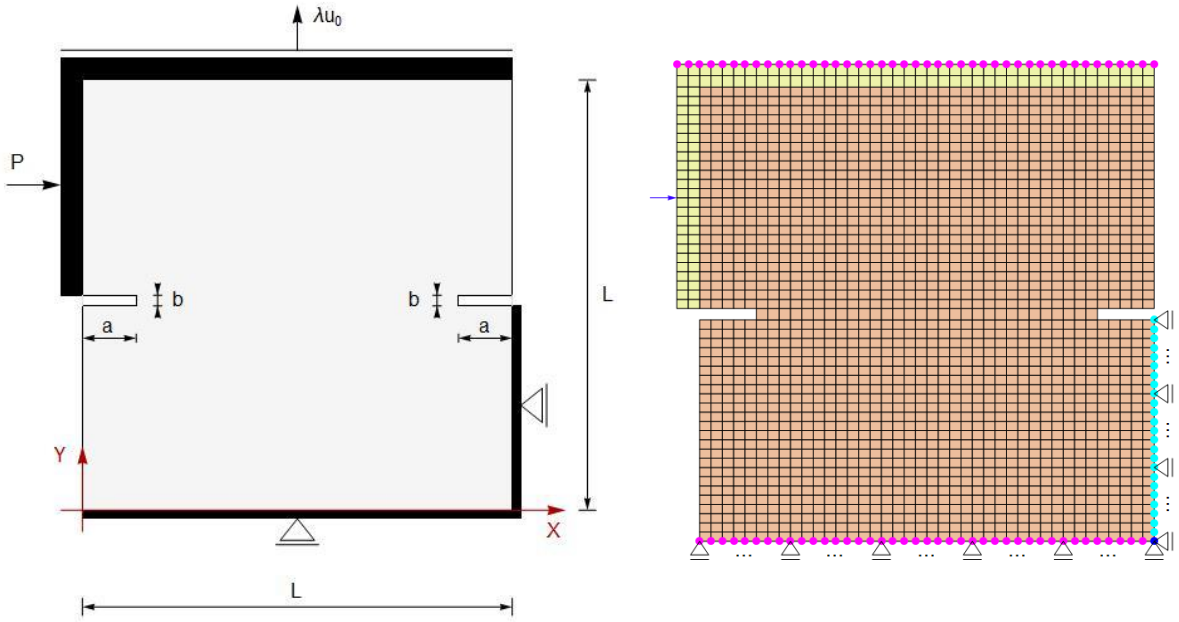

Figure 6.19: Nooru-Mohamed's test: Left: geometry, boundary conditions and load. Right: Finite element mesh.

Slika 6.19: Test Nooru-Mohamed: Levo: geometrija, robni pogoji in obremenitev. Desno: Mreža končnih elementov.

The complete analysis was conducted in two steps. First, the analysis was performed for a horizontal force $P = 10$ kN. Next, prescribed displacement $u_y = \lambda u_0$ ($u_0 = 1$ mm) was applied along the top edge of the loading frame (see Figure 6.19) at fixed horizontal force $P = 10$ kN. The mesh on Figure 6.19 shows that the upper part of the loading frame was also meshed (the frame width is $d = 50$ mm and the frame thickness equals 10 mm) with ideal bond between the concrete block and the frame. The influence of the lower part of the loading frame was modelled by restricting the displacements at edges of the concrete block: the horizontal displacement was restricted on the vertical edge and the vertical displacement was restricted on the bottom horizontal edge.

For computation of this example we used Q4 and Q6 ED-FEM finite elements that differ with respect to $\overline{\widehat{\boldsymbol{G}}}_m, m = 1, \cdots 4$, operators. The elements "n0 + m0" use $\overline{\widehat{\boldsymbol{G}}}_1$ and $\overline{\widehat{\boldsymbol{G}}}_3$ from (Dujc et al., 2010). The elements "Mode I" use $\overline{\widehat{\boldsymbol{G}}}_1$ and $\overline{\widehat{\boldsymbol{G}}}_2$ from (Dujc et al., 2010). The elements with $\overline{\widehat{\boldsymbol{G}}}_m, m = 1, \cdots 4$, from (Dujc et al., 2010) are denoted as "Mode I + II [G-Dujc]". The elements with $\overline{\widehat{\boldsymbol{G}}}_m, m = 1, \cdots 4$, from (Linder and Armero, 2007) are denoted as "Mode I + II [G-Linder]". The elements with $\overline{\widehat{\boldsymbol{G}}}_1$ and $\overline{\widehat{\boldsymbol{G}}}_2$ from (Dujc et al., 2010) and with $\overline{\widehat{\boldsymbol{G}}}_3$ and $\overline{\widehat{\boldsymbol{G}}}_4$ from (Linder and Armero, 2007) are as "Mode I + II".

6.3.1 Analysis with crack tracing algorithm

In this section we present results obtained by using the crack tracing algorithm. We note that the crack tracing algorithm was switched on already from the beginning of the computations, and not only at the second part of the computations where the top edge displacement was imposed. The experimental results (Nooru-Mohamed, 1992) show that one crack propagates from each notch: there is one crack in the top part of the specimen and one crack in the bottom part of the specimen. At the beginning of the analysis, two crack initiation points were chosen: one for the crack starting from the left notch and another one for the crack starting from the right notch.

COMPARISON WITH THE EXPERIMENT

The computed results are presented in the Figure 6.20. We note that the reaction force R_y versus applied prescribed displacement u_y curves are quite similar. The force R_y is sum of nodal reactions at the upper-edge nodes, where the prescribed displacement $u_y = \lambda u_0$ is applied. The elements with constant separation modes "n0 + m0" are the most efficient. Element"Q6: n0 + m0" produces the longest force-displacement curve. It is interesting to note that our computed limit loads are considerable higher from the experimentally observed limit load, see Figure 6.20 and Figure 6.21. This is also true for the computations of (Wu et al., 2015). The important reason for that is the applied linear elastic constitutive law for the bulk, which, of course, does not catch micro-damage before the appearance of a macro-crack. The micro-damage would have been taken into account by using elasto-damage constitutive model for the bulk. Another reason might be rather high value of tensile strength σ_{un}. Nevertheless, Figure 6.22 shows that the computed crack paths are in nice agreement with the experimental results of (Nooru-Mohamed, 1992). The experimental results (Nooru-Mohamed, 1992) provide two crack lines; one was read at the front side and the second line at the rear side of the specimen. The computed crack paths are similar. The "Q6: n0 + m0" computes the upper crack right to the specimen's edge, thus completely separating the specimen into the two parts. The specimen material (i.e. concrete) is non-homogeneous, thus the experimental crack lines are non-smooth and even non-continuous. On the contrary, due to the considered model and computational assumptions, the computed crack lines are smooth and continuous.

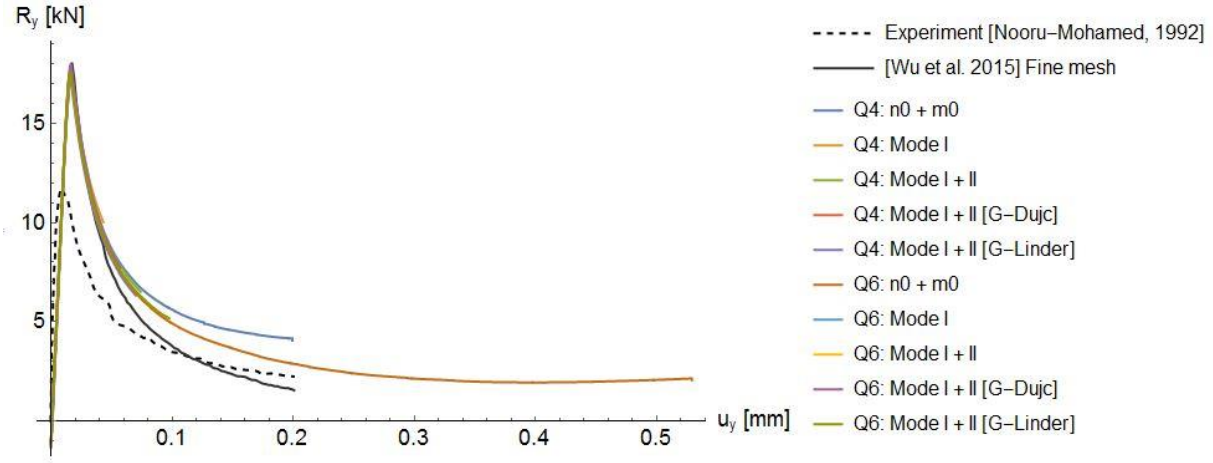

Figure 6.20: Comparison of the results: Reaction force R_y versus applied prescribed displacement u_y curves.

Slika 6.20: Primerjava rezultatov: Diagrami reakcijske sile R_y v odvisnosti od predpisanega pomika u_y

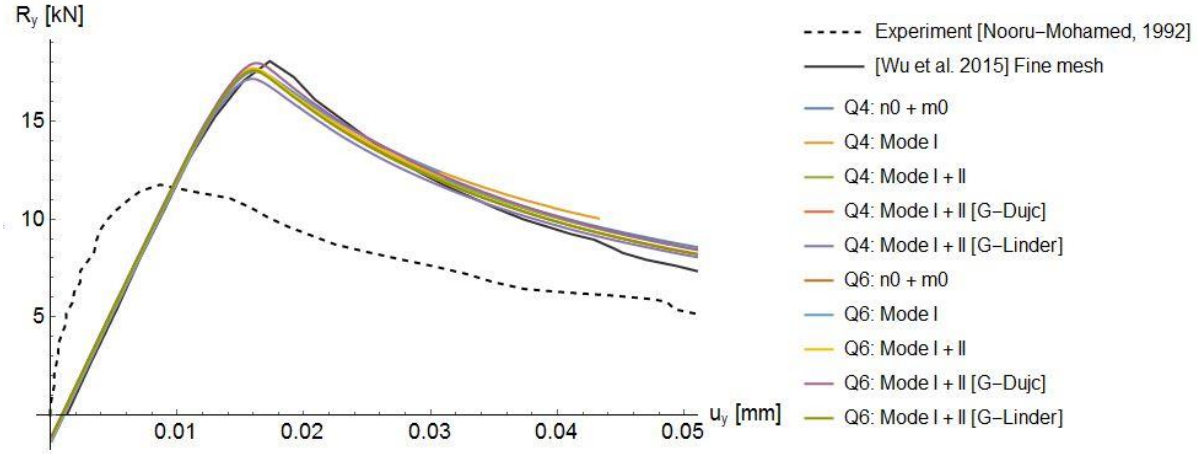

Figure 6.21: Comparison of the results: Reaction force R_y versus applied prescribed displacement u_y curves.

Slika 6.21: Primerjava rezultatov: Diagrami reakcijske sile R_y v odvisnosti od predpisanega pomika u_y.

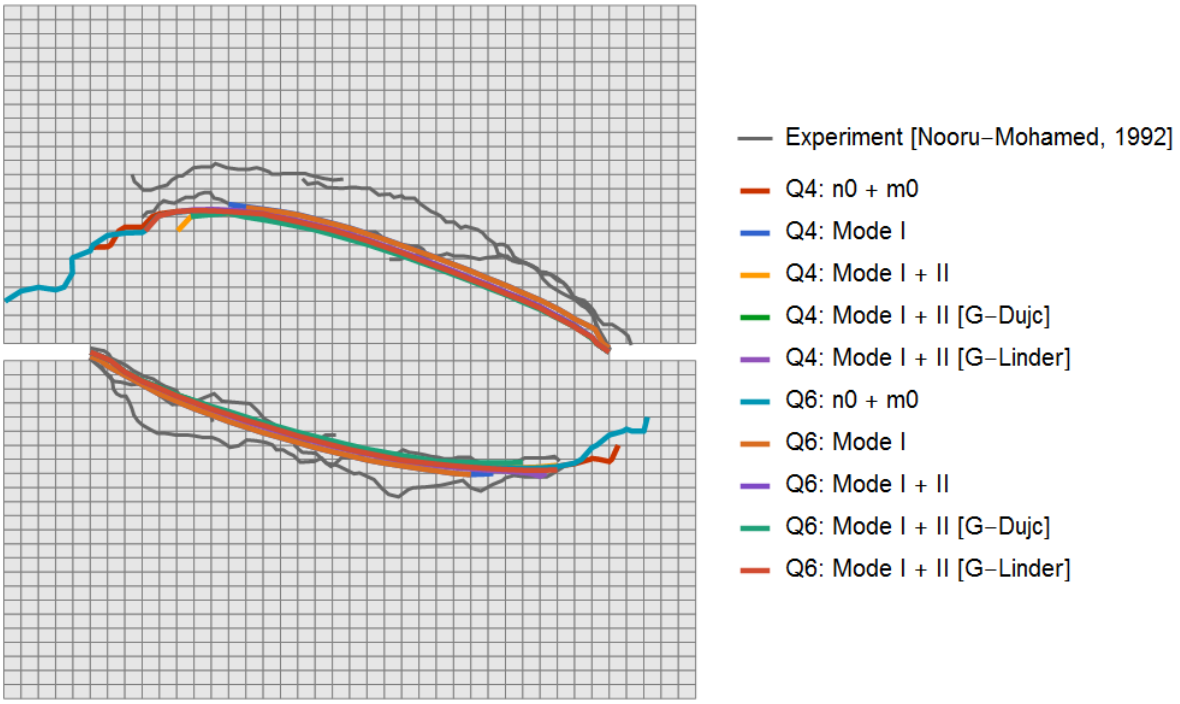

Figure 6.22: The crack paths of all computations.

Slika 6.22: Poti razpoke za vse izračune.

CONSTANT SEPARATION MODES (N0 AND M0) ELEMENTS

The results of "n0+m0" elements are presented in Figure 6.23 to Figure 6.25. Recall, that the elements use $\overline{\overline{\boldsymbol{G}}}_1$ and $\overline{\overline{\boldsymbol{G}}}_3$ operators from (Dujc et al., 2010). The starting point for the lower crack was chosen as $x = 25$ mm, $y = 100$ mm and the starting point for the upper crack was chosen as $x = 175$ mm, $y = 100$ mm.

Figure 6.23 presents the reaction force R_y versus prescribed displacement u_y curves. It is interesting to note that the "Q6: n0+m0" curve does not drop to zero even when the upper crack reaches the edge and thus separates the specimen into two parts, see Figure 6.24. One reason, but probably not the predominant one, is the use of exponental softening when evaluating the tractions in the crack. Therefore the tractions in the crack are limitating towards zero with crack opening but they never completely vanish. Figure 6.23 shows that the "Q6: n0+m0" curve even slightly increases towards the end, indicating a slight increase of resistance between two separated parts of the specimen, which is obviously not realistic. The reason that the $R_y(u_y)$ curve does not limitate close to zero needs to be further investigated.

The combined mode opening of the crack is a characteristic of this example. In all cracked elements, both the mode I opening and the mode II sliding are active. The combined mode opening of the crack can be observed also from Figure 6.25.

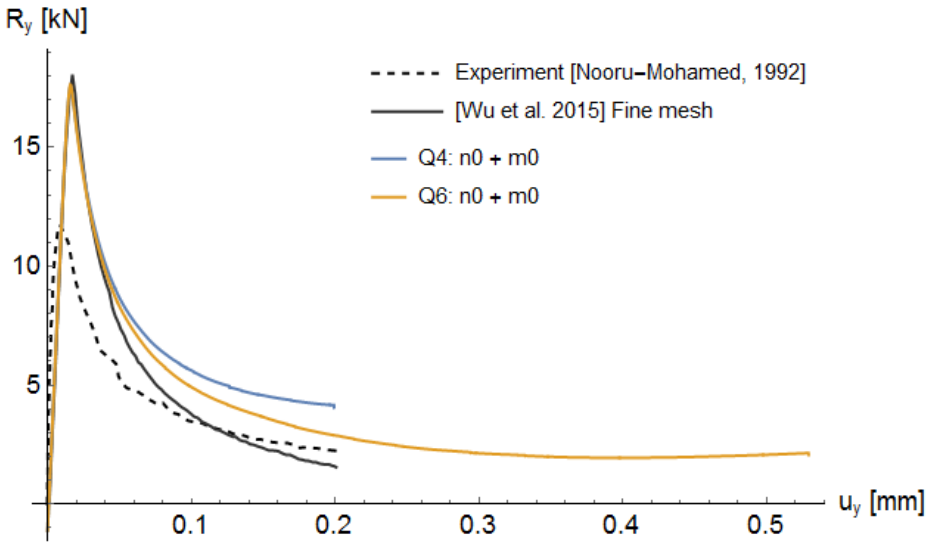

Figure 6.23: R_y versus prescribed displacement u_y curves for "n0+m0" elements.

Slika 6.23: Diagrami reakcije R_y v odvisnosti od predpisanega pomika u_y za "n0+m0" elemente.

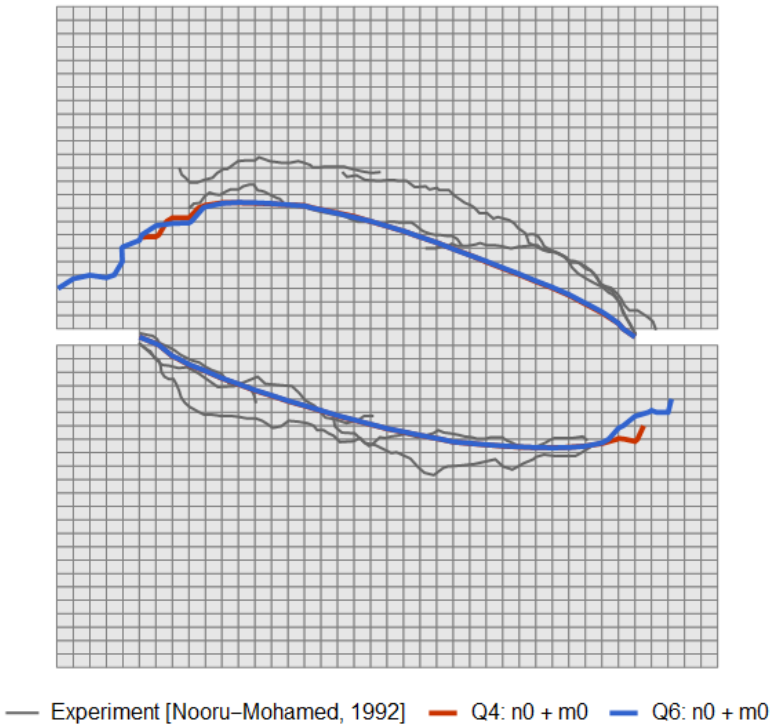

Figure 6.24: The crack paths for "n0+m0" elements.

Slika 6.24: Poti razpoke za "n0+m0" elemente.

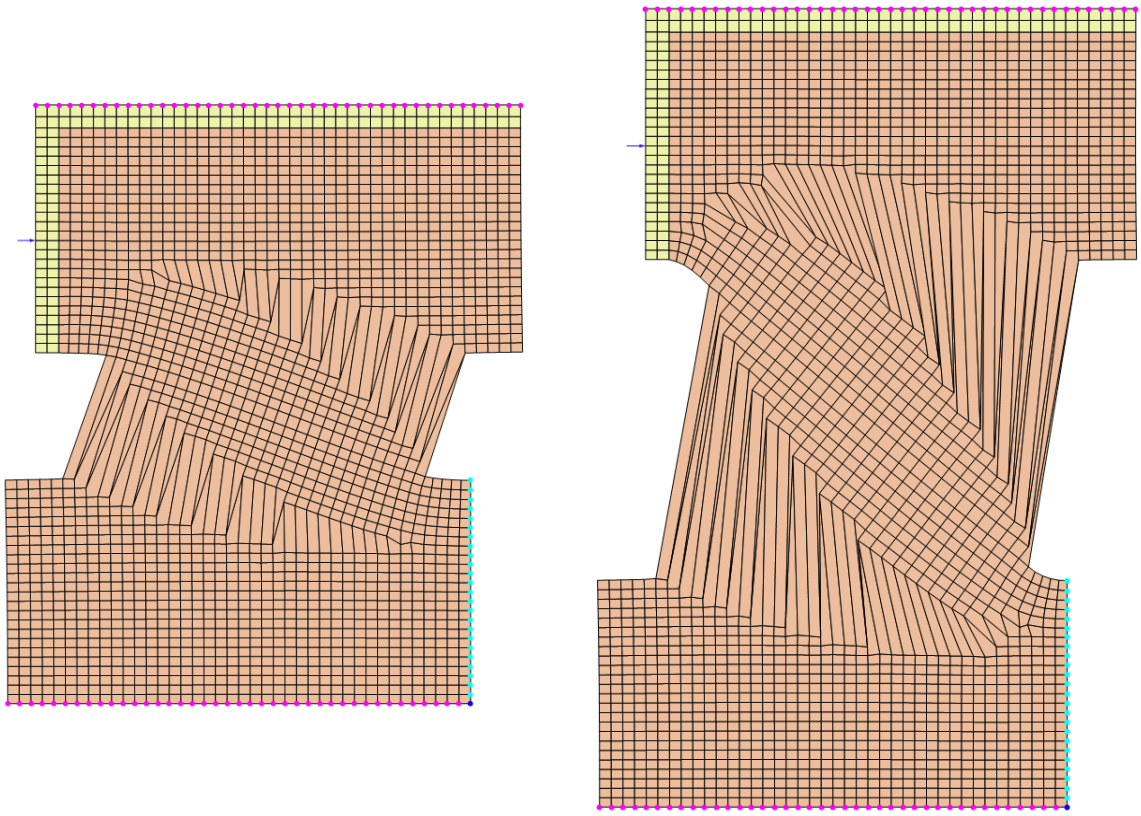

Figure 6.25: Deformed meshes (the displacements are 250-times magnified) for "n0 + m0" elements at the end of the analysis. Left: Q4. Right: Q6.

Slika 6.25: Deformacijski konfiguraciji mrež končnih elementov (pomiki so 250-krat povečani) za "n0 + m0" elemente na koncu analize. Levo: Q4. Desno: Q6.

LINEAR SEPARATION MODE IN NORMAL DIRECTION n (n0 AND n1)

The results of "Mode I" elements are presented in Figure 6.26. Recall, that the elements use $\overline{\widehat{\boldsymbol{G}}}_1$ and $\overline{\widehat{\boldsymbol{G}}}_2$ operators from (Dujc et al., 2010). The starting point for the lower crack was chosen as $x = 25$ mm, $y = 101.25$ mm and the starting point for the upper crack was chosen as $x = 175$ mm, $y = 98.75$ mm. Such choice of the starting points are optimal to perform the crack tracing algorithm. One can see that the analyses failed fairly quickly after the limit point. This is expected, since the combined mode crack opening is taking place with this example, which, of course, cannot be represented correctly by modelling mode I crack opening only.

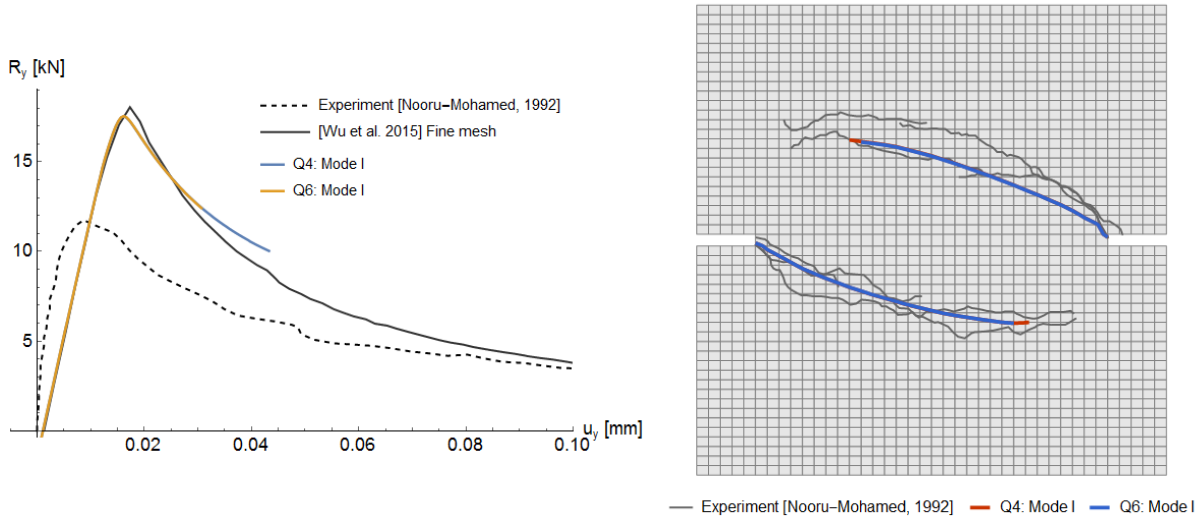

Figure 6.26: Left: R_y versus prescribed displacement u_y curves for "Mode I" elements. Right: The crack paths for "Mode I" elements.

Slika 6.26: Levo: Diagrami reakcijske sile R_y v odvisnosti od predpisanega pomika u_y za "Mode I" elemente. Desno: Poti razpoke za "Mode I" elemente.

ELEMENTS WITH ALL FOUR BASIC SEPARATION MODES ("Mode I + II")

The results for "Mode I + II" elements are presented in Figure 6.27 to Figure 6.29. The starting point for the lower crack was chosen as $x = 25$ mm, $y = 100$ mm and the starting point for the upper crack was chosen as $x = 175$ mm, $y = 100$ mm. The convergence was achieved only for the stabilization parameter $\kappa \geq 10^7$. The role of stabilization parameter κ is explained in (Linder and Armero, 2007) (see *Remark 5.5*). Figure 6.27 presents reaction force R_y versus prescribed displacement u_y curves. Results for Q4 and Q6 elements are presented separately in Figure 6.28 and Figure 6.29.

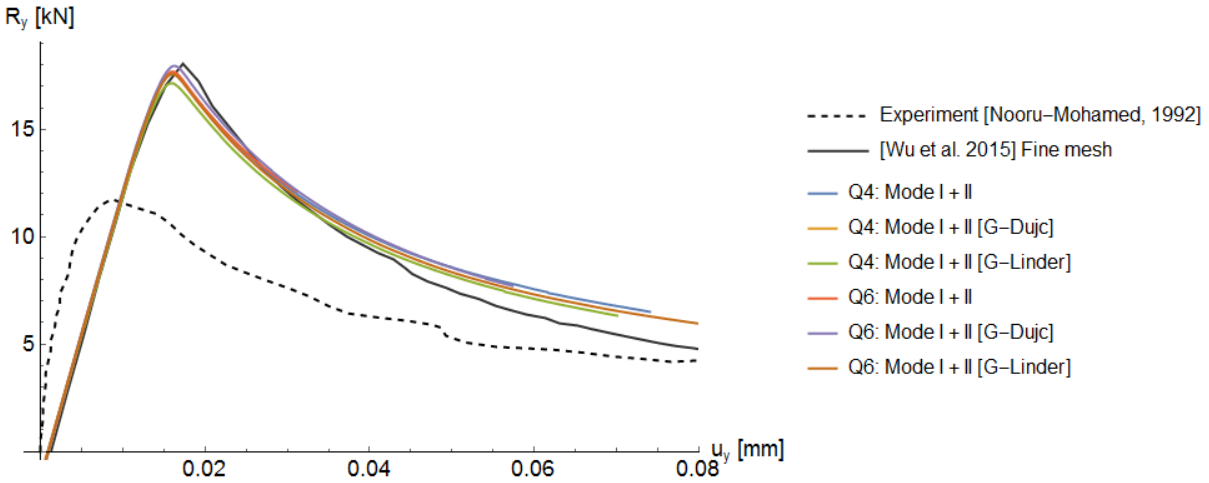

Figure 6.27: R_y versus prescribed displacement u_y curves for "Mode I + II" elements.

Slika 6.27: Diagrami reakcijskih sil R_y v odvisnosti od predpisanega pomika u_y za »Mode I + II« elemente.

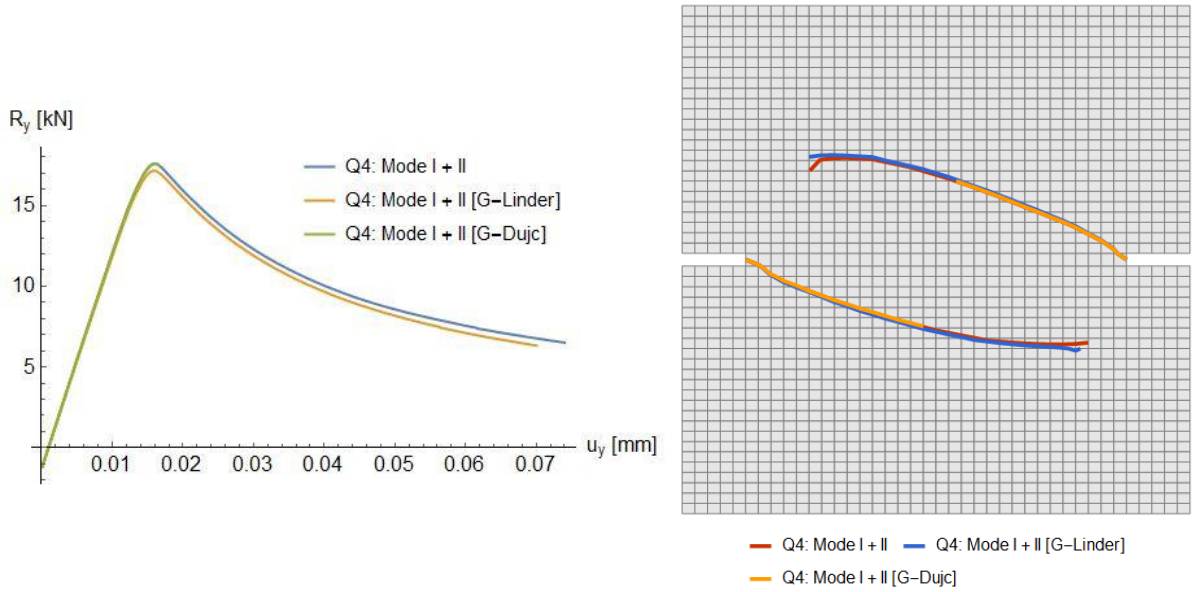

Figure 6.28: Results for Q4 "Mode I + II" elements.

Slika 6.28: Rezultati za Q4 "Mode I + II" elemente.

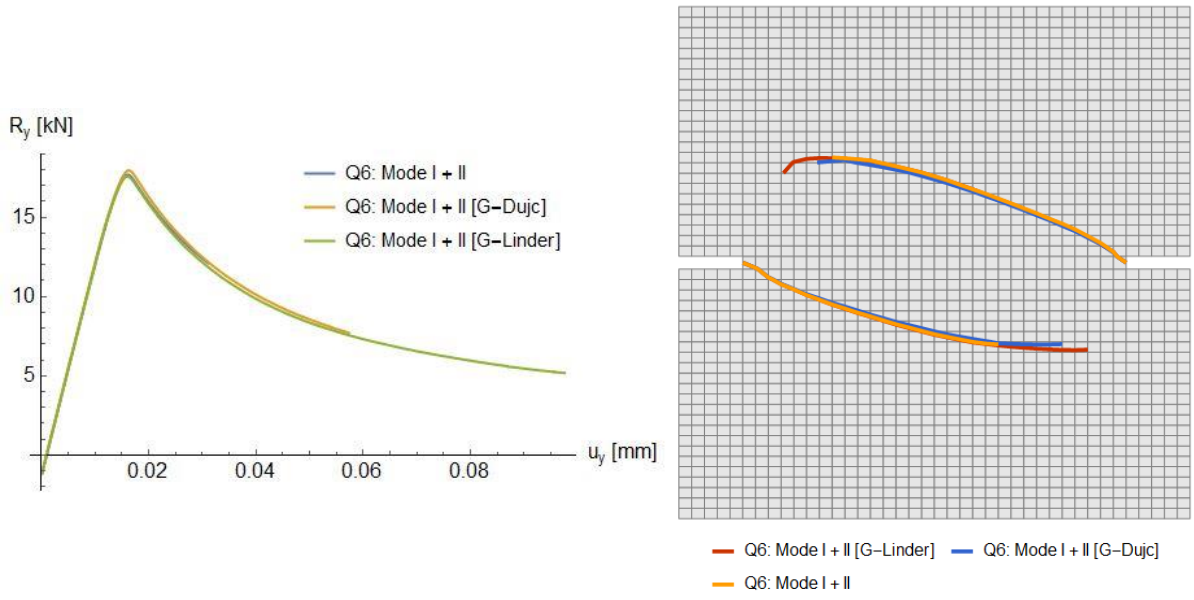

Figure 6.29: Results for Q6 "Mode I + II" elements.

Slika 6.29: Rezultati za Q6 "Mode I + II" elemente.

6.3.2 Analysis without crack tracing algorithm

The same example was recomputed without the crack tracing algorithm in order to check results of such analysis. The embedded-discontinuity elements were used only for the part of the mesh (area without the loading frame), which is presented in Figure 6.19 (Right) and Figure 6.31. The crack was embedded at the element when the criterion (4.113) was fulfilled in such a way that it crossed the center of the element.

The comparison of successfully computed results is presented in Figure 6.30. The element "Q4: n0 + m0" failed soon and therefore its results are not presented.

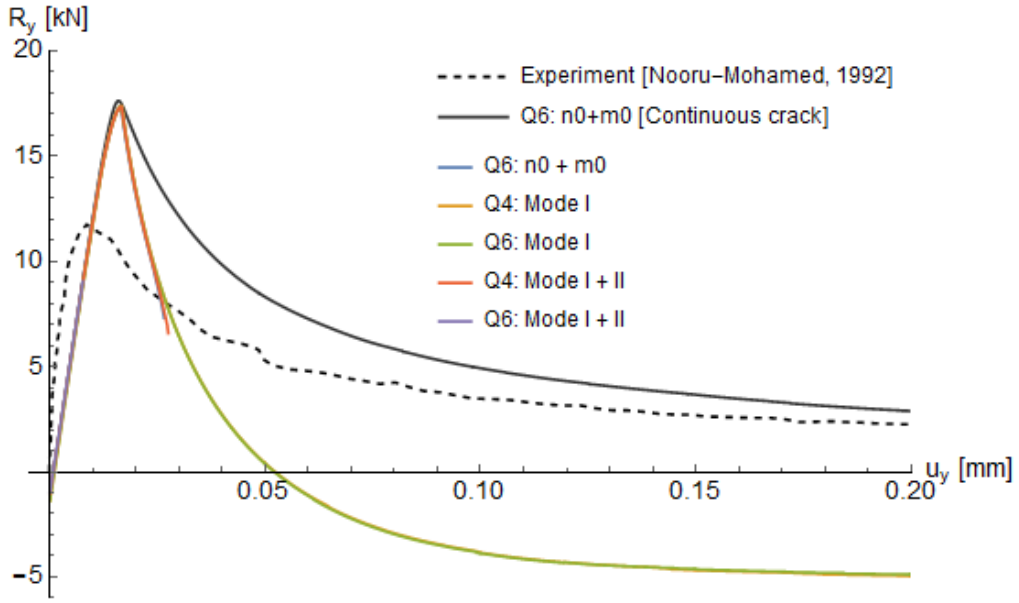

Figure 6.30: Comparison of the results: Reaction force R_y versus applied prescribed displacement u_y curves.

Slika 6.30: Diagrami reakcijske sile R_y v odvisnosti od predpisanega pomika u_y za analize brez algoritma za sledenje razpoki.

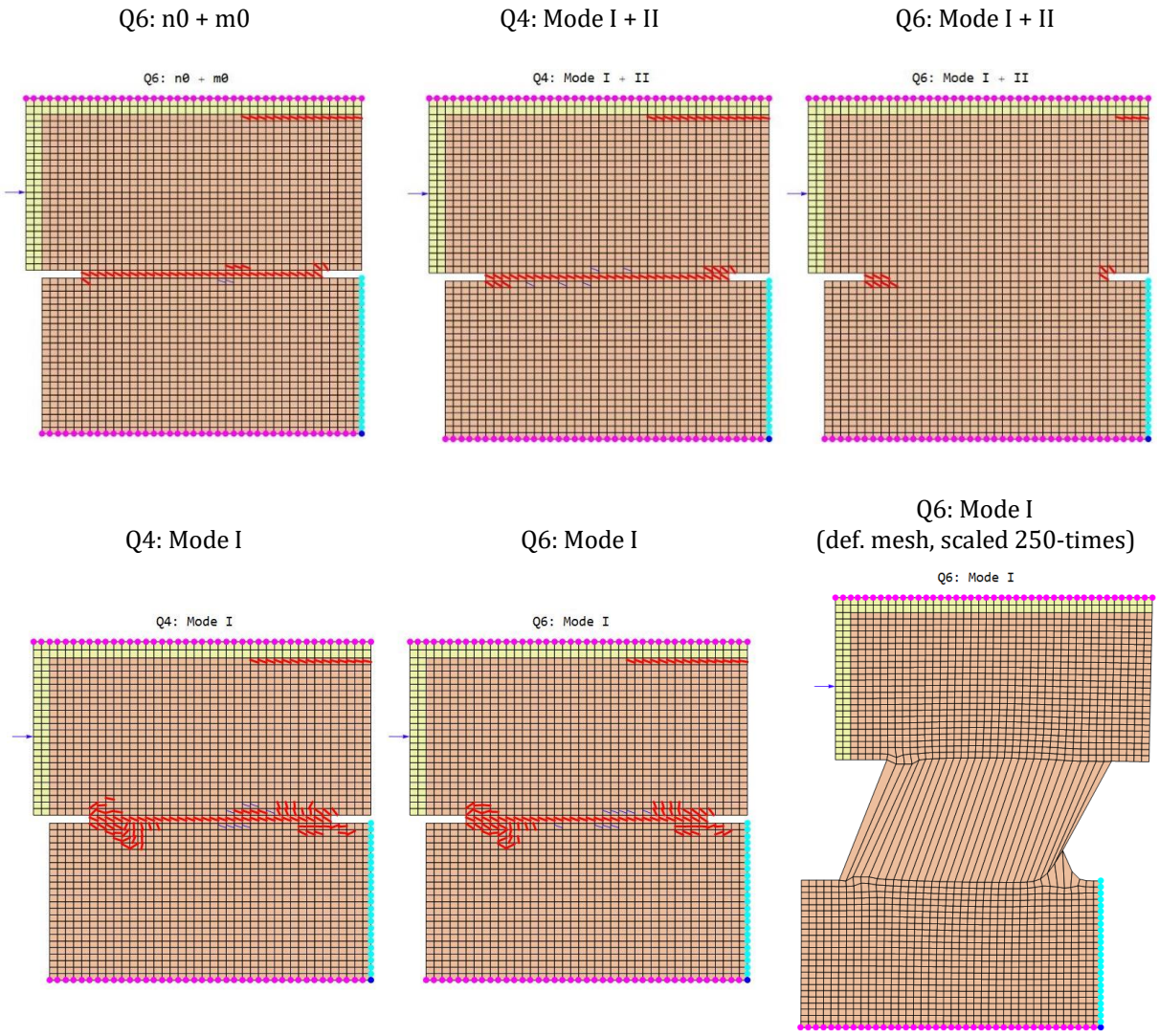

Figure 6.31: Crack patterns and deformed mesh at the end of the curve from Figure 6.30 (displacements are magnified 250 times).

Slika 6.31: Vzorci razpok in deformacijska konfiguracija mreže na koncu ravnotežnih poti iz Slika 6.30 (pomiki so 250-krat povečane).

7 CONCLUSIONS

The thesis studies: (i) the methods for failure analysis of solids and structures, and (ii) the embedded strong discontinuity finite elements for modelling material failures in quasi brittle 2d solids.

As for the failure analysis, the consistently linearized path-following method with quadratic constraint equation is first presented and studied in detail. We note that the term »consistently linearized« is here used in a sense that all governing equations, i.e. the equilibrium equations and the constraint equation, are linearized when searching for the solution of those equations in the framework of path-following method. The derived path-following method can be applied in the nonlinear finite element analysis of solids and structures in order to compute a highly nonlinear solution path. When the nonlinear problems with the localized material failures (i.e. material softening) are analysed, standard path-following methods can fail. For this reason we derived new versions of the path-following method, with other constraint functions, more suited for problems that take into account localized material failures. One version is based on adaptive one-degree-of-freedom constraint equation, which proved to be relatively successful in analysing problems with the material softening that are modelled by the embedded-discontinuity finite elements. The control degree-of-freedom may change from one increment to another. We presented the procedure of choosing a suitable degree-of-freedom candidate that will enter the constraint equation.

We derived the explicit and implicit constraint equations that are based on controlling incremental plastic dissipation or plastic work in an inelastic structure. It turned out that the resulting path-following method can be superior to the standard arc-length method. Moreover, one should have in mind that the latter method sometimes allows for unrealistic, spurious elastic unloading of a complete structure. This cannot happen with the dissipation-based path following method, since elastic unloading of complete structure is not possible.

We derived displacement-based embedded-strong-discontinuity quadrilateral finite element for 2d problems, i.e. for plane stress and plane strain structures. We restrict ourselves to quasi-brittle materials, such as concrete, masonry and stone, therefore the rigid-damage softening law is employed. The formulation allows for linear crack opening in both mode I and mode II.

We studied the formulations which are based either on classical, displacement-based element or on element with incompatible displacements. Additionally, we check two suggestions for the G-operators provided by (Dujc et al., 2010) and (Linder and Armero, 2007). We performed simple small tests to check the effectiveness of the embedded discontinuity model, when softening is active. Based on the small tests results, we recommend setting the [G-Dujc] operators for all separation modes except for linear Mode II. For linear Mode II, the [G-Linder] operator is suggested (see Section 5). However, the crack separation Mode II needs to be further investigated.

We investigated the propagation of cracks during the analysis. We proposed a crack tracing algorithm that enforces the crack continuity through the mesh. One or even more elements can develop a crack in single solution increment. The algorithm enables also tracing one or more crack lines in finite element mesh. Numerical examples show that the best computational performance is reached when a crack tracing

algorithm is used. The analysis without the algorithm returns the wrong results. Namely, the crack distribution throughout the mesh (the crack pattern) and their orientations seems to be such that the structural cracking mechanism cannot manifest in a clear way. This results in a false response after certain number of elements with the crack.

The incompatible mode method significantly improves the behaviour of the embedded-discontinuity finite elements in bending problems (see Section 5.3). For the combined mode problems (Section 6), the element formulation with constant separation modes behaves very well.

8 RAZŠIRJENI POVZETEK

METODE SLEDENJA RAVNOTEŽNE POTI ZA ANALIZO PORUŠITVE KONSTRUKCIJ

Podrobno preučimo konsistentno linearizirano metodo sledenja poti, ki se lahko uporabi za analizo trdnih teles in konstrukcij po metodi končnih elementov. Vrsta metode sledenja ravnotežne poti se nanaša na obliko dodatne vezne enačbe. V tem poglavju obravnavamo dve različni dodatni vezni enačbi: kvadratno vezno enačbo in vezno enačbo za kontrolo izbrane prostostne stopnje. Prva metoda je uspešna pri reševanju geometrijsko nelinearnih in standardnih ne-elastičnih problemov. Za probleme z materialnim mehčanjem, ki so modelirani s končnimi elementi z vgrajeno nezveznostjo (*embedded discontinuity finite elements*), je najbolj učinkovita metoda sledenja ravnotežne poti s kontrolo pomika. Prednosti in slabosti obeh metod so predstavljeni na številnih numeričnih primerih. Nekaj primerov vključuje direkten izračun kritičnih točk in sledenje ravnotežni poti po sekundarni veji. Direkten izračun kritičnih točk se izvede po enakem konceptu kot se uporablja pri metodah sledenja ravnotežne poti le, da uporabimo takšno vezno enačbo, ki ni odvisna od lastnih vektorjev in je primerna za določitev kritične točke.

SISTEM NELINEARNIH ENAČB

Kadar rešujemo geometrijsko in/ali materialno nelinearne statične konstrukcijske probleme po metodi končnih elementov, je potrebno uporabiti ustrezno metodo sledenja ravnotežne poti (ang. *path-following method*). Pri tem gre za iterativno reševanje razširjenega sistema nelinearnih enačb, ki ga tvorijo: (i) vozliščne ravnotežne enačbe, ki so rezultat diskretizacije šibke oblike robnega problema, in (ii) vezna enačba:

$$\boldsymbol{G}\big(\boldsymbol{p}(t),\lambda(t)\big)=\begin{Bmatrix}\boldsymbol{R}(\boldsymbol{p}(t),\lambda(t))\\ g\big(\boldsymbol{p}(t)-\boldsymbol{p}(t-\Delta t),\lambda(t)-\lambda(t-\Delta t)\big)\end{Bmatrix}=\boldsymbol{0}$$

V sistemu enačb $\boldsymbol{G}\big(\boldsymbol{p}(t),\lambda(t)\big)=\boldsymbol{0}$, $t\geq 0$ predstavlja monotono naraščajoči parameter, ki ga imenujemo psevdo-čas, Δ je majhna (inkrementalna) sprememba, $\boldsymbol{p}$ je vektor neznanih pomikov v mreži končnih elementov (termin "pomiki" se uporablja za pomike in zasuke), λ je obtežni faktor, g je vezna funkcija, in $\boldsymbol{R}$ je rezidualni vektor:

$$\boldsymbol{R}\big(\boldsymbol{p}(t),\lambda(t)\big)=\boldsymbol{R}^{int}\big(\boldsymbol{p}(t)\big)-\boldsymbol{R}^{ext}\big(\boldsymbol{p}(t),\lambda(t)\big),$$

$\boldsymbol{R}^{int}$ in $\boldsymbol{R}^{ext}$ sta vektorja notranjih in zunanjih sil v mreži končnih elementov (termin "sile" zajema sile in momente). Rešitev razširjenega sistema enačb iščemo aproksimativno, po korakih, v diskretnih točkah: $0=t_0,t_1,\cdots,t_n,t_{n+1},\cdots,t_{final}$. Denimo, da poznamo konfiguracijo mreže končnih elementov v psevdo-času t_n definirano s $\{\boldsymbol{p}(t_n),\lambda(t_n)\}\equiv\{\boldsymbol{p}_n,\lambda_n\}$, potem lahko izračunamo novo konfiguracijo v psevdo-času $t_{n+1}=t_n+\Delta t_n$. To naredimo tako, da razstavimo $\boldsymbol{p}_{n+1}$ in λ_{n+1} na dva dela:

$$\boldsymbol{p}_{n+1} = \boldsymbol{p}_n + \Delta\boldsymbol{p}_n, \qquad \lambda_{n+1} = \lambda_n + \Delta\lambda_n$$

$\Delta\boldsymbol{p}_n$ je inkrement vektorja pomikov in $\Delta\lambda_n$ je inkrement faktorja obtežbe. Upoštevajoč slednja inkrementa, lahko razširjeni sistem enačb (2.1) zapišemo v drugi obliki, v psevdo-času t_{n+1} kot:

$$\boldsymbol{G}_{n+1}(\boldsymbol{p}_n, \lambda_n; \Delta\boldsymbol{p}_n, \Delta\lambda_n) = \begin{Bmatrix} \boldsymbol{R}_{n+1}(\boldsymbol{p}_n, \lambda_n; \Delta\boldsymbol{p}_n, \Delta\lambda_n) \\ g_{n+1}(\Delta\boldsymbol{p}_n, \Delta\lambda_n) \end{Bmatrix} = \boldsymbol{0},$$

pri čemer $\boldsymbol{p}_n$ in λ_n poznamo, $\Delta\boldsymbol{p}_n$ in $\Delta\lambda_n$ pa sta neznanki.

V tem poglavju obravnavamo t.i. konsistentno linearizirano metodo sledenja ravnotežne poti. Izraz »konsistentno« pomeni, da so vse enačbe v razširjenem sistemu $\boldsymbol{G}_{n+1} = \boldsymbol{0}$ linearizirane med iskanjem rešitve v okviru metode sledenja poti:

$$\begin{bmatrix} \boldsymbol{K}^i_{n+1}(\boldsymbol{p}^i_{n+1}, \lambda^i_{n+1}) & \boldsymbol{R}^i_{n+1,\lambda}(\boldsymbol{p}^i_{n+1}, \lambda^i_{n+1}) \\ \left[g^i_{n+1,\boldsymbol{p}}(\Delta\boldsymbol{p}^i_n)\right]^T & g^i_{n+1,\lambda}(\Delta\lambda^i_n) \end{bmatrix} \begin{Bmatrix} \Delta\tilde{\boldsymbol{p}}^i_n \\ \Delta\tilde{\lambda}^i_n \end{Bmatrix} = - \begin{Bmatrix} \boldsymbol{R}^i_{n+1}(\boldsymbol{p}^i_{n+1}, \lambda^i_{n+1}) \\ g^i_{n+1}(\Delta\boldsymbol{p}^i_n, \Delta\lambda^i_n) \end{Bmatrix}$$

Neznanki sta iterativna popravka $\{\Delta\tilde{\boldsymbol{p}}^i_n, \Delta\tilde{\lambda}^i_n\}$.

V razširjenem sistemu enačb (2.7) $\boldsymbol{K}^i_{n+1}$ je tangentna togostna matrika, druge člene izračunamo kot:

$$\boldsymbol{R}^i_{n+1,\lambda} = \frac{\partial \boldsymbol{R}^i_{n+1}}{\partial\Delta\lambda^i_n} = -\frac{\partial \boldsymbol{R}^{ext,i}_{n+1}}{\partial\Delta\lambda^i_{n+1}} \qquad g^i_{n+1,\boldsymbol{p}} = \frac{\partial g^i_{n+1}}{\partial\Delta\boldsymbol{p}^i_n} \qquad g^i_{n+1,\lambda} = \frac{\partial g^i_{n+1}}{\partial\Delta\lambda^i_n}$$

Iterativno reševanje razširjenega sistema enačb (2.7) poteka v dveh fazah. Prva faza se imenuje prediktor in se zgodi v prvi iteraciji. Prediktor vrne začetni približek za inkrement vektorja pomikov $\Delta\boldsymbol{p}^*_n$ in inkrement faktorja obtežbe $\Delta\lambda^*_n$ (glej poglavje 2.1.4.1). V naslednjih iteracijah računamo popravke inkrementov $\{\Delta\tilde{\boldsymbol{p}}^i_n, \Delta\tilde{\lambda}^i_n\}$, zato se ta faza imenuje korektor. Zanka za iterativno reševanje inkrementa se izvaja toliko časa, dokler ni izpolnjen pogoj (2.24). Rezultat je nova ravnotežna točka $\{\boldsymbol{p}_{n+1}, \lambda_{n+1}\}$.

METODA SLEDENJA RAVNOTEŽNE POTI S KVADRATNO VEZNO ENAČBO

Kvadratna vezna enačba ima naslednjo obliko:

$$g_{n+1}(\Delta\boldsymbol{p}_n, \Delta\lambda_n) = \Delta\boldsymbol{p}_n^T\boldsymbol{W}_n\Delta\boldsymbol{p}_n + \psi_1^2\Delta\lambda_n^2\boldsymbol{q}_n^T\boldsymbol{H}_n\boldsymbol{q}_n + \psi_2^2\Delta\lambda_n^2\hat{\boldsymbol{p}}_{ref}^T\widehat{\boldsymbol{W}}_n\hat{\boldsymbol{p}}_{ref} - \Delta l_n^2 = 0\,,$$

kjer sta $\psi_1 \geq 0$ in $\psi_2 \geq 0$ faktorja povečave, Δl_n je vhodni podatek za inkrement $[t_n, t_{n+1}]$, $\boldsymbol{W}_n$, $\boldsymbol{H}_n$ in $\widehat{\boldsymbol{W}}_n$ so regulatorne diagonalne matrike (indeks *n* nakazuje, da se lahko spreminjajo od inkrementa do inkrementa). Če v kvadratni vezni enačbi nastavimo $\psi_2 = 0$ in $\boldsymbol{W}_n = \boldsymbol{H}_n = \boldsymbol{I}$ ($\boldsymbol{I}$ je enotska matrika), dobimo t.i. vezno enačbo za sferično metodo ločne dolžine (Crisfield, 1991). Za cilindrično metodo ločne dolžine (Crisfield, 1991) je potrebno v kvadratni vezni enačbi nastaviti $\psi_1 = \psi_2 = 0$ in $\boldsymbol{W}_n = \boldsymbol{I}$.

Pod drobnogled vzamemo dodatno vezno enačbo (2.6), ko velja $\boldsymbol{W}_n = \boldsymbol{H}_n = \widehat{\boldsymbol{W}}_n = \boldsymbol{I}$ in $\psi_2 = 0$. Kvadratna vezna enačba (2.6) povezuje inkrement pomikov z inkrementom obtežbe. Želimo poiskati takšno regulacijo, da bo razmerje obeh delov v vezni enačbi enakovredno. Očitno je, da so vrednosti obeh delov odvisni od merskih enot, ki jih uporabljamo za pomike in sile, in od vrednosti faktorja ψ_1. Namesto, da zadržimo merske enote vhodnih podatkov in iščemo primerno vrednost za skalarni faktor ψ_1, raje nastavimo $\psi_1 = 1$ in poiščemo primerne merske enote, v katerih podajamo vhodne podatke. Predlagamo preprost test (Preglednica 2.1), ki naj se izvede pred analizo po metodi s kvadratno vezno enačbo. Če izbrani vhodni podatki izpolnijo test, poženemo analizo s skalarnim faktorjem $\psi_1 = 1$. V nasprotnem primeru drugi del vezne enačbe (2.6) dominira in vpliva na potek analize, zato v takšnem primeru uporabimo $\psi_1 = 0$.

METODA SLEDENJA RAVNOTEŽNE POTI S KONTROLO POMIKA

Metoda sledenja ravnotežne poti s kvadratno vezno enačbo pogosto odpove pri reševanju problemov z mehčanjem v materialu (metoda končnih elementov z vgrajeno močno nezveznostjo). V tem primeru izberemo alternativno metodo, pri kateri vodimo izbrano prostostno stopnjo.

Kvadratno vezno enačbo (2.6) nadomestimo z drugo obliko:

$$g_{n+1}(\Delta \boldsymbol{p}_n) = \boldsymbol{w}_{n+1}^T \Delta \boldsymbol{p}_n - s_{n+1} \Delta \widehat{D}_n = 0, \qquad s_{n+1} = \text{sign}(\boldsymbol{w}_{n+1}^T \Delta \boldsymbol{p}_n)$$

V vektorju $\boldsymbol{w}_{n+1}$ so vsi členi enaki nič, razen enega člena, ki je enak 1 in določa, katero prostostno stopnjo iz vektorja $\Delta \boldsymbol{p}_n$ kontroliramo v trenutnem inkrementu. Vrednost predpisanega inkrementa kontroliranega pomika je $\Delta \widehat{D}_n > 0$.

Metodo s kontrolo prostostne stopnje uporabimo potem, ko se začne mehčanje v vsaj enem elementu v mreži končnih elementov. V nalogi je mehčanje materiala zajeto s končnimi elementi z vgrajeno nezveznostjo s kondenziranimi parametri za vgrajeno nezveznost (ED-FEM). Postopek izbire prostostne stopnje za vodenje je opisan v poglavju 2.2.2. Postopek reševanja razširjenega sistema enačb je enak kot v primeru metode s kvadratno vezno enačbo.

Tovrstna metoda ločne dolžine temelji na vodenju izbrane prostostne stopnje, t.j. vodenju pomika. Zelo pomembno je v vsakem inkrementu izbrati primeren pomik za vodenje. Analiza deluje le, če je trenutni vodeni pomik monotono naraščajoč ali monotono padajoč na celem intervalu inkrementa. V vsakem inkrementu lahko vodimo drugo prostostno stopnjo.

STABILNOSTNA ANALIZA

Vzporedno z izbrano metodo vodenja ravnotežne poti lahko izvajamo tudi stabilnostno analizo. Osnovna predpostavka: vsak inkrement vsebuje največ eno kritično točko. Ko zaznamo spremembo števila negativnih pivotov, izvedemo t.i. direkten izračun kritične točke. V ta namen nastavimo naslednjo vezno enačbo:

$$g_{n+1} = det\boldsymbol{K}_{n+1} = \prod_{i=1}^{N} U_{ii,n+1},$$

kjer je N dimenzija vektorja, $\boldsymbol{p}_{n+1}$ in $U_{ii,n+1}$ so diagonalni členi zgornje trikotne matrike v dekompoziciji tangentne matrike $\boldsymbol{K}_{n+1} = \boldsymbol{L}_{n+1}\boldsymbol{U}_{n+1}$. Iz vezne enačbe je očitno, da pogoj $det\boldsymbol{K}_{n+1} = 0$ velja za iskano konfiguracijo $\{\boldsymbol{p}_{n+1}, \lambda_{n+1}\}$, t.j. iskana konfiguracija je kritična točka.

Klasifikacija kritične točke (limitna točka in bifurkacijska točka) je pojasnjena v poglavju 2.4.2.

Običajno v inženirskih problemih stabilnosti srečujemo enostavne bifurkacijske točke. V tem primeru lahko izvedemo prehod na sekundarno vejo ravnotežne poti s posebno vezno enačbo (Parente Junior et al., 2006):

$$g_{n+1}(\Delta\boldsymbol{p}_n, \Delta\lambda_n) = (\Delta\boldsymbol{p}_n^T\boldsymbol{\phi})^2 - \Delta l_n^{(\mathrm{b})^2} = 0$$

Zgornjo vezno enačbo uporabimo samo v prvem inkrementu potem, ko smo zaznali bifurkacijsko točko. $\boldsymbol{\phi}$ je prvi lastni vektor tangentne matrike v točki $\{\Delta\boldsymbol{p}_n, \Delta\lambda_n\}$, $\Delta l_n^{(\mathrm{b})}$ je dolžina inkrementa.

NUMERIČNI PRIMERI

V poglavju 2.4 so predstavljeni različni numerični primeri uporabe metod sledenja ravnotežnih poti do porušitve. Metodo s kvadratno vezno enačbo smo uporabili pri analizi preskoka sistema tričlenskega loka, palične kupole, cilindričnega panela, zelo tankega cilindričnega panela, L-plošče in osno-obremenjenega cilindričnega panela. Nato smo pripravili modele s končnimi elementi z vgrajeno nezveznostjo, ki se uporabljajo za modeliranje lokalnega mehčanja v materialu. To so ravninski jekleni okvir, simetrični 3-etažni okvir, betonski nosilec z zarezo in primer razslojevanja nosilca. Primere smo uspešno izračunali z metodo sledenja ravnotežne poti z vezno enačbo, pri kateri vodimo izbrano prostostno stopnjo.

METODA SLEDENJA RAVNOTEŽNE POTI, KI TEMELJI NA KONTROLI PLASTIČNE DISIPACIJE ALI PLASTIČNEGA DELA

V tretjem poglavju predstavljamo metodo sledenja ravnotežne poti, ki temelji na kontroli plastične disipacije ali plastičnega dela v neelastičnem trdnem telesu ali konstrukciji. Metoda je lahko učinkovita za probleme z izrazito materialno in geometrijsko nelinearnostjo. Ta metoda se lahko uporablja za elasto-plastične probleme, kjer standardna metoda ločne dolžine odpove, ali ko se želimo izogniti umetnemu in neželjenemu elastičnemu razbremenjevanju celotne konstrukcije med analizo.

V drugem poglavju smo predstavili standardne metode sledenja ravnotežne poti, ki se lahko uspešno uporabijo pri reševanju mnogih geometrijsko nelinearnih problemov kot tudi geometrijsko in materialno nelinearnih problemov. Standardne metode lahko odpovedo pri reševanju posebno zahtevnih nelinearnih problemov, kot je npr. problem povezan s porušitvijo konstrukcije zaradi odpovedi materiala.

Karakteristični del metode sledenja ravnotežne poti je vezna enačba. V članku (Verhoosel et al., 2009) avtor predstavi različne oblike veznih enačb za kontrolo disipacije energije v neelastičnem materialu, in sicer za geometrijsko linearen problem, geometrijsko nelinearen problem z elasto-poškodbenim materialom in geometrijsko linearen problem z elasto-plastičnim materialom (brez utrjevanja). V doktorski disertaciji razširimo idejo od (Verhoosel et al., 2009) na geometrijsko nelinearne probleme z elasto-plastičnim materialom. Izpeljemo eksplicitno vezno enačbo in implicitno vezno enačbo, pri kateri vodimo plastično disipacijo za majhne specifične deformacije v elasto-plastičnem materialu z utrjevanjem.

METODA SLEDENJA RAVNOTEŽNE POTI

V nelinearni metodi končnih elementov za trdna telesa in konstrukcije je potrebno rešiti naslednji sistem nelinearnih ravnotežnih enačb:

$$\boldsymbol{R}\big(\boldsymbol{u}(t),\lambda(t)\big) = \boldsymbol{R}^{int}\big(\boldsymbol{u}(t)\big) - \boldsymbol{f}^{ext}\big(\lambda(t)\big) = \boldsymbol{0}$$

$\boldsymbol{R}^{int}$ in $\boldsymbol{f}^{ext}$ sta vektorja notranjih in zunanjih sil (in momentov), $\boldsymbol{u}$ je vektor neznanih vozliščnih pomikov (in rotacij), λ je faktor obtežbe, in $t \geq 0$ je monotono naraščajoči parameter, ki ga imenujemo psevdo-čas. V številnih primerih, sistem ravnotežnih enačb je možno rešiti samo skupaj z dodatno vezno enačbo:

$$g\big(\boldsymbol{u}(t) - \boldsymbol{u}(t-\Delta t), \lambda(t) - \lambda(t-\Delta t)\big) = 0$$

Δ je majhna (inkrementalna) sprememba. Simultano reševanje sistema enačb (3.1) in (3.2) se imenuje metoda sledenja ravnotežne poti.

Rešitev enačb (3.1) in (3.2) se išče na enak način kot pri standardni metodi sledenja ravnotežne poti. Predpostavimo, da poznamo konfiguracijo v psevdo-času t_n in jo definiramo s $\{\boldsymbol{u}(t_n), \lambda(t_n)\} = \{\boldsymbol{u}_n, \lambda_n\}$. Pri iskanju naslednje konfiguracije v psevdo-času $t_{n+1} = t_n + \Delta t_n$, aditivno razstavimo $\boldsymbol{u}_{n+1}$ in λ_{n+1} kot $\boldsymbol{u}_{n+1} = \boldsymbol{u}_n + \Delta\boldsymbol{u}_n$ in $\lambda_{n+1} = \lambda_n + \Delta\lambda_n$, kjer sta $\Delta\boldsymbol{u}_n$ in λ_n inkrement pomikov in inkrement faktorja obtežbe. Enačbi (3.1) in (3.2) sedaj zapišemo za čas t_{n+1} kot

$$\boldsymbol{R}_{n+1}(\boldsymbol{u}_n, \lambda_n; \Delta\boldsymbol{u}_n, \Delta\lambda_n) = \boldsymbol{0}$$

$$g_{n+1}(\Delta\boldsymbol{u}_n, \Delta\lambda_n) = 0$$

$\Delta\boldsymbol{u}_n$ in $\Delta\lambda_n$ sta neznanki. Rešitev enačb (3.3) se išče iteravno z Newton-Raphsonovo metodo. V i-ti iteraciji iščemo rešitev lineariziranega sistema enačb:

$$\begin{bmatrix} \boldsymbol{K}^i_{n+1} & \boldsymbol{R}^i_{n+1,\lambda} \\ \big[g^i_{n+1,\boldsymbol{u}}\big]^T & g^i_{n+1,\lambda} \end{bmatrix} \begin{Bmatrix} \Delta\tilde{\boldsymbol{u}}^i_n \\ \Delta\tilde{\lambda}^i_n \end{Bmatrix} = - \begin{Bmatrix} \boldsymbol{R}^i_{n+1} \\ g^i_{n+1} \end{Bmatrix}$$

za iterativni par neznank $\{\Delta\tilde{\boldsymbol{u}}^i_n, \Delta\tilde{\lambda}^i_n\}$, kjer je $(°)_{,\lambda}$ odvod (°) po $\Delta\lambda^i_n$ in $(°)_{,\boldsymbol{u}}$ je odvod (°) po $\Delta\boldsymbol{u}^i_n$, ter $\boldsymbol{K}^i_{n+1} = \boldsymbol{R}^i_{n+1,\boldsymbol{u}}$ je tangentna togostna matrika. Novi iterativni približek inkrementov dobimo kot $\Delta\boldsymbol{u}^{i+1}_{n+1} = \Delta\boldsymbol{u}^i_n + \Delta\tilde{\boldsymbol{u}}^i_n$ in $\Delta\lambda^i_{n+1} = \Delta\lambda^i_n + \Delta\tilde{\lambda}^i_n$.

Iterativna zanka se zaključi, ko je izpolnjen kriterij konvergence, tedaj smo dobili konvergirani rešitvi za $\Delta\boldsymbol{u}_n$ in $\Delta\lambda_n$. Konfiguracija $\{\boldsymbol{u}_{n+1}, \lambda_{n+1}\}$ v psevdo-času t_{n+1} je zdaj znana in lahko se začne iskanje nove ravnotežne točke.

Opisani postopek reševanja velja za katerokoli dodatno vezno enačbo g_{n+1} v (3.3). V nadaljevanju poglavja predstavljamo različne možnosti za izpeljavo vezne enačbe $g_{n+1} = 0$ za kontrolo inkrementalne plastične disipacije za geometrijsko nelinearne probleme z elasto-plastičnim materialom.

EKSPLICITNA OBLIKA VEZNE ENAČBE ZA VODENJE PLASTIČNE DISIPACIJE (VERZIJA 1)

Stopnjo plastične disipacije v elasto-plastičnem telesu ali konstrukciji lahko definiramo kot $\dot{D} = \dot{P} - \dot{\Psi}$, kjer je $\dot{P}$ odvod mehanskega dela po psevdo-času in $\dot{\Psi}$ je odvod termodinamičnega potenciala za plastičen material po psevdo-času. Za diskretizirani model v okviru geometrijske nelinearnosti in neelastičnega materiala lahko količino $\dot{P}$ zapišemo kot:

$$\dot{P} = \sum_e \int_{V^e} \boldsymbol{S}^T \dot{\boldsymbol{E}}\, dV = \boldsymbol{f}^{ext,T}\dot{\boldsymbol{u}} = \lambda \hat{\boldsymbol{f}}^{ext,T}\dot{\boldsymbol{u}}$$

e je indeks elementa v mreži končnih elementov, $\boldsymbol{S}$ je drugi Piola-Kirchhoffov tenzor napetosti, $\boldsymbol{E}$ so Green-Lagrangeve deformacije in V^e je začetni volumen elementa. V enačbi (3.5) predpostavimo, da so zunanje sile konzervativne in jih izrazimo kot $\boldsymbol{f}^{ext} = \lambda \hat{\boldsymbol{f}}^{ext}$, kjer je $\hat{\boldsymbol{f}}^{ext}$ referenčni vektor zunanjih sil. Potencial proste energije Ψ v modelu temelji na St. Venant-Kirchhoff elastičnosti in plastičnosti z linearnim izotropnim utrjevanjem. Ψ je vsota proste energije zaradi elastičnih deformacij U:

$$U = \sum_e \int_{V^e} \frac{1}{2}\boldsymbol{E}^{el,T}\boldsymbol{D}\boldsymbol{E}^{el}\, dV = \sum_e \int_{V^e} \frac{1}{2}\boldsymbol{S}^T\boldsymbol{D}^{-1}\boldsymbol{S}\, dV$$

in proste energije zaradi utrjevanja v materialu H:

$$H = \sum_e \int_{V^e} \frac{1}{2}\mathrm{K}_h \xi_h^2\, dV$$

$\boldsymbol{E}^{el} = \boldsymbol{E} - \boldsymbol{E}^p$ je vektor elastičnih deformacij, $\boldsymbol{E}^p$ je vektor plastičnih deformacij, $\boldsymbol{D}$ je simetrična konstitutivna matrika, ki povezuje napetosti z elastičnimi deformacijami $\boldsymbol{S} = \boldsymbol{D}\boldsymbol{E}^{el}$, K_h je modul utrjevanja, in ξ_h je spremenljivka, ki kontrolira linearno izotropno utrjevanje.

Vzemimo eksplicitno Eulerjevo metodo numerične integracije in izrazimo plastično disipacijo v psevdo-času t_{n+1}, t.j. $D_{n+1} = D_n + \dot{D}_n \Delta t_n$, kjer je $\Delta t_n = t_{n+1} - t_n$. Sedaj lahko definiramo dodatno vezno enačbo:

$$g_{n+1} = D_{n+1} - D_n - \tau_n = 0 \quad \Rightarrow \quad g_{n+1} = \dot{D}_n \Delta t_n - \tau_n = 0$$

τ_n je predpisana vrednost plastične disipacije v psevdo-koraku $[t_n, t_{n+1}]$. S sklepanjem $\dot{D}_n = \dot{P}_n - \dot{\Psi}_n = \dot{P}_n - \dot{\mathrm{U}}_n - \dot{H}_n$ in upoštevanjem enačb (3.5), (3.8) in (3.9), vezno enačbo (3.10) lahko zapišemo kot

$$g_{n+1} = \dot{D}_n \Delta t_n - \tau_n = \Delta \boldsymbol{u}_n^T \left(\lambda_n \hat{\boldsymbol{f}}^{ext} - \boldsymbol{f}_n^*\right) - \tau_n = 0$$

$\Delta \boldsymbol{u}_n = \dot{\boldsymbol{u}}_n \Delta t_n$ je trenutni iterativni popravek inkrementa pomikov (indeks iteracije *i* je izpuščen) in vektor $\boldsymbol{f}_n^*$ izrazimo kot:

$$\boldsymbol{f}_n^* = \mathbb{A}_e \left[\int_{V^e} \boldsymbol{B}^T \boldsymbol{C}^{ep} \boldsymbol{D}^{-1} \boldsymbol{S} \, dV + \int_{V^e} \mathrm{K}_h \xi_h \left(\frac{\partial \xi_h}{\partial \boldsymbol{u}^e} \right)_n dV \right]$$

EKSPLICITNA OBLIKA VEZNE ENAČBE ZA VODENJE PLASTIČNEGA DELA (VERZIJA 1)

Vrednost drugega integrala na desni strani enačbe (3.12) je praviloma manjša od vrednosti prvega integrala, kar dovoljuje poenostavitev pri izračunu vektorja $\boldsymbol{f}_n^*$. V vezni enačbi (3.11) uporabimo aproksimacijo vektorja $\boldsymbol{f}_n^*$, ki je izražena kot:

$$\boldsymbol{f}_n^* \;\rightarrow\; \boldsymbol{f}_n^{*,app} = \mathbb{A}_e \left[\int_{V^e} \boldsymbol{B}_n^T \boldsymbol{C}_n^{ep} \boldsymbol{D}^{-1} \boldsymbol{S}_n \, dV \right]$$

EKSPLICITNA OBLIKA VEZNE ENAČBE ZA VODENJE PLASTIČNE DISIPACIJE (VERZIJA 2)

Stopnjo plastične disipacije v elasto-plastičnem telesu ali konstrukciji lahko zapišemo tudi kot (glej (Ibrahimbegovic, 2009)):

$$\dot{D} = \dot{\boldsymbol{u}}^T \mathbb{A}_e \left[\int_{V^e} \boldsymbol{B}^T (\boldsymbol{I} - \boldsymbol{D}^{-1} \boldsymbol{C}^{ep})^T \boldsymbol{S} \, dV \right] - \sum_e \int_{V^e} \mathrm{K}_h \xi_h \dot{\xi}_h \, dV$$

Če zgornjo enačbo uporabimo za $\dot{D}_n$, potem lahko zapišemo izraz za vezno enačbo:

$$g_{n+1} = \dot{D}_n \Delta t_n - \tau_n = \Delta \boldsymbol{u}_n^T \bar{\boldsymbol{f}}_n - \tau_n = 0$$

kjer je

$$\bar{\boldsymbol{f}}_n = \mathbb{A}_e \left[\int_{V^e} \boldsymbol{B}^T (\boldsymbol{I} - \boldsymbol{D}^{-1} \boldsymbol{C}^{ep})^T \boldsymbol{S}_n \, dV - \int_{V^e} \mathrm{K}_h \xi_{h,n} \left(\frac{\partial \xi_h}{\partial \boldsymbol{u}^e} \right)_n dV \right]$$

Če upoštevamo enakost $(\boldsymbol{I} - \boldsymbol{D}^{-1} \boldsymbol{C}^{ep})^T = \boldsymbol{I} - \boldsymbol{C}^{ep} \boldsymbol{D}^{-1}$, saj sta $\boldsymbol{C}^{ep}$ in $\boldsymbol{D}$ obe simetrični, primerjava enačb (3.11) in (3.12) z izrazi (3.17) in (3.18) pokaže, da velja:

$$\lambda_n \hat{\boldsymbol{f}}^{ext} = \mathbb{A}_e \left[\int_{V^e} \boldsymbol{B}_n^T \boldsymbol{S}_n \, dV \right]$$

Enačba (3.19) definira ravnotežje v psevdo-času t_n, glej (Ibrahimbegovic, 2009), kar je tudi pogoj, ki je izpolnjen na začetku trenutnega psevdo-koraka $[t_n, t_{n+1}]$. To vodi do zaključka, da sta vezni enačbi (3.11) in (3.17) enakovredni. Z drugimi besedami, izpeljavi Verzija 1 in Verzija 2 vrneta isto končno obliko vezne enačbe.

EKSPLICITNA OBLIKA VEZNE ENAČBE ZA VODENJE PLASTIČNEGA DELA (VERZIJA 2)

Če zanemarimo prispevek utrjevanja v materialu, potem lahko poenostavljeno zapišemo aproksimacijo za stopnjo plastične disipacije (3.16) in aproksimacijo vektorja $\bar{\boldsymbol{f}}_n$ v (3.19):

$$\dot{D} \;\rightarrow\; \dot{D}^{approx} = \sum_e \int_{V^e} \dot{\boldsymbol{E}}^{p,T} \boldsymbol{S} \, dV$$

$$\bar{\boldsymbol{f}}_n \;\rightarrow\; \bar{\boldsymbol{f}}_n^{approx} = \mathbb{A}_e \left[\int_{V^e} \boldsymbol{B}_n^T \left(\boldsymbol{I} - \boldsymbol{D}^{-1} \boldsymbol{C}_n^{ep} \right)^T \boldsymbol{S}_n \, dV \right]$$

Prvi izraz v (3.20) je stopnja plastičnega dela.

IMPLICITNA OBLIKA VEZNE ENAČBE

V tem razdelku uporabimo implicitno Eulerjevo metodo za numerično integracijo, pri čemer plastično disipacijo v psevdo-času t_{n+1} izrazimo kot:

$$D_{n+1} = D_n + \dot{D}_{n+1} \Delta t_n, \;\; \Delta t_n = t_{n+1} - t_n$$

kar vodi do naslednje dodatne vezne enačbe

$$g_{n+1} = \dot{D}_{n+1} \Delta t_n - \tau_n = \Delta \boldsymbol{u}_n^T \left(\lambda_{n+1} \hat{\boldsymbol{f}}^{ext} - \boldsymbol{f}_{n+1}^* \right) - \tau_n = 0$$

Vektor $\boldsymbol{f}_{n+1}^*$ je:

$$\boldsymbol{f}_{n+1}^* = \mathbb{A}_e \left[\int_{V^e} \boldsymbol{B}_{n+1}^T \boldsymbol{C}_{n+1}^{ep} \boldsymbol{D}^{-1} \boldsymbol{S}_{n+1} \, dV + \int_{V^e} \mathrm{K}_h \xi_{h,n+1} \left(\frac{\partial \xi_h}{\partial \boldsymbol{u}^e} \right)_n dV \right]$$

Na tem mestu poudarimo, da je $\Delta \boldsymbol{u}_n$ v (3.22) tokrat definiran kot $\Delta \boldsymbol{u}_n = \dot{\boldsymbol{u}}_{n+1} \Delta t_n$.

Vezno enačbo (3.22) lahko izrazimo tudi kot:

$$g_{n+1} = \dot{D}_{n+1}\Delta t_n - \tau_n = \Delta \boldsymbol{u}_n^T \bar{\boldsymbol{f}}_{n+1} - \tau_n = 0$$

kjer

$$\bar{\boldsymbol{f}}_{n+1} = \mathbb{A}_e \left[\int_{V^e} \boldsymbol{B}_{n+1}^T \left(\boldsymbol{I} - \boldsymbol{D}^{-1} \boldsymbol{C}_{n+1}^{ep} \right)^T \boldsymbol{S}_{n+1} \, dV - \int_{V^e} \mathrm{K}_h \xi_{h,n+1} \left(\frac{\partial \xi_h}{\partial \boldsymbol{u}^e} \right)_{n+1} dV \right]$$

NUMERIČNI PRIMERI

Na koncu so prikazani rezultati analize primerov z metodo sledenja ravnotežne poti, pri kateri vodimo plastično disipacijo. Na primeru cilindričnega panela smo pokazali, da dobimo enake rezultate kot z analizo po cilindrični metodi ločne dolžine. Z novo metodo smo izračunali težje primere: polovica sfere in vpeti cilinder, pri katerih metoda ločne dolžine ne deluje dobro.

ŠTIRIVOZLIŠČNI KONČNI ELEMENTI Z VGRAJENO MOČNO NEZVEZNOSTJO ZA OBRAVNAVO 2D TRDNIN

Nastanek ene ali več makroskopskih razpok v konstrukcijskem elementu je resna poškodba, saj se razpoke lahko širijo in ustvarijo mehanizem, katerega možna posledica je porušitev konstrukcijskega elementa. V tem poglavju predstavimo različne formulacije končnih elementov z vgrajeno močno nezveznostjo v pomikih (ang. »*the Embedded Strong Discontinuity Finite Element Method*«, krajše *ED-FEM*), ki jih lahko uporabimo za 2d probleme v ravninskem napetostnem ali ravninskem deformacijskem stanju. Omejimo se na krhke materiale, kot so npr. beton, kamen in opeka.

PLOSKOVNI ELEMENT Z VGRAJENO MOČNO NEZVEZNOSTJO V POMIKIH

V tem poglavju izpeljemo štirikotni končni element z vgrajeno nezveznostjo, ki se lahko uporablja za modeliranje problemov v ravninskem napetostnem stanju. Formulacija omogoča linearno širjenje nezveznosti oz. razpoke tako v normalni in kot tangentni smeri.

Slika 4.2 prikazuje skico štirikotnega končnega elementa z domeno $\Omega^e \subset R^2$. Ravna linija Γ^e predstavlja diskontinuiteto oz. razpoko, ki razdeli domeno končnega elementa na dve poddomeni Ω^{e+} in Ω^{e-}. Vpeljemo parametre α_m, $m = 1, \ldots, 4$, za štiri osnovne oblike širjenja razpoke (Slika 4.3). Prvi dve osnovni obliki širjenja razpoke ($m = 1$ in $m = 2$), opisujeta način odpiranja razpoke v smeri normale $\boldsymbol{n}$ (tip I) in zadnji dve osnovni obliki ($m = 3$ in $m = 4$) pa sta povezani z odpiranjem razpoke v tangentni smeri $\boldsymbol{m}$ (tip II).

Aproksimacijo pomikov po domeni končnega elementa zapišemo kot:

$$\boldsymbol{u}(\boldsymbol{\xi}, \Gamma^{\mathrm{e}}) = \sum_{a=1}^{4} N_a(\boldsymbol{\xi})\, \boldsymbol{d}_a + \sum_{m=1}^{4} \boldsymbol{p}_m(\boldsymbol{\xi}, \Gamma^{\mathrm{e}})\, \alpha_m$$

Vektor pomikov ima dve komponenti $\boldsymbol{u} = \left[u_x, u_y\right]^T$, $\boldsymbol{d}_a = \left[u_{xa}, u_{ya}\right]^T$ sta pomika v vozlišču a, in $\boldsymbol{p}_m = \left[p_{mx}, p_{my}\right]^T$ je vektor interpolacijskih funkcij (4.6) - (4.9) povezan s parametrom α_m in osnovno obliko širjenja m.

Tenzor majhnih deformacij za ravninsko napetostno stanje in ravninsko deformacijsko stanje je definirano kot $\nabla^s \boldsymbol{u} = \frac{1}{2}(\nabla \otimes \boldsymbol{u} + \boldsymbol{u} \otimes \nabla)$, pri čemer $\nabla = \left[\frac{\partial}{\partial x}, \frac{\partial}{\partial y}\right]^T$ in $\otimes$ je tenzorski produkt. Člene, ki nastopajo v simetričnem tenzorju deformacij, lahko razporedimo v vektor:

$$\boldsymbol{\epsilon} = \left[\frac{\partial u_x}{\partial x}, \frac{\partial u_y}{\partial y}, \frac{\partial u_x}{\partial y} + \frac{\partial u_y}{\partial x}\right]^T = \left[\epsilon_{xx}, \epsilon_{yy}, \gamma_{xy}\right]^T$$

Vektor deformacij lahko izrazimo z vozliščnimi pomiki $\boldsymbol{d}_a$ in parametri širjenja α_m:

$$\boldsymbol{\epsilon}(\boldsymbol{\xi}, \Gamma^{\mathrm{e}}) = \sum_{a=1}^{4} \boldsymbol{B}_a(\boldsymbol{\xi}) \boldsymbol{d}_a + \sum_{m=1}^{4} \boldsymbol{G}_m(\boldsymbol{\xi}, \Gamma^{\mathrm{e}}) \alpha_m$$

kjer $\boldsymbol{G}_m = \left[\frac{\partial p_{mx}}{\partial x}, \frac{\partial p_{my}}{\partial y}, \frac{\partial p_{mx}}{\partial y} + \frac{\partial p_{my}}{\partial x}\right]^T$. Eksplicitni izrazi za vektorje $\boldsymbol{G}_m$ so (4.13)-(4.16). Iz (4.1)-(4.16) lahko sklepamo, da so vektorji $\boldsymbol{G}_m$ sestavljeni iz dveh delov:

$$\boldsymbol{G}_m = \overline{\boldsymbol{G}}_m + \overline{\overline{\boldsymbol{G}}}_m$$

kjer $\overline{\boldsymbol{G}}_m$ je omejen (t.j. regularen) in $\overline{\overline{\boldsymbol{G}}}_m$ je neomejen (t.j. singularen) zaradi δ_Γ. Posledično lahko vektor deformacij $\boldsymbol{\epsilon}$ razdelimo na regularni del $\overline{\boldsymbol{\epsilon}}$ in singularni del $\overline{\overline{\boldsymbol{\epsilon}}}$:

$$\boldsymbol{\epsilon} = \underbrace{\sum_{a=1}^{4} \boldsymbol{B}_a \boldsymbol{d}_a + \sum_{m=1}^{4} \overline{\boldsymbol{G}}_m \alpha_m}_{\overline{\boldsymbol{\epsilon}}} + \underbrace{\sum_{m=1}^{4} \overline{\overline{\boldsymbol{G}}}_m \alpha_m}_{\overline{\overline{\boldsymbol{\epsilon}}}}$$

Končni elementi z vgrajeno nezveznostjo, ki so izpeljani v tem poglavju, bodo temeljili na Petrov-Galerkinovi aproksimaciji, ki uporablja različne interpolacije za realne in virtualne deformacije. Namreč, tovrstna aproksimacija je najbolj primerna za končne elemente z vgrajeno močno nezveznostjo, kar je prikazano npr. v (Jirasek, 2000), kjer so poimenovani kot »SKON formulacije«.

Vektor virtualnih deformacij je sestavljen iz dveh delov:

$$\hat{\boldsymbol{\epsilon}}(\boldsymbol{\xi}, \Gamma^{\mathrm{e}}) = \sum_{a=1}^{4} \boldsymbol{B}_a(\boldsymbol{\xi}) \hat{\boldsymbol{d}}_a + \sum_{m=1}^{4} \widehat{\boldsymbol{G}}_m(\boldsymbol{\xi}, \Gamma^{\mathrm{e}}) \hat{\alpha}_m$$

V zgornji enačbi (4.25), $\widehat{\boldsymbol{d}}_a$ so virtualni pomiki vozlišča a in $\hat{\alpha}_m$ je virtualni ekvivalent parametra α_m.

V disertaciji smo povzeli dva različna koncepta za definicijo vektorjev $\widehat{\boldsymbol{G}}_m$. Prvi koncept (poglavje 4.2.3.1) je predstavljen v (Dujc et al, 2010), drugi (poglavje 4.2.3.2) pa je predlagan v (Linder and Armero, 2007).

Za dvodimenzionalno telo diskretizirano z N_e štirivozliščnimi elementi z vgrajeno nezveznostjo lahko zapišemo princip virtualnega dela (t.j. šibko obliko ravnotežnih enačb):

$$\mathbb{A}_{e=1}^{N_e}(G^{int,e} - G^{ext,e}) = 0$$

$G^{ext,e} = \sum_{a=1}^{4} \widehat{\boldsymbol{d}}_a^T \boldsymbol{f}_a^{ext,e}$ je virtualno delo zunanjih sil in $G^{int,e}$ je virtualno delo notranjih sil:

$$G^{int,e} = t^e \int_{\Omega^e} \hat{\boldsymbol{\epsilon}}(\boldsymbol{\xi}, \Gamma^{\mathrm{e}}) \cdot \boldsymbol{\sigma}(\boldsymbol{\xi})\, d\Omega$$

t^e je (konstantna) debelina elementa, $\boldsymbol{\sigma} = \left[\sigma_{xx}, \sigma_{yy}, \sigma_{xy}\right]^T$ je vektor napetosti, in $\hat{\boldsymbol{\epsilon}}$ je vektor virtualnih deformacij (4.25). Če upoštevamo enačbi (4.50) in (4.51), lahko princip virtualnega dela (4.48) izrazimo kot:

$$\mathbb{A}_{e=1}^{N_e}\left(\sum_{a=1}^{4} \widehat{\boldsymbol{d}}_a^T\left(\boldsymbol{f}_a^{int,e} - \boldsymbol{f}_a^{ext,e}\right)\right) + \mathbb{A}_{e=1}^{N_e}\left(\sum_{m=1}^{4} t^e \int_{\Omega^e} \hat{\alpha}_m \widehat{\boldsymbol{G}}_m^T \boldsymbol{\sigma}\, d\Omega\right) = 0$$

Ker so komponente vektorja virtualnih pomikov $\widehat{\boldsymbol{d}}_a$ poljubne (in kinematično dopustne), iz prvega dela enačbe (4.52) dobimo globalni sistem ravnotežnih enačb:

$$\mathbb{A}_{e=1}^{N_e} \underbrace{\left(\boldsymbol{f}^{int,e} - \boldsymbol{f}^{ext,e}\right)}_{\boldsymbol{R}_d^e} = \boldsymbol{0}$$

Če upoštevamo, da je virtualni parameter $\hat{\alpha}_m$ poljuben, potem iz drugega dela enačbe (4.52) dobimo:

$$t^e \int_{\Omega^e} \widehat{\boldsymbol{G}}_m^T \boldsymbol{\sigma}\, d\Omega = 0 \quad \text{za } \forall\, m = 1, \cdots, 4 \text{ in } \forall\, e = 1, \cdots, N_e$$

Slednji izraz predstavlja sistem lokalnih ravnotežnih enačb, ki se rešuje na nivoju elementa z vgrajeno nezveznostjo. Izrazi (4.68)-(4.71) so lokalne ravnotežne enačbe napisane v odvisnosti od kohezijskih napetosti v razpoki.

V območju $\Omega^e \setminus \Gamma^e$ uporabimo linearno elastičen konstitutivni zakon:

$$\boldsymbol{\sigma} = \boldsymbol{C}\bar{\boldsymbol{\epsilon}}$$

Razpoka se lahko širi v smeri normale $\boldsymbol{n}$ (tip I) in tudi v smeri tangente na razpoko $\boldsymbol{m}$ (tip II). Kohezijske napetosti v razpoki opišemo z dvema nepovezanima poškodbenima konstitutivnima zakonoma; eden velja za normalno smer $\boldsymbol{n}$, drugi pa za tangentno (strižno) smer $\boldsymbol{m}$. Bistvena dela takšnega zakona sta funkcija porušitve materiala $\bar{\bar{\phi}}$ in funkcija mehčanja $\bar{\bar{q}}$.

V normalni smeri $\boldsymbol{n}$, upoštevamo samo natezne kohezijske napetosti, t.j. $t_n \geq 0$. Porušitvena funkcija je tako:

$$\bar{\bar{\phi}}_n\left(\bar{\bar{t}}_n, \bar{\bar{q}}_n\right) = t_n - (\sigma_{un} - \bar{\bar{q}}_n) = 0$$

kjer je σ_{un} natezna trdnost materiala, in $\bar{\bar{q}}_n$ eksponentna funkcija mehčanja v normalni smeri:

$$\bar{\bar{q}}_n\left(\bar{\bar{\xi}}_n\right) = \sigma_{un}\left(1 - e^{-\frac{\sigma_{un}}{G_{fn}}\bar{\bar{\xi}}_n}\right)$$

V tangentni smeri $\boldsymbol{m}$, upoštevamo tako pozitivne kot tudi negativne tangentne kohezijske napetosti t_m. Porušitvena funkcija je tako:

$$\bar{\bar{\phi}}_m\left(\bar{\bar{t}}_m, \bar{\bar{q}}_m\right) = |t_m| - (\sigma_{um} - \bar{\bar{q}}_m) = 0$$

kjer je σ_{um} strižna trdnost materiala, in $\bar{\bar{q}}_m$ eksponentna funkcija mehčanja v smeri tangente:

$$\bar{\bar{q}}_m\left(\bar{\bar{\xi}}_m\right) = \sigma_{um}\left(1 - e^{-\frac{\sigma_{um}}{G_{fm}}\bar{\bar{\xi}}_m}\right)$$

METODA NEKOMPATIBILNIH OBLIK ZA ELEMENTE Z VGRAJENO NEZVEZNOSTJO

Formulacijo standardnih ploskovnih končnih elementov (Q4) lahko nadgradimo z uporabo metode nekompatibilnih oblik. Polje pomikov v Q4 izboljšamo z nekompatibilnimi oblikami za pomike tako, da štirim interpolacijskim funkcijam N_a, $a = 1, \cdots, 4$ dodamo interpolacijski funkciji $M_b, b = 1, 2$. Novi element označimo z Q6.

V nadaljevanju na kratko prikažemo izpeljavo elementa Q6 z vgrajeno nezveznostjo. Zapišimo interpolacijo pomikov po elementu z upoštevanjem nekompatibilnih pomikov:

$$\boldsymbol{u}(\boldsymbol{\xi}, \Gamma^{\mathrm{e}}) = \sum_{a=1}^{4} N_a(\boldsymbol{\xi})\, \boldsymbol{d}_a + \sum_{b=1}^{2} M_b(\boldsymbol{\xi})\, \boldsymbol{\rho}_b + \sum_{m=1}^{4} \boldsymbol{p}_m(\boldsymbol{\xi}, \Gamma^{\mathrm{e}})\, \alpha_m,$$

kjer je drugi člen vsote povezan z nekompatibilnimi pomiki, $M_1(\xi) = 1 - \xi^2$ in $M_2(\eta) = 1 - \eta^2$ sta interpolacijski funkciji (velja $N_a \cap M_b = \emptyset$ za $\forall\, a, b$), in $\boldsymbol{\rho}_1 = [\rho_{11}, \rho_{12}]^T$, $\boldsymbol{\rho}_2 = [\rho_{21}, \rho_{22}]^T$ so parametri nekompatibilnih pomikov v končnem element e. Odvod (4.11) pomikov (4.90) vrne izraz za deformacije:

$$\boldsymbol{\epsilon}(\boldsymbol{\xi}, \Gamma^{\mathrm{e}}) = \sum_{a=1}^{4} \boldsymbol{B}_a(\boldsymbol{\xi})\boldsymbol{d}_a + \sum_{b=1}^{2} \widetilde{\boldsymbol{G}}_b(\boldsymbol{\xi})\, \boldsymbol{\rho}_b + \sum_{m=1}^{4} \boldsymbol{G}_m(\boldsymbol{\xi}, \Gamma^{\mathrm{e}})\alpha_m$$

z $\widetilde{\boldsymbol{G}}_b$, ki je modificirani vektor $\boldsymbol{G}_b$:

$$\widetilde{\boldsymbol{G}}_b = \boldsymbol{G}_b - \frac{1}{A_{\Omega^e}} \int_{\Omega^e} \boldsymbol{G}_b \, d\Omega, \quad \boldsymbol{G}_b = \left[\left[\frac{\partial M_b}{\partial x}, 0, \frac{\partial M_b}{\partial y} \right]^T, \left[0, \frac{\partial M_b}{\partial y}, \frac{\partial M_b}{\partial x} \right]^T \right]$$

tako, da velja

$$\int_{\Omega^e} \widetilde{\boldsymbol{G}}_b d\Omega = \boldsymbol{0}$$

Zaradi aditivnih lastnosti $\boldsymbol{G}_m$ (glej (4.23)), deformacije (4.91) lahko zapišemo kot:

$$\boldsymbol{\epsilon} = \underbrace{\sum_{a=1}^{4} \boldsymbol{B}_a \boldsymbol{d}_a + \sum_{b=1}^{2} \widetilde{\boldsymbol{G}}_b \, \boldsymbol{\rho}_b + \sum_{m=1}^{4} \overline{\boldsymbol{G}}_m \alpha_m}_{\bar{\boldsymbol{\epsilon}}} + \underbrace{\sum_{m=1}^{4} \overline{\overline{\boldsymbol{G}}}_m \alpha_m}_{\bar{\bar{\boldsymbol{\epsilon}}}}$$

$\bar{\boldsymbol{\epsilon}}(\boldsymbol{\xi})$ so omejene deformacije po elementu Ω^e/Γ^e in $\bar{\bar{\boldsymbol{\epsilon}}}$ so neomejene deformacije v Γ^e.

Izrazimo virtualne deformacije v Q6 elementu:

$$\hat{\boldsymbol{\epsilon}}(\boldsymbol{\xi}, \Gamma^e) = \underbrace{\sum_{a=1}^{4} \boldsymbol{B}_a(\boldsymbol{\xi}) \hat{\boldsymbol{d}}_a}_{\hat{\boldsymbol{\epsilon}}^d} + \underbrace{\sum_{b=1}^{2} \widetilde{\boldsymbol{G}}_b(\boldsymbol{\xi}) \, \hat{\boldsymbol{\rho}}_b + \sum_{m=1}^{4} \hat{\boldsymbol{G}}_m(\boldsymbol{\xi}, \Gamma^e) \hat{\alpha}_m}_{\hat{\bar{\boldsymbol{\epsilon}}}^\beta}$$

$\hat{\bar{\boldsymbol{\epsilon}}}^d(\boldsymbol{\xi})$ so virtualne deformacije zaradi virtualnih vozliščnih pomikov in $\hat{\bar{\boldsymbol{\epsilon}}}^\beta(\boldsymbol{\xi})$ so virtualne deformacije zaradi vseh dodatnih parametrov, t.j. parametrov za nekompatibilne pomike in parametrov širjenja razpoke. Poudarimo, da se interpolacija realnih deformacij razlikuje od interpolacije virtualnih deformacij, v smislu Petrov-Galerkinove aproksimacije, ki je priznana za najbolj primerno za končne elemente z vgrajeno nezveznostjo.

Podobno kot pri standardnem elementu Q4, tudi za element Q6 izpeljemo dve ravnotežni enačbi na podlagi principa o virtualnem delu.

Prva ravnotežna enačba se glasi:

$$G^{int,e,1} - G^{ext,e} = 0$$

$G^{ext,e} = \sum_{a=1}^{4} \hat{\boldsymbol{d}}_a^T \boldsymbol{f}_a^{ext,e}$ je virtualno delo zunanjh sil, ki delujejo na element. Virtualno delo notranjih sil $G^{int,e,1}$ je po definiciji enako

$$G^{int,e,1} = t^e \int_{\Omega^e} \hat{\bar{\boldsymbol{\epsilon}}}^d \cdot \boldsymbol{C} \bar{\boldsymbol{\epsilon}} \, d\Omega$$

Virtualne deformacije zaradi virtualnih vozliščnih pomikov $\hat{\bar{\boldsymbol{\epsilon}}}^d$ in realne deformacija $\bar{\boldsymbol{\epsilon}}$ so podani v (4.94) in (4.95),

$$G^{int,e,1} = \sum_{a=1}^{4} \hat{\boldsymbol{d}}_a^T \boldsymbol{f}_a^{int,e,1}$$

kjer je vozliščni vektor notranjih sil enak:

$$\boldsymbol{f}_a^{int,e,1} = t^e \int_{\Omega^e} \boldsymbol{B}_a \, \boldsymbol{C} \left(\sum_{c=1}^{4} \boldsymbol{B}_c \boldsymbol{d}_c + \sum_{b=1}^{2} \widetilde{\boldsymbol{G}}_b \, \boldsymbol{\rho}_b + \sum_{m=1}^{4} \overline{\boldsymbol{G}}_m \alpha_m \right) d\Omega$$

Sedaj lahko za 2d diskretizirano telo z N_e elementi izrazimo globalni sistem ravnotežnih enačb:

$$\mathbb{A}_{e=1}^{N_e} \underbrace{\left(\boldsymbol{f}^{int,e,1} - \boldsymbol{f}^{ext,e} \right)}_{\boldsymbol{R}_d^e} = \boldsymbol{0}$$

$\mathbb{A}$ je operator za združevanje končnih elementov v sistem, ki upošteva tudi robne pogoje.

Druga oz. lokalna ravnotežna enačba je po definiciji enaka:

$$G^{int,e,2} = t^e \int_{\Omega^e} \hat{\boldsymbol{\epsilon}}^{\beta} \cdot \boldsymbol{C} \bar{\boldsymbol{\epsilon}} \, d\Omega = 0$$

kjer sta $\hat{\boldsymbol{\epsilon}}^{\beta}$ in $\bar{\boldsymbol{\epsilon}}$ podani v (4.94) in (4.95). Ob upoštevanju izrazov (4.94), (4.95) in (4.33), zgornjo enačbo lahko preoblikujemo v:

$$G^{int,e,2} = t^e \int_{\Omega^e} \left(\sum_{b=1}^{2} \widetilde{\boldsymbol{G}}_b \, \hat{\boldsymbol{\rho}}_b + \sum_{m=1}^{4} \left(\bar{\bar{\boldsymbol{G}}}_m + \bar{\bar{\bar{\boldsymbol{G}}}}_m \right) \hat{\alpha}_m \right) \cdot \boldsymbol{\sigma} \, d\Omega = 0$$

Poudarimo, da $G^{int,e,1} + G^{int,e,2} = G^{ext,e}$, skupaj z $G^{int,e,1}$ iz (4.97), $G^{int,e,2}$ iz (4.103), in $\boldsymbol{\sigma} = \boldsymbol{C}\bar{\boldsymbol{\epsilon}}$ (glej (4.105)), je enako enačbi za virtualno delo. Za razliko od standardnega elementa Q4, pri elementu Q6 napetost $\boldsymbol{\sigma}$ je definirana z (4.105), kar tudi upoštevamo v lokalnih ravnotežnih enačbah (4.107)-(4.110). Dodatno, iz izraza (4.106) sledijo dodatne enačbe:

$$\underbrace{t^e \int_{\Omega^e} \widetilde{\boldsymbol{G}}_b^T \boldsymbol{\sigma} \, d\Omega}_{\boldsymbol{R}_{\rho,b}} = \boldsymbol{0}, b = 1,2$$

ALGORITEM SLEDENJA RAZPOKI

Kriterij za umestitev razpoke temelji na največji glavni napetosti v elementu. Namreč, ko je največja glavna napetost v elementu večja ali enaka natezni trdnosti materiala

$$\sigma_1 \geq \sigma_{un},$$

potem je razpoka (nezveznost) vgrajena v element. Glavno napetost v elementu σ_1 izračunamo po splošni enačbi (4.114) tako, da upoštevamo vektor povprečne napetosti v elementu.

Najbolj enostavna strategija za analizo razpok v 2d telesu je dovoliti vsakemu elementu v mreži končnih elementov, da razvije razpoko, če je za isti element izpolnjen pogoj umestitve razpoke (4.113). Vendar takšna strategija ne privede do pravih rešitev, kot je prikazano v poglavju 6.

Druga možnost je uporaba algoritma za povezane razpoke (Slika 4.6), ki sledi eni razpoki v vnaprej določeni domeni mreže. V tej strategiji lahko samo t.i. prednji element (*the crack-front element*) razvije razpoko. Rob, na katerem leži zadnja točka zvezne razpoke, določa prednji element, glej Slika 4.5.

POSTOPEK REŠEVANJA ENAČB

V tem razdelku izpeljemo rešitev nelinearnih enačb. Rešitev se išče v diskretnih psevdo-časovnih točkah, $0, \tau_1, \cdots, \tau_n, \tau_{n+1}, \cdots, T$. Uporabimo bodisi standardno inkrementalno-iterativno Newtonovo metodo ali metodo sledenja ravnotežne poti. V obeh primerih izvedemo linearizacijo nelinearnih enačb. V nadaljevanju prikažemo iteracijo i, ko iščemo rešitev v psevdo-časovni točki τ_{n+1} v okviru Newtonove metode.

REŠITEV ENAČB ZA Q4 ELEMENT Z VGRAJENO NEZVEZNOSTJO V POMIKIH

Če ni razpok v mreži N_e končnih elementov, naslednji sistem enačb mora biti rešen za neznane iterativne vozliščne pomike:

$$\mathbb{A}_{e=1}^{N_e}\left(\boldsymbol{K}_{dd,n+1}^{e,i}\Delta\boldsymbol{d}_{n+1}^{e,i}\right) = \mathbb{A}_{e=1}^{N_e}\left(-\boldsymbol{R}_{d,n+1}^{e,i}\right)$$

kjer sta:

$$\boldsymbol{K}_{dd,n+1}^{e,i} = \left.\frac{\partial \boldsymbol{R}_d^e}{\partial \boldsymbol{d}^e}\right|_{n+1}^{i}, \qquad \boldsymbol{R}_{d,n+1}^{e,i} = (\boldsymbol{f}^{int,e} - \boldsymbol{f}^{ext,e})_{n+1}^{i}$$

in $\boldsymbol{d}^e = \left[\boldsymbol{d}_a^{e,T}\right]^T$. Rezidualni vektor $\boldsymbol{R}_d^e$ izračunamo po enačbi (4.53) z upoštevanjem $\alpha_m = 0$. Rešitev sistema enačb (4.116) je $\Delta\boldsymbol{d}_{n+1}^{e,i}$ in se upošteva kot iterativni prirastek totalnega pomika v elementu kot:

$$\boldsymbol{d}_{n+1}^{e,i} = \boldsymbol{d}_{n+1}^{e,i-1} + \Delta\boldsymbol{d}_{n+1}^{e,i}$$

Če je v mreži končnih elementov eden ali več elementov z razpoko, potem je potrebno rešiti naslednji sistem enačb za iterativne vozliščne pomike:

$$\mathbb{A}_{e=1}^{N_e}\left(\boldsymbol{K}_{cond,n+1}^{e,i}\Delta\boldsymbol{d}_{n+1}^{e,i}\right) = \mathbb{A}_{e=1}^{N_e}\left(-\boldsymbol{R}_{cond,n+1}^{e,i}\right)$$

Za element *e* brez razpoke velja:

$$\boldsymbol{K}_{cond,n+1}^{e,i} = \boldsymbol{K}_{dd,n+1}^{e,i}, \quad \boldsymbol{R}_{cond,n+1}^{e,i} = \boldsymbol{R}_{d,n+1}^{e,i}$$

Togostna matrika elementa $\boldsymbol{K}_{dd,n+1}^{e,i}$ in rezidual $\boldsymbol{R}_{d,n+1}^{e,i}$ sta definirana v (4.117). Za elemente z razpoko izvedemo statično kondenzacijo naslednjega sistema enačb:

$$\begin{bmatrix} \boldsymbol{K}^{e}_{dd} & \boldsymbol{K}^{e}_{d\alpha} \\ \boldsymbol{K}^{e}_{\alpha d} & \boldsymbol{K}^{e}_{\alpha\alpha} \end{bmatrix}^{e,i}_{n+1} \begin{Bmatrix} \Delta\boldsymbol{d}^{e,i}_{n+1} \\ \Delta\boldsymbol{\alpha}^{e,i}_{n+1} \end{Bmatrix} = \begin{Bmatrix} -\boldsymbol{R}^{e,i}_{d,n+1} \\ -\boldsymbol{h}^{e,i}_{n+1} \end{Bmatrix}$$

Člene $\boldsymbol{K}^{e,i}_{dd,n+1}$, $\boldsymbol{K}^{e,i}_{d\alpha,n+1}$, $\boldsymbol{K}^{e,i}_{\alpha d,n+1}$, $\boldsymbol{K}^{e,i}_{\alpha\alpha,n+1}$, $\boldsymbol{R}^{e,i}_{d,n+1}$ in $\boldsymbol{h}^{e,i}_{n+1}$ izračunamo po izrazih (4.117), (4.122) in (4.123).

Parametre širjenja kondenziramo tako, da iz druge enačbe v (4.121) izrazimo $\Delta\boldsymbol{\alpha}^{e,i}_{n+1}$ v odvisnosti od $\Delta\boldsymbol{d}^{e,i}_{n+1}$ kot:

$$\Delta\boldsymbol{\alpha}^{e,i}_{n+1} = -\left[\boldsymbol{K}^{e,i}_{\alpha\alpha,n+1}\right]^{-1}\left(-\boldsymbol{h}^{e,i}_{\alpha,n+1} - \boldsymbol{K}^{e,i}_{\alpha d,n+1}\,\Delta\boldsymbol{d}^{e,i}_{n+1}\right)$$

Če vstavimo zgornjo relacijo v prvo enačbo (4.121), potem dobimo

$$\boldsymbol{K}^{e,i}_{cond,n+1}\Delta\boldsymbol{d}^{e,i}_{n+1} = -\boldsymbol{R}^{e,i}_{cond,n+1}$$

kjer sta

$$\boldsymbol{K}^{e,i}_{cond,n+1} = \boldsymbol{K}^{e,i}_{dd,n+1} - \boldsymbol{K}^{e,i}_{d\alpha,n+1}\left[\boldsymbol{K}^{e,i}_{\alpha\alpha,n+1}\right]^{-1}\boldsymbol{K}^{e,i}_{\alpha d,n+1}$$

$$\boldsymbol{R}^{e,i}_{cond,n+1} = \boldsymbol{R}^{e,i}_{d,n+1} - \boldsymbol{K}^{e,i}_{d\alpha,n+1}\left[\boldsymbol{K}^{e,i}_{\alpha\alpha,n+1}\right]^{-1}\boldsymbol{h}^{e,i}_{n+1}$$

Torej, za element z razpoko, izraza (4.126) in (4.127) vstavimo v (4.119). Rešitev sistema enačb (4.119) za $\Delta\boldsymbol{d}^{e,i}_{n+1}$ in izvrednotenje enačbe (4.124) za $\Delta\boldsymbol{\alpha}^{e,i}_{n+1}$ po elementih $e = 1, \cdots, N^e$, pripelje do novih iterativnih vrednosti za totalne pomike in parametre širjenja razpoke:

$$\boldsymbol{d}^{e,i}_{n+1} = \boldsymbol{d}^{e,i-1}_{n+1} + \Delta\boldsymbol{d}^{e,i}_{n+1}\,, \quad \boldsymbol{\alpha}^{e,i}_{n+1} = \boldsymbol{\alpha}^{e,i-1}_{n+1} + \Delta\boldsymbol{\alpha}^{e,i}_{n+1}$$

Če je dosežena toleranca za konvergenco, potem (4.128) so vozliščni pomiki elementa in parametri razpoke rešitev v τ_{n+1}, sicer se izvede nova iteracija z nastavkom $i+1 \rightarrow i$.

REŠITEV ENAČB ZA Q6 ELEMENT Z VGRAJENO NEZVEZNOSTJO V POMIKIH

Ko ni razpok v mreži N_e končnih elementov, naslednji sistem enačb moramo rešiti za neznane iterativne vozliščne pomike in iterativne nekompatibilne parametre:

$$\mathbb{A}_{e=1}^{N_e}\left(\begin{bmatrix} \boldsymbol{K}^{e}_{dd} & \boldsymbol{K}^{e}_{d\rho} \\ \boldsymbol{K}^{e}_{\rho d} & \boldsymbol{K}^{e}_{\rho\rho} \end{bmatrix}^{e,i}_{n+1} \begin{Bmatrix} \Delta\boldsymbol{d}^{e,i}_{n+1} \\ \Delta\boldsymbol{\rho}^{e,i}_{n+1} \end{Bmatrix}\right) = \mathbb{A}_{e=1}^{N_e}\left(\begin{Bmatrix} -\boldsymbol{R}^{e,i}_{d,n+1} \\ -\boldsymbol{R}^{e,i}_{\rho,n+1} \end{Bmatrix}\right)$$

kjer $\boldsymbol{K}^{e,i}_{dd,n+1}$, $\boldsymbol{K}^{e,i}_{d\rho,n+1}$, $\boldsymbol{K}^{e,i}_{\rho d,n+1}$, $\boldsymbol{K}^{e,i}_{\rho\rho,n+1}$ so (4.130) in $\boldsymbol{\rho}^e = [\rho_{11}, \rho_{12}, \rho_{21}, \rho_{22}]^T$. Vektorja $\boldsymbol{R}^e_d$ in $\boldsymbol{R}^e_\rho$ sta iz (4.102) in (4.112), pri čemer je $\alpha_m = 0$. Sistem (4.129) poenostavimo tako, da izvedemo statično kondenzacijo nekompatibilnih parametrov na nivoju elementa in dobimo naslednje relacije:

$$\Delta\boldsymbol{\rho}_{n+1}^{e,i} = -\left[\boldsymbol{K}_{\rho\rho,n+1}^{e,i}\right]^{-1}\left(-\boldsymbol{R}_{\rho,n+1}^{e,i} - \boldsymbol{K}_{\rho d,n+1}^{e,i}\Delta\boldsymbol{d}_{n+1}^{e,i}\right)$$

in

$$\boldsymbol{K}_{cond,n+1}^{e,i} = \boldsymbol{K}_{dd,n+1}^{e,i} - \boldsymbol{K}_{d\rho,n+1}^{e,i}\left[\boldsymbol{K}_{\rho\rho,n+1}^{e,i}\right]^{-1}\boldsymbol{K}_{\rho d,n+1}^{e,i}$$

$$\boldsymbol{R}_{cond,n+1}^{e,i} = \boldsymbol{R}_{d,n+1}^{e,i} - \boldsymbol{K}_{d\rho,n+1}^{e,i}\left[\boldsymbol{K}_{\rho\rho,n+1}^{e,i}\right]^{-1}\boldsymbol{R}_{\rho,n+1}^{e,i}$$

Zaradi statične kondenzacije nekompatibilnih parametrov na nivoju elementa, sistem ravnotežnih enačb (4.129) nadomestimo s:

$$\mathbb{A}_{e=1}^{N_e}\left(\boldsymbol{K}_{cond,n+1}^{e,i}\Delta\boldsymbol{d}_{n+1}^{e,i}\right) = \mathbb{A}_{e=1}^{N_e}\left(-\boldsymbol{R}_{cond,n+1}^{e,i}\right)$$

in (4.131). Rešitev kondenziranega sistema (4.133) vrne iterativni popravek pomikov $\Delta\boldsymbol{d}_{n+1}^{e,i}$, ki ga uporabimo v enačbi (4.131) za izračun iterativnih popravkov nekompatibilnih parametrov $\Delta\boldsymbol{\rho}_{n+1}^{e,i}$. Za elemente $e = 1, \cdots, N^e$ izračunamo nove iterativne vrednosti totalnih pomikov in nekompatibilnih parametrov:

$$\boldsymbol{d}_{n+1}^{e,i} = \boldsymbol{d}_{n+1}^{e,i-1} + \Delta\boldsymbol{d}_{n+1}^{e,i}, \qquad \boldsymbol{\rho}_{n+1}^{e,i} = \boldsymbol{\rho}_{n+1}^{e,i-1} + \Delta\boldsymbol{\rho}_{n+1}^{e,i}$$

Če je toleranca za konvergenco dosežena, potem so zgornji vozliščni pomiki elementa in nekompatibilni parametri (4.134) rešitev v τ_{n+1}, sicer se izvede nova iteracija z nastavkom $i + 1 \rightarrow i$.

Ko je v mreži končnih elementov eden ali več elementov z razpoko, potem je potrebno rešiti naslednji sistem enačb za iterativne vozliščne pomike:

$$\mathbb{A}_{e=1}^{N_e}\left(\boldsymbol{K}_{cond,n+1}^{e,i}\Delta\boldsymbol{d}_{n+1}^{e,i}\right) = \mathbb{A}_{e=1}^{N_e}\left(-\boldsymbol{R}_{cond,n+1}^{e,i}\right)$$

Za element *e* brez razpoke prispevka $\boldsymbol{K}_{cond,n+1}^{e,i}$ in $\boldsymbol{R}_{cond,n+1}^{e,i}$ sta enaka (4.132). Za elemente z razpoko izvedemo statično kondenzacijo naslednjega sistema enačb, pri čemer kondenziramo nekompatibilne parametre in parametre širjenja razpoke:

$$\begin{bmatrix} \boldsymbol{K}_{dd}^{e} & \boldsymbol{K}_{d\rho}^{e} & \boldsymbol{K}_{d\alpha}^{e} \\ \boldsymbol{K}_{\rho d}^{e} & \boldsymbol{K}_{\rho\rho}^{e} & \boldsymbol{K}_{\rho\alpha}^{e} \\ \boldsymbol{K}_{\alpha d}^{e} & \boldsymbol{K}_{\alpha\rho}^{e} & \boldsymbol{K}_{\alpha\alpha}^{e} \end{bmatrix}_{n+1}^{e,i} \begin{Bmatrix} \Delta\boldsymbol{d}_{n+1}^{e,i} \\ \Delta\boldsymbol{\rho}_{n+1}^{e,i} \\ \Delta\boldsymbol{\alpha}_{n+1}^{e,i} \end{Bmatrix} = \begin{Bmatrix} -\boldsymbol{R}_{d,n+1}^{e,i} \\ -\boldsymbol{R}_{\rho,n+1}^{e,i} \\ -\boldsymbol{h}_{n+1}^{e,i} \end{Bmatrix}$$

Členi $\boldsymbol{K}_{dd,n+1}^{e,i}$, $\boldsymbol{K}_{d\rho,n+1}^{e,i}$, $\boldsymbol{K}_{\rho d,n+1}^{e,i}$, $\boldsymbol{K}_{\rho\rho,n+1}^{e,i}$ so definirani z (4.130), členi $\boldsymbol{K}_{d\alpha,n+1}^{e,i}$, $\boldsymbol{K}_{\rho\alpha,n+1}^{e,i}$, $\boldsymbol{K}_{\alpha d,n+1}^{e,i}$, $\boldsymbol{K}_{\alpha\rho,n+1}^{e,i}$, $\boldsymbol{K}_{\alpha\alpha,n+1}^{e,i}$ pa so definirani z (4.137). Vektorja $\boldsymbol{R}_{d}^{e}$ in $\boldsymbol{R}_{\rho}^{e}$ izračunamo po enačbah (4.102) in (4.112), lokalne ravnotežne enačbe $h_m, m = 1, \cdots, 4$, v $\boldsymbol{h}_{n+1}^{e,i} = [h_1, h_2, h_3, h_4]^T|_{n+1}^{i}$ so podane v (4.107)-(4.110). Razširjeni sistem ravnotežnih enačb za element *e* (4.136) lahko zapišemo v kompaktni obliki:

$$\begin{bmatrix} \boldsymbol{K}^e_{dd} & \boldsymbol{K}^e_{d\beta} \\ \boldsymbol{K}^e_{\beta d} & \boldsymbol{K}^e_{\beta\beta} \end{bmatrix}^i_{n+1} \begin{Bmatrix} \Delta\boldsymbol{d}^{e,i}_{n+1} \\ \Delta\boldsymbol{\beta}^{e,i}_{n+1} \end{Bmatrix} = -\begin{Bmatrix} \boldsymbol{R}^{e,i}_{d,n+1} \\ \boldsymbol{R}^{e,i}_{\beta,n+1} \end{Bmatrix}$$

kjer so

$$\boldsymbol{K}^{e,i}_{\beta\beta,n+1} = \begin{bmatrix} \boldsymbol{K}^e_{\rho\rho} & \boldsymbol{K}^e_{\rho\alpha} \\ \boldsymbol{K}^e_{\alpha\rho} & \boldsymbol{K}^e_{\alpha\alpha} \end{bmatrix}^i_{n+1} \qquad \boldsymbol{K}^{e,i}_{d\beta,n+1} = [\boldsymbol{K}^e_{d\rho} \quad \boldsymbol{K}^e_{d\alpha}]^i_{n+1} \qquad \boldsymbol{K}^{e,i}_{\beta d,n+1} = \begin{bmatrix} \boldsymbol{K}^e_{\rho d} \\ \boldsymbol{K}^e_{\alpha d} \end{bmatrix}^i_{n+1}$$

in

$$\Delta\boldsymbol{\beta}^{e,i}_{n+1} = \begin{Bmatrix} \Delta\boldsymbol{\rho}^{e,i}_{n+1} \\ \Delta\boldsymbol{\alpha}^{e,i}_{n+1} \end{Bmatrix} \qquad \boldsymbol{R}^{e,i}_{\beta,n+1} = \begin{Bmatrix} \boldsymbol{R}^{e,i}_{\rho,n+1} \\ \boldsymbol{h}^{e,i}_{n+1} \end{Bmatrix}$$

Statična kondenzacija sistema enačb (4.138) vrne naslednje enačbe:

$$\Delta\boldsymbol{\beta}^{e,i}_{n+1} = -\left[\boldsymbol{K}^{e,i}_{\beta\beta,n+1}\right]^{-1}\left(-\boldsymbol{R}^{e,i}_{\beta,n+1} - \boldsymbol{K}^{e,i}_{\beta d,n+1}\Delta\boldsymbol{d}^{e,i}_{n+1}\right)$$

in

$$\boldsymbol{K}^{e,i}_{cond,n+1} = \boldsymbol{K}^{e,i}_{dd,n+1} - \boldsymbol{K}^{e,i}_{d\beta,n+1}\left[\boldsymbol{K}^{e,i}_{\beta\beta,n+1}\right]^{-1}\boldsymbol{K}^{e,i}_{\beta d,n+1}$$

$$\boldsymbol{R}^{e,i}_{cond,n+1} = \boldsymbol{R}^{e,i}_{d,n+1} - \boldsymbol{K}^{e,i}_{d\beta,n+1}\left[\boldsymbol{K}^{e,i}_{\beta\beta,n+1}\right]^{-1}\boldsymbol{R}^{e,i}_{\beta,n+1}$$

Za element *e* z razpoko, izrazi (4.140) so uporabljeni v (4.135). Rešitev sistema enačb (4.135) za $\Delta\boldsymbol{d}^{e,i}_{n+1}$ in izvrednotenje enačbe (4.139) za $\Delta\boldsymbol{\rho}^{e,i}_{n+1}$ in $\Delta\boldsymbol{\alpha}^{e,i}_{n+1}$, po elementih $e = 1, \cdots, N^e$, pripelje do novih iterativnih vrednosti za totalne pomike, nekompatibilne parametre in parametre širjenja razpoke:

$$\boldsymbol{d}^{e,i}_{n+1} = \boldsymbol{d}^{e,i-1}_{n+1} + \Delta\boldsymbol{d}^{e,i}_{n+1}, \;\; \boldsymbol{\rho}^{e,i}_{n+1} = \boldsymbol{\rho}^{e,i-1}_{n+1} + \Delta\boldsymbol{\rho}^{e,i}_{n+1}, \;\; \boldsymbol{\alpha}^{e,i}_{n+1} = \boldsymbol{\alpha}^{e,i-1}_{n+1} + \Delta\boldsymbol{\alpha}^{e,i}_{n+1}$$

Če je toleranca za konvergenco dosežena, potem so zgornji vozliščni pomiki elementa, nekompatibilni parametri in parametri širjenja razpoke (4.141) rešitev v τ_{n+1}, sicer se izvede nova iteracija z nastavkom $i + 1 \rightarrow i$.

TANGENTNI OPERATOR ZA KOHEZIVNE NAPETOSTI

V poglavju 4.5.3 smo izpeljali eksplicitna izraza za t.i. tangentna operatorja $\left.\frac{\partial t_n}{\partial \bar{\bar{u}}}\right|^i_{n+1}$ in $\left.\frac{\partial t_m}{\partial \bar{\bar{v}}}\right|^i_{n+1}$, ki nastopata v matriki $\boldsymbol{K}^{e,i}_{\alpha\alpha,n+1} = \left.\frac{\partial \boldsymbol{h}^e}{\partial \boldsymbol{\alpha}^e}\right|^i_{n+1}$, glej enačbi (4.121) in (4.136). Izrazimo ju kot:

$$\left.\frac{\partial t_n}{\partial \bar{\bar{u}}}\right|^i_{n+1} = \frac{\partial t_n}{\partial \bar{\bar{\gamma}}_n} \cdot \left.\frac{\partial \bar{\bar{\gamma}}_n}{\partial \bar{\bar{u}}}\right|^i_{n+1} = \left[\frac{\frac{\partial \bar{\bar{q}}_n}{\partial \bar{\bar{\gamma}}_n}}{\bar{\bar{Q}}_n \cdot \left(\bar{\bar{u}} \cdot \frac{\partial \left(\bar{\bar{Q}}_n\right)^{-1}}{\partial \bar{\bar{\gamma}}_n} + \frac{\partial \bar{\bar{q}}_n}{\partial \bar{\bar{\gamma}}_n}\right)}\right]^i_{n+1}$$

$$\left.\frac{\partial t_m}{\partial \bar{\bar{v}}}\right|_{n+1}^{i} = \frac{\partial t_m}{\partial \bar{\bar{\gamma}}_m} \cdot \left.\frac{\partial \bar{\bar{\gamma}}_m}{\partial \bar{\bar{v}}}\right|_{n+1}^{i} = \left[\frac{\frac{\partial \bar{\bar{q}}_m}{\partial \bar{\bar{\gamma}}_m}}{\bar{\bar{Q}}_m \cdot \left(sign\left[t_{m,n+1}^{i}\right] \cdot \bar{\bar{v}} \cdot \frac{\partial \left(\bar{\bar{Q}}_m\right)^{-1}}{\partial \bar{\bar{\gamma}}_m} + \frac{\partial \bar{\bar{q}}_m}{\partial \bar{\bar{\gamma}}_m} \right)}\right]_{n+1}^{i}$$

PRIMERJAVA G OPERATORJEV

Ko je nezveznost vgrajena v element, je potrebo rešiti lokalne ravnotežne enačbe (4.54). G operatorji imajo pomembno vlogo v ravnotežnih enačbah: povezujejo kohezivne napetosti v razpoki in napetosti v elementu. Na enostavnem kvadratnem končnem elementu smo numerično in grafično primerjali funkcije G operatorjev, ki smo jih izpeljali v poglavju 4.2. Označimo jih z [G-Dujc] (poglavje 4.2.3.1) in [G-Linder] (poglavje 4.2.3.2). Pri tem smo obravnavali dve situaciji, ki se razlikujeta v tem, kako razpoka prečka element (Element A). V prvem načinu razpoka prečka element tako, da gre vertikalno skozi center elementa in seka nasprotna robova (Element B). Druga situacija pa zajema razpoko, ki seka sosednja robova v elementu. Če razpoka prečka nasprotna robova elementa (Element A), potem sta [G-Dujc] in [G-Linder] enaka operatorja samo za konstantna načina širjenja razpoke (n0 in m0). V ostalih primerih (Element A – linearen način širjenja, Element B - vsi načini širjenja razpoke) pa sta [G-Dujc] in [G-Linder] povsem različna G-operatorja.

ENOSTAVNI (ENO- IN DVOELEMENTNI) TESTI ZA ŠTIRIVOZLIŠČNE KONČNE ELEMENTE Z VGRAJENO MOČNO NEZVEZNOSTJO

Izvedli smo dve različni skupini testov za novo izpeljane štirivozliščne končne elemente z vgrajeno nezveznostjo (Q4 in Q6). V prvem delu smo na enostavnih primerih izvedli osnovne teste delovanja vektorjev $\widehat{\boldsymbol{G}}_m$, $m = 1, \ldots, 4$, ki nastopajo v lokalni ravnotežni enačbi na razpoki ((4.68)-(4.71) in (4.107)-(4.110)). Pripravili smo enostavne modele z enim oziroma največ dvema končnima elementoma in izračunali natezni test, upogibni test in strižni test. Upogibni test pokaže, da metoda nekompatibilnih oblik zelo izboljša obnašanje elementov. Prišli smo do ugotovitve, da so za način širjenja razpoke v linearnem načinu Mode I najbolj primerni vektorji $\widehat{\boldsymbol{G}}_m$ iz (Dujc et al., 2010) in za način širjenja razpoke v linearnem Mode II pa vektorji $\widehat{\boldsymbol{G}}_m$ iz (Linder in Armero, 2007).

NUMERIČNI PRIMERI ZA ŠTIRIVOZLIŠČNE KONČNE ELEMENTE Z VGRAJENO MOČNO NEZVEZNOSTJO

V drugi skupini numeričnih primerov za ravninske končne elemente z vgrajeno nezveznostjo smo pri modeliranju upoštevali ugotovitve iz predhodnega poglavja. Obravnavali smo t.i. velike primere: tri-točkovni test, štiri-točkovni test in test Nooru-Mohamed. V nalogi so predstavljeni rezultati analiz z

algoritmom za sledenje razpoki (Slika 4.6) in brez. Najbolj uspešne simulacije so izvedene v kombinaciji z algoritmom za sledenje razpoki. Po drugi strani pa analiza brez algoritma vrne napačne rešitve. Namreč, porazdelitev razpok po mreži končnih elementov (vzorci razpok) in njihova usmerjenost se kažejo na to, da se mehanizem širjenja razpok v konstrukciji ne more razviti na jasen način. To rezultira v napačen odziv modela po določenem številu razpokanih elementov.

ZAKLJUČKI

Doktorska disertacija obravnava: (i) metode za porušno analizo trdnih teles in konstrukcij, ter (ii) končne elemente z vgrajeno močno nezveznostjo za modeliranje materialne porušitve v kvazi-krhkih 2d trdnih telesih.

Za porušno analizo smo najprej preučili konsistentno linearizirano metodo sledenja ravnotežne poti s kvadratno vezno enačbo (metoda krožnega loka). Izraz »konsistentno linearizirano« pomeni, da so vse enačbe (t.j. ravnotežne enačbe in vezna enačba) linearizirane, ko iščemo rešitev sistema po metodi sledenja ravnotežne poti. Metoda omogoča izračun analize nelinearnih modelov, ki imajo izrazito nelinearno ravnotežno pot. Kljub temu standardne metode sledenja poti lahko odpovedo, kadar analiziramo nelinearne probleme z lokalizirano materialno porušitvijo (mehčanje materiala). Zato smo izpeljali nove različice metode sledenja poti z drugimi veznimi enačbami, ki so bolj primerne za probleme z lokalizirano porušitvijo materiala. Ena različica temelji na adaptivni vezni enačbi, pri kateri vodimo izbrano prostostno stopnjo. Izkazalo se je, da je metoda relativno uspešna pri analizi problemov z materialnim mehčanjem, ki so modelirani s končnimi elementi z vgrajeno nezveznostjo. Kontrolna prostostna stopnja se lahko zamenja v vsakem inkrementu. Predstavili smo postopek izbire prostostne stopnje, ki nastopa v vezni enačbi.

Izpeljali smo eksplicitne vezne enačbe in implicitno vezno enačbo, ki temeljijo na kontroli plastične disipacije ali plastičnega dela v neelastičnem trdnem telesu ali konstrukciji. Nova metoda za sledenje poti se je v nekaterih primerih pokazala za boljšo od standardne metode ločne dolžine. Slednja metoda včasih dopušča neželjeno razbremenjevanje celotne konstrukcije. To se ne more zgoditi z metodo sledenja ravnotežne poti, pri kateri vodimo disipacijo, saj elastično razbremenjevanje celotne konstrukcije ni možno.

Izpeljali smo štirikotni končni element z vgrajeno nezveznostjo za 2d probleme v ravninskem napetostnem stanju in ravninskem deformacijskem stanju. Pri tem smo se omejili na krhke materiale kot so beton, opeka in kamen, zato smo privzeli poškodbeni zakon mehčanja. Formulacija omogoča širjenje razpok obeh načinih (tip I in tip II).

Za osnovno formulacijo štirikotnega elementa smo vzeli bodisi klasično, ki temelji na pomikih, bodisi izboljšano z nekompatibilnimi pomiki. Dodatno smo preverili dva predloga za G-operatorje iz (Dujc et al., 2010) in (Linder in Armero, 2007). Izvedli smo enostavne male teste, da bi preverili učinkovitost modela z vgrajeno nezveznostjo, ko je mehčanje aktivno. Glede na rezultate malih testov, priporočamo uporabo G-operatorjev iz (Dujc et al., 2010) za vse načine širjenja razpoke razen za linearno širjenje razpoke v tangentni smeri (m1). Za linearen način širjenja razpoke v smeri tangente priporočamo G-operator iz (Linder in Armero, 2007). Kakorkoli, način širjenja razpoke v smeri tangente je potrebno še raziskati.

Raziskali smo tudi širjenje razpoke med analizo. Predlagali smo algoritem za sledenje razpoki, ki naredi da so razpoke povezane na nivoju mreže. Eden ali več elementov lahko razvije razpoko v enem inkrementu. Algoritem omogoča sledenje eni ali več zveznim razpokam v mreži končnih elementov. Numerični primeri pokažejo, da najboljšo izvedbo analize dosežemo, če uporabimo algoritem za sledenje razpoki. Analiza brez algoritma za sledenje razpoki vrne napačne rezultate. Namreč, porazdelitev razpok po mreži končnih elementov (vzorec razpok) in njihove orientacije se zdijo kakor, da se mehanizem razpokanosti v konstrukciji ne more jasno manifestirati. To vodi v napačen odziv modela po nekaj razpokanih elementih.

Metoda nekompatibilnih oblik občutno izboljša obnašanje končnih elementov z vgrajeno nezveznostjo v upogibnih primerih. Za kombinirane probleme (4-točkovni upogibni test in Nooru Mohamedov test) so najboljši končni elementi, ki dovoljujejo samo konstantne načine širjenja razpok.

BIBLIOGRAPHY

ABAQUS Analysis User's Manual, Version 6.13; 2015.

Alfano, G., Crisfield, M.A. 2001. Finite element interface models for the delamination analysis of laminated composites: mechanical and computational issues. International Journal for Numerical Methods in Engineering 50: 1701-1736.

Alfano, G., Crisfield, M.A. 2003. Solution strategies for the delamination analysis based on a combination of local-control arc-length and line searches. International Journal for Numerical Methods in Engineering 58: 999-1048.

Armero, F., Ehrlich, D. 2006. Numerical modeling of softening hinges in thin EulerBernoulli beams. Computers and Structures 84: 641-656.

Arrea, M., Ingraffea, A.R. 1982. Mixed-mode Crack Propagation in Mortar and Concrete, Report No. 81-13, Department of Structural Engineering, Cornell University, Ithaca, New York.

Bathe, K.-J., Dvorkin, E. 1985. A Four-Node Plate Bending Element Based on Mindlin/Reissner Plate Theory and Mixed Interpolation, International Journal for Numerical Methods in Engineering 21: 367-383.

Betsch, P., Menzel, A., Stein, E. 1998. On the parametrization of finite rotations in computational mechanics - A classification of concepts with application to smooth shells, Computer Methods in Applied Mechanics and Engineering 155: 273-305.

Brancherie, D., Ibrahimbegovic, A. 2009. Novel anisotropic continuum-discrete damage model capable of representing localized failure of massive structures: Part I: theoretical formulation and numerical implementation. Engineering Computations 26: 100–127.

Brank, B., Damjanić, F.B., Perić, D. 1995. On implementation of a nonlinear four node shell finite element for thin multilayered elastic shells., Computational Mechanics 16: 341-359.

Brank, B., Perić, D., Damjanić, F. 1997. On large deformations of thin elasto-plastic shells: implementation of a finite rotation model for quadrilateral shell element. International journal for numerical methods in engineering 40: 689-726.

Brank, B., Carrera, E. 2000. A family of shear-deformable shell finite elements for composite structures. Computers and Structures 76: 287-297.

Brank, B. Ibrahimbegovic, A. 2001. On the relation between different parametrizations of finite rotations for shells. Engineering Computations 18: 950-973.

Brank, B., Korelc, J., Ibrahimbegovic A. 2002. Nonlinear shell problem formulation accounting for through-the-thickness stretching and its finite element implementation. Computers and Structures 80: 699-717.

Brank, B. 2005. Nonlinear shell models with seven kinematic parameters. Computer Methods in Applied Mechanics and Engineering 194: 2336-2362.

Brank, B. 2008. Assessment of 4-node EAS-ANS shell elements for large deformation analysis. Computational Mechanics 42: 39-51.

Brank, B., Stanić, A., Ibrahimbegovic, A. 2016. A path-following method based on plastic dissipation control. Computational Methods in Applied Sciences, volume 41: 29-47.

Bude, J. 2015. Ductile fracture simulation using the strong discontinuity method. Université de Technologie de Compiègne, France: 178 p.

Carrera, E. 1994. A study on arc-length-type methods and their operation failures illustrated by a simple model. Computers and Structures 50: 217-229.

Caseiro, J.F., Alves de Sousa, R.J., Valente, R.A.F. 2013. A systematic development of EAS three-dimensional finite elements for the alleviation of locking phenomena. Finite Elements in Analysis and Design 73: 30-40.

Crisfield, M.A. 1981. A fast incremental/iterative solution procedure that handles 'snap-through'. Computers and Structures 13: 55-62.

Crisfield, M.A. 1991. Non-linear Finite Element Analysis of Solids and Structures, Vol. 1: Essentials. Chichester, John Wiley & Sons: 345 p.

Crisfield, M.A., Peng, X. 1996, Instabilities induced by coarse meshes for a nonlinear shell problem, Engineering Computations 13: 110-114.

Crisfield, M.A. 1997. Non-linear Finite Element Analysis of Solids and Structures, Vol. 2: Advanced topic., Chichester, John Wiley & Sons: 494 p.

de Borst, R. 1987. Computation of post-bifurcation and post-failure behavior of strain-softening solids. Computers and Structures 25 (2): 211-224.

de Souza Neto, E.A., Feng, Y.T. 1999. On the determination of the path direction for arc-length methods in the presence of bifurcations and »snap-backs«. Computer Methods in Applied Mechanics and Engineering 179: 81-89.

Dujc, J., Brank, B. 2008. On stress resultant plasticity and viscoplasticity for metal plates. Finite Elements in Analysis and Design. 44 (4): 174-185.

Dujc, J., Brank, B., Ibrahimbegovic, A. 2010. Multi-scale computational model for failure analysis of metal frames that includes softening and local buckling. Computer Methods Applied Mechanics and Engineering 199 (21-22): 1371-1385.

Dujc, J., Brank, B., Ibrahimbegovic, A. 2010b. Quadrilateral finite element with embedded strong discontinuity for failure analysis of solids. Computer Modeling in Engineering and Sciences 69 (3): 223-259.

Dujc, J., Brank, B. 2012. Stress resultant plasticity for shells revisited. Computer Methods in Applied Mechanics and Engineering 247/248: 146-165.

Dujc, J., Brank, B., Ibrahimbegovic, A. 2013. Stress-hybrid quadrilateral finite element with embedded strong discontinuity for failure analysis of plane stress solids. International Journal for Numerical Methods in Engineering 94 (12): 1075-1098.

Eriksson, A. 1989. On linear constraints for Newton-Raphson corrections and critical point searches in structural F.E. problems. International Journal for Numerical Methods in Engineering 28 (6): 1317-1334.

Eriksson, A. 1998. Structural instability analyses based on generalised path-following. Computer Methods in Applied Mechanics and Engineering 156 (1-4): 45-74.

Eriksson, A., Pacoste, C., Zdunek, A. 1999. Numerical analysis of complex instability behaviour using incremental-iterative strategies. Computer Methods in Applied Mechanics and Engineering 179 (3-4): 265-305.

Feng, Y.T, Perić, D., Owen, D.R.J. 1995. Determination of travel directions in path-following methods. Mathematical Computer Modelling 21 (7): 43-59.

Feng, Y.T, Perić, D., Owen, D.R.J. 1996. A new criterion for determination of initial loading parameter in arc-length methods. Computers and Structures 58 (3): 479-485.

Geers, M.G.D. 1999. Enhanced solution control for physically and geometrically non-linear problems. Part I-The subplane control approach. International Journal for Numerical methods in Engineering, 46: 177-204.

Geers, M.G.D. 1999b. Enhanced solution control for physically and geometrically non-linear problems. Part II-Comparative performance analysis, 46: 205-230.

Ibrahimbegovic, A., Wilson, E.L. 1991. A modified method of incompatible modes. Communications in Applied Numerical Methods, 7: 187-194.

Ibrahimbegovic, A., Taylor, R.L. 2002. On the role of frame-invariance in structural mechanics models at finite rotations. Computer methods in applied mechanics and engineering, 191: 5159-5176.

Ibrahimbegovic, A. 2009. Nonlinear Solid Mechanics. Theoretical Formulations and Finite Element Solution Methods. Dordrecht, Springer: 574 p.

Ibrahimbegovic, A., Brank, B., Courtois, P. 2001. Stress resultant geometrically exact form of classical shell model and vector-like parametrization of constrained finite rotations, International Journal for Numerical Methods in Engineering 52: 1235-1252.

Jelenić, G., Saje, M. 1995. A kinematically exact space finite strain beam model – finite element formulation by generalized virtual work principle, Computer Methods Applied Mechanics and Engineering 120: 131-161.

Jelenić, G., Crisfield, M.A. 1999. Geometrically exact 3D beam theory: implementation of a strain-invariant finite element for statics and dynamics, Computer Methods Applied Mechanics and Engineering 171: 141-171.

Jirásek, M. 2000. Comparative study on finite elements with embedded discontinuities. Computer methods in applied mechanics and engineering 188: 307-330.

Jun, S.M., Hong, C.S. 1988. Buckling behavior of laminated composite cylindrical panels under axial compression. Computers and Structures 29: 479–490.

Jukić, M., Brank, B., Ibrahimbegovic, A. 2013. Embedded discontinuity finite element formulation for failure analysis of planar reinforced concrete beams and frames. Engineering Structures 50: 115-125.

Jukić, M., Brank, B., Ibrahimbegovic, A. 2014. Failure analysis of reinforced concrete frames by beam finite element that combines damage, plasticity and embedded discontinuity. Engineering Structures 75: 507-527.

Kegl, M., Brank, B., Harl, B., Oblak, M. 2008. Efficient handling of stability problems in shell optimization by asymmetric 'worst-case' shape imperfection. International Journal for Numerical Methods in Engineering 73: 1197-1216.

Korelc, J. 2010. Direct computation of critical points based on Crout's elimination and diagonal subset test function. Computers and Structures 88: 189-197.

Korelc, J. 2015. AceGen manual, AceFEM manual. Available at http://symech.fgg.uni-lj.si/

Kouhia, R., Mikkola, M. 1999. Tracing the equilibrium path beyond compound critical points. International Journal for Numerical Methods in Engineering 46: 1049-1074.

Linder, C., Armero, F. 2007. Finite elements with embedded strong discontinuities for the modeling of failure in solids. International Journal for Numerical Methods in Engineering 72: 1391-1433.

Lopez S. 2002. Post-critical analysis of structures with a nonlinear pre-buckling state in the presence of imperfections. Computer Methods in Applied Mechanics and Engineering 191: 4421-4440.

Manzoli O.L., Shing, P.B. 2006. A general technique to embed non-uniform discontinuities into standard solid finite elements. Computers and Structures 84: 742-757.

Mosler, J. 2004. On the modelling of highly localized deformations induced by material failure: the strong discontinuity approach. Archives of Computational Methods in Engineering 11 (4): 389-446.

Noguchi, H., Fujii, F. 2003. Eigenvector-free indicator, pinpointing and branch-switching for bifurcation. Communication in Numerical Methods in Engineering 19 (6): 445-457.

Nooru-Mohamed, M. B. 1992. Mixed-mode fracture of concrete: an experimental approach. Delft University of Technology, Delft: 151 p.

Ohsaki M., Ikeda K. 2007. Stability and optimization of structures. Generalized sensitivity analysis. New York, Springer: 269 p.

Parente Junior, E., de Holanda, A.S., Bastos Afonso da Silva, S.M. 2006. Tracing nonlinear equilibrium paths of structures subjected to thermal loading. Computational Mechanics 38 (6): 505-520.

Petersson, P. E. 1981. Crack growth and development of fracture zones in plain concrete and similar materials. Report No. TVBM-1006, Division of Building Materials, University of Lund, Lund, Sweden, 1981.

Pian, T., Sumihara, K. 1985. Rational approach for assumed stress finite elements. International Journal for Numerical Methods in Engineering 20: 1685-1695.

Piculin, S., Brank, B. 2015. Weak coupling of shell and beam computational models for failure analysis of steel frames. Finite elements in analysis and design 97: 20-42.

Pirmanšek, K., Češarek, P., Zupan, D., Saje, M. 2017. Material softening and strain localization in spatial geometrically exact beam finite element method with embedded discontinuity. Computers and Structures 182: 267-283.

Pohl, T., Ramm, E., Bischoff, M. 2014. Adaptive path following schemes for problems with softening. Finite elements in analysis and design 86: 12-22.

Ramm, E. 1981. Strategies for tracing nonlinear response near limit points. In: Wunderlich, W., Stein, E., Bathe, K. J. (Eds.). Nonlinear Finite Element Analysis in Structural Mechanics. Springer, New York: 63-89.

Rheinboldt, W.C. 1986. Numerical analysis of parametrized nonlinear equations. New York, Wiley: 299 p.

Rigobello, R., Breves Coda, H., Munaiar Neto, J. 2013. Inelastic analysis of steel frames with a solid-like finite element. Journal of Constructional Steel Research 86: 140-152.

Riks, E. 1979. An incremental approach to the solution of snapping and buckling problems. International Journal of Solids and Structures 15: 529-551.

Ritto-Correa, M., Camotim, D. 2008. On the arc-length and other quadratic control methods: Established, less known and new implementation procedures. Computers and structures 86: 1353-1368.

Rots, J. G., Nauta, P., Kusters, G. M. A., Blaauwendraad. 1985. Smeared crack approach and fracture localization in concrete. Heron 30 (1): 48 p.

Sabir, A.B., Lock, A.C. 1972. The application of finite elements to the large-deflection geometrically nonlinear behaviour of cylindrical shells. In: Brebbia, C. A., Tottenham, H. (Eds.) Variational Methods in Engineering. Southampton University Press, Southampton: 7/54-7/65.

Schweizerhof, K.H., Wriggers, P. 1986. Consistent linearization for path following methods in nonlinear FE analysis. Computer Methods in Applied Mechanics and Engineering 59: 261-279.

Simo, J.C., Fox, D.D. , Rifai, M.S. 1990. On a stress resultant geometrically exact shell model. Part III: Computational aspects of the nonlinear theory. Computer methods in applied mechanics and engineering 79: 21-70.

Simo, J.C., Vu-Quoc, L. 1986. A three-dimensional finite-strain rod model. Part II: Computational aspects. Computer methods in applied mechanics and engineering 58: 79-116.

Simo J.C., Armero F. 1992. Geometrically non-linear enhanced strain mixed methods and the method of incompatible modes. International Journal for Numerical Methods in Engineering 33:1413-1449.

Simo, J.C., Hughes, T.J.R. 2000. Computational Inelasticity. New York. Springer.

Sze, K.Y., Liu, X.H., Lo, S.H. 2004. Popular benchmark problems for geometric nonlinear analysis of shells. Finite Elements in Analysis and Design 40: 1551-1569.

Stanić, A., Brank, B., Korelc, J. 2016. On path-following methods for structural failure problems. Computational Mechanics 58 (2): 281-306.

Stanić, A., Brank, B., Ibrahimbegovic, A. 2016b. A path following method based on plastic dissipation control. In: Ibrahimbegovic, A. (ed.) 2016. Computational Methods for Solids and Fluids, Springer, Computational Methods in Applied Sciences 41: 29 – 47 p.

Stanić, A., Brank, B. 2017. A path-following method for elasto-plastic solids and structures based on control of plastic dissipation and plastic work. Finite Elements in Analysis and Design 123: 1-8.

Thai, H.-T., Kim S.-E. 2009. Large deflection inelastic analysis of space trusses using generalized displacement control method. Journal of Constructional Steel Research 65: 1987-1994.

Verhoosel, C.V., Remmers, J.J.C., Gutierrez, M.A. 2009. A dissipation-based arc-length method for robust simulation of brittle and ductile failure. International Journal for Numerical Methods in Engineering 77: 1290-1321.

Zhou, Y., Stanciulescu I., Eason, T., Spottswood M. 2015. Nonlinear elastic buckling and postbuckling analysis of cylindrical panels, Finite Elements in Analysis and Design 96: 41-50.

Wagner, W., Gruttmann, F. 2005. A robust non-linear mixed hybrid quadrilateral shell element. International Journal for Numerical Methods in Engineering, 64: 635-666.

Wagner, W., Wriggers, P. 1988. A simple method for the calculation of postcritical branches. Engineering Computations 5: 103-109.

Wolfram Research, Inc. 2016. Mathematica. Version 10.4. Wolfram Research, Inc., Champaign, Illinois.

Wriggers, P. 2008. Nonlinear Finite Element Methods. Berlin, Springer: 560 p.

Wriggers, P, Simo, J.C. 1990. A general procedure for the direct computation of turning and bifurcation points. International Journal for Numerical Methods in Engineering 30: 155–167.

Wu, J.-Y., Li, F.-B., Xu, S.-L. 2015. Extended embedded finite elements with continuous displacement jumps for the modeling of localized failure in solids. Computer methods in applied mechanics and engineering 285: 346-378.